DEPARTAMENT D' ENGINYERIA ELECTRÒNICA

USE OF ACOUSTO-OPTIC FILTERS IN IMAGING APPLICATIONS. A CONTRIBUTION TO THE SMARTSPECTRA PROJECT.

JOAN VILA FRANCÉS

UNIVERSITAT DE VALÈNCIA
Servei de Publicacions
2009

Aquesta Tesi Doctoral va ser presentada a València el dia 14 d'octubre de 2009 davant un tribunal format per:

- Dr. Filiberto Plà Bañón
- Dr. Joseph Connell
- Dr. John Arthur Marchant
- Dr. Colin Lyden
- Dr. Luis Gómez Chova

Va ser dirigida per:
Dr. Javier Calpe Maravilla

Dipòsit legal: V-950-2011
I.S.B.N.: 978-84-370-7717-8
Edita: Universitat de València
Servei de Publicacions
C/ Arts Gràfiques, 13 baix
46010 València
Spain
Telèfon:(0034)963864115

PhD THESIS / TESIS DOCTORAL

Use of Acousto-Optic Filters in imaging applications. A contribution to the SmartSpectra Project.

Joan Vila Francés

Thesis Advisor / Director de Tesis
Dr. Javier Calpe Maravilla

Dept. Enginyeria Electrònica. Escola Tècnica Superior d'Enginyeria.
UNIVERSITAT DE VALÈNCIA – ESTUDI GENERAL
Valencia – Junio 2009.

Agradecimientos

La realización de una Tesis doctoral es un largo camino en el cual he encontrado a muchas personas que me ha ayudado a seguir adelante. Gracias a ellas he podido terminar el trabajo de investigación recogido en esta Tesis doctoral.

Agradezco en primer lugar a mi director de Tesis, el Dr. Javier Calpe Maravilla, todo el apoyo y la ayuda que me ha dado para finalizar esta Tesis. Su implicación en este trabajo ha sido absoluta y ha ido mucho más allá de una simple relación académica. Hago extensivos los agradecimientos a todos mis compañeros del Grupo de Procesado Digital de Señales (GPDS) y del Image Processing Laboratory (IPL): Alfredo, Antonio, Emilio, Emma, Gus, Javi, Joseba, Jordi, Jovi, Juan, Juanito, Julia, Manolo, Marsel y Rafa. Especialmente agradezco al Dr. Luis Gómez y a Julia Amorós su colaboración en el procesado de imágenes en MATLAB y sus aportaciones en la revisión del borrador de la Tesis.

No quiero pasar por alto la ayuda del grupo de investigación de Óptica del departamento de Ciencias Experimentales de la Universitat Jaume I, que ha colaborado en la implementación del montaje óptico del instrumento ATFS, uno de los pilares fundamentales de esta Tesis. Igualmente, es justo agradecer el apoyo del resto de los grupos integrantes del consorcio SmartSpectra (Universitat Jaume I, Analog Devices, Cork Institute of Technology, Silsoe Research Institute, Dismuntel), así como la ayuda de Think Spectrally, y muy especialmente la del Dr. Emilio Ribes en la revisión del borrador de la Tesis.

Además de las ayudas en el ámbito académico, ha sido motivador el apoyo incondicional de mi familia y amigos. Agradezco a mis padres el haberme dado la oportunidad de poder defender esta Tesis, y a mis hermanos Alfonso y Paco su apoyo y su paciencia conmigo –especialmente Paco, que no ha podido contar con mi colaboración en muchas ocasiones–. También quiero agradecer el interés de mis amigos: Antonio, Carmen, Consuelo, Gonzalo, Luis, Mauro, Raúl, Vicent y Vives –que dentro de muy poco también pasará por esto–. Por último, agradezco a la persona que más me ha sufrido estos últimos años por culpa de la Tesis, Vicente, por su comprensión y cercanía.

El camino es largo. Pero al ver dónde te ha conducido, quién te ha acompañado y lo que has recorrido y vivido, sabes que merece la pena. Gracias a todos por haber caminado conmigo.

Index

Abstract

This Thesis analyses the use of an acousto-optic tunable filter (AOTF) for the realisation of spectral imaging systems. An AOTF is an electronically tunable spectral bandpass optical filter. It consists on a crystal that, excited with acoustic waves, diffracts and then separates a single wavelength of light from a broadband source. The wavelength of selected light is a function of the frequency of the signal applied to the crystal.

We have implemented a spectral imaging instrument called Autonomous Tunable Filtering System (ATFS) that includes an AOTF in order to acquire multispectral images with a monochrome digital camera. Careful design and calibration permits its use in spectroscopic applications. By using a convenient radio-frequency source, it is possible to configure the spectral filtering performance of the AOTF. This Thesis presents two different excitation techniques: the use of a Direct Digital Synthesiser, and the use of a high-speed Digital-to-Analog Converter. Both methods achieve a configurable broadening of the spectral bandwidth characteristic of the AOTF.

In this Thesis we evaluate the use of AOTF's in spectral imaging applications by means of the implemented instrument. We present a methodology to fully characterise the spectral performance of the AOTF's respect to the parameters of the driving signal, and we apply this methodology for the characterisation of three different AOTF models from different manufacturers. Imaging performance of the AOTF's presents some problems due to their low efficiency and chromatic aberration. However, we propose a methodology to overcome the drawbacks of this filtering technology.

Finally, the Thesis demonstrates this spectral imaging technology in several applications, including the mapping of the spectral reflectance and transmittance indexes of plant leaves, and the multispectral imaging of different objects.

This Thesis concludes that AOTF technology can be successfully applied to spectral imaging systems. Imaging performance of such systems is good, but a proper image processing is needed. Spectral performance of AOTF's is accurate, allowing their use in quantitative measuring applications, although they require a careful calibration process.

Overview

Multispectral imaging is a technique consisting on the analysis of the electromagnetic spectrum of objects. Multispectral imagers collect information as a set of "images". Each image represents a range of the electromagnetic spectrum which is also known as spectral band. These images are then combined forming a three dimensional hyperspectral cube, in which two dimensions represent the spatial domain of the image and the third dimension represents the spectral domain.

In the multispectral imagers of staring type, the spectral information is acquired sequentially by means of a tunable spectral filter put in front of a two-dimensional imaging sensor. There are different tunable filter technologies, being the most important ones the electronically tunable filters and the wheel filters. On the first ones, spectral band selection is achieved by means of an electrical signal, while on the second ones the selection is mechanical. Electrical tunable filters present several advantages over the wheel filters: a higher selection speed and a more flexible band selection.

Two different types of electronically tunable filters exist: Liquid Crystal Tunable Filters (LCTF) and Acousto-Optic Tunable Filter (AOTF). AOTF's are special devices with a birefringent crystal in which the filtered wavelength can be rapidly tuned across a wide spectral range by changing an acoustic wave applied to the crystal. The acoustic wave is generated as a RF electrical signal converted to acoustic by means of a piezoelectric transducer bonded to the crystal. Changing the characteristics of the RF signal allows to electronically tune the filter behaviour, allowing a configurable bandpass selection.

A recent research initiative is trying to apply the multispectral imaging techniques to the industrial and scientific domain. This initiative has led to the development of a European-funding R+D project called SmartSpectra, through which a new concept of imaging spectrometer is being build.

In the context of the SmartSpectra project, this Thesis addresses the implementation of a multispectral imaging sensor based on an AOTF, with a special emphasis on the design of the RF driver. The driver must allow a high flexibility on the signal generation, which means working with a broad range of powers and frequencies, a fast switching time, and a quick and easy configuration. We can summarise the objectives of this work on the following points:

- Study of the AOTF working principle. Analyse how these filters work and how they need to be driven.
- Analysis of the AOTF market and selection of a suitable commercial device. Contact the manufacturers and compare between specifications of different crystals.
- Analysis of the AOTF performance. Study of the real performance of the crystals in terms of efficiency and spectral purity.
- Design of a proper RF driver. The driver will present several novelties over the existing systems:
    - Configurable filtering bandwidth
    - Multiband filtering
- Implementation of a complete multispectral imaging instrument.
- Analysis of the instrument performance.
- Design of algorithms for the pre-processing of the acquired images.

- Evaluation of the instrument on a practical application.

This Thesis summarises all the work carried out by the author on the application of an acousto-optic tunable filter to multispectral imaging. The work has been divided in four parts: (1) an introduction to the work, (2) the implementation of a multispectral imaging system, (3) the evaluation of the system performance, and (4) the summary and conclusions of the finished work:

Part I reviews the problem of multispectral imaging, and describes the working principle of Acousto-Optic Tunable Filters.

Part II describes the implementation of a multispectral imaging system based on an AOTF. We present the developed Autonomous Tunable Filtering System, focussing on the development of the RF driver. The software that controls the instrument is also presented.

Part III evaluates the performance of the implemented system. First, we show the RF performance of the developed RF driver, and then we follow with the characterisation of a number of AOTF devices. This part shows also the spectral performance of the ATFS instrument and finally describes its imaging performance in several applications.

Part IV summarises the accomplished objectives, discusses the main conclusions and proposes future research lines.

During the elaboration of this Thesis, the author has programmed several toolboxes of functions in the MATLAB programming language. Due to the extension of these functions, we have decided to attach a CD to the dissertation document with the listing of all the created functions.

Part I
Introduction

The problem of multispectral imaging

There is an increasing interest on the development of non-invasive analytical methodologies. One of the most promising methodologies is multispectral imaging, which consists on the analysis of the optical spectrum of an object and its rendering on a two-dimensional image. A multispectral image is formed by a three-dimensional dataset where two dimensions represent the spatial coordinates of the object (as pixels in a conventional image) and the third dimension corresponds to the spectral bands. This additional spectral information can be used to identify the primary elements in a scene, improve classification tasks, or estimate biophysical indexes [Treitz, 1999; Casa, 2004; Chang, 2007].

The electromagnetic spectrum is the range of all possible electromagnetic radiation frequencies. The electromagnetic spectrum (usually referred as just spectrum) of an object is the characteristic distribution of electromagnetic radiation either reflected or emitted from that particular object. The electromagnetic spectrum is described by the frequency or wavelength of the electromagnetic waves, where wavelength is inversely proportional to the wave frequency. The electromagnetic radiation is classified into regions depending on their wavelength. From longer to shorter wavelengths, these regions are: radio wave, microwave, infrared, visible spectrum, ultraviolet, X-rays and gamma rays (Figure 1.1).

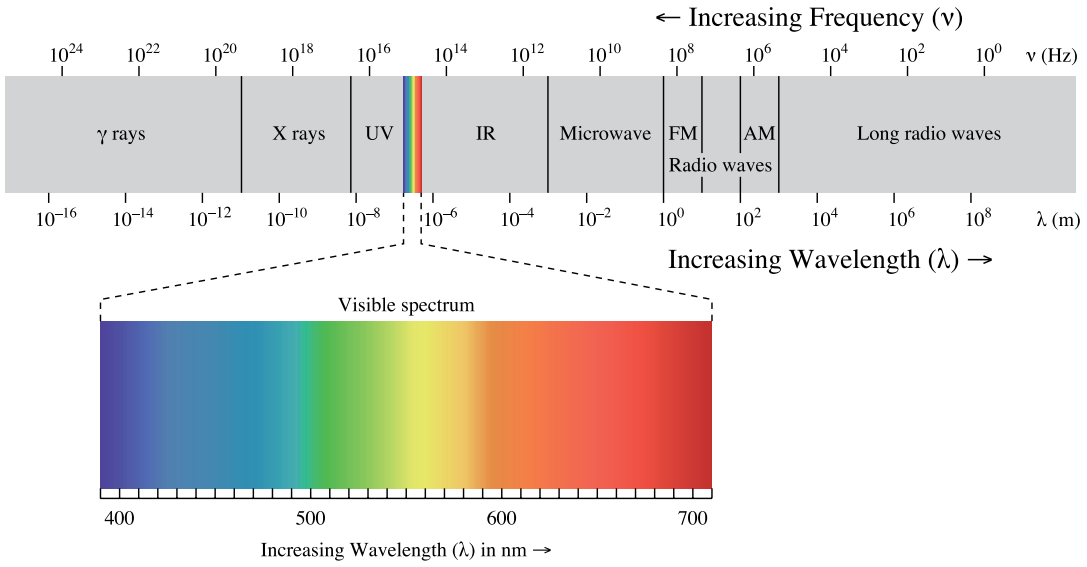

Figure 1.1. Electromagnetic spectrum.

Spectroscopy is the study of electromagnetic radiation that is emitted or reflected from materials and its energy variation with wavelength. During the last years, spectroscopy has revealed itself as a powerful analysis tool in a vast range of scientific and industrial fields. Spectroscopic measurements provide information of the optical spectra that is emitted or interacts in some way with objects. Therefore, spectroscopic information is a non-destructive way of retrieving information about the content or composition of materials. Spectral measurements are used for example in the field of remote sensing [Bowker et al., 1985], chemical analysis [Creaser and Davies, 1988] and industrial applications [Swatland, 1989; Cogdill and Drenne, 2005].

Spectroscopic analysis traditionally covers the spectrum from the ultra-violet (UV) region, 200nm, to the long wave infrared region (LWIR), 10000nm. However, the most used regions are the visible (VIS), 400–700nm, and Near InfraRed region (NIR), 700–1000nm, which are commonly used for imaging spectroscopy; also the Short Wave InfraRed (SWIR), 1000–2500nm, is broadly used for chemical analysis. We should remark that these different regions are usually covered by different sensing technologies since there is no single technology that covers the full spectrum and this poses a challenge when it comes to normalise results both in the spatial domain and in magnitude.

There are three main techniques for generating a multispectral image. The three techniques differ in the sequence in which spatial and spectral information is acquired from the target. In whiskbroom spectrometers (Figure 1.2), the detector is a point spectrometer attached to an electromechanical scanner. The detector measures the spectral information of a single pixel at a time, so that the instrument obtains a complete multispectral image by performing a double scanning in the two spatial dimensions. In pushbroom spectrometers (Figure 1.3), an array of detectors is used to measure one spatial dimension and the spectral dimension at the same time. Therefore, the instrument needs to scan over a single dimension in order to obtain a complete multispectral image. Last of all, staring or framing camera imaging spectrometers (Figure 1.4), use area imaging arrays to collect a two dimensional image where spectral bands are acquired sequentially. Typically, this is achieved by using electronically tunable filters between the target and the imaging sensor, like Acousto-Optic Tunable Filters (AOTF) or Liquid Crystal Tunable Filters (LCTF), or by means of a filter wheel.

Both whiskbroom and pushbroom imagers scan the whole spectral range at the same time, and that implies the same exposure time for all the bands. As the spectral energy can differ greatly between spectral bands, the dynamic range of the sensor needs to be very high. On the other hand, on staring spectrometers, the exposure time can be adjusted for each spectral band to maximise the use of the dynamic range of the sensor. Moreover, the two former methods use moving parts that can be avoided with the use of tunable filters on a staring spectrometer.

While the two first spectroscopy techniques are well-established analytical methodologies, staring imaging spectroscopy is a rather new scientific technique with many potential applications but with some unsolved challenging issues. AOTF's are a promising technology, but its use has been constrained by the problems of the driving signal generation and optical aberrations. This Thesis work is a structured attempt to solve most of these problems and simplify the use of multispectral imaging techniques to the scientific and industrial community. In this work, we present a new imaging spectrometer based on an AOTF that allows the sequential acquisition of spectral images with a configurable bandwidth and central wavelength. This instrument uses two different novel approaches to electronically tune the filter behaviour, using a RF driver based on a Direct Digital Synthesiser (DDS) or a high speed Digital to Analog Converter (DAC).

1.1. Importance of multispectral imaging

The study of the spectral behaviour of matter reveals much more information than the observation within a single or very few broad bands of the spectrum (as in the case of the monochrome –1 band– or colour cameras –3 bands–). Moreover, the use of multispectral imaging can be extended beyond the visible, to the NIR and the SWIR regions of the electromagnetic spectrum.

Nowadays, spectrometry has become very useful in a very broad range of applications. Spectral analysis is effective to estimate the composition of objects from a far observation point or when performing a non-

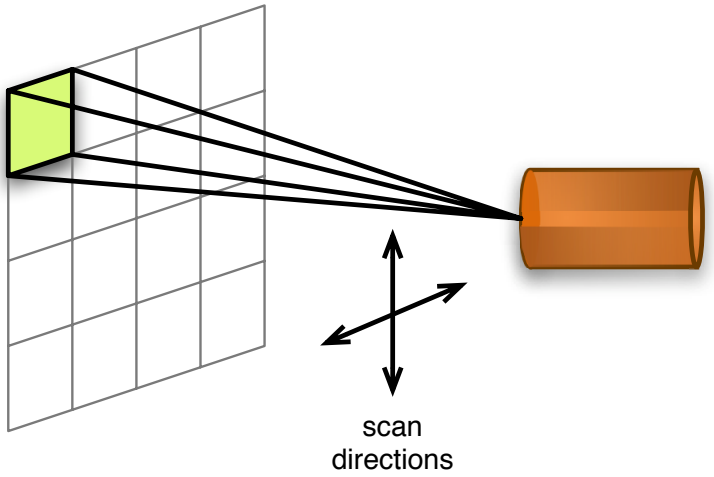

Figure 1.2. Whiskbroom spectrometer. One pixel is acquired at a time for all the spectral bands considered.

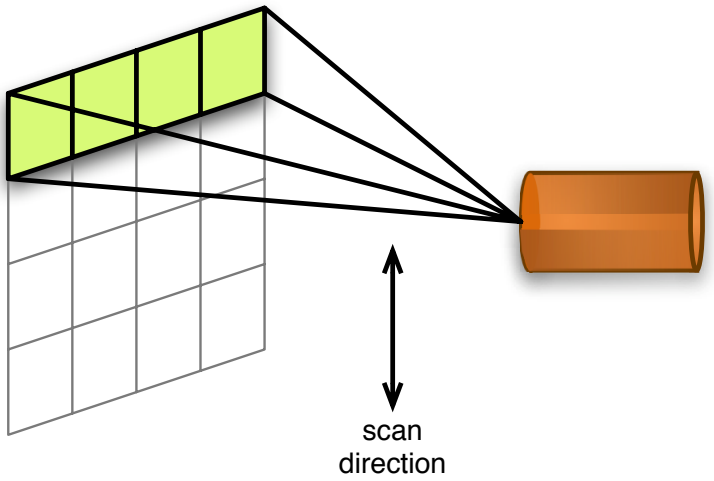

Figure 1.3. Pushbroom spectrometer. One line of pixels is acquired at a time for all the spectral bands considered.

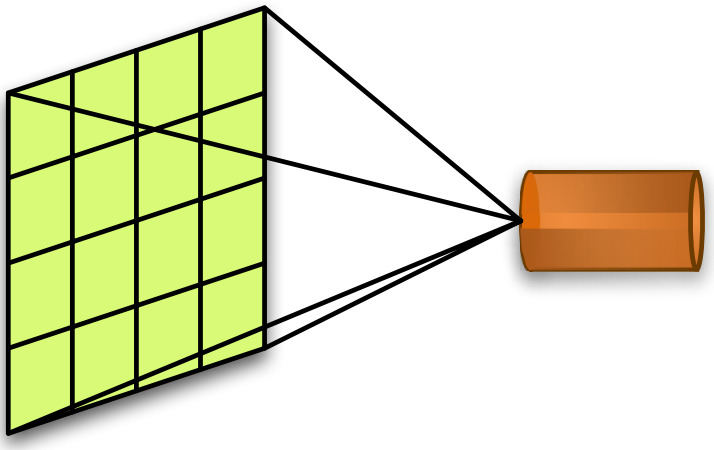

Figure 1.4. Staring imaging spectrometer (also know as framing camera imaging spectrometer). All the pixels are acquired at a time for a single spectral band.

destructive analysis. Therefore, applications of multispectral imaging are commonly found in remote sensing, industrial process control, quality assurance and medical diagnosis. Some examples are:

- **Remote sensing** [Goetz et al., 1985]: VIS/NIR hyperspectral/multispectral[1] images acquired from satellite are used, among others, for crop classification [Gómez-Chova, 2002], biophysical parameters estimation (pigment content, LAI, stomatal conductance…) [Calpe-Maravilla, 2005; Camps-Valls, 2005], urban/non-urban classification [Gómez-Chova, 2004], water quality monitoring [Brando and Dekker, 2003], and geological analysis [Clark, 1999]. Depending on the application, the requirements on the position and width of the bands are different.
- **Industrial machine vision**: Spectral machine vision systems are used in the industry for online precise colour sorting and quality monitoring in real-time applications like manufacturing and assembling lines [Truchetet, 2008; Carlsohn, 2006]. Some industrial applications are:
    - timber and wood product classification based on knots, pitch stripes, blue stain, etc.
    - ceramic tile, marble and other decorative stones in construction
    - leather and furniture
    - paper colour
    - glass or plastic bottle sorting
    - colour in food and drinks: fruit, meat, bread, candy, soft drinks, etc.
    - textile dyeing
    - printing control
    - inspection of colour matching in car parts, cosmetics, etc.
- **Food industry**: the non-invasiveness and high accuracy of multispectral systems make them ideal for quality control on food industrial processes [Chen et al., 2002], as for example on the detection of contamination on poultry carcasses [Park et al., 2001], and real-time food safety control [Gowen et al., 2007].
- **Agriculture**: multispectral imaging can help in monitoring the development and health of crops [Lacar, 2001]. Multispectral data is used also to detect the nutrient and water status of plants [Ferwerda, 2005; Tilling et al., 2007].
- **Medical diagnosis**: Recently, medical diagnosis has started to benefit from multispectral image analysis [Carrasco, 2003], as for example in the examination and classification of tissues [Papadakis et al., 2003]. Satisfactory results have been found in the detection of prostatic cancer cells in prostate biopsy [Manyak et al., 2006]. Similar results are obtained in the detection of human melanoma [Martin, 2006].
- **Investigation on paintings**: hyperspectral imaging is a non-invasive examination method used to retrieve hidden features and identify original painting techniques. [Fischer and Kakoulli, 2006; Pelagotti et al., 2008].
- **Chemical analysis**: multispectral imaging in the NIR region is used as a non-destructive method to analyse the chemical composition of objects. This technique is widely used in the pharmaceutical industry [Hamilton and Lodder, 2002; Grahn and Geladi, 2007] and astronomy [Hillman, 2000]

[1] The terms hyperspectral and multispectral are both referred indifferently to the acquisition of spectral information. The distinction between hyperspectral and multispectral is related to the number of spectral bands. Multispectral data contain from tens to hundreds of bands, while hyperspectral data contain hundreds to thousands of bands. Normally, hyperspectral data are formed by a set of continuous bands, while multispectral data can be formed by a set of optimally chosen spectral bands that are not contiguous and can be collected from different sensors.

1.2. Multispectral imaging systems

This thesis describes the implementation of a framing camera type imaging spectrometer, which scans the spectral plane sequentially while the spatial domain is acquired in both dimensions simultaneously. The result is a three-dimensional image, called hypercube, where one dimension represents the spectral content of the image and the other two corresponds to the spatial domain. This implementation is performed by using a tunable filter that is mounted in front of a monochrome camera producing a stack of images corresponding to different wavelengths.

Among the tunable filters, the electronically tunable filters such as the AOTF or LCTF are the most used ones [Gat, 2000]. On both cases, the filter can change its spectral transmission depending on an electronic signal.

An AOTF consists of a properly oriented birefringent uniaxial crystal to which a piezoelectric transducer is bonded. The application of a RF signal to the transducer produces an acoustic wave that propagates inside the crystal. The travelling acoustic wave modulates the refraction index of the material periodically, due to the elasto-optic effect. The process acts like a volume phase grating, leading to the diffraction of a particular wavelength that satisfies a specific momentum-matching condition inside the birefringent medium. The wavelength filtered by the crystal can be rapidly tuned across a wide spectral range by changing the applied RF signal [Chang, 1976].

An LCTF is based on the Lyot filter design and uses a stack of polarisers and tunable retardation (birefringent) liquid crystal plates [Chrien, 1993; Gat, 2000]. The plates are progressively thicker along the device. Each plate of the stack presents a characteristic transmission when polarised electrically. The resulting transmission of the complete system is the product of the transmission of all the stacks.

The wheel of filters is the last alternative, and consists on a wheel filled with filters with different transmission spectra. As the wheel rotates, different filters are put in front of the sensor. The filter wheel has a very low flexibility and mechanical limitations.

LCTF's and AOTF's are both very flexible in terms of wavelength selection, and present no moving parts. A brief comparison between LCTF's and AOTF's is shown in Table 1.1.

Table 1.1. Comparison between AOTF and LCTF performance [Gat, 2000; Poger and Angelopoulou, 2001; Fellers and Davidson, 2004].

Attributes	LCTF	AOTF
Tunability time	~50ms	1-100 µs
Operating spectral range(*)	400-1800nm	200-5000nm
Max. width of tunable range	450nm (visible and NIR) 950nm (MIR)	700nm (visible and NIR) 3900nm (MIR)
Min. output bandwidth	5nm	0.4nm
Max. output bandwidth	30nm (multispectral designs) 100nm (tri-chromatic designs)	50nm (dependant on the RF driving signal)
Mean error in central wavelength	0.5nm	1nm (varies with wavelength)
Average transmission rate	20-50% (random light)	98% (polarised light)
Range of aperture sizes	20-35mm	3-10mm
Incident light limitations	none	requires collimated light

**Note: the operating spectral range indicates the whole range in which the filter technology can work. However, a single device works on a much smaller range, indicated on the table as the maximum width of tunable range.*

Considering the objectives of this study, we have chosen the AOTF technology for the following reasons:

- AOTF's show better specifications in terms of minimum bandwidth, switching time and efficiency.
- AOTF crystals are more robust than LCTF devices.
- Additionally, the AOTF driving technique allows increasing arbitrarily the bandwidth of the output spectra by combining multiple signals.

1.2.1. State-of-the-art

Several research groups and companies have developed different multispectral imaging systems based on a tunable filter.

A commercial multispectral system based on LCTF is available from Opto-Knowledge Systems Inc. (www.oksi.com). The system is formed by a VIS or NIR LCTF from Cambridge Research & Instrumentation Inc. (www.cri-inc.com) coupled to a standard C-mount camera, and the control and acquisition software on the computer side [Gat, 2000].

Scientific spectral imagers based on AOTF have been built by different research groups from diverse backgrounds. J. Romier [Romier et al., 1998] has built an AOTF-based imaging system for remote sensing applications. On the field of military applications, the group headed by N. Gupta (U.S. Army Research Lab.) and L.J. Denes (Carnegie Mellon Research Institute) has developed a spectro-polarimetric imager [Gupta, 1999]. The astronomical use of AOTF imagers is exploited by V.Y. Molchanov, from the Acousto-Optical Research Center (Moscow Institute of Steel and Alloys) [Molchanov, 2002]. They have developed several hyperspectral imagers to be attached to telescopes. In the medical field, AOTFs are typically used in microscopy systems [Farkas and Becker, 2001]. A commercial AOTF-based spectral imaging system is manufactured by Brimrose Corp. (www.brimrose.com). This system has a broad working range (400-1000nm) thanks to the use of two transducers, but this fact degrades the efficiency of the crystal [Calpe et al, 2006]. Moreover, this system has a poor optical implementation and does not provides a proper acquisition and control software.

1.3. The SmartSpectra project

In the context of the multispectral imaging, a new concept of imaging spectrometer has been built. This spectrometer has been developed under a RTD project supported by the European Commission. The project, called SmartSpectra[2], consisted on the design of a new imaging spectrometer instrument, the development of all the needed software for image correction, processing and analysis, and the technology demonstration on several applications. The author has led the design and development of the SmartSpectra instrument, named Autonomous Tunable Filtering System (ATFS).

The SmartSpectra instrument was conceived as a smart multispectral system that fits somewhere between conventional imaging (monochrome and colour) and spectroscopy. The ATFS instrument acts as a digital filter which, coupled to a camera, acquires sequentially spectral bands with fully configurable central wavelength and bandwidth from snapshot to snapshot, in the range of 400nm to 1000nm. Each band can be as narrow as 5nm or as wide as an RGB band (100nm). At the same time, the specificity on the band selection reduces the global acquisition time yet maintaining the relevant spectral information. The use of a specifically developed software application also reduces the subsequent processing time, encouraging the use of the system in real-time applications. SmartSpectra technology is somehow affordable while assuring robustness. The system is intended to make multispectral techniques accessible to industrial, environmental, and commercial applications.

[2] SmartSpectra is a RTD project supported by the European Commission under the Information Society Technologies Programme (Fifth Framework). The aim of the project is the design and implementation of a Smart Multispectral System. SmartSpectra was submitted by a consortium of research groups from the University Jaume I (Spain), University of Valencia (Spain), Dismuntel SAL (Spain), Silsoe Research Institute (UK), Cork Institute of Technology (Ireland) and Analog Devices BV (Ireland). More information about the project can be found on the website: http://www.smartspectra.com.

1.3.1. Description of the ATFS instrument

The ATFS instrument can be divided into two blocks (Figure 1.5): the multispectral sensor, and the host computer software. The multispectral sensor is based on an AOTF that performs the spectral band selection. On the host computer, a software package acquires and processes the digitalised image and sends the control commands to the generator and camera.

The multispectral sensor is formed by:

- The AOTF, which performs the band selection.
- A commercially available high-resolution digital camera, which acquires sequentially the different bands of the image.
- A set of lenses that focuses the images correctly in each optical element (AOTF and sensor) while assuring properties such as telecentricity.
- The RF generator, which drives the AOTF.

On the other side, the software package has two parts:

- The control driver for the camera and filter.
- The ATFS user application.

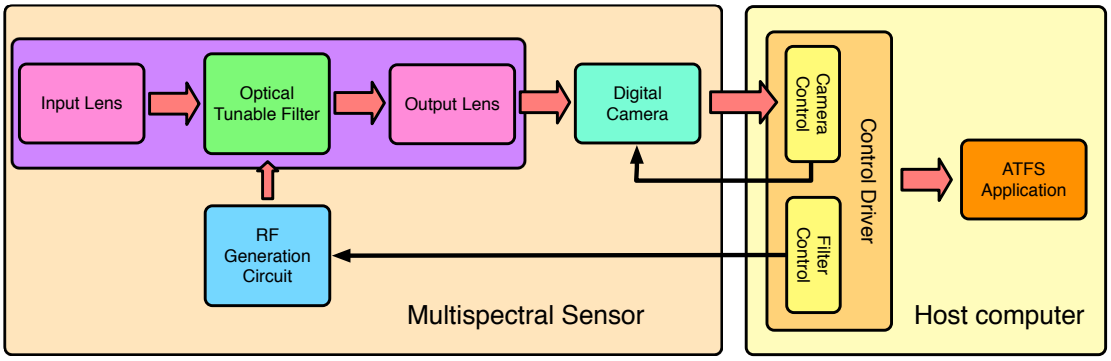

Figure 1.5. Block diagram of the ATFS instrument.

On the multispectral sensor system, the imaged object is projected through an input lens and focused into an AOTF. The AOTF filters the selected band from the imaged light and directs it to a high-resolution digital camera. An RF generator board based on a digital synthesiser (DDS or DAC) drives the AOTF. The central wavelength and bandwidth of the selected band is determined by the characteristics of the RF signal. On the host computer side, a software package acquires the digitalised image and sends the control commands to the generator and camera.

Acousto-Optic Tunable Filters

AOTF's are solid state optical filters that act as electronically tunable spectral bandpass filters. An AOTF consists of a properly oriented birefringent uniaxial crystal to which a piezoelectric transducer is bonded. The application of an RF signal to the transducer produces an acoustic wave that propagates inside the crystal. The wave interacts with photons diffracting a single narrow-bandpass wavelength that satisfies a specific momentum-matching condition. The wavelength filtered by the crystal may be rapidly varied by changing the acoustic frequency.

2.1. Brief historical background

In 1922, Léon Brillouin [Brillouin, 1922] predicted the light diffraction by an acoustic wave when propagated in a medium of interaction. In spite of outlining several experiments to examine these postulates, Brillouin never performed these experiments.

Ten years later, Debye and Sears in the US [Debye and Sears, 1932], and Lucas and Biquard in France [Lucas and Biquard, 1932] carried out the first experiments to check the acousto-optic phenomenon. They applied an acoustic vibration to organic solvents and saw how visible light was diffracted in multiple orders.

The mathematical description of the AOTF behaviour was developed by [Dixon, 1967]. Two years later, [Harris and Wallace, 1969] announced the first AOTF. They used a collinear configuration, in which the non-diffracted light exiting the AOTF was coincident in space with the diffracted wavelength.

In 1975, I.C. Chang [Chang, 1975, 1976] developed the principles of the non-collinear AOTF configuration. In this arrangement, diffracted and non-diffracted light are angularly separated as they exit the AOTF. Korpel and Poon developed in 1980 the current mathematical description of the interaction of planar waves of sound and light [Korpel and Poon, 1980]. These works led to the development of Acousto Optic (AO) deflectors and modulators. Advances in AO materials development allowed Yano and Watanabe to create the first paratellurite (TeO_2) AOTF [Yano and Watanabe, 1976]. This material produces excellent operational characteristics, durability and operates in the VIS and NIR spectral regions. Currently, TeO_2 is used in most of the commercial AOTF's.

Excellent historical reviews of the AO devices have been published [Yano and Watanabe, 1976; Bei et al., 2004; Korpel, 1988; Xu and Stroud, 1992; Tran, 1992; Goutzoulis and Pape, 1994; Tran, 2000].

2.2. Principles of AOTF operation

An acousto-optic crystal presents optical properties that are altered in the presence of an acoustic wave. When an acoustic wave propagates through such a material, the crystal lattice structure is alternatively compressed and relaxed in response to the oscillating wave-front. The mechanism that produces the acousto-

optic interaction is known as the elasto-optic effect. Periodic regions of lattice compression and rarefaction throughout the crystal are manifested as refractive index fluctuations that can produce diffraction of incident light. The behaviour is similar to that of a diffraction grating, but in an acousto-optic filter the diffraction occurs over an extended volume of the crystal rather than at a planar surface, and only a limited band of spectral frequencies are affected. The crystal diffracts only the range of the incident light that satisfies the appropriate phase-matching (momentum-matching) conditions. For a particular acoustic frequency, only a limited band satisfies the phase-matching condition. Varying the acoustic frequency across the crystal changes the centre of the spectral passband, as required to maintain the phase-matching condition.

Additionally, the polarisation of the diffracted wavelength is rotated. For instance, if the incident radiation is an ordinary ray (o-ray), it will be converted into an extraordinary ray (e-ray) for the selected wavelength upon interaction with the acoustic wave.

The incoming light can be imagined as a beam of photons while the acoustic wave moving through the crystal consists of phonons [Chang, 1976]. The sum of momentums of the incident light (M_i) and the acoustic wave (M_a) is equal to that of the diffracted radiation (M_d):

$$M_i \pm M_a = M_d \qquad \textbf{(Eq. 2.1)}$$

This relationship can be expressed in a vector form. If we denote the incident wave vector as $\mathbf{k_i}$, the acoustic wave vector as $\mathbf{k_a}$ and the diffracted wave vector as $\mathbf{k_d}$, the phase matching of the optical and acoustic beams requires that:

$$\mathbf{k_i} = \mathbf{k_a} + \mathbf{k_d} \qquad \textbf{(Eq. 2.2)}$$

The magnitudes of the wave vectors are given by:

$$|\mathbf{k_i}| = 2\pi n_i/\lambda, \qquad |\mathbf{k_d}| = 2\pi n_d/\lambda, \qquad |\mathbf{k_a}| = 2\pi f/v \qquad \textbf{(Eq. 2.3)}$$

where f is the acoustic frequency, v is the acoustic speed in the crystal, λ is the optical wavelength, and $n_{i,d}$ is the crystal index of refraction for the incident and diffracted beams, respectively. This vector relationship is expressed on the wave-vector diagram shown in Figure 2.1, where θ_I and θ_d are the angles between incident and diffracted beam wave vectors and the optic axis, respectively; n_e and n_o are the extraordinary and ordinary refraction indices, respectively; and α is the angle between the acoustic wave vector, k_a, and the acoustic axis.

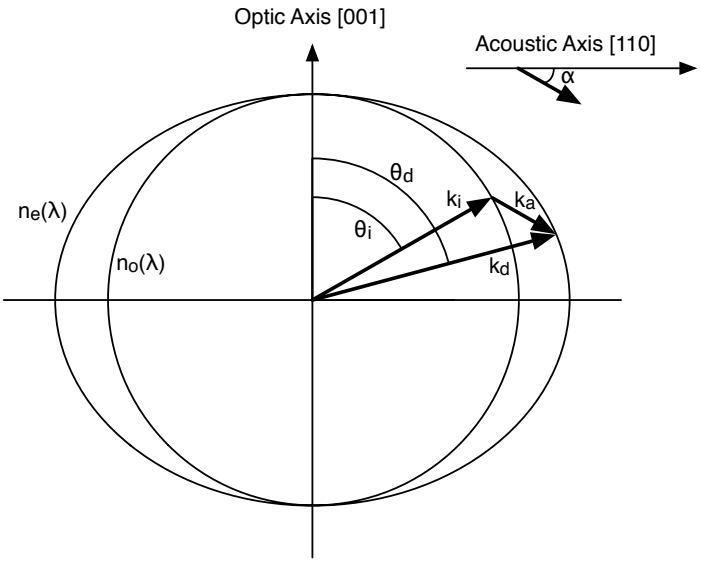

Figure 2.1. Wave-vector diagram for a AO crystal.

The velocity and direction of the diffracted photons in some AOTF configurations are shifted according to the differences in the refractive indices (Δn). Assuming that the incident radiation is an o-ray and incorporating the incident angle (θ_i) momentum considerations yields [Bei et al., 2004]:

$$\lambda = \frac{v\Delta n}{f}\sqrt{\sin^4\theta_i + \sin^2 2\theta_i} \qquad \textbf{(Eq. 2.4)}$$

2.3. AOTF configurations

There are two different AOTF configurations, collinear and noncollinear. The name refers to the angle between acoustic waves and optical beam directions inside the crystal.

In the initial AOTF design, the incident light beam and acoustic wave propagation are coincident (collinear). A narrow band of spectral wavelengths is diffracted into a polarisation direction orthogonal to that of the incident beam. In this case, the nondiffracted and diffracted photons exit the AOTF collinearly and the diffracted wavelengths may be separated by placing a polariser at the output.

Figure 2.2 shows a collinear AOTF configuration. In this example, white light o-rays are directed to the crystal. The acoustic wave is directed into the crystal as a longitudinal compression wave. Upon reflection from a face of the crystal, this compression wave is converted to a shear wave and directed collinearly with the optical radiation. Separation occurs converting radiation of wavelength λ to an e-ray. The diffracted and zero-order beams emerge collinearly from the AOTF. Since the polarisation of the diffracted beam is orthogonal to that of the transmitted beam, it can be separated by a polariser.

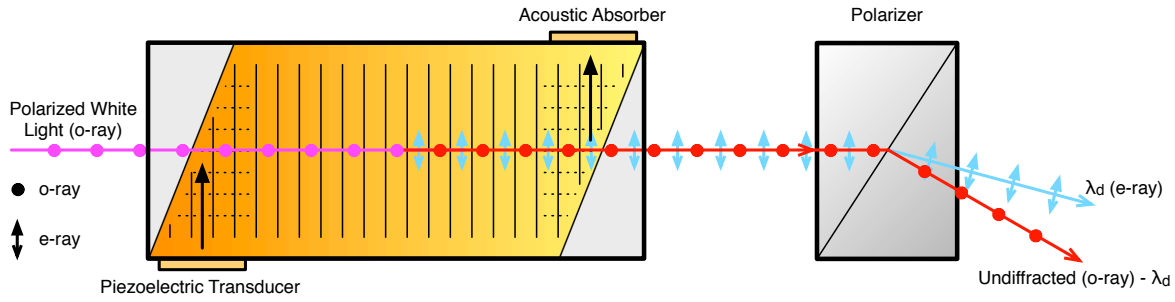

Figure 2.2. Collinear AOTF configuration.

In 1975, Chang set the principles for the noncollinear AOTF configuration [Chang, 1975], where the acoustic and optical waves are noncollinear (Figure 2.3). In this design, the narrowband diffracted light and incident broadband light are physically separated and exit the crystal through different pathways. Polarisers are not required to separate both light beams since the undiffracted beam can be blocked by a beam stopper.

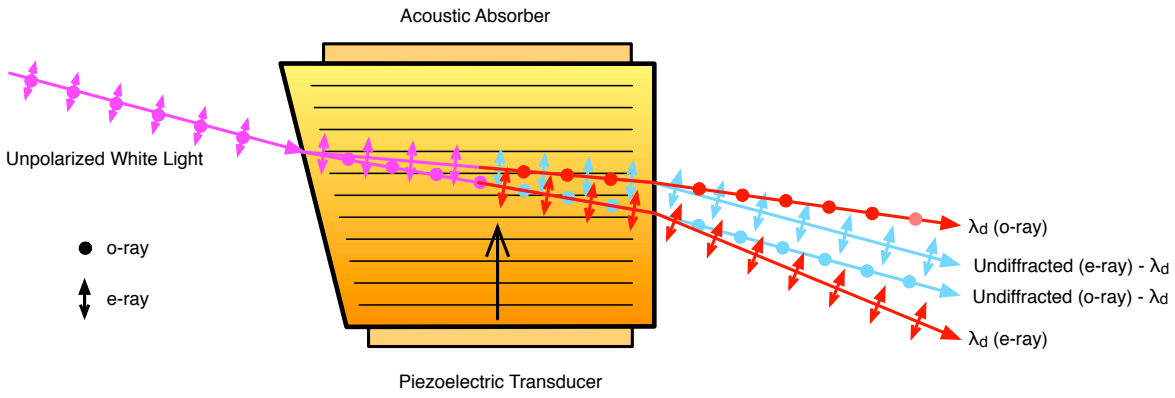

Figure 2.3. Noncollinear AOTF configuration.

When an unpolarised incident beam is employed in the noncollinear configuration, the diffracted portion of the beam contains two spatially separated beams, which are orthogonally polarised. As in the collinear case, the momentum of the diffracted photon is equal to that of the incident photon plus/minus the phonon. These two radiations are said to be first-order plus and minus diffraction. The remaining incident light traverses the AOTF and forms the zeroth-order undiffracted outputs. However, if the input beam to the crystal is linearly polarised, only one diffracted beam exits the device, whose polarisation is rotated 90 degrees relative to the input polarisation axis.

The two orthogonally polarised first-order beams do not separate until they leave the crystal, and they diverge at a fixed angle. The diffraction angle does not change with wavelength.

The first order and zero order beams are typically separated by a small deflection angle, which is a function of the device design. The deflection angle can be increased by utilising crystals with large birefringence values, achieving then a desirable good separation between the diffracted and undiffracted beams by using a beam stopper instead of a polariser.

The most used material for noncollinear AOTF devices is TeO_2. The deflection angle is at a minimum for this crystal when the incidence angle is parallel to the [110] axis (at 90 degrees to the optical axis) and increases up to a practical limit between 8 and 9 degrees as the incidence angle increases with respect to the [110] axis.

The deflection angle has the following relationship to the birefringence of the crystal material:

$$\theta i - \theta d = \Delta n \ \sin(2 \cdot \theta i) \qquad \textbf{(Eq. 2.5)}$$

In the expression above, θ_i and θ_d are the angles of the incident and diffracted beams relative to the optic axis, respectively; Δn denotes the birefringence of the crystal.

2.4. AOTF characteristics

2.4.1. Acceptance angles and apertures

Large acceptance angles increase the optical apertures of the filter, which is desirable since we capture more light. However, the bandwidth of the pass-band is increased and the frequency resolution is degraded as the range of incident angles is augmented, causing chromatic aberrations for imaging applications. This is caused by the fact that changes in the incidence angle produce momentum mismatches, making the diffracted wavelength to be slightly different for each incident angle. This effect can be avoided only if the incoming radiation is perfectly collimated.

2.4.2. Diffracted light bandwidth

Although the diffracted light must follow the momentum-matching criterion, diffraction can occur for radiation in which the phase is not perfectly matched with that of the phonon. In this case, radiation of wavelengths nearby the central wavelength λ (given by Eq. 2.4) will be transmitted. The bandwidth is the width of the diffracted radiation band. The bandwidth may be defined as the full-width at half-maximum intensity (FWHM or $\Delta\lambda$). The bandwidth for an AOTF is described by the following equation:

$$\Delta\lambda = \frac{0.9\lambda^2}{\Delta n L \sin^2 \theta_i} \qquad \textbf{(Eq. 2.6)}$$

Where L is the interaction length. If all other terms are assumed to be approximately constant, $\Delta\lambda$ is proportional to the square of the wavelength. Then, an ultraviolet diffracted radiation would have a smaller bandwidth than that of a NIR radiation, for the same device.

Secondly, the phase matching condition dictates that:

$$T = T_o \sin^2\left(\frac{\Delta k L}{2\pi}\right) \qquad \textbf{(Eq. 2.7)}$$

where T is the intensity of the transmitted radiation for an input radiation of intensity T_o and Δk is the phase mismatch parameter. This phase mismatch parameter is proportional to the differences in the momentum vectors of the e- and o- rays as a function of optical wavelength. Then, the output appears as a *sinc* function with side "lobes".

2.4.3. AOTF materials

In the recent years, the development of improved materials for the fabrication of AO devices has increased the number of applications. The selection of an appropriate material depends on the specific device target function. Specific requirements include high optical transparency in the wavelength region of interest, availability of sufficiently large single crystals, and reasonable cost. A common term used for evaluating a material's performance is the AO figure of merit (FOM). Even though there are several proposals, a widely accepted one is proposed in [Fellers and Davidson, 2004]:

$$M_{2a} = \frac{n_o^3 n_e^3 p^2}{\rho v^3} \qquad \textbf{(Eq. 2.8)}$$

Where p is the effective photoelastic coefficient and ρ is the material density. The FOM is a reflection of AOTF efficiency as the diffracted radiation intensity is proportional to M_{2a}. Therefore, a material with a greater FOM will be more efficient. Table 2.1 lists a number of these properties for common AOTF materials [Goutzoulis and Pape, 1994; Xu and Stroud, 1992]. As one can deduce from these values, TeO_2 is the most used material for the VIS and NIR spectral regions, while crystalline quartz is used in the ultraviolet region and thallium arsenic selenium in the IR one.

Table 2.1. Properties of selected AOTF crystals.

Crystal	Transmission range (μm)	Refractive indices	Acoustic velocity (m/s)	AO FOM (10^{-18} s^3/kg)	AOTF type
α-Quartz	0.12–6.5	no=1.539 ne=1.548	5960	1.51	Collinear Noncollinear
$LiNbO_3$	0.4–4.5	no=2.29 ne=2.20	6570	6.95	Collinear
TeO_2	0.35–4.5	no=2.26 ne=2.41	616	1200	Noncollinear
Tl_3AsSe_3	1.25–17	no=3.34 ne=3.15	2050	628	Collinear Noncollinear
Hg_2Cl_2	0.4–20	no=1.96 ne=2.62	347	1060	Noncollinear

Because the AO FOM for quartz is about 1000 smaller than that of the TeO2, quartz-based AOTFs present lower diffraction efficiency and require much higher power values to drive the RF transducer in comparison to a TeO_2 filter.

2.5. AOTF excitation

AO devices are excited by an acoustic signal in the RF range (20-200 MHz approximately) for the visible and NIR working range. This signal is created as an RF electric signal and converted to acoustic waves by a proper piezo-electric transducer. The frequency content of the RF signal determines the frequency content

of the acoustic waves, which, in turn, determines the diffraction of different wavelengths of the incoming light. The amplitude of the acoustic wave depends on the RF power of the signal applied to the transducer. Therefore, the diffraction efficiency also depends on the RF signal power. The spectral purity of the electric signal will influence the bandwidth of the diffracted light.

Therefore, the characteristics that the RF signal must show are:

- Pure spectral shape, to allow narrow bands to be filtered.
- Very fast frequency switching, to increase dynamic performance of the system.
- High dynamic range, to allow the system to vary the RF power.
- High frequency generation range, to allow the use of multiple AOTF's with the same generator.

Normally, the piezo-electric transducer uses a 50Ω matching network to meet the low impedance of the transducer (a few ohms) with the output impedance of the standard RF power equipment. This network seriously affects the theoretical expected response, leading to an uneven behaviour of the AOTF with respect to frequency [Chang, 1976].

AOTF's can be driven by several RF signals simultaneously, leading to the diffraction of multiple wavelengths according to the driving signal frequencies [Ward et al., 2006; Fellers and Davidson, 2004]. This fact can be used to generate a broadband diffracted output, by using closely spaced RF driving signals.

This approach has been only reported by [Suhre and Theodore, 1996], who used a multiband RF source to generate a white light diffracted output from 40 overlapped passbands. However, these authors created a fairly complex set-up for the multiple band generation, which used a local oscillator for each generated signal and a 40-channel power supply for driving the signals to the AOTF.

Therefore, more versatile and robust generation methods are required to fully exploit this capability of the AOTF. In [Vila-Francés, 2003], we explored different RF generation techniques that can be applied to drive an AOTF in a broadband configuration. These techniques consist on the generation of a broadband signal on the baseband (centred at DC), and the up-conversion of this signal to the proper RF range by a Local Oscillator (LO) generator and an RF mixer. The author evaluated two different baseband generation techniques: a white-noise generator with a configurable bandwidth, and a digital multisine signal generator implemented on a Digital Signal Processor (DSP). Both techniques presented the same drawbacks:

- The RF up-converting step introduced many harmonics and a decrease on the dynamic range of the system, because more noise is introduced to the signal chain.
- The LO signal must be provided by an external source. This signal needs to be stable and fast to switch between frequencies. Normally the LO signal is generated by a PLL circuit, which can be stable at the cost of a slow switching rate or vice versa, but not both characteristics at the same time.

In this work we have evaluated a different approach to the RF generation. The approach consists on generating the signal directly on the RF range rather than on the baseband. The principal idea behind this approach is the use of a high speed Digital-to-Analog Converter (DAC) capable of generating a sine directly in the proper RF domain. However, this approach requires state-of-the-art digital electronics that were not available until recent years.

The use of a DAC to generate directly the RF signal presents different advantages:

- The harmonics and the noise of the RF signal are reduced because less electronic components are involved on the signal chain.
- Provided a stable clock source at a fixed frequency, the output is also stable at any frequency in a very broad range. This is feasible with a properly configured PLL circuit.
- The output frequency can be changed at a very high speed.

By using this approach, the generation of a broadband signal can be achieved by two ways:

- Sweeping the RF frequency very fast. The diffracted light presents also a sweeping central wavelength. By adjusting the exposure time of the camera on the system to a multiple of the sweeping time, the image acquired in the camera becomes the integral of the light along the swept range.
- Generating multiple sine signals simultaneously. It is known that an AOTF behaves linearly when multiple signals with different frequencies are applied simultaneously to it [Ward et al., 2006; Fellers and Davidson, 2004]. Therefore, the diffracted light is the result of the sum of the diffracted wavelengths produced by each applied sine.

This Thesis work presents the performance of diverse AOTF models from different manufacturers when using both driving techniques.

2.6. List of AOTF manufacturers

In the context of the SmartSpectra project, an extensive search of AOTF manufacturers was done. Some of them were contacted in order to buy them different AOTF models. Table 2.2 summarises the list of contacted manufacturers with their main details.

Table 2.2. List of AOTF manufacturers.

Company	Products
ELECTRO-OPTICAL PRODUCTS CORPORATION (USA) www.eopc.com	•There are no direct references to AOTF systems on imaging applications.
INTRA-ACTION CORPORATION (USA) www.intraaction.com	•In general, these AOTFs are for VIS or IR, but not both, so wavelength intervals are around 400 – 700 nm. •Aperture sizes are 5 x 5 mm for the VIS •Diffraction efficiencies >90% (at 633nm) •Apodized AOTF are also available, but aperture size for the VIS ones are no more than 4x4mm •Interesting model(s): ATF-805APJ1
ISOMET (USA and UK) www.isomet.com	•In general, these AOTFs are for VIS or IR, but not both, so wavelength intervals are around 400 – 700 nm. •Aperture sizes are 5 x 5 mm for the VIS •Diffraction efficiencies >85% •Interesting model(s): AOTF614 Series
BRIMROSE (USA) www.brimrose.com	•VIS-NIR AOTF: 400-1000, although subject to the RF octave. •Aperture sizes are up to 10x10 mm •Diffraction efficiencies between 70 and 90 %
AA OPTO ELECTRONICS (France) www.a-a.fr	•VIS Spectrum 400-700 nm •Aperture size max. of 5 x 5mm •Diffraction efficiency around 80% •Interesting the Series AA.AOTF.xx
GOOCH AND HOUSEGO (UK) www.goochandhousego.com	•TF1450-500-3-F2X with: •370-4500 nm (one octave conditioning) •Aperture size up to 10x10mm •Customisation available

Company	Products
MOLTECH (Germany) www.mt-berlin.com	•Models in the VIS range (440-760nm) and NIR (800-1600nm) •Optical aperture up to 10 x 10 mm •Efficiency up to 80% in the VIS •MT-5101: Special model for imaging in the range 630-1200nm, with 25 x 25mm optical aperture

From these companies, the SmartSpectra research team took the decision of buying four different AOTF models, according to the following parameters:

- The AOTF should have maximum acceptance angle.
- The AOTF should have maximum usable optical aperture.
- The AOTF crystal should give maximum diffraction efficiency.
- The chromatic aberration in the crystal introduced by the diffraction angle should be optically corrected (i.e. no chromatic aberration).
- The manufacturer should preferably be European.
- The availability of the AOTF system should be optimised (AOTF customisation, delivery times, after-sale support, etc).
- The price should be according to project budget.

After evaluating the options and contacting the different manufacturers, the SmartSpectra research team decided to buy the following AOTF models:

- Isomet 614-08 (see Table 2.3)
- Gooch and Housego TF15-230-4-5-VU1 (see Table 2.4)
- AA Opto Electronics AA.AOTF-3/LR (see Table 2.4)
- MolTech AOTF-MT VIS (see Table 2.4)

Table 2.3. Characteristics of the 614-08 AOTF from Isomet Co.

Isomet 614-08	
Crystal material	TeO_2
Nominal wavelength range	400-700nm
Effective wavelength range	450-800nm
Driving frequency	108-51 MHz
Spectral resolution	4nm @ 600nm
Optical aperture	5x5 mm^2
Acceptance angle	>4.2º

Table 2.4. Characteristics of the purchased AOTFs from Gooch & Housego, AA Opto-Electronics and Moltech.

Model	Nominal wavelength range	Driving frequency	Maximum power
AA.AOTF-3/LR	400-700 nm	60-135 MHz	1 W
TF515-230-4-5-VU1	400-630 nm	70-140 MHz	0.5W
AOTF-MT VIS	440-820 nm	60-135 MHz	1W

We selected the Isomet model, which was the first model bought by the SmartSpectra Consortium, to be mounted on an optical layout as part of the Autonomous Tunable Filtering System (ATFS). The other models were evaluated and characterised on an optical testbench.

Part II
Implementation of a multispectral imaging system

III

Multispectral sensor

On the context of the SmartSpectra project, the author has implemented a multispectral imaging instrument based on the spectral filtering capabilities of the AOTF. This instrument is called Autonomous Tunable Filtering System (ATFS). This instrument, coupled to a video camera, acts as a staring type imaging spectrometer in which acquired bands are configurable in terms of central wavelength and bandwidth.

The ATFS is an imaging spectrometer formed by a multispectral sensor system and its corresponding control software running on a computer. The multispectral sensor is the hardware subsystem of the ATFS instrument. It is composed by three elements: the optical subsystem, the digital camera, and the RF generation circuit. The optical subsystem is made from commercial off-the-shelf (COTS) elements, but following a new optical layout. The camera is a scientific grade model that can be easily programmed from the computer. Finally, the RF generator is a custom designed board. The AOTF and optical systems are housed into a specifically designed box that contains all the optical elements.

3.1. Optical subsystem

The optical subsystem comprises the AOTF and two sets of lenses in front and behind it. The input lenses focus the image on the AOTF. The output lenses separate the first-order diffracted light (filtered band), which is projected onto the sensor plane, from the zero-order light, which must be cancelled. The ATFS instrument uses the 614-08 AOTF model from Isomet Co. (www.isomet.com), whose characteristics are summarised in the Table 2.3 of Chapter 2.

The optical deployment of the instrument has been optimised for the particular behaviour of the AOTF's. Due to the restricted angular acceptance of these devices, the input optics must convert the incoming light to a parallel beam at the crystal surface. In our design, this is achieved with a telecentric optics at the second optical stage. The first optical stage is left unconstrained, so that the user can use different incoming optics for diverse scenarios, while maintaining the telecentricity at the crystal surface.

In order to cancel the zero-order light at the sensor plane, there are two techniques: the use of a beamstopper in the optical path, or the use of cross polarisers. However, neither of them alone is completely efficient [Vila-Francés, 2006]. Therefore, our system combines a conjugated-pupil telecentric arrangement with polarisers. Such set-up allows two ways of zero-order cancellation. Firstly, the conjugated pupil elements (diaphragms), are adjusted so that the second diaphragm acts as a beamstopper; secondly, introducing the crossed polarisation. Figure 3.3 shows a schematic representation of this optical arrangement. Optical objective 1 and diaphragm 1 form a telecentric optics, which restricts the angle of the light entering the AOTF. Optical objective 2 and diaphragm 2 form an imaging optics, which projects the input image on the sensor plane.

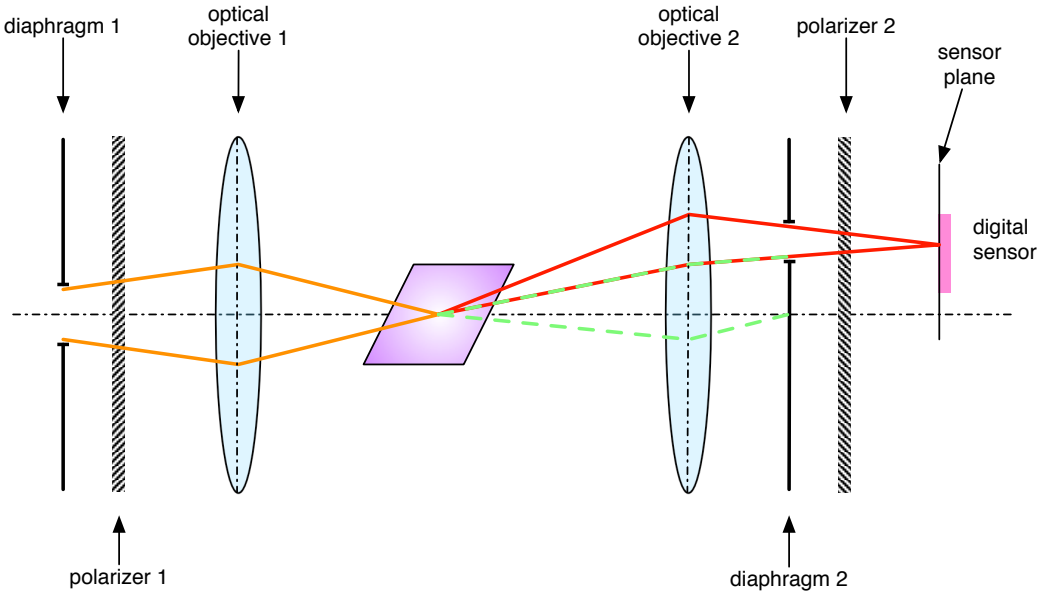

Figure 3.2. Conjugated-pupil telecentric arrangement for zero-order cancellation.

In the ATFS instrument, the telecentric optics is formed by an Schneider Xenoplan 1.9/35mm objective and a Linos iris diaphragm. The imaging optics is formed by another Xenoplan 1.9/35mm objective. The optical system was mounted and optimised on an optical breadboard using off-the-shelf components. Then, the system layout was measured and reproduced on a custom box, which also presents threads for inserting the adapting optics on the front of the instrument and the camera head at the rear. Figure 3.3 shows a picture of the optical arrangement without the cover.

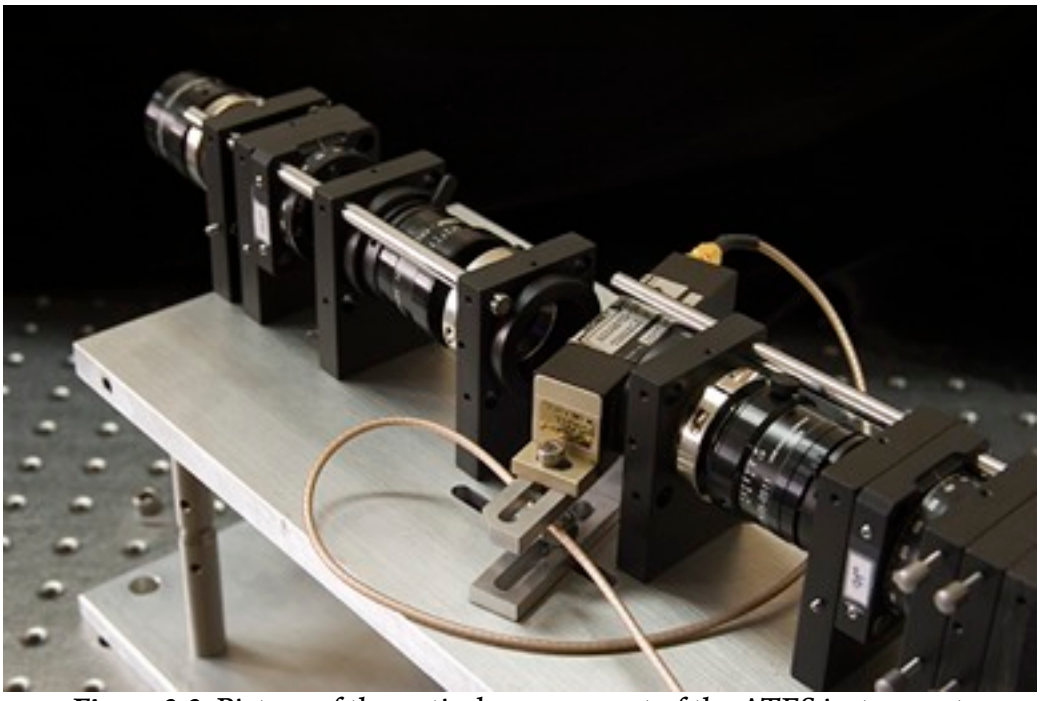

Figure 3.3. Picture of the optical arrangement of the ATFS instrument.

For further details on the optical layout, see [SmartSpectra, 2005a].

3.2. High performance camera

The ATFS instrument can work with any digital video camera that can be physically attached to the optics output (C-mount thread). However, the host computer software has been designed to control a few camera models. Specifically, the software can control any Firewire camera that follows the D-CAM specifications, and the Firewire cameras from the manufacturers Retiga and Photonic Science Co.

The instrument was tested with three camera models: Basler A302fs, Retiga QImaging, EX and Photonic Science Coolview EM1000. The first model is an industrial grade D-CAM compliant camera, while the other two are scientific grade high-resolution cameras. Table 3.1 summarises the characteristics of the three models.

Table 3.1. Specifications of the cameras tested with the ATFS instrument software.

	Basler A302fs	Retiga QImaging EX	Coolview EM100
Resolution	782 x 582	1360 x 1036	1002 x 1004
Pixel size	8.3 x 8.3 µm	6.45 x 6.45 µm	8 x8 µm
Bit resolution	8 bit	12 bit	12 bit
Integration time	20µs – 81,92ms	40 µs – 15 min	few ms (digital output mode) to > 1 hour in photon counting mode
Cooling	No	Yes	Yes
Readout noise	not available	8e-	<1e-
Dark current	not available	0.15e-/pixel/s (cooled)	<1e-/pixel/s

The camera that gives the best performance is the Coolview EM1000, due to the use of an Electron Multiplying CCD technology (EMCCD). The EMCCD technology uses an in-circuit amplifier stage that increases the CCD gain without increasing the noise [Hynecek, 2001; Denvir, 2003].

All the cameras use a Firewire interface.

3.3. Excitation subsystem

We have evaluated two different approaches to excite an AOTF with a broadband RF signal, based on two different digital signal generation techniques. The first one creates the effect of a broadband signal by generating a fast sweeping RF signal with a DDS, while the second one consists on the simultaneous multiple band generation with a DAC. In this section, we explain the working principle and the driver developed for each approach.

3.3.1. Sweeping sine RF generation

This Thesis proposes a new design for an RF sweeping signal generator for AOTF imaging systems based on a Direct Digital Synthesiser (DDS). A DDS is capable of generating digitally any frequency in its working range almost instantly. Concretely, the part we have chosen, the AD9858 from Analog Devices Inc. (www.analog.com), can work with clock frequencies up to 1GHz and thus generate RF signals from DC to 400MHz. Moreover, this DDS presents an interesting sweeping mode that allows a broadband filtering mode in the case of AOTF systems such as our ATFS.

3.3.1.1. Direct Digital Synthesisers

A DDS is a digital circuit that can generate multiple frequencies from a reference frequency source. The basic architecture of a DDS is shown in Figure 3.5. In this simplified model, a stable clock drives a Programmable Read Only Memory (PROM), which stores one or more integral number of cycles of a sinewave (or

other arbitrary waveform). As the address counter steps through each memory location, the corresponding digital amplitude of the signal at each location drives a DAC, which in turn generates the analogue output signal. The spectral purity of the final analogue output signal is primarily determined by the DAC, while the phase noise is basically that of the reference clock.

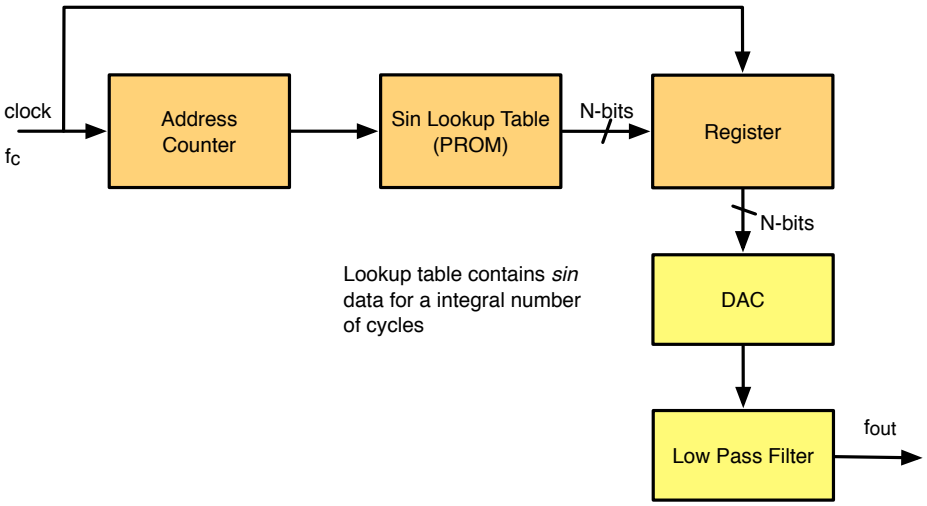

Figure 3.5. Basic DDS architecture.

This simple DDS system lacks flexibility in changing the output frequency. The only manner to change the output frequency is modifying the reference clock frequency or reprogramming the PROM. A practical DDS system implements this basic function in a much more flexible and efficient way using a digital hardware called Numerically Controlled Oscillator (NCO). A block diagram of such a system is shown in Figure 3.6.

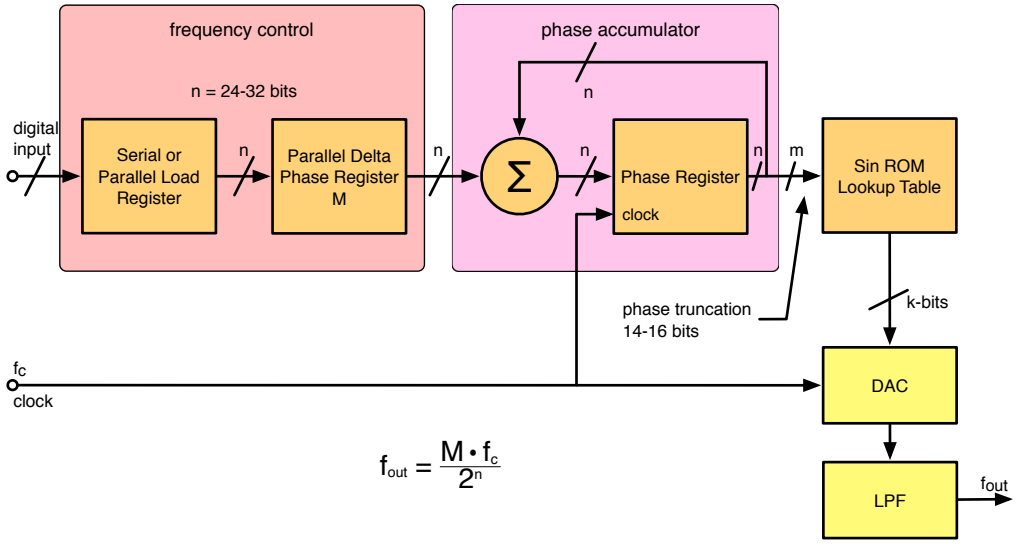

Figure 3.6. Flexible DDS system.

In this system, a phase accumulator, whose content is updated once every clock cycle, replaces the address counter. Each time the phase accumulator is updated, the digital value M, stored in the *delta phase register*, is added to the number in the phase accumulator register. The truncated output of the phase accumulator is used as the address to a sine look-up table (LUT). Each address in the LUT corresponds to a phase point on the sinewave from 0º to 360º. The content of the LUT is the amplitude information for each phase point. Therefore, the LUT maps the phase information from the phase accumulator into a digital amplitude word, which in turn drives the DAC.

For an n-bit phase accumulator, the LUT contains 2^n possible phase points. The digital word M is the amount that the phase accumulator is incremented each clock cycle. Therefore, for a given clock frequency f_c, the frequency of the output sine wave is given by the so-called DDS tuning equation:

$$f_o = \frac{M \cdot f_c}{2^n} \qquad \textbf{(Eq. 3.1)}$$

3.3.1.2. Analog Devices AD9858 DDS

The AD9858 is a 1GSPS (Giga–Sample Per Second) DDS from Analog Devices Inc. (www.analog.com). Its most relevant features are:

- 1 GSPS internal clock speed.
- Up to 2 GHz input clock.
- Integrated 10-bit DAC.
- 32-bit programmable frequency register.
- Automatic frequency sweeping capabilities.

The AD9858 uses advanced DDS technology, coupled with an internal high speed, high performance D/A converter to form a digitally programmable, complete high frequency synthesiser capable of generating a frequency-agile analogue output sine wave at up to 400 MHz. Its 32-bit frequency tuning word allows for fine tuning resolution (232,83 mHz at 1 GHz).

The device consists of an NCO with 32-bit phase accumulator, 14-bit phase offset adjustment, a power efficient DDS core, and a 1 GSPS 10-bit DAC. The AD9858 incorporates additional capabilities for automated frequency sweeping. Although not used in our circuitry, the AD9858 also offers an analogue mixer capable of operating at 2 GHz, a phase frequency detector (PFD), and a programmable charge pump with advanced fast-lock capability. A functional block diagram of the device can be seen in Figure 3.7.

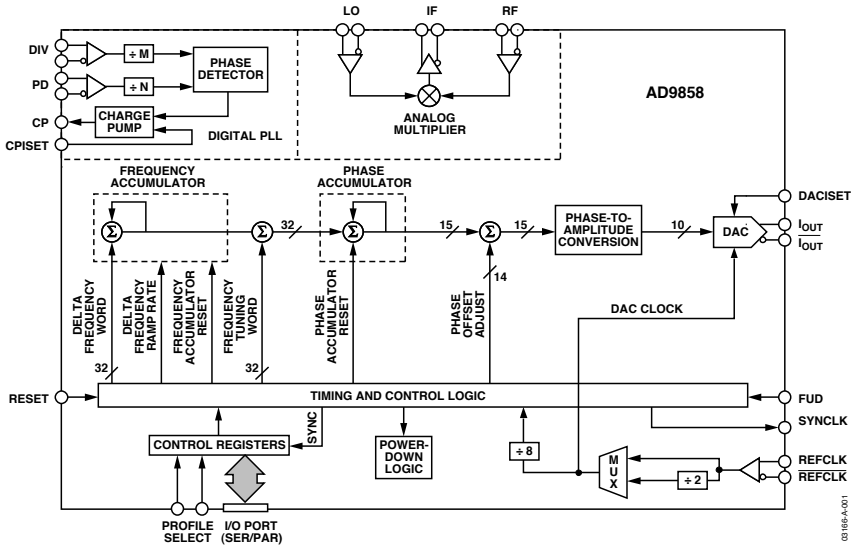

Figure 3.7. Functional block diagram of AD9858.

The AD9858 provides automated frequency sweeping capability. This feature is implemented with a frequency accumulator (which is different from the phase accumulator). The frequency accumulator adds periodically a frequency incremental quantity to the current frequency tuning word, thereby creating new instantaneous tuning words. Therefore, the frequency generated by the DDS changes with time.

The frequency step size, which can be positive or negative, is loaded into the Delta Frequency Tuning Word (DFTW). The rate at which the frequency is updated is set by the Delta Frequency Ramp Rate Word (DFRRW). These two registers enable the AD9858 to sweep from an initial frequency set by the FTW, upwards or downwards, at a desired rate and frequency step size. The result is a linear frequency sweep or chirp.

The DFRRW acts as a countdown timer whose update rate is SYSCLK/8. Therefore, the frequency can be incremented at a maximum rate of 125 MHz (when DFRRW is loaded with 0xFFFF and the SYSCLK is 1 GHz). By the other hand, the DFRRW is a 16-bit word so that the maximum counter period is 65536 counts. This value corresponds to a maximum update period of 524,3 μs. In general, the time between each frequency step (Δt) is given by:

$$\Delta t = \frac{8 \times \mathrm{DFRRW}}{\mathrm{SYSCLK}} \qquad \textbf{(Eq. 3.2)}$$

The DFTW must specify whether the frequency sweep should go on upwards or downwards from the starting frequency (FTW). Therefore, the DFTW is expressed in binary two-complement format, in which positive values indicate up direction and negative indicate down. The frequency step size programmed with the DFTW value is given by:

$$\Delta f = \frac{\mathrm{DFTW} \times \mathrm{SYSCLK}}{2^{32}} \qquad \textbf{(Eq. 3.3)}$$

The AD9858 does not provide any mechanism to stop the sweep at a given frequency or time. However, the DDS can be returned to the sweep starting frequency at any time during a sweep, just clearing the control bit "autoclear frequency accumulator". Setting this control bit to zero instantly returns the DDS to the frequency stored as FTW. As the original FTW does not change during a sweeping operation, it contains the sweep starting frequency.

The fast-switching capability of the AD9858 is used to create a broadband generation signal for driving the AOTF. As the RF frequency can be changed much faster than the integration time of the imaging sensor, but slower than the acoustic crossing time of the crystal (tens of microseconds, [Fellers and Davidson, 2004]), a range of diffracted wavelengths can be acquired in a single image.

This approach was proposed and implemented in the SmartSpectra RF generator. By using the sweeping mode of the AD9858 DDS, this generator drives the AOTF with a sweeping frequency. That is, the frequency applied to the crystal varies cyclically from an initial frequency to a final frequency in constant steps. By choosing an integration time that is multiple of the complete sweeping period, the acquired image is proportional to the intensity of the light covered by the different diffracted wavelengths.

The AD9858 contains a series of registers that configure the operation of the device. These registers can be programmed through a serial or a parallel port. Regardless of the method used to control the device, the transfer of data to the DDS core is a two-step process. In a write operation, the user first writes the data to the I/O buffer using either the parallel or the serial port. However, the DDS core cannot access the data until it is latched into the memory registers from the I/O buffer. The I/O buffer is updated into the core's register memory toggling the Frequency Update (FUD) pin or changing one of the profile select pins.

In serial programming mode, the I/O port uses a chip select pin (CS/), a serial clock pin (SCLK), an I/O reset pin (IORESET), and either 1 or 2 serial data pins (SDIO and SDO). The serial port can be configured to use 2 or 3 wires. In 2-wire operation the SDIO pin is used as a bidirectional serial data pin, whereas in 3-wire operation the SDIO pin is used as a serial data input pin and the SDO as a serial data output pin.

The serial port is an SPI compatible serial interface. Serial port communication occurs in two phases. Phase 1 is an instruction cycle, in which an 8-bit word is sent to the core. The MSB of the instruction byte indicates the direction of the operation (read or write). The 6 LSBs define the serial address of the target register

as defined in the register map. Phase 2 contains the data to be transferred to or from the addressed register. The number of bytes transferred during phase 2 depends on the length of the target register.

In the implemented RF driver, the AD9858 is programmed from the on-board microcontroller, which executes a firmware program written on 8051 ASM language. The code of the microcontroller firmware is described on Appendix B and listed on the attached CD.

3.3.1.3. DDS-based RF generator

We have developed an RF driver for AOTF's based on the AD9858 DDS. The DDS is used to generate a frequency-adjustable RF sine signal that can be applied to the AOTF in order to diffract different wavelengths.

The DDS-based RF board can generate an RF signal with the frequency and power required to drive a great variety of AOTF's. The board is divided into a series of functional blocks as depicted in Figure 3.8.

The signal is synthesised by the AD9858, which is clocked by a 1GHz signal generated by the AD4360-2 integrated synthesiser and Voltage-Controlled Oscillator (VCO). The RF output signal of the DDS goes through a Variable Gain Amplifier (VGA) that adjusts the signal amplitude and then feeds a RF power amplifier, which gives the RF signal the power required to drive the transducer of the AOTF. All the programmable circuits on the board are controlled by an ADuC842 microcontroller (µC), which also communicates with the host computer through a USB bus. Another integrated circuit, the AD8361, provides a control feedback of the output power.

The VGA is a THS7530 chip from Texas Instruments (www.ti.com) and the power amplifier is implemented with two cascaded HELA-10 power amplifiers from MiniCircuits (www.minicircuits.com).

The maximum output power of the board is +30dBm, given by the HELA-10 power specifications. The theoretical RF output range of the board is from DC to 400MHZ, which is the working range of the DDS chip, but the HELA-10 amplifiers limit the working frequencies to the range 20-200MHz.

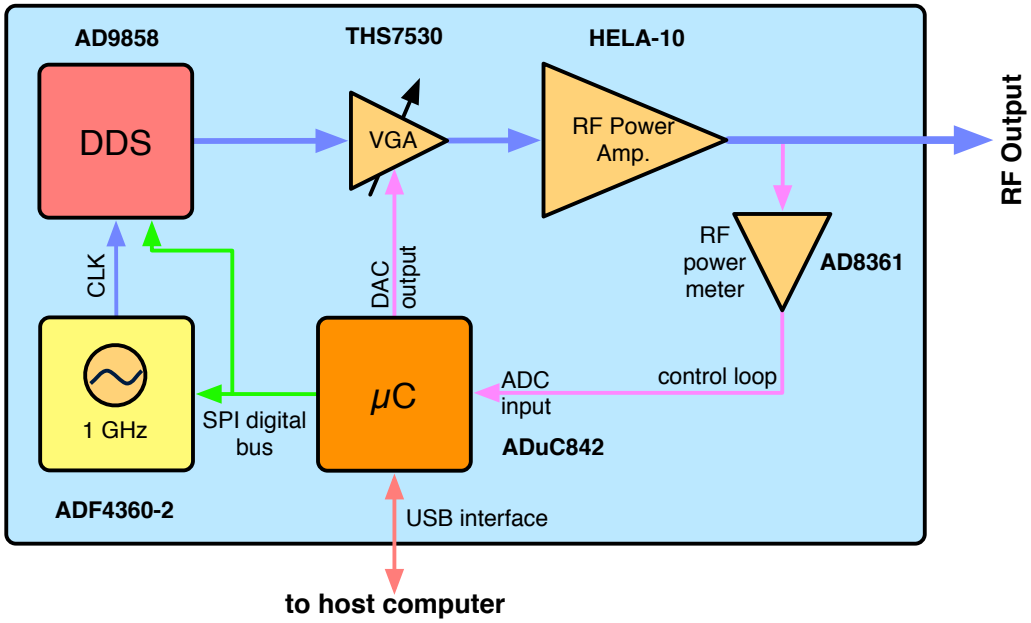

Figure 3.8. Block diagram of the RF generator.

The RF board has been implemented into a single Printed Circuit Board (PCB), which has been carefully laid out in order to assure the signal integrity of the RF signals and the correct thermal dissipation of the power components. The details of the implementation, including the circuit schematics of the board can be found on Appendix A. Figure 3.9 shows a picture of the board.

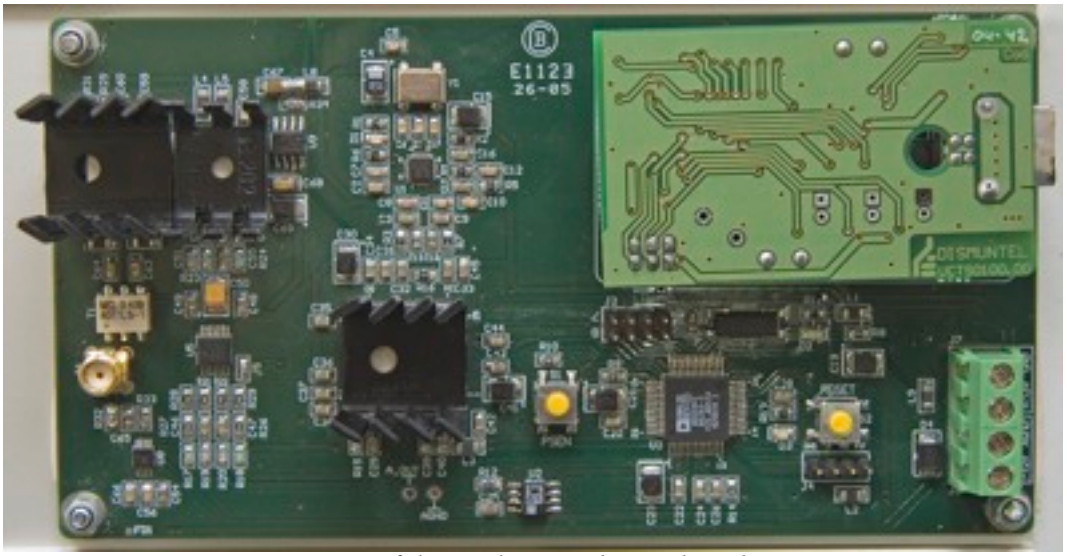

Figure 3.9. Picture of the implemented DDS-based RF generator.

RF board firmware

The μC on the implemented board runs a control program (firmware) that manages the RF generation. The μC controls the rest of the blocks on the circuit except for the Power Amplifier, which has no programmability. This program is stored on the internal flash program memory of the μC.

The firmware implements three main functions:

- Initialisation and configuration of the DDS to generate the desired RF signal.
- Communication with the host controller with a defined control protocol.
- Implementation of a control loop of the RF output power.

Appendix B describes the programmed firmware and the implemented communication protocol.

3.3.2. Multiple sine signal generation

This driving technique relies on the AOTF spectral linearity: when multiple frequencies are applied to the crystal, the pass-band shape is equivalent to the combined pass-band shape that each individual frequency produces [Suhre and Theodore, 1996]. Therefore, when an AOTF is excited with a sum of closely spaced RF sine signals, the device shows a broader bandpass.

A composite RF signal can be generated easily in the digital domain, and after that the signal can be converted to the analogue domain by means of a high speed DAC. However, the direct generation of a digital multisine signal in the range required by an AOTF is a challenging problem, because it requires the DAC to work at a very high rate. It is common practice to use a high-speed digital circuitry (e.g. an FPGA) to generate the composite signal and feed the DAC in real-time. However, this approach requires the FPGA link to the DAC to work at a very high speed.

Nowadays, there are several DAC parts working in the needed frequency range (up to 250 MHz). However, the main technological problem when using them is that they require a digital circuit to generate the waveform and feed the DAC at a very high transfer rate. There are FPGA parts capable of delivering such performance, but their programming and design are quite complex.

The preferred solution is the MB86064, a DAC from Fujitsu (www.fujitsu.com) that implements an internal high-speed memory that can store any complex waveform. This circuit eliminates the problem of the generation and transfer of the composite waveform in real-time at a very high speed. In this way, the DAC can be programmed at a relatively low data transfer rate with a multisine RF signal previously synthesised on the digital domain, and then the DAC will read and convert the waveform stored in the internal memory at the sampling rate without any intervention from the generation circuitry.

3.3.2.1. Fujitsu MB86064 DAC

The MB86064 is a dual 14-bit DAC capable of working at 1Gsps. Apart from a Double Data Rate (DDR) LVDS port for feeding the DAC, this chip can use two internal 16k point programmable on-chip waveform memories. To simplify system integration the DAC operates from a clock running at half the DAC conversion rate.

The configuration of the DAC functionality is done through a 4-wire serial control interface. This control interface is also used to program the internal memories with an arbitrary waveform composed of up to 16ksamples. Fujitsu supplies a PC-USB programming cable for controlling the DAC through this 4-wire interface from a host PC. The PC-USB cable can be configured as a virtual serial port, allowing the direct control of the DAC by any program with access to the serial port,as, for example, MATLAB.

3.3.2.2. DAC-based RF generator

In contrast to the DDS driving approach where a custom circuit was built, we have evaluated the performance of the DAC generator with a testbench prototype. Therefore, the development time is reduced and attention can be paid to the circuit performance. The block diagram of the prototype is represented in Figure 3.4.

The prototype is based on the DK86064-2 evaluation board for the MB86064. This board allows using the MB86064 as an arbitrary waveform generator that makes use of the internal memory module of the part. The DAC is programmed by a host PC through the PC-USB cable and no real-time data generation and transfer in needed.

The evaluation board requires an external clock signal, which was generated in this case by a PROMAX GR-104 RF signal generator. The frequency is fixed to 500MHz to get a 1GHz conversion rate (the DAC has an interval PLL circuitry that generates a x2 frequency clock from the clock input).

The RF output signal of the evaluation board has a maximum power of 0dBm. As this power is far from the requirements of the used AOTF, we have connected an RF power amplifier at the DAC output. We have chosen the AP5300-2 RF amplifier from R.F.P.A. (www.rfpa.com), which has a nominal gain of 33dB and a maximum output power of 2W (+33dBm).

Note that this circuit has a fixed gain, which has been adjusted to produce a +33dBm power level on the AOTF when driving the crystal with a single sine at maximum amplitude. However, as the number of sine signals that are simultaneously generated increases, the amplitude of each sine is reduced on the composite signal that is fed to the DAC. Therefore, for n simultaneous components, the power applied in each sine to the AOTF is reduced in a factor of n^2, and the total amount of power applied to the AOTF is reduced in a factor of n.

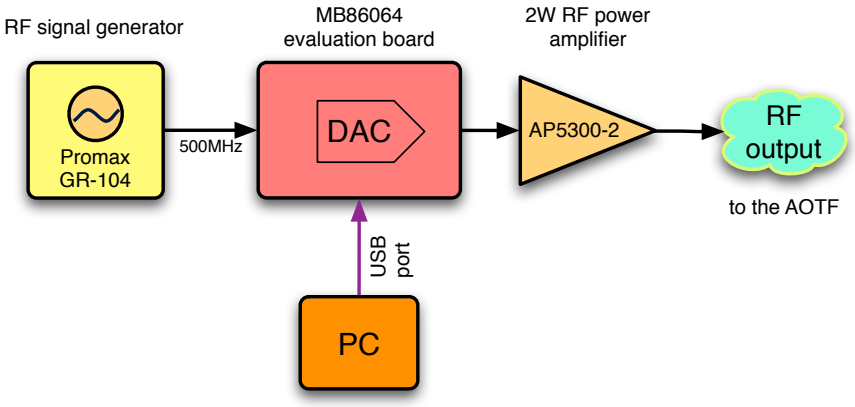

Figure 3.4. Block diagram of the DAC-based driver prototype.

Figure 3.5. DAC-based driver prototype.

A picture of complete DAC-based driver prototype is shown in Figure 3.5. In this picture, we can see the DK86064-2 evaluation board PCB, which is connected to the host computer through the PC-USB cable and clocked by a PROMAX RF signal generator.

3.3.2.3. Programming the MB86064

The 4-wire serial interface of the MB86064 uses pins SERIAL_IN, SERIAL_OUT, SERIAL_CLK and SERIAL_EN. Additionally, the input pin RESET can be used to generate a hardware reset in the circuit. All these five pins are connected to the PC-USB programming cable. Programmed settings are stored in a number of registers that are individually accessible using their corresponding address word. Data may be written or read from each of these registers.

The PC-USB cable implements a USB to 8-bit parallel conversion. The USB communication is handled by an FTDI USB FIFO IC (FT245BM), which converts serial data to 8-bit parallel. This data is buffered and latched before outputting to the I/O pins of the PC-USB cable.

The protocol is straightforward. A single byte of data is sent to the PC-USB cable over the USB interface (using the appropriate FTDI USB driver), and this data is decoded and latched onto the 8-bit wide I/O. As the output is latched, the data will not change until a different byte of data is sent. A data pattern can be generated by sending a string of bytes to the PC-USB cable.

For DK86064-2 the data bit assignments are as follows:

- Bit 0 = SERIAL_IN (when writing to the DAC) / SERIAL_OUT (when reading from the DAC)
- Bit 1 = SERIAL_CLK
- Bit 2 = SERIAL_EN
- Bit 3 = X_RESET

To read data back from the USB cable set Bit 7 to logic high. The rising edge of Bit 7 triggers a read of the R7-0 I/O pins.

All the data sent to the DAC follow the same sequence, described on the MB86064 datasheet [Fujitsu, 2005]. The sequence starts specifying the address of the register to be programmed, followed by a 'write' bit ('1') and the new contents of the register itself. All the data are sent MSB first. The address is either a 7-bit

(waveform memory module, WMM) or 10-bit (DAC core registers) word. The contents of the register are zero-filled at the MSB bit when the number of bits to program is less than 28 (DAC core registers) or 64 (WMM).

We have implemented a function in MATLAB that programs the internal registers of the DAC though the PC-USB cable, making use of the Virtual Port driver of the FTDI USB chip. The code for this function is listed in the attached CD.

The programming of the MB86064 comprises two steps. First, it is necessary to configure the DAC in order to use the internal waveform module rather than the LVDS data inputs, as well as other setup values. After this initial setup, the DAC is ready to accept a waveform to be programmed on the internal memory. In order to send any waveform to the DAC, it is necessary to reformat the waveform vector generated in MATLAB to the order required by the DAC serial control interface. This conversion is done by a set of MATLAB functions, listed also on the attached CD. The format of the waveform requires that the even and odd points of the signal are sent separately, in blocks of 4 points packed as 64-bit words.

IV

Host computer software

The ATFS instrument is controlled from a PC through a custom software. The software is divided into three main tasks: Control of the multispectral sensor, image acquisition, and image processing. The output of the application is a complete hyperspectral image of the target (hypercube) in ENVI format, containing raw data (digital counts), or normalised information (reflectance or transmittance). The ATFS control software is organised into two layers (Figure 4.1): a driver layer for the control of the camera and the RF generator, and an application layer with a user interface for the image acquisition, processing and storage.

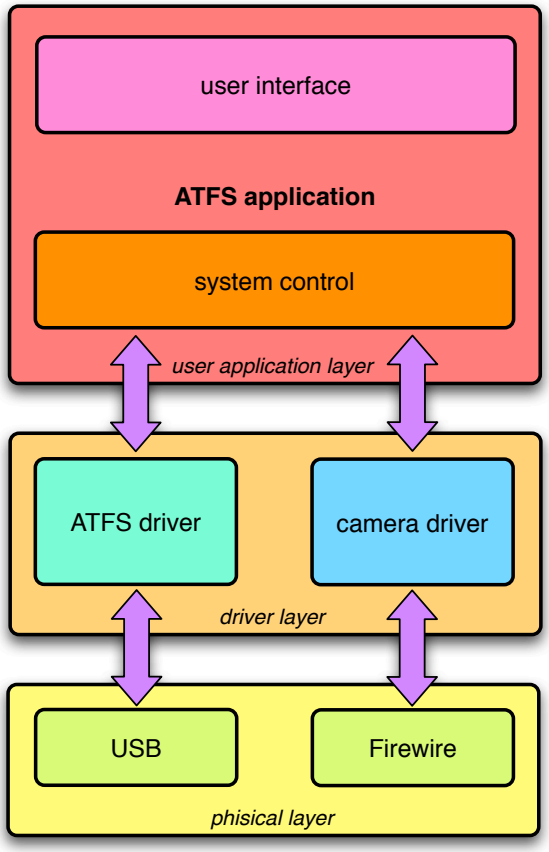

Figure 4.1. ATFS software layers.

4.1. Driver layer

The application uses two drivers, one that controls the camera and another one that controls the RF generator. The camera driver controls the camera through the Firewire interface. It is a standard driver supplied by the camera manufacturer. The implemented software detects the connected camera on the Firewire bus and loads automatically the correct driver. On the other hand, the RF generator is controlled through the USB interface by a custom driver, which has been designed to benefit from all the advantages of the DDS-based signal generation.

4.1.1. Camera driver

Each camera model uses a different driver, but the user application automatically detects the actual camera on the instrument and uses the appropriate driver. All the drivers are used in a similar way, and are composed by a set of functions that configure the camera and perform the image acquisition. The drivers allow high flexibility on the camera control. Among other possibilities, the drivers execute the following actions: adjustment of the exposure time, adjustment of the gain, selection of single image acquisition or continuous video mode, adjustment of a Region of Interest (ROI) or binning in the image, and asynchronous start of an image capture. Some camera models present more features than others, and that fact is reflected on their correspondent drivers. For example, the Coolview EM1000 camera has an adjustment for the Electron-Multiplying gain, which is different from the video gain, also present on the other models.

4.1.2. DDS-based RF generator driver

The RF generator driver (RFGD) configures the DDS-based RF generator in order to output the adequate RF signal for the required AOTF diffraction, just in synchronisation with the camera acquisition. The driver transforms the band characteristics defined by the user (in terms of central wavelength and bandwidth) into the RF board numerical requirements (initial sweep frequency, frequency step value, time step value, and output power). This transformation comprises various steps, summarised on the flow diagram of Figure 4.2. The parameters required for the transformation come from an accurate AOTF calibration performed during the initial instrument set-up.

The synchronisation is achieved through serial commands. The driver sends two commands to start and stop the RF generation, while the RF board issues another command to confirm the validity of the RF output each time a new band is configured.

4.1.2.1. Numerical transformations

The ATFS instrument can filter broad bands of light when driven by a sweeping RF signal. The sweep is generated on the DDS, which needs to be configured properly by programming three registers: Frequency Tuning Word (FTW), Delta Frequency Tuning Word (DFTW), and Delta Frequency Ramp Rate Word (DFRRW). The DDS generates a sweeping RF signal starting from the frequency set by the FTW, and increases the output frequency by discrete steps fixed by the DFTW at a rate defined by the DFRRW. In the DDS-based generator, the total duration for each sweep was fixed to 5ms.

The bands are defined according to their central wavelength and bandwidth. These characteristics determine the initial and final wavelengths over which the AOTF will sweep. These two wavelengths are converted to the initial and final frequencies of the RF sweep, which are finally translated to the three DDS words and sent to the RF board. The AOTF presents a certain bandwidth at the filtered output, even when it is driven by a pure sinusoidal signal. The bandwidth value depends on the central wavelength. These values are characterised for the ATFS instrument. Therefore, the initial and final wavelength of the sweep are given by:

$$\lambda_{initial} = \lambda_{central} - \frac{BW}{2} + \frac{BW_{\lambda_{central} - BW/2}}{2}$$

$$\lambda_{final} = \lambda_{central} + \frac{BW}{2} - \frac{BW_{\lambda_{central} - BW/2}}{2} \qquad \textbf{(Eq. 4.1)}$$

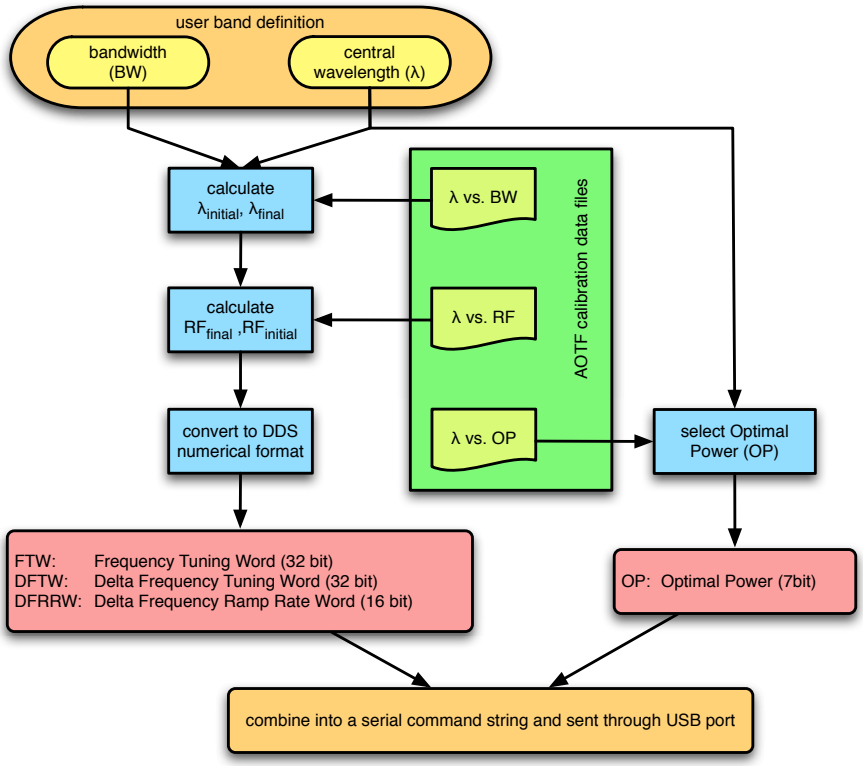

Figure 4.2. Flow chart of the RF Generator Driver.

where $\lambda_{central}$ and BW are the central wavelength and bandwidth defined by the user, respectively, and BW_λ is the bandwidth of the instrument at wavelength λ.

The relationship between wavelength and RF frequency is linear, and it has been fully characterised for the ATFS instrument. The RF frequency decreases with the wavelength increase, and therefore the final wavelength value is used as the initial RF frequency for the sweep, and vice versa. The initial RF frequency value in MHz is converted to the FTW register value as detailed on Appendix B (RF board firmware).

The frequency step and the change rate depend on the number of frequency steps on the sweep. This number is calculated according to the following algorithm:

$$\begin{aligned} &\textit{if } RF_{initial} > 90\ MHz \\ &\quad \begin{cases} N = \dfrac{RF_{final} - RF_{initial}}{0.5\ kHz} \end{cases} \\ &\textit{else} \\ &\quad \begin{cases} N = \dfrac{RF_{final} - RF_{initial}}{0.75\ kHz} \end{cases} \end{aligned} \qquad \textbf{(Eq. 4.2)}$$

N is rounded to the nearest integer. If N<10, a value of 10 is used. From this calculation, the other two parameters can be calculated:

$$\begin{aligned} \Delta t &= \frac{5ms}{N} = \frac{5000\,\mu s}{N} \\ \Delta f &= \frac{f_{final} - f_{inicial}}{N} \end{aligned} \qquad \textbf{(Eq. 4.3)}$$

The contents for the registers DFTW and DFRRW are directly obtained from these two values (see Appendix B). After that, the contents of the three registers are sent to the RF board following the defined protocol. Finally, the driver completes the band configuration by sending the value of the output power, according to an optimal power calibration table. This table was obtained empirically from a previous ATFS calibration procedure. The complete optimal power estimation procedure is detailed on [SmartSpectra 2006c].

4.1.2.2. Camera synchronisation

The camera is synchronised with the RF generator so that the image is acquired only when the RF signal is stable. When the RFGD sends the new band characteristics, it waits until the RF board updates its output. After sending a new band configuration, the RF board firmware adjusts the power of the RF output until it reaches the desired value. Then, it sends an "updated output" command to the RFGD, which in turns triggers the camera acquisition. Figure 4.3 shows the flow chart of this synchronisation process.

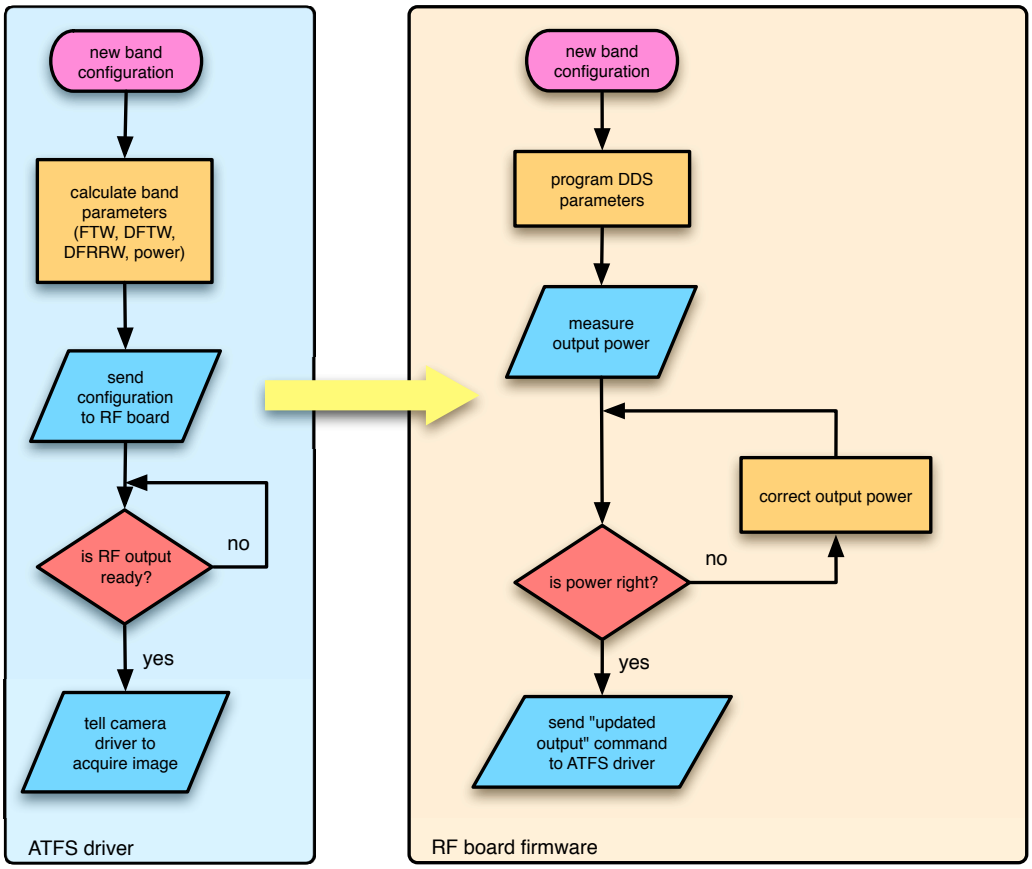

Figure 4.3. Flow chart of the synchronisation process between the RF board and the image acquisition.

4.1.3. DAC-based RF generator driver

Opposite to the DDS-based RF generator, on the DAC-based generator the RF waveform is generated on the host computer and then transferred to the internal memory of the DAC, from which is reproduced cyclically.

Therefore, the DAC-based RF generator driver creates digitally a waveform that, once programmed to the internal memory of the DAC, will generate the required RF signal to drive the AOTF. The driver also manages the transfer of the waveform to the DAC memory.

4.1.3.1. Waveform generation

The internal memory of the chip can hold up to 16kpoint of data for a single waveform. It is necessary to generate a complete waveform period in order to eliminate unwanted harmonics on the RF output signal.

By limiting the maximum waveform length to 10kpoints, the frequency resolution of the generated sine is 100kHz (using a 1GHz conversion rate). In this way, the driver can generate any single or composite waveform with a period of 10k point or a sub-multiple of this value. This restriction has minimum impact on the precision of the central wavelength of the filtered signals. Simulations run on the calibrated wavelength to RF curve for the Isomet AOTF show a wavelength shift of less than 1nm in all the working range.

The driver generates the single band waveforms with the following equation:

$$s = 1 + 0.5 \cdot \sin\left(2 \cdot \pi \cdot {}^{f}\!/_{1GHz} \cdot time\right) \qquad \textbf{(Eq. 4.4)}$$

where *f* is the desired frequency for the RF output, rounded to the nearest 0.1MHz multiple, and *time* is a vector of 10kpoints from 0 to 9999. The waveform is scaled to the range [0-1], because the used DAC works with unsigned 14-bit integers.

According to the desired power amplitude, the output of this equation is scaled and converted to a fixed-point 14-bit unsigned integer. Therefore, for the maximum output amplitude, the resulting waveform spans from 0 to 16383. For an arbitrary output amplitude, the waveform is scaled proportionally:

$$output = \text{round}\left(s \cdot \frac{16383}{amplitude}\right) \qquad \textbf{(Eq. 4.5)}$$

where *amplitude* is the desired output amplitude normalised to the range [0-1].

For the generation of a multiband waveform, the driver uses the following equation:

$$s = \sum_{i=1}^{n}\left(1 + 0.5 \cdot \sin\left(2 \cdot \pi \cdot {}^{f_i}\!/_{1GHz} \cdot time\right)\right) \qquad \textbf{(Eq. 4.6)}$$

where f_i with i=1..n are the frequencies of the waveform components, rounded to the nearest 0.1MHz multiple.

The output of this equation is scaled according to the desired amplitude and converted to a fixed-point 14-bit unsigned integer:

$$output = \text{round}\left(\frac{s \cdot 16383}{\max(s) \cdot amplitude}\right) \qquad \textbf{(Eq. 4.7)}$$

4.1.3.2. Waveform transfer to the DAC

The DAC-based RF generator driver manages the transfer of the waveform to the internal memory of the DAC. The communication between the DAC board and the host computer is implemented with a USB interface that is accessed by means of a virtual serial port driver.

The driver converts the generated output vector to the byte stream using the communication protocol defined by the manufacturer [Fujitsu, 2005].

4.2. User layer

The user of the ATFS instrument controls the image acquisition of a target from a software application that runs over the driver layer. This application is responsible for automating the image acquisition from the user band requests and the subsequent image processing. As a result, the user gets a multispectral image (hypercube) of the reflectance / transmittance of the imaged target.

The author has implemented two different user layer applications for the ATFS instrument, depending on the used RF driver. For the DDS-based generator, a GUI application has been developed in C++ with the Microsoft Visual Studio package. On the other hand, for the DAC-based generator the instrument control has been implemented through a MATLAB command-line toolbox.

4.2.1. ATFS image characteristics

Due to the non-ideal functionality of the AOTF's and digital cameras, the images acquired with the ATFS instrument present several drawbacks that need to be worked out. The main problems are: spatial non-homogeneity, stray light and dark current (SL+DC), and chromatic aberration (CA).

4.2.1.1. Spatial non-homogeneity

The diffraction efficiency of the AOTF's is not constant along their crystal surface. Therefore, the images acquired through this kind of filters present a spatial non-homogeneity pattern. This non-homogeneity has been proved to be constant for each particular RF signal applied to the crystal. Therefore, this effect can be corrected on the acquired images with a spatial normalisation respect to the non-homogeneity.

This normalisation can be implemented in two ways:

- Characterising the spatial non-homogeneity for the used RF signals. This is done by imaging a completely flat spatial pattern (as for example an integrating sphere). Images are corrected by dividing them with the corresponding spatial characterised non-homogeneity pattern.
- Using a ratio of two images acquired using the same RF signal (as for example when calculating a reflectance or transmittance index). As both images present the same spatial non-homogeneity pattern, the non-homogeneity effect is removed.

4.2.1.2. Stray light and dark current

All the images acquired with the CCD camera of the ATFS system are contaminated by stray light and dark current (SL+DC). SL consists on all the light coming from out of the selected spectra that reaches the sensor, due to the non perfect blocking of the zero-order diffraction. Moreover, as the exposure times of the system are quite high (more than a second), the effect of the DC on the generated images is relevant and cannot be neglected. DC arises from thermal energy within the silicon lattice comprising the CCD. Electrons are created over time that are independent of the light falling on the detector. Those electrons are captured by the CCD's potential wells and counted as signal. Additionally, this increase in signal also carries a statistical fluctuation known as dark current noise.

Both stray light (SL) and dark current (DC) are proportional to the exposure time of the image. In fact, both contributions can be jointly modelled as an offset plus a signal intensity that is linearly proportional to the exposure time. Therefore, by measuring the contribution of the SL + DC signals at several exposure times we can estimate this contribution in any image given its exposure time. Then, we can remove this contribution from the acquired images.

The DC + SL (abbreviated as DC) contribution to the acquired signals depends on the exposure time according to the following equation:

$$DC = DC_{offset} + DC_{slope} \cdot t_{\exp} \qquad \textbf{(Eq. 4.8)}$$

As a verification of the DC linearity, we have acquired the DC contribution to the images for 25 different exposure times (from 1 to 25 seconds). We have estimated for each image the mean value of the DC (represented in Figure 4.4 as a function of the exposure time).

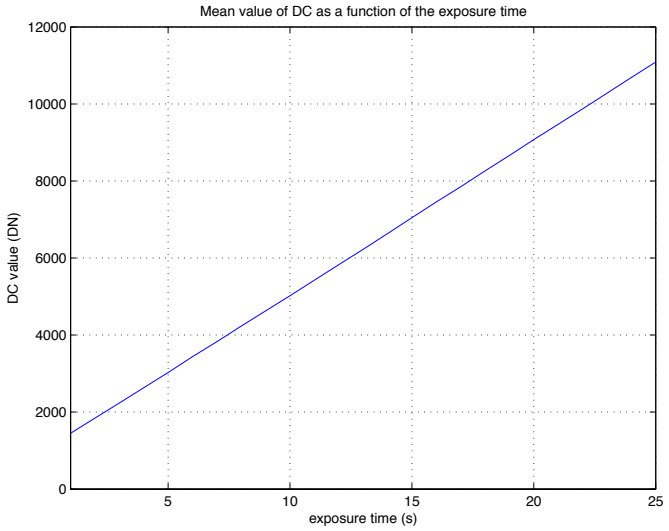

Figure 4.4. Mean value of the DC as a function of the exposure time.

We estimate the values of DC_{offset} and DC_{slope} in this equation by acquiring two images with the AOTF switched off and two different exposure times (1 and 10 seconds). From these two images, we calculate the DC_{offset} and DC_{slope} of the sensor for this given configuration as:

$$DC_{offset} = \frac{10 \cdot DC_{IM(1)} - DC_{IM(10)}}{9}$$
$$DC_{slope} = \frac{DC_{IM(10)} - DC_{IM(1)}}{9} \qquad \textbf{(Eq. 4.9)}$$

where $DC_{IM(t)}$ is the DC image taken with an exposure time of *t*. This equation is applied pixel by pixel, generating two maps of the offset and slope of the DC. From these values we estimate the DC contribution to each image, according to Eq. 4.8, which is removed from the final images.

The order of magnitude of the DC contribution can be seen on Figure 4.5 and Figure 4.6, which show the averages for the DC_{offset} and DC_{slope} over the 25 images used for the verification of the DC linearity.

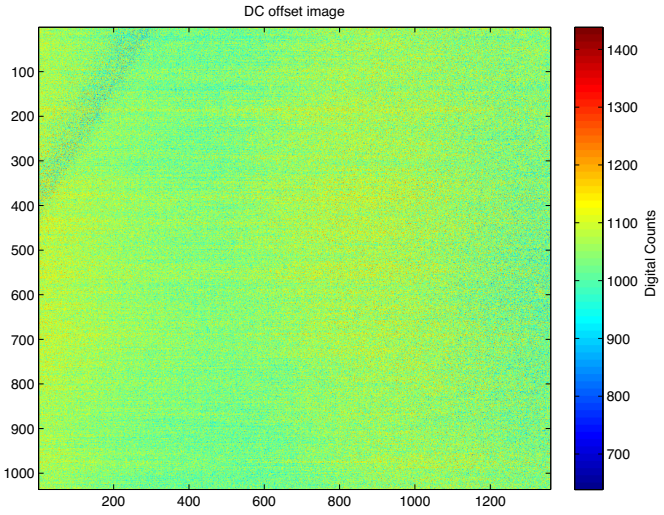

Figure 4.5. Estimated DC_{offset} for the 25 images used on the analysis of the DC, expressed as Digital Counts.

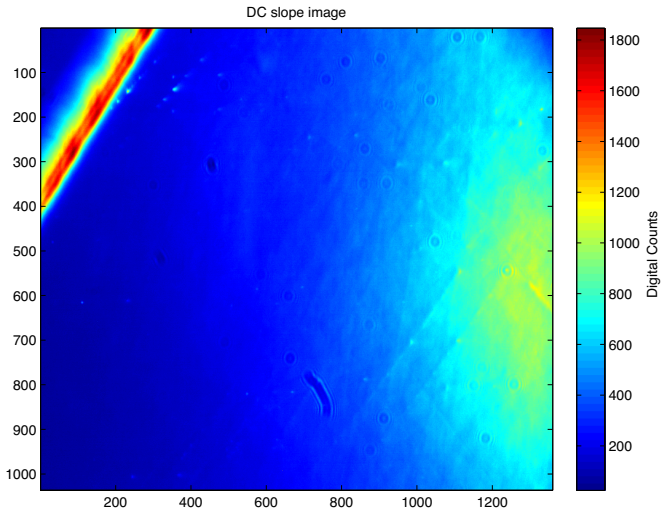

Figure 4.6. Estimated DC_{slope} for the 25 images used on the analysis of the DC, expressed as Digital Counts.

From this images we appreciate that the DC_{offset} is quite homogeneous for all the picture, because it depends mainly the Dark Current of the CCD sensor, while the DC_{slope} presents a spatial pattern related to the Stray Light that crosses the optical layout. On this stray light pattern we can distinguish the contribution of the target illumination on the right side of the image (in this experiment, the light source was located at the right of the imaged target), and a bright line on the upper left corner that is due to an internal reflectance of light inside the ATFS box.

4.2.1.3. Chromatic Aberration

The diffraction angle of the AOTF output light varies slightly with the applied RF frequency. This fact causes a chromatic aberration (CA) on the acquired image hypercubes, as the different band images present a spatial shift.

Measuring the shift as a function of the wavelength and applying the opposite shift to the acquired images can partially compensate for the CA. However, multiband images cannot be corrected in terms of CA, as they present different shifts on each single image due to the contribution of the different wavelengths.

We have calibrated the shift of our ATFS system in all the working range, and generate a MATLAB function than automatically applies the opposite shift to the images as a function of the wavelength.

For the calibration of the CA we have measured the spatial shift between an image on the lower wavelength end (450nm) and the higher end (750nm). The shift has been measured with the image registration tools provided by MATLAB. On a course approach, we manually select several control points on both images with the 'cpselect' function. The control points are pairs of image coordinates that correspond to the same image feature in both images. Then, we perform a automatic fine-tune of the control points with the 'cpcorr' function, which calculates the correlation between both images by shifting around the control points and adjusting them to the maximum value. The shift of the system is then assigned to the average value of the measured shift (separation in pixels between the control points). On the attached CD we list the MATLAB script used for this CA calibration.

This calibration assumes that the CA is linear along the working range, but this assumption need to be corroborated. We have implemented another MATLAB script that verifies the linearity of the CA by measuring the shift for all the acquired bands respect to the first one (450nm). In this script, we choose several control points on the first image. Assuming a linear shift, the script estimates the shift for each band and measures the actual shift from this estimation by means of the 'cpcorr' function. Figure 4.7 shows the measured horizontal shift values for all the bands respect to the first band, and the estimated linear shift; Figure 4.8 represents the same figures for the vertical dimension. Note that the apparent higher dispersion of the vertical

values is due to the fact that the plotted scale on the vertical shift is much smaller, because the chromatic aberration of the AOTF occurs mainly along the horizontal dimension. By looking at these figures, we can affirm that the shift is linear with respect to wavelength. Instead of using the estimated shift value, we calculate a 1st order polynomial fitting of the shift value using all the bands and then we use the polynomial coefficients for the compensation of the acquired images.

For applying the CA compensation, we perform an affine transform to the band to be corrected using the following transformation matrix:

$$\mathbf{T}=\begin{bmatrix} 1 & 0 & 0 \\ 0 & 1 & 0 \\ t_x & t_y & 1 \end{bmatrix}$$

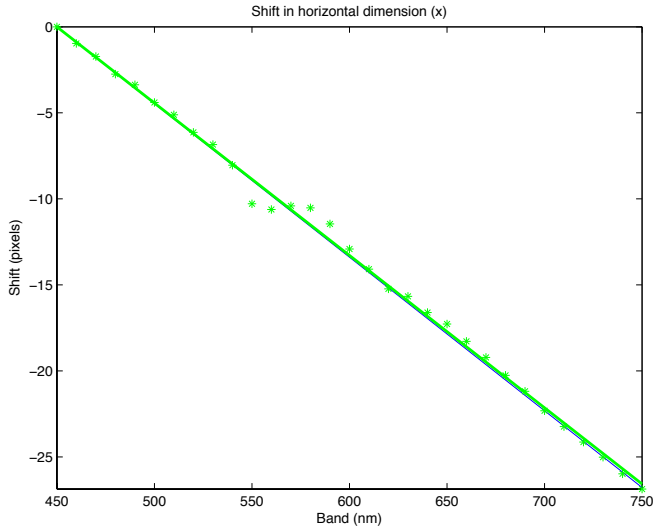

Figure 4.7. Horizontal shift of the ATFS. In blue line the estimated shift taking into account the first and the last bands; in green asterisk, the measured shift for all the bands respect to the first one; in green line the linear approximation to the measured values.

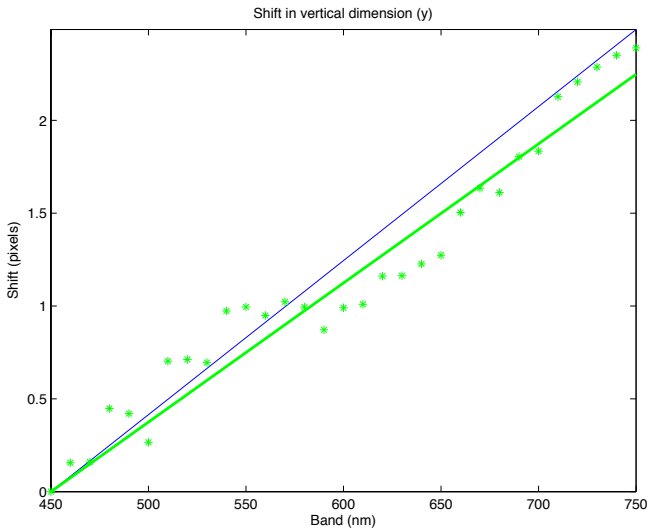

Figure 4.8. Vertical shift of the ATFS instrument. In blue line the estimated shift taking into account the first and the last bands; in green asterisk, the measured shift for all the bands respect to the first one; in green line the linear approximation to the measured values.

where t_x is the displacement along the x axis of the image and t_y is the displacement along the y axis. The transform is applied with the 'imtransform' function from the Image Processing Toolbox of MATLAB. The displacement values are obtained evaluating the polynomial fitting of the CA at the image wavelength. The CA compensation algorithm has been implemented inside a MATLAB function called 'getband', which retrieves the image corresponding to a given wavelength from an ENVI hypercube. The listing of this function can be found on the attached CD.

4.2.2. Image acquisition

The user application software automates the acquisition of an image hypercube with the ATFS instrument. Normally, the user wants to acquire the reflectance or transmittance image of a target, which requires the sequential acquisition of a white reference (WR) for all the bands and next the acquisition of the target itself.

The user defines the bands to be acquired and, in the case of the DDS-based generator, the desired bandwidth of each band. The application can estimate automatically the optimal exposure time for each band, or the user can define the desired value. For the estimation of the optimal exposure times, the application acquires an image at each defined band with a very short exposure time, and analyses the image intensity to get the required exposure time that maximises the dynamic range of the sensor without saturating the image.

Finally, the application acquires four sets of images:

1. Two images at different exposure times of the WR with the AOTF switched off. These images are used for the DC compensation of the WR images. These images form the DC dataset of the WR.
2. The sequence of images at the selected bands for the WR. These images form the raw image dataset of the WR.
3. Two images at different exposure times of the target with the AOTF switched off. These images are used for the DC compensation of the target images. These images form the DC dataset of the target.
4. The sequence of images at the selected bands for the target. These images form the raw image dataset of the target.

This acquisition workflow is summarised schematically on the Figure 4.9.

4.2.3. Image processing

The user application processes the four sets of acquired images in order to obtain a final hyperspectral cube of the reflectance or transmittance of the target. The processing comprises several steps for the correction of the AOTF-related effects on the acquired images, and finally, the estimation of the reflectance or transmittance.

The image processing workflow is summarised on Figure 4.10. The first step of the processing is the correction of the DC of the raw image datasets, using the information from the DC datasets. The correction is implemented as described on Section 4.2.1.2.

Then, the CA of the images is corrected, by applying a band-by-band spatial shift on the images. The value of this shift is the opposite of the estimated shift of the band, obtained from a previously calibrated polynomial.

Finally, the corrected datasets of the WR and the target are combined to create the resulting reflectance or transmittance hyperspectral cube. The reflectance (or transmittance) is calculated as the ratio between the target and the WR pixel values, using the following expression (for the band λ):

$$\text{reflectance}(\lambda) = \frac{DN_{IM}(\lambda) \cdot t_{exp,WR}(\lambda)}{DN_{WR}(\lambda) \cdot t_{exp,IM}(\lambda)} \qquad \textbf{(Eq. 4.10)}$$

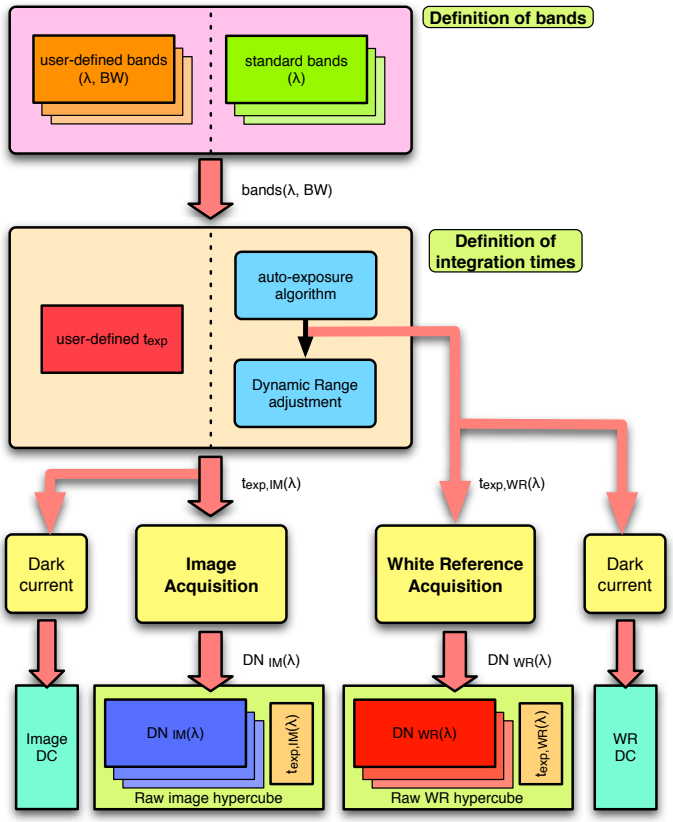

Figure 4.9. Acquisition workflow.

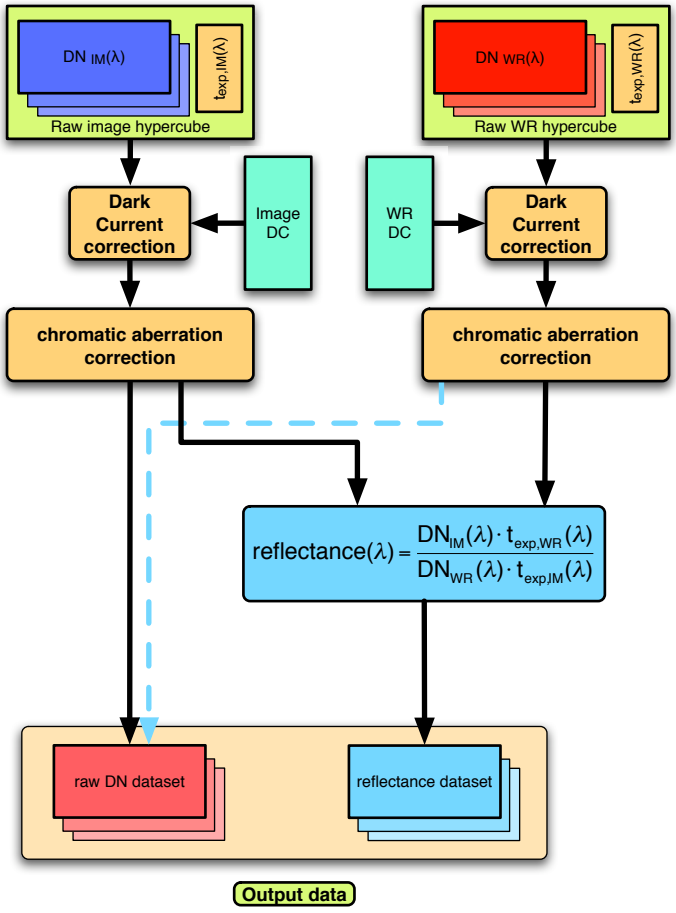

Figure 4.10. Processing workflow.

Where $DN_{IM}(\lambda)$ is the intensity Digital Number (DN) of a pixel from the target image, after the acquisition corrections; $DN_{WR}(\lambda)$ is the intensity DN of a pixel from the WR image, after the acquisition corrections; $t_{exp,IM}(\lambda)$ is the integration time used for acquiring the image; and $t_{exp,WR}(\lambda)$ is the integration time used for acquiring the White Reference. The system can use a single White Reference hypercube for multiple images acquired under the same illumination conditions.

4.2.4. ATFS GUI application

The ATFS GUI application is an implementation of the user layer of the ATFS instrument software for the case of the DDS-based RF generator. The ATFS GUI application implements all the steps of a complete multispectral image acquisition, based on the user parameters and the initial calibration data.

The user application is divided into two main tasks: image acquisition and image processing, which are controlled from two different windows. The application has also a video window, which can show a real-time preview of one band or the acquired images as they are taken. Figure 4.11 shows an screenshot of the main window of the application.

The image acquisition performs sequentially all the tasks related to the image acquisition. The first task is the definition of the acquisition bands. Then, the integration times are adjusted. Using those parameters, the images of the different bands are acquired. Finally, the images are corrected in terms of spatial non-homogeneity and chromatic aberration, and saved as a raw data hypercube file. Additionally, a white reference or a dark current set of images can be acquired and stored separately.

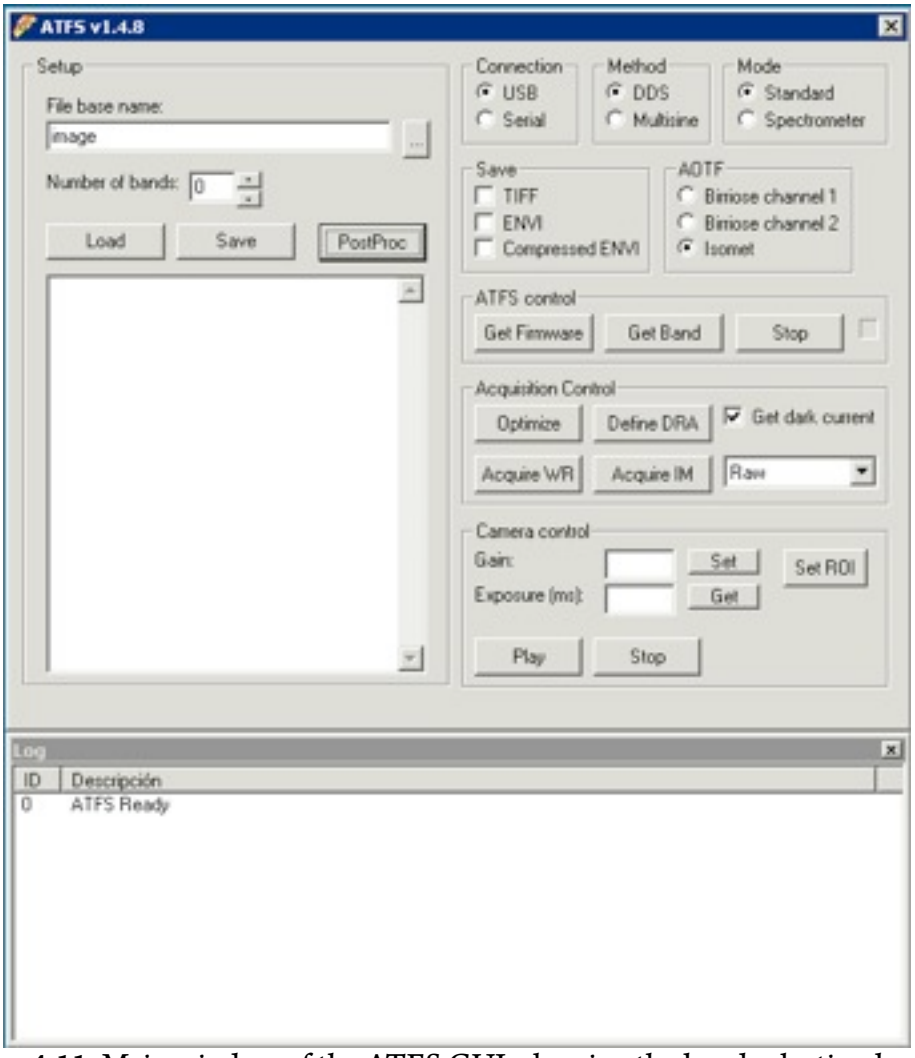

Figure 4.11. Main window of the ATFS GUI, showing the band selection box and the image acquisition controls.

The image processing performs a reflectance calculation to the acquired images. The processed images are stored as a hypercube of Reflectance band images.

4.2.4.1. Image acquisition

The application acquires sequentially all the bands defined by the user. The application manages separately the acquisition of a white reference and the acquisition of target images. The white reference images are treated in a different way in order to permit later calculations on the target images (reflectance and transmittance computations).

The integration times can be specified from a file or calculated with the auto-exposure algorithm. This algorithm adjusts the optimal dynamic range for a White Reference target (by changing the exposure time of the camera). When imaging a target, the dynamic range can be readapted to the maximum estimated reflectance by applying a factor to the calculated integration times. This factor depends on the acquired wavelength, and is called "Dynamic Range Adjustment" vector.

When performing any set of band acquisitions, the system records the dark current of the system for two different exposure times. This information is used to compensate for the dark current on every image on the set, independently of their exposure times, because the application estimates the correct DC value for each time using a linear model.

Band selection

The user specifies in a text box or loads from a file the set of bands to be acquired. Each band is defined by a central wavelength, a bandwidth and an exposure time. The central wavelength and the bandwidth define the spectral characteristics of the image that will be acquired, while the exposure time depends on the sensitivity of the system for each band. The user needs not to specify the exposure time, since the application calculates the optimal time for each band with an iterative algorithm. This algorithm adjusts the exposure time of each band so that the dynamic range of the camera is fully employed.

Auto-exposure algorithm

The auto-exposure algorithm maximises the dynamic range of the sensor. The efficiency of the system varies significantly for each wavelength, since it depends on sensor sensitivity, incoming light, reflectance, and bandwidth. Consequently, the integration time of each selected band must be adjusted independently in order to achieve the maximum dynamic range of the sensor (normally 12 bits, which is more than 72dB). This algorithm estimates the optimal integration time for each band by evaluating a white reference target so that the maximum grey level in the image is a 90% of the Dynamic Range (DR). The algorithm is described in detail on [SmartSpectra, 2005b].

In most targets, the reflectivity of the measured objects is not higher than 60%. Therefore, the algorithm can apply a multiplier factor to the obtained integration times in order that a lower reflectivity can fill the entire DR of the sensor. The factor is defined as the maximum Estimated Reflectivity (ER) of the image, in percentage. This ER is configured by the user as one value for all the bands or as a multiplier function dependent on the wavelength, and then the new integration time is calculated as follows:

$$t_{exp(image)} = \frac{t_{exp(WR)}}{ER/100} \qquad \textbf{(Eq. 4.11)}$$

This process is called "Dynamic Range Adjustment" (DRA).

The ER factor can be specified by the user through an application window, or it can be read from a file.

4.2.4.2. Image processing

The ATFS GUI application can perform an image processing to the acquired data (Figure 4.12). After the acquisition of the full set of bands, the system performs two automatic corrections before saving the data.

The first one is the compensation of the dark current of the images. The second one is the correction of the chromatic aberration (CA) of the AOTF. The CA correction is based on a calibration file of the AOTF obtained during the initial system calibration. The dark current compensation depends on the characteristics of the image, and therefore it is derived from the two dark current images acquired for each set of images.

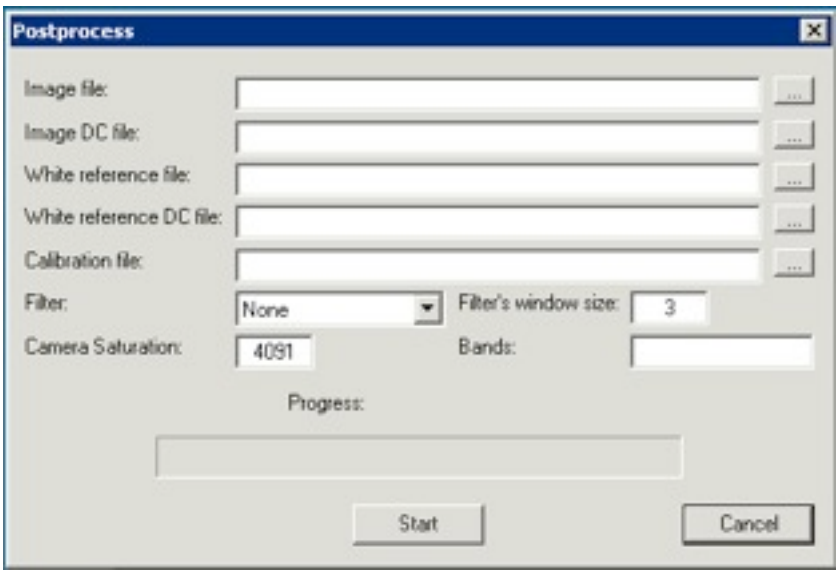

Figure 4.12. Post-processing window of the ATFS software.

The images can be optionally processed to retrieve the reflectance or transmittance information of the acquired scene. In this case, the user specifies in the post-processing window the image and white reference files, and the software performs the reflectance or transmittance calculations. The software assumes that the radiance acquired for the white reference image is equal to the radiance that the object receives (that is, the object and the white reference are acquired from the same point of view with a constant illumination). The software can apply a smoothing spatial filter to the images in order to reduce the acquisition noise.

The software can store the acquired images in two modes: as raw DN or as reflectance/transmittance values. The application can always save the raw DN of any image (from the target or the White Reference) but the reflectance/transmittance mode will only work when the system has previously acquired a White Reference hypercube for the same bands of the target image.

The processing and storage of the images is independent of the acquisition. Therefore, an image can be acquired but not processed, or the same White Reference image can be applied to calculate the reflectance of different target images. On the other hand, the image processing can be applied to a set of images previously acquired and stored as raw DN.

4.2.5. MATLAB hyperspectral acquisition toolbox

The MATLAB hyperspectral acquisition toolbox is an implementation of the user layer of the ATFS instrument software for the DAC-based based generator. It consists on a series of MATLAB functions that automates the image acquisition, processing, and storage in ENVI compatible format. Table 4.1 lists the functions implemented on the toolbox.

Table 4.1. Description of the functions of the MATLAB hyperspectral acquisition toolbox.

Function	Description
hypercube=hyperspectral_acquire(bands, powers, filename)	Captures an image for a given band or vector of bands with the specified power. Returns an hypercube of images of 1036x1360xN pixels with 12-bit (uint16), where N is the number of bands.

Function	Description
[reflectance, keywords]=get_reflectance(target, wr, bands, filename)	Calculates the reflectance of the image 'target' using the white reference on 'wr', for the bands on the vector 'bands' and stores the results on a ENVI file with the name 'filename'.
IM=getband(file,band,varargin)	Returns a reflectance image of the band specified by 'index' from the reflectance hypercube stored on the specified memampfile 'file'.
Auxiliary functions	
out=correct_ca(image, wavelength)	Corrects the chromatic aberration from the image at the specified wavelength.

The user defines the desired bands to acquire as a vector of wavelengths. The function 'hyperspectral_acquire' takes this vector as an input argument and acquires a sequence of images of the specified bands. The function adjusts automatically the exposure time of each band to maximise the dynamic range of the images. This function generates an output structure that contains the DC dataset of the image and a raw data hypercube as an ENVI band sequential (bsq) file.

For the measurement of the reflectance or transmittance of a target, the user must call this function twice, one to acquire the hypercube of the WR and another to acquire the hypercube of the target itself.

The images are processed with the function 'get_reflectance', which corrects the DC and CA and calculates the reflectance / transmittance from the two acquired hypercube. The function 'get_band' can be used to read a single band from the resulting reflectance / transmittance hypercube.

Multiband spectral images can be also acquired by calling the function 'multiband_acquire'. This function acquires a single image corresponding to the response of the ATFS instrument to a multiband signal, which components are passed as a vector of frequencies to the function.

The listing of all the functions of the MATLAB hyperspectral acquisition toolbox can be found on the attached CD.

Part III
System performance

V

RF performance

In this section, we analyse and compare the performance of the two developed RF drivers as part of the ATFS implementation: the DDS-based driver and the DAC-based one. Apart from the usual single band RF generation mode, both drivers have been designed to generate a broadband RF signal, which has the effect of diffracting an adjustable passband of light on the AOTF. The DDS driver generates a fast sweeping signal that acts on the AOTF crystal as a broadband signal when considering a long integration time (compared with the sweep time). In the other side, the DAC driver generates a composite RF signal, whose components are close enough to act as a single broadband on the AOTF crystal.

The RF performance was analysed connecting the RF output of the drivers to a spectrum analyser, and driving the circuits in different conditions of frequency and power output, in both narrowband and broadband generation modes.

5.1. Experimental set-up

All the measurements were performed using the same equipment and protocol for both drivers. The RF spectrum was acquired with an Anritsu MS2661C Spectrum Analyser (SA). As the output power of the drivers is too high for the SA input, we inserted an RF attenuator in the signal path. All measurements were automated using MATLAB. Both drivers are controlled by USB (emulating a serial port), and the SA is controlled by GPIB through a USB/GPIB interface from Agilent Technologies (model 82357B). The experimental set-ups are shown on Figure 5.1 (DDS) and Figure 5.2 (DAC).

In order to control the drivers and the SA, the author developed several MATLAB Toolboxes, whose functions are described on Table 5.1. The listing of the functions can be found on the attached CD.

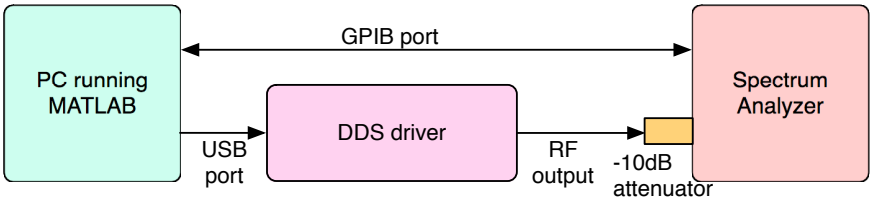

Figure 5.1. Experimental set-up for the RF characterisation of the DDS driver.

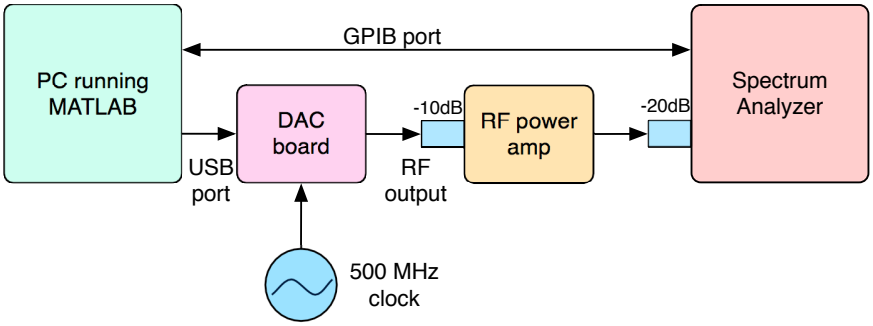

Figure 5.2. Experimental set-up for the RF characterisation of the DAC driver.

Table 5.1. List of functions of the developed MATLAB Toolboxes.

Function	Description
Spectrum Analyser control toolbox	
spectra = spectra_acquire_gpib(fs, fe)	Acquires the RF spectrum from frequency *fs* to frequency *fe*
[hf, hl] = spectra_harmonics_gpib	Returns the frequency and level of the 10 highest harmonics of the RF spectrum
spectra_initialize_gpib	Initialises GPIB port and configures SA to communicate with MATLAB
[pf, pl] = spectra_peak_gpib	Returns the frequency and level of the highest RF peak of the spectrum
spectra_plot(spectra)	Plots in MATLAB the RF spectrum stored on the structure spectra
Auxiliary functions (called by other functions of the toolbox)	
out=spectra_query_gpib(query)	Performs a query on the SA through the GPIB port
DDS-based driver control toolbox	
atfs_open_port	Configures and opens the ATFS communication serial port
atfs_performance_function(pf_code)	Asks the driver to execute the performance function specified by the code *pf_code*
atfs_send_freq(f_start, f_stop)	Sends the commands to configure the DDS in sweeping mode from *f_start* to *f_stop*
atfs_send_power(power)	Adjusts the driver output power to the specified value power
DAC-based driver control toolbox	
crea_multiseno_1000(freq, range, p)	Generates a waveform vector of 1000 points, composed by a multisine signal with the frequencies and powers specified by the parameters
crea_multiseno_10000(freq, range, p)	Generates a waveform vector of 10000 points, composed by a multisine signal with the frequencies and powers specified by the parameters
crea_seno_1000(freq, range, p)	Generates a waveform vector of 1000 points, composed by a sine signal with the frequency and power specified by the parameters

Function	Description
crea_seno_10000(freq, range, p)	Generates a waveform vector of 10000 points, composed by a sine signal with the frequency and power specified by the parameters
dac_send_config	Opens the communication serial port and writes configuration data to driver
dac_send_vector(vector)	Sends a waveform vector to the DAC trough the serial port
Auxiliary functions (called by other functions of the toolbox)	
serial_stream = dac_bitstream2serial(bitstream)	Converts a binary bitstream to the corresponding serial array to be send through the serial port
data_array = dac_data2bitstream(hexdata, ln)	Converts a hexadecimal address/data value into a logical array of *ln* elements (MSB first)
dac_data_bitstream = dac_vector2bitstream(data)	Converts a register data expressed as uint16 into a bitstream
write_array = write2dac(address_bitstream, data_bitstream)	Generates the string of bytes to be written into the DAC registers
[even, odd] = reshape_vector(vector)	Splits a waveform vector to be sent to the even/odd memory locations of the DAC

5.2. RF performance results

The RF performance of both generators was analysed in single and multiple band configurations at different output powers. For the single band case performance, the driver was configured to sequentially generate a pure frequency signal in the range from 50MHz to 120MHz in 10MHz steps, and the resulting spectra were captured. As an example of the obtained results, Figure 5.3 shows the RF output spectrum of the DDS-based driver at 90MHz for different power settings, in two different spectral ranges. Figure 5.4 shows the spectrum for the same frequency with the DAC driver.

The RF output amplitude was also recorded for all the frequencies between 50MHz and 120MHz with 1MHz steps. Figure 5.5 shows the RF output peak amplitude of the DDS driver at three different power settings (the plots correspond to the average value from three different sets of measurements). The same measurement is shown in Figure 5.6 for the DAC driver. The DDS shows a constant output power with frequency, thanks to the implemented control loop. However, the output power of the DAC driver decreases with frequency, following the characteristic sinc-shaped behaviour of DAC systems [Kester, 1996].

We took another set of measurements for the multitone mode generation, with the same experimental set-up. In the case of the DDS, the system does not generate a real multitone signal, but a sweeping signal that generates sequentially the required tones within a period of 5ms. The sweeping time of the spectrum analyser was set to a much longer time (5 seconds), so that it integrated the sweeping signal as a multitone signal. Figure 5.7 shows the RF output spectrum of a sweeping signal formed by 11 frequency steps from 87MHz to 93MHz in 0.6MHz steps. The equivalent configuration for the DAC driver is a composite signal of 11 components from 87MHz to 93MHz in 0.6MHz steps. However, the output power in this configuration is an eleventh part of the output power in single-band mode, because the amplitude of each component had to be reduced to 1/11 in order to do not saturate the DAC output circuitry. This fact is noticeable in Figure 5.8, which shows the spectrum for the DAC driver in this configuration.

Figure 5.3. RF output spectra of the DDS driver when generating a 90MHz single tone, at three different power settings (minimum, medium, and maximum), shown in the range from 85MHz to 95MHz (*top*) and from 20MHz to 280MHz (*bottom*).

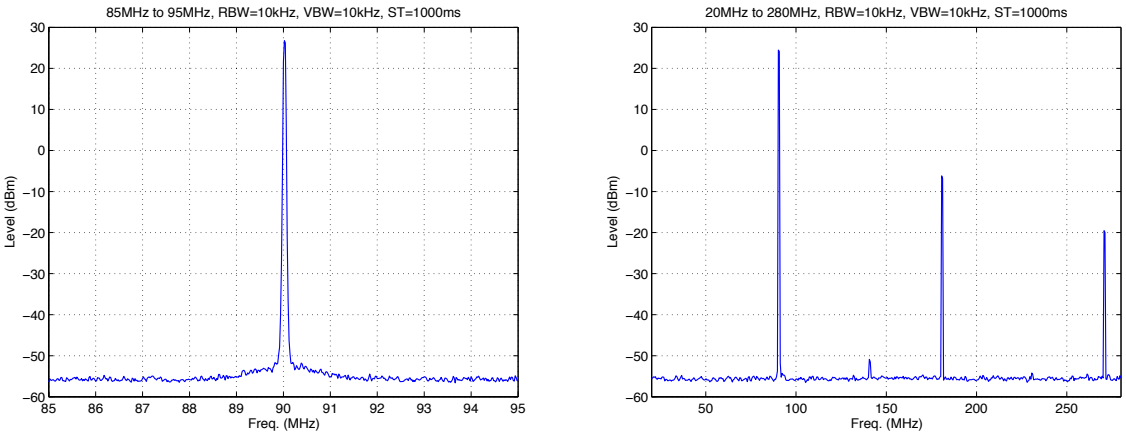

Figure 5.4. RF output spectra of the DAC driver when generating a 90MHz single tone, shown in the range from 85MHz to 95MHz (*left*) and from 20MHz to 280MHz (*right*).

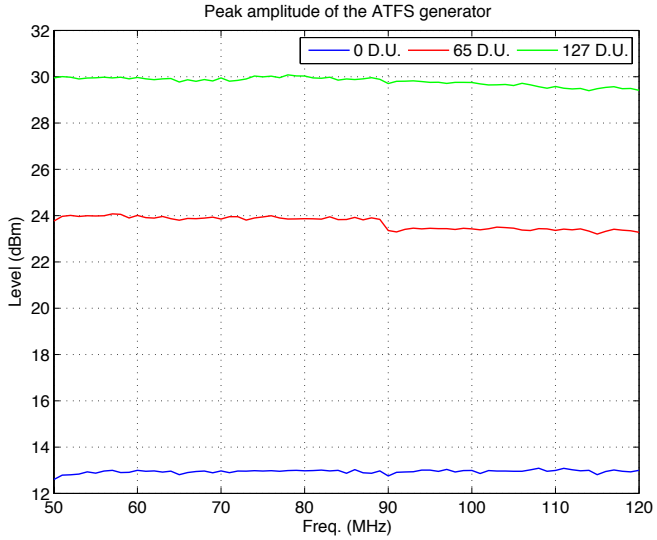

Figure 5.5. RF peak output amplitude of the DDS driver in single tone mode at three different power settings (minimum, medium, and maximum).

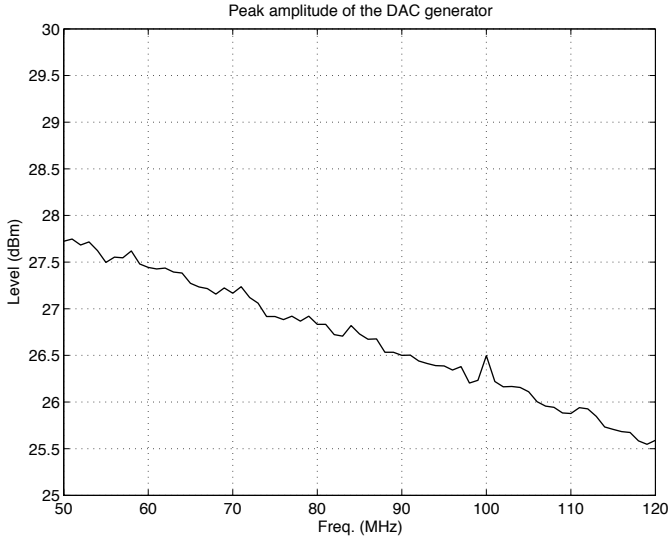

Figure 5.6. RF peak output amplitude of the DAC driver in single tone mode.

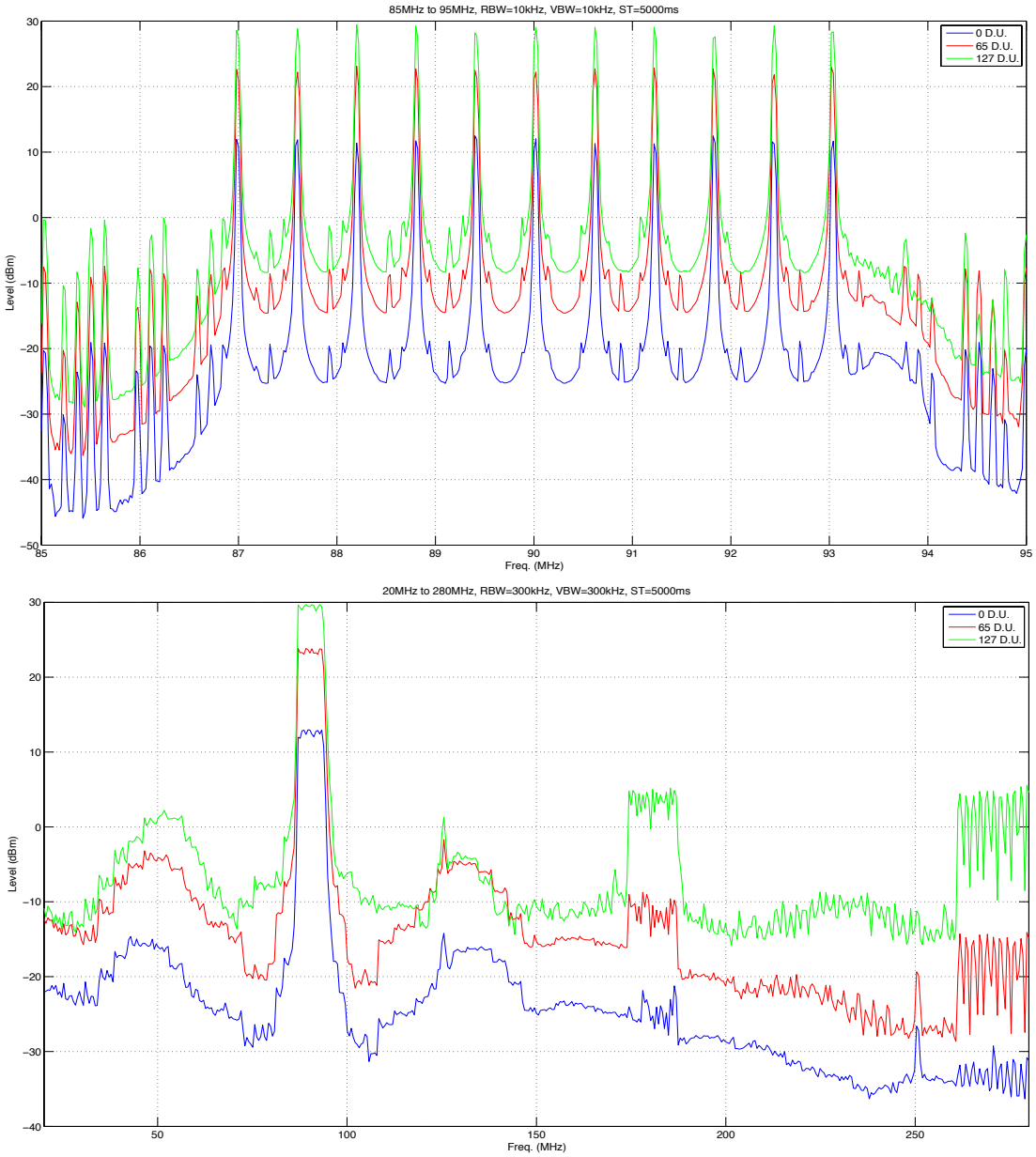

Figure 5.7. RF output spectra of the DDS driver when generating a multitone of 11 components (87MHz to 93MHz in 0.6MHz steps), at three different power settings (minimum, middle and maximum), shown in the range 85–95 MHz (*top*) and 20 – 280 MHz (*bottom*).

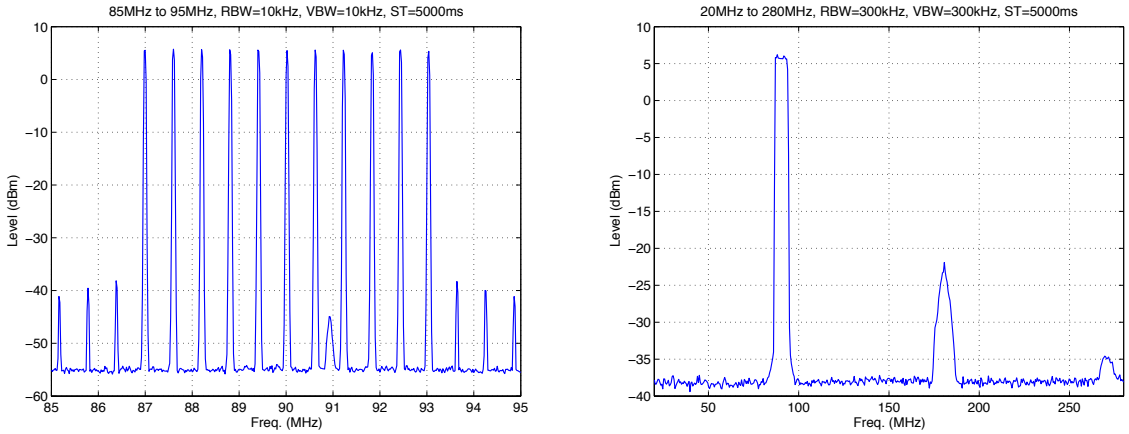

Figure 5.8. RF output spectrum of the DAC driver when generating a multitone of 11 components (from 87MHz to 93MHz in 0.6MHz steps), shown in the range from 85MHz to 95MHz (*left*), and 20MHz to 280MHz (*right*).

These figures show that the DAC driver provides a better signal to noise ratio and less harmonic distortion, specially in the case of the broadband signal generation. The main reason are the differences on the amplification stage of both drivers. While the DDS driver uses a discrete RF amplification circuit formed by two cascaded power ICs traced over a standard PCB, the DAC driver uses a commercial stand-alone RF power amplifier. The VGA chip on the DDS driver introduces an additional noise source on the signal chain which also degrades the output of this circuit.

VI

AOTF characterisation

AOTF's present a great variability in their specifications due to the manufacturing process. Moreover, the construction of the ATFS instrument involves the manual adjustment of the crystal on the optical path. Diffraction efficiency and output bandwidth depend on the transducer matching on the crystal, and the chromatic aberration depends on the angle between incident light and the crystal front plane. Even the relationship between the RF driving frequency and the central wavelength of the diffracted light depends on the angle between the output light direction and the sensor array plane. Therefore, the exact behavior of each instrument is not known until it is measured in its final setup.

In the context of the SmartSpectra project, several AOTF's were bought from different manufacturers. Their characteristics are described on Chapter 2, and Table 6.1 shows a brief summary. Some of them are custom made models, and others are off-the-shelf crystals. However, no one presents a reliable specifications sheet. Therefore, it is necessary to fully characterise each one of them. In order to evaluate the performance of the crystals in a comparable way, we have developed a characterisation measurement protocol.

Table 6.1. Main characteristics of the purchased AOTF's.

Model	Manufacturer	Spectral range	Driving frequency	Maximum power
AA.AOTF-3/LR	AA Opto-electronic	400-700 nm	60-135 MHz	1 W
TF515-230-4-5-VU1	Gooch & Housego	400-630 nm	70-140 MHz	0.5W
AOTF-MT VIS	Moltech	440-820 nm	60-135 MHz	1W

***Note**: the listed characteristics are the ones given by the respective manufacturers, and were slightly different from the measured values, as it will be shown later in this chapter*

For each AOTF model, we performed a complete characterisation procedure in order to obtain the real performance of the crystal for all the required working conditions. The characterisation procedure consisted on determining the optimal incident angle for each AOTF, and then evaluating the diffracted output performance of the crystal (diffraction efficiency and bandwidth) for a combination of RF frequencies and powers at the optimal incident angle. For the analysis we have used the DAC-based RF driver, which gives a better RF performance.

6.1. Description of the characterisation methodology

The characterisation methodology for the AOTF crystal consisted on mounting an experimental set-up on an optical workbench and developing a repetitive and reliable measuring procedure that was applied to all the crystals.

6.1.1. Experimental set-up

All the studied crystals work approximately on the same spectral range, requiring similar RF frequencies. However, the optimal incident angle of the incoming light depends on the model or even on the specific crystal. Therefore, the measurement set-up was fixed for all the elements except for the crystal support, which was held on a rotary optical stage. The light source was a collimated KI-120 Koehler Illuminator from LabSphere (www.labsphere.com), which provided a well-known and stable light spectrum (Figure 6.2). The diffracted light was acquired with a FieldSpec FR spectroradiometer from ASD Inc. The FieldSpec spectroradiometer includes a sensor in the 350nm to 1000nm band (using the VNIR sensor[1]) with a spectral resolution of 1nm and a nominal bandwidth of 3nm. For blocking the zero order diffraction we used an optical diaphragm acting as a beam-stopper between the crystal and the sensor of the spectroradiometer.

The complete diagram of the measurement set-up is shown on Figure 6.1.

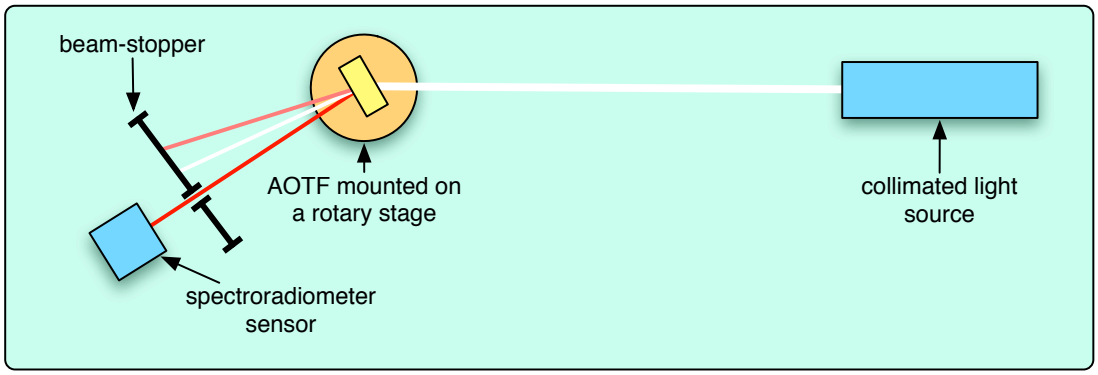

Figure 6.1. Experimental set-up for the AOTF characterisation.

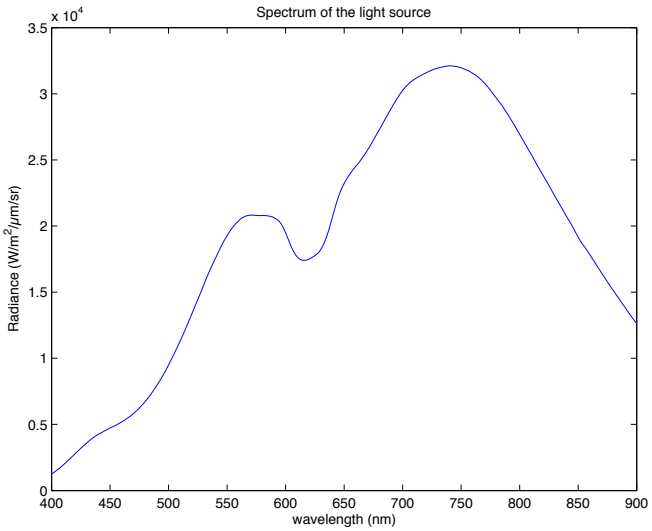

Figure 6.2. Spectrum of the light source used on the experimental set-up.

6.1.2. Measuring procedure

We have repeated the same measuring procedure for all the crystals. First, we adjusted the position of all the elements of the set-up, and then we took three series of measurements. The first one measured the variation

[1] The complete measurement range of the FieldSpec FR spectroradiometer goes from 350nm to 2500nm, acquired with three different sensors: one Si-based sensor on the VNIR spectrum, and two Thermo-electrically cooled InGaAs detectors for the ranges 1000 to 1800nm and 1800 to 2500nm. However, we configured the instrument to measure only the VIS-NIR spectrum using the VNIR sensor. This working configuration allows us to widely control the integration time for each acquisition.

of the diffracted output spectra when changing the incident angle of the light to the crystal. Then, we performed the remaining experiments adjusting the crystal to the optimal angle determined by the first experiment. Second and third experiments measured the variation of the diffracted spectra respect to the RF frequency and power, respectively.

6.1.2.1. Adjusting the experimental set-up

The above-mentioned experimental set-up needed to be adjusted for each AOTF, due to the particularities on the physical characteristics of each crystal and the differences on the incident angle. The adjusting procedure was the same for all the crystals. The first step consists on fixing the AOTF to the rotary optical stage and connecting the RF input to the power amplifier of the DAC-based driver. Then, we adjust the height of the crystal to be in the same plane as the rest of the optical elements (light, beam-stopper and sensor), which are fixed. Next, we turn on the RF generator at an intermediate frequency on the RF range of all the crystals (90MHz) and adjust manually the optimal incident angle of the crystal respect to the light, looking at the projected output light on a white piece of paper (this is just a rough approximation that will be fine-tuned in the next procedure step).

The angle of the diffracted light at the crystal output respect to the incident light is fixed for each crystal, and it does not depend on the angle between the crystal and the incident light. Therefore, next step is to adjust the position of the beam-stopper and spectroradiometer sensor in order to receive the diffracted light. We manually vary the angle between the crystal and the sensor until we find the one that gives the maximum diffracted light while removing all the zero-order diffraction. The final step consists on fine-tuning the optimal angle of the crystal respect to the light by looking at the diffracted spectra with the ASD instrument. The optimal angle is the one that gives the apparently 'best diffracted' spectrum (narrower band). This angle will be considered the 0º angle for each crystal. We will analyse the variation of the diffracted light when changing this angle in a range of -10º to +10º from its optimal position (positive values positions the crystal surface closer to the perpendicular to incident light, negative values moves it closer to the direction the incident light) in order to evaluate the sensitivity with respect to this parameter.

6.1.3. Characterisation measurements

Once the experimental set-up was completely adjusted following the exposed procedure, we performed three consecutive series of characterisation analysis.

For the first analysis, we chose an intermediate RF power (0.5W for the G&H AOTF and 2/3W for the remaining AOTF's) and we analysed the performance for the different incident angles from -10º to +10º respect to the optimum angle, in 2º steps. For each angle, we acquired the diffracted spectrum for all the working RF range of the crystal in 5MHz steps (55 to 130MHz for the AA and MolTech crystals and 60 to 140MHz for the G&H one). Table 6.2 summarises the performed acquisitions for all the crystals.

Table 6.2. Summary of the first set of measurements for each crystal, characterising the incident angle.

AOTF model	Incident angle	RF frequency
AA	-10º to +10º (2º steps)	55MHz to 140MHz (5MHz steps)
MolTech	-10º to +10º (2º steps)	55MHz to 140MHz (5MHz steps)
Gooch & Housego	-10º to +10º (2º steps)	60MHz to 135MHz (5MHz steps)

The measurements were semi-automated with a MATLAB script. The MATLAB script adjusted the RF frequency and power of the DAC-driver through the developed USB driver, and triggered the spectroradiometer acquisition on the FieldSpec control PC through a serial port command. However, the angle of the crystal needed to be adjusted manually. Therefore, the MATLAB script automated the RF adjustment and spec-

troradiometer acquisition for all the frequencies corresponding to each angle, and asked the user to change the angle in one step. The complete listing of the MATLAB script can be found in the attached CD.

From this set of measurements and considering a combination of three different factors the optimal incident angle was determined. This optimal angle was used as the incident angle of the crystal for the following experiments.

Once determined the optimal angle for each crystal, that value was used on the following analysis. For the second analysis, we used ten different powers (from maximum allowed power to 30dB below the maximum) and, for each power, we generated all the possible RF frequencies on the crystal range (in 1MHz steps). This analysis was used to characterise the RF performance of the crystals. Table 3 summarises the performed analysis.

Table 6.3. Summary of the second set of measurements for each crystal, characterising the RF performance.

AOTF model	RF power (*)	RF frequency
AA Opto Electronics AA.AOTF-3/LR	33dBm to 3dBm (3 dB steps)	55MHz to 140MHz (1MHz steps)
MolTech AOTF-MT-VIS	33dBm to 3dBm (3 dB steps)	55MHz to 140MHz (1MHz steps)
Gooch & Housego TF515-230-4-5-VU1	21dBm to -9dBm (3 dB steps)	60MHz to 135MHz (1MHz steps)

**Note: the maximum power (33dBm) corresponds to the maximum output signal amplitude of the DAC, which was adjusted to deliver a 2W signal on a 50Ω load for a frequency of 90MHz.*

Finally, for the third analysis we used several RF frequencies (all the useful range of each crystal taken in 10MHz steps) and a wide range of different powers (41 values, starting from maximum power in 0.6dB steps). With this analysis we characterised the response of the crystal respect to power variations. Table 6.4 summarises the performed analysis.

Table 6.4. Summary of the third set of measurements for each crystal, characterising the power performance.

AOTF model	RF power (*)	RF frequency
AA Opto Electronics AA.AOTF-3/LR	33dBm to 9dBm (0.6 dB steps)	50MHz to 130MHz (10MHz steps)
MolTech AOTF-MT-VIS	33dBm to 9dBm (0.6 dB steps)	50MHz to 130MHz (10MHz steps)
Gooch & Housego TF515-230-4-5-VU1	21dBm to -3dBm (0.6 dB steps)	60MHz to 130MHz (10MHz steps)

**Note: the maximum power (33dBm) corresponds to the maximum output signal amplitude of the DAC, which was adjusted to deliver a 2W signal on a 50Ω load for a frequency of 90MHz.*

The measurements were semi-automated with two MATLAB scripts. The MATLAB scripts adjusted the RF frequency and power of the DAC-driver through the developed USB driver, and triggered the spectroradiometer acquisition on the FieldSpec control PC through a serial port command[2]. However, the integration time of the spectroradiometer must be adjusted manually for each set of frequency or power values, in order to maximise the signal to noise ratio of the sensor (the integration time of the spectrometer cannot be set through a serial command). Therefore, for the second analysis, the MATLAB script configures the DAC driver for a given power, waits for the user to adjust the integration time on the laptop controlling the spec-

[2] The spectroradiometer is connected to a dedicated laptop PC running the control software. The MATLAB automated script is running on another computer connected to the DAC driver through the USB port and to the spectroradiometer laptop through the serial port.

troradiometer, and then automates the spectroradiometer acquisitions for all the selected frequencies at that power. On the other hand, for the third analysis the script configures the DAC driver for a given frequency and prompts the user to adjust the integration time. Then it triggers the acquisitions for all the power values at that frequency. The complete listing of both MATLAB scripts can be found on the attached CD.

6.2. Results

As mentioned before, three series of characterisation analysis for each AOTF were performed. On the first series, we evaluated the influence of the incident angle, while the second series studied the effect of the RF frequency, and finally the third one analysed the effect of the RF power on the diffraction efficiency.

6.2.1. Generic considerations

6.2.1.1. Incident angle

All the studied AOTF's present a similar behaviour with respect to the incident angle. As we vary the incident angle of the crystal, we observe a variation on the wavelength and shape of the spectrum of the diffracted light. The central wavelength shifts to higher values as we move the angle from the optimal position (towards higher and lower values), and the bandwidth of the diffracted band increases also as we move from the optimal position to both extremes, while the diffraction efficiency decreases, showing a strong degradation on the shape of the diffracted light. However, some AOTF models presented a higher degradation than others.

6.2.1.2. Generation of the results

We have analysed the acquired spectra with MATLAB. By using the spectrum of the collimated light source, acquired before this experiment with the same spectroradiometer, we convert the radiance corresponding to the diffracted spectrum to relative transmittance of the crystal with a simple division:

$$T(\lambda)=O(\lambda) / WR(\lambda) \qquad \textbf{(Eq. 5.1)}$$

Where $O(\lambda)$ is the measured diffracted spectrum for the wavelength λ and $WR(\lambda)$ is the radiance of the light source on a white reference panel for the same wavelength. Note that $T(\lambda)$ does not correspond to absolute units because $WR(\lambda)$ does not correspond to the radiance of the incoming light entering the crystal, but to a proportional value. Therefore, the expressed transmittance is normalised to a different scale for each crystal because the incident radiation to the ASD sensor was optimised individually for each crystal by changing the integration time and the diameter of the diaphragm acting as a beam-stopper.

For each acquired spectrum, which corresponds to the diffracted output for a certain combination of RF frequency and incident angle, we evaluate the central wavelength and bandwidth characteristics of the diffracted light. Those values have been obtained by adjusting a Gaussian curve to the output spectra using the MATLAB "fit" function. This function approximates the diffracted spectra to this Gaussian expression:

$$Y = a_1 \cdot e^{-\left(\frac{x-b_1}{c_1}\right)^2} \qquad \textbf{(Eq. 5.2)}$$

We take the output parameter b_1 as the central wavelength and c_1 as the bandwidth. However, for some combinations of frequency and incident angle, the diffracted output cannot be approximated to a single Gaussian because the residual zero order light is comparable in amplitude to the first order diffracted light, and therefore the "fit" function could not adjust the Gaussian curve. In those cases, we use an approximation consisting on two Gaussian curves:

$$Y = a_1 \cdot e^{-\left(\frac{x-b_1}{c_1}\right)^2} + a_2 \cdot e^{-\left(\frac{x-b_2}{c_2}\right)^2} \quad \textbf{(Eq. 5.3)}$$

Despite the fact that the residual light is not Gaussian, the first curve tries to approximate this light, while the second one fits the desired diffracted spectrum. In this case we use the b_2 and c_2 parameters as the central wavelength and bandwidth of the diffracted spectrum, respectively. The implemented MATLAB script decides automatically the number of Gaussian curves to use depending on the spectrum characteristics. The complete code of the MATLAB script that analyses all the spectra and generates the results is listed on the attached CD.

6.2.2. Determination of the optimal angle

As the following section will show, there is a huge variation in performance of the crystals when changing the incident angle. The variation of the incident angle produces a variation on the position of the central wavelength of the diffracted band, and affects the diffraction efficiency and the bandwidth of the main lobe.

We determine the optimal incident angle by looking for the angle that provides better performance respect to three different features:

- **Central wavelength**: the central wavelength of the diffracted light presents a minimum at the optimal angle. As we move away from this angle towards both directions, the wavelength shifts towards longer wavelengths.
- **Diffraction efficiency**: the efficiency of the crystal diffracting the first-order light is maximum at the optimal angle.
- **Diffracted bandwidth**: for all the analysed crystals, we observe that the bandwidth of the diffracted light is higher as the incident angle approximates the angle of the incident light (which corresponds to positive values in our reference system), and decreases as we rotate the crystal respect to the incident light. However, the diffraction efficiency also varies. Therefore, we use a normalised bandwidth respect to the peak of the diffraction efficiency. The optimal angle is the one that gives the minimum normalised bandwidth.

We analyse these three factors for each one of the studied crystals, taking the result as the incident angle value used for the remaining experiments.

6.2.2.1. AA AOTF

Next figures show the performance of the AA.AOTF-3/LR AOTF model from AA Opto Electronics (AA). Figure 6.3 to Figure 6.5 show the diffracted spectra for all the range of studied angles at 60, 90, and 120 MHz, respectively. Figure 6.6, Figure 6.7, and Figure 6.8 show the peak of the diffraction efficiency, central wavelength, and bandwidth of the diffracted spectra, respectively, for all the frequencies and incident angles.

The values of the bandwidth are not relevant on their own since the effective bandwidth also depends on the peak of the diffraction efficiency. Therefore, we have calculated also a normalised bandwidth index, by dividing each bandwidth by the peak of DE measured at that frequency and angle. The results are shown on the Figure 6.9.

This figure shows that, although the bandwidth decreases as the incident angle is also decreased, the normalised bandwidth presents a minimum for the optimal angle, but increases as the angle diverges from this value.

From the results of this analysis we determine the optimum incident angle looking at three factors: minimum of central wavelength, minimum relative bandwidth and maximum peak diffraction efficiency. We use a *spline* interpolation in order to achieve higher resolution on the angle position from the measured data. The script used for this analysis is also listed on the attached CD. Last of all, Figure 6.10 shows the optimal angle found as a function of the RF frequency for the three considered factors. According to this figures, an

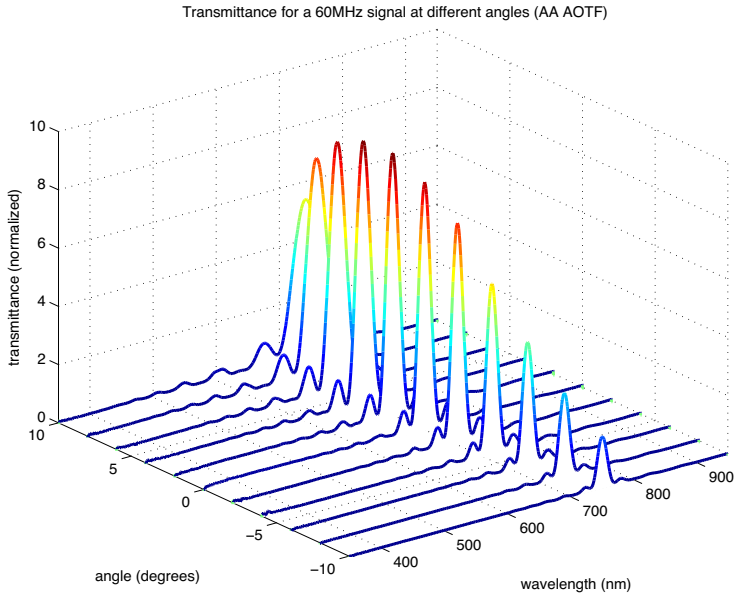

Figure 6.3. Diffraction efficiency of the AA AOTF for an RF signal of 60MHz at different incident angles.

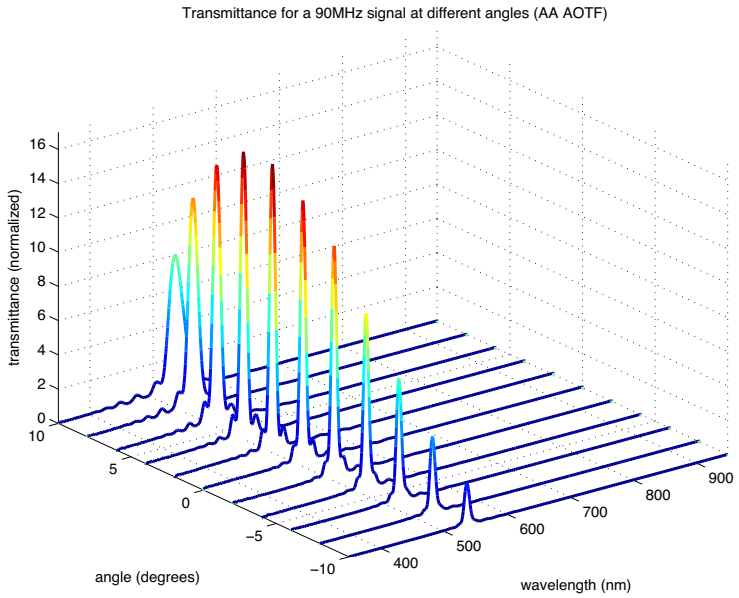

Figure 6.4. Diffraction efficiency of the AA AOTF for an RF signal of 90MHz at different incident angles.

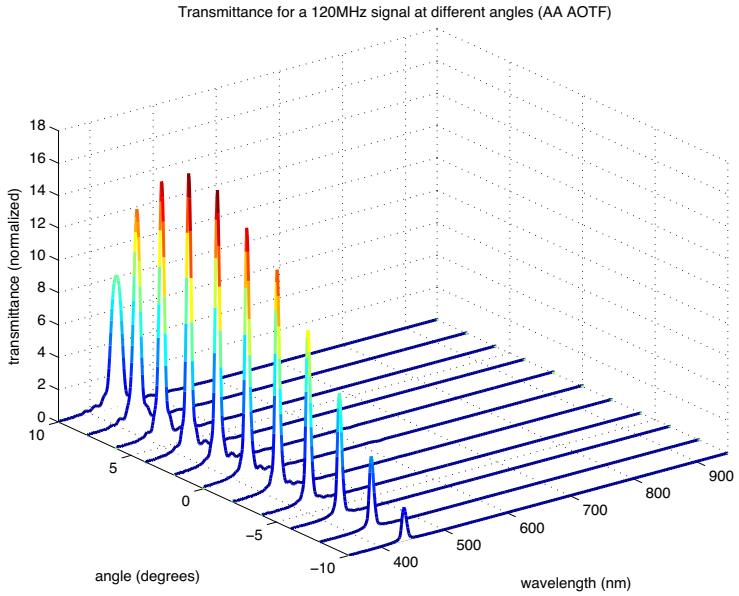

Figure 6.5. Diffraction efficiency of the AA AOTF for an RF signal of 120MHz at different incident angles.

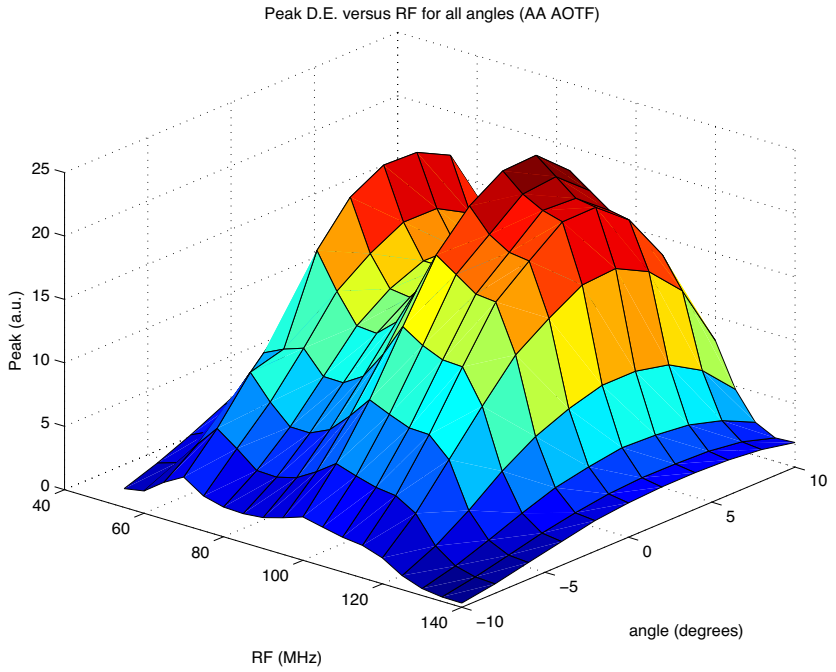

Figure 6.6. Peak of the diffraction efficiency of the AA AOTF as a function of RF frequency and incident angle.

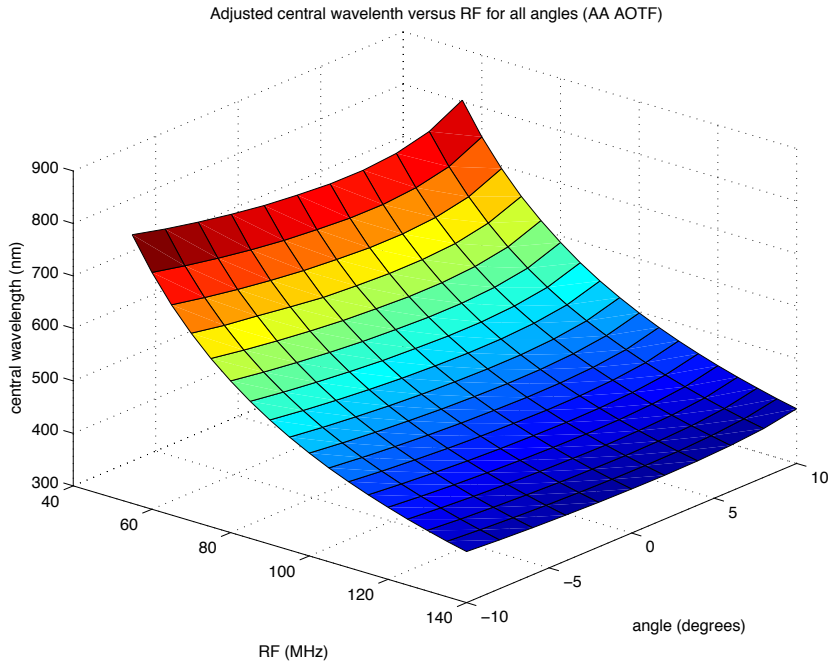

Figure 6.7. Central wavelength of the diffracted light (Gaussian adjustment) as a function of RF frequency and incident angle for the AA AOTF.

incident angle of 3º was set.

On the case of the AA AOTF, we found a good correlation between the three estimations of the optimal angle at higher frequencies, but not at lower frequencies, where the bandwidth of the output spectra is narrower for lower incident angles. Nevertheless, the optimal angle considering the normalised bandwidth is not very relevant, because it can lead to the use of the crystal on very low efficiency positions.

6.2.2.2. MolTech AOTF

Next figures show the performance of the MolTech AOTF-MT-VIS model (MT). Figure 6.11, Figure 6.12, and Figure 6.13 show the diffracted spectra for all the studied angles at 60, 90 and 120 MHz, respectively. Figure 6.14, Figure 6.15, and Figure 6.16 show the central wavelength, peak DE and bandwidth of the dif-

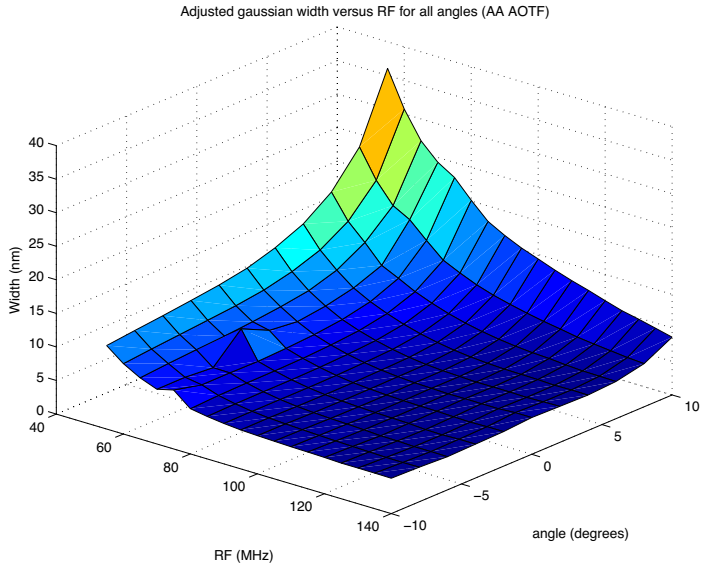

Figure 6.8. Bandwidth of the diffracted light (Gaussian adjustment) as a function of RF frequency and incident angle for the AA AOTF.

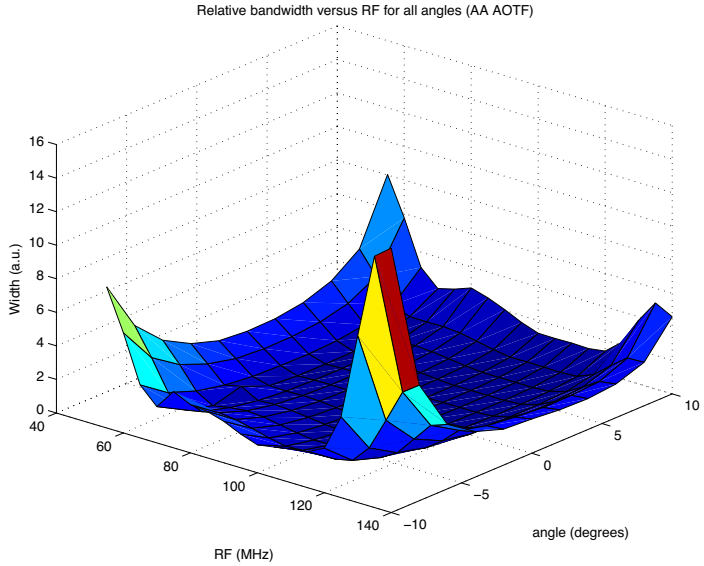

Figure 6.9. BW/DE index of the diffracted light for all the analysed combinations of frequency and incident angle for the AA AOTF.

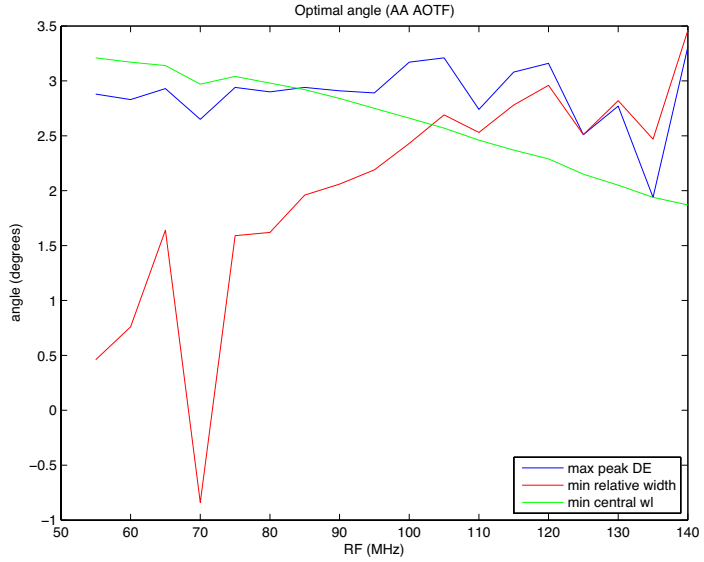

Figure 6.10. Optimal incident angle of the AA AOTF as a function of the RF frequency, according to three different criteria.

fracted spectra, respectively, for all the frequencies and incident angles.

As done for the AA AOTF, we have also evaluated the relative bandwidth considering the peak efficiency of the crystal. The results are shown in Figure 6.17.

The analysis of the data gave the values of the optimal incident angle of this crystal according to the three considered factors. Those values are represented on Figure 6.18 as a function of the RF frequency. The incident angle was set to -0.5º for this crystal.

On the MolTech AOTF we observe a narrower passband in all cases when compared to the AA crystal. However, it also shows a higher shift of the central wavelength and higher degradation of the bandwidth as we move the incident angle to the extreme of the positive values.

The optimal angle considering the central wavelength is constant for the whole working RF range, while this angle increases slightly with frequency when considering the other two factors.

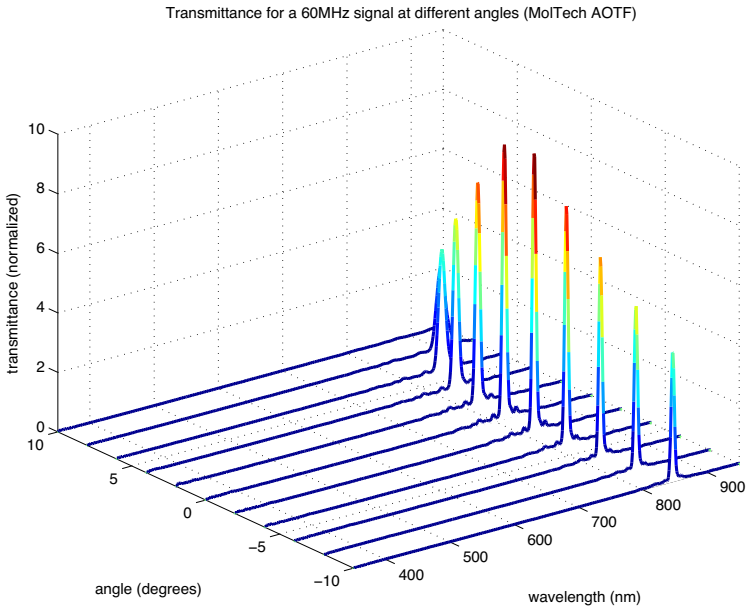

Figure 6.11. Diffraction efficiency of the MolTech AOTF for an RF signal of 60MHz at different incident angles.

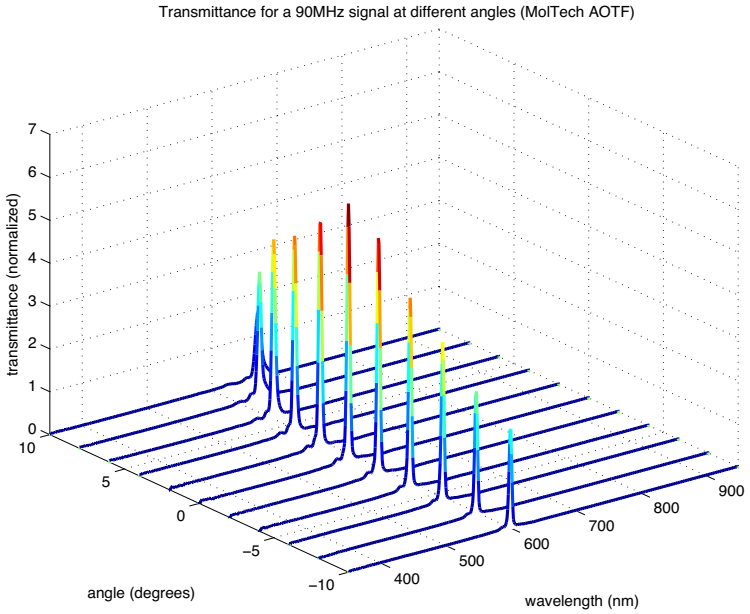

Figure 6.12. Diffraction efficiency of the MolTech AOTF for an RF signal of 90MHz at different incident angles.

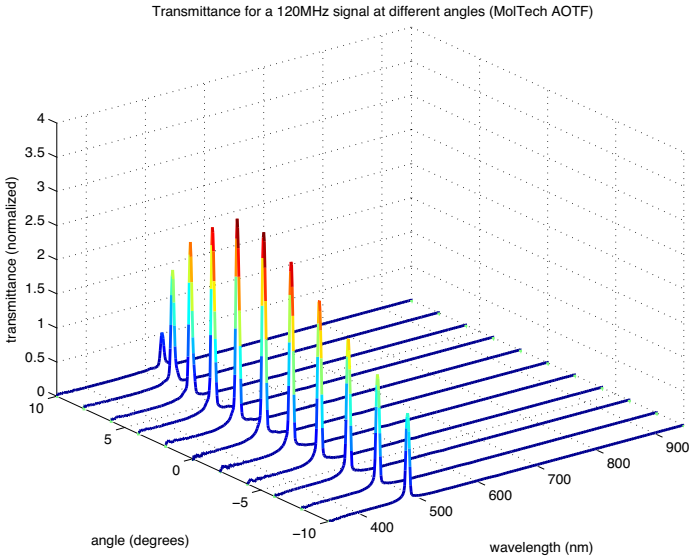

Figure 6.13. Diffraction efficiency of the MolTech AOTF for an RF signal of 120MHz at different incident angles.

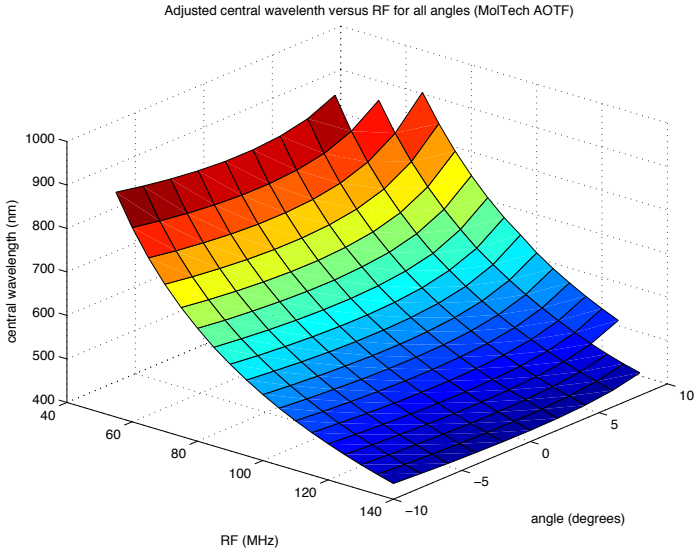

Figure 6.14. Central wavelength of the diffracted light (Gaussian adjustment) as a function of RF frequency and incident angle for the MolTech AOTF.

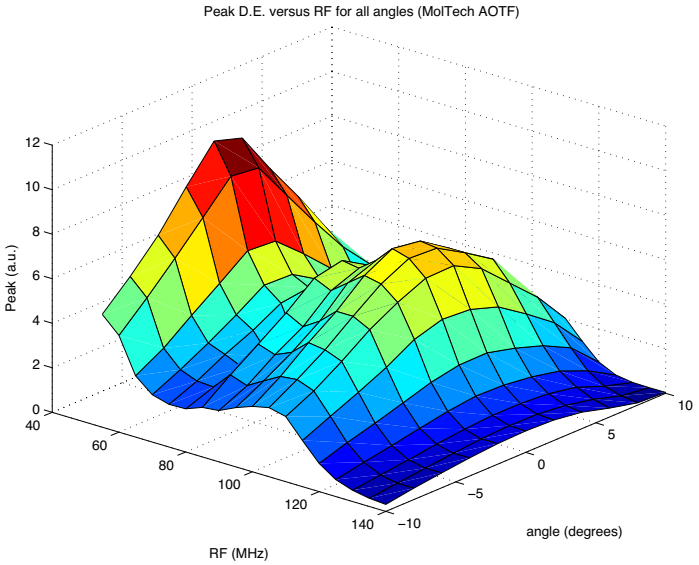

Figure 6.15. Peak of the diffraction efficiency of the MolTech AOTF as a function of RF frequency and incident angle.

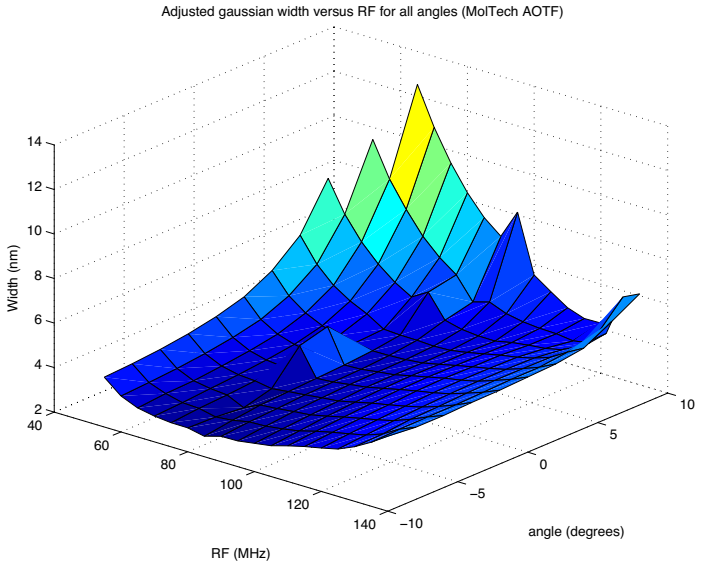

Figure 6.16. Bandwidth of the diffracted light (Gaussian adjustment) as a function of RF frequency and incident angle for the MolTech AOTF.

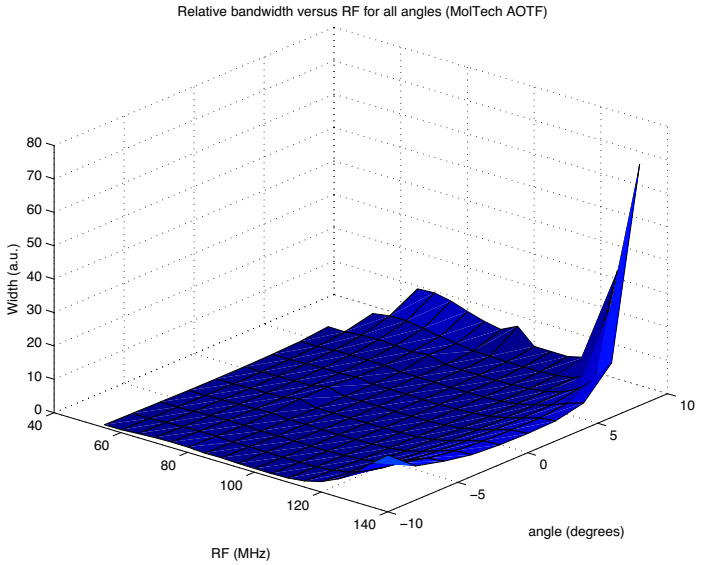

Figure 6.17. BW/DE index of the diffracted light as a function of RF frequency and incident angle for the MolTech AOTF.

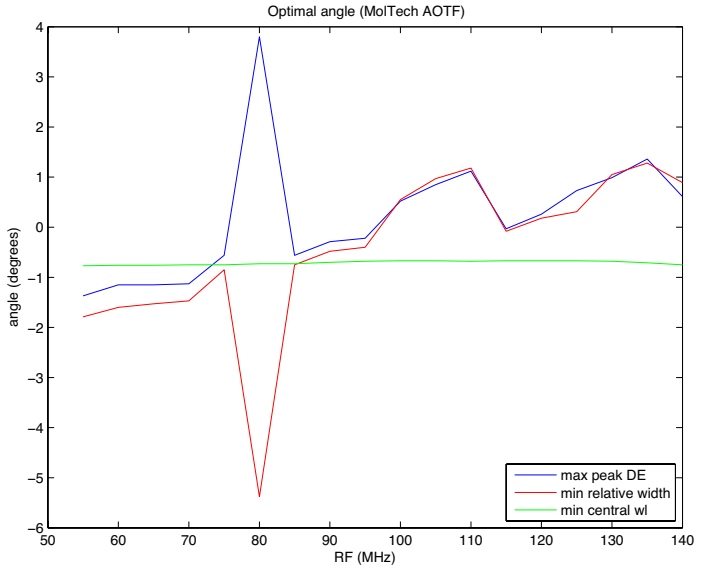

Figure 6.18. Optimal incident angle of the MolTech AOTF as a function of the RF frequency, according to three different criteria.

The optimal angle of incident of the crystal has been shown to be very close to the preliminary chosen angle (corresponding to 0º on the dataset).

6.2.2.3. Gooch & Housego AOTF

Next figures show the performance of the TF515-230-4-5-VU1 model from Gooch & Housego (GH). Figure 6.19, Figure 6.20, and Figure 6.21 show the diffracted spectra for all the studied angles at 60, 90 and 120 MHz, respectively. Figure 6.22, Figure 6.23, and Figure 6.24 show the central wavelength and bandwidth of the diffracted spectra for all the frequencies and incident angles. Note that for the lowest frequency (60MHz), the diffracted spectra do not form the typical Gaussian bandpass shape of the AOTF diffraction, but they feature a two-peak shape, which are especially noticeable at the highest incident angles.

Again, we have also estimated the relative bandwidth by considering the peak DE for each combination of angle and RF frequency (Figure 6.25). Finally, the optimal angles considering the three used factors are shown in Figure 6.26. The angle was set to 3.7º.

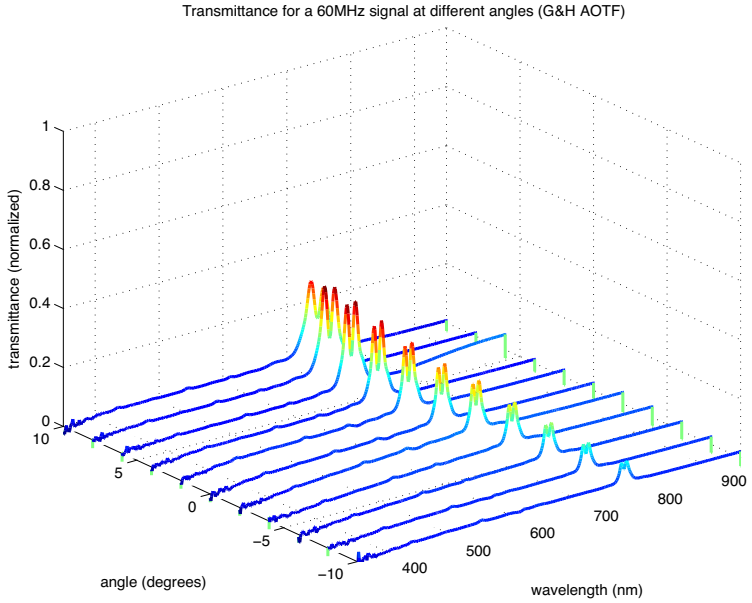

Figure 6.19. Diffraction efficiency of the Gooch & Housego AOTF for an RF signal of 60MHz at different incident angles.

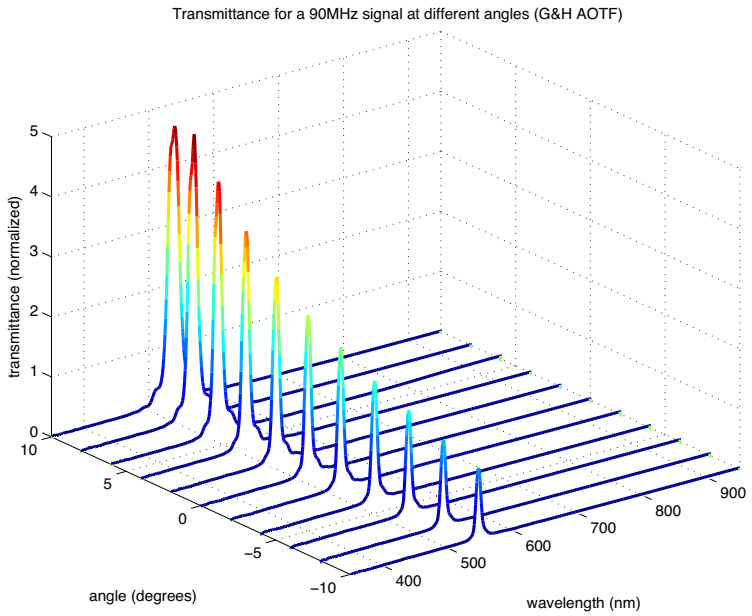

Figure 6.20. Diffraction efficiency of the Gooch & Housego AOTF for an RF signal of 90MHz at different incident angles.

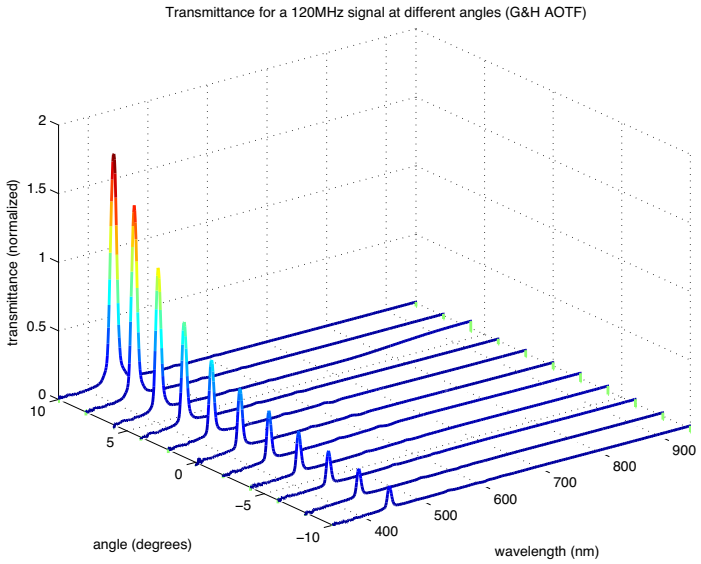

Figure 6.21. Diffraction efficiency of the Gooch & Housego AOTF for an RF signal of 120MHz at different incident angles.

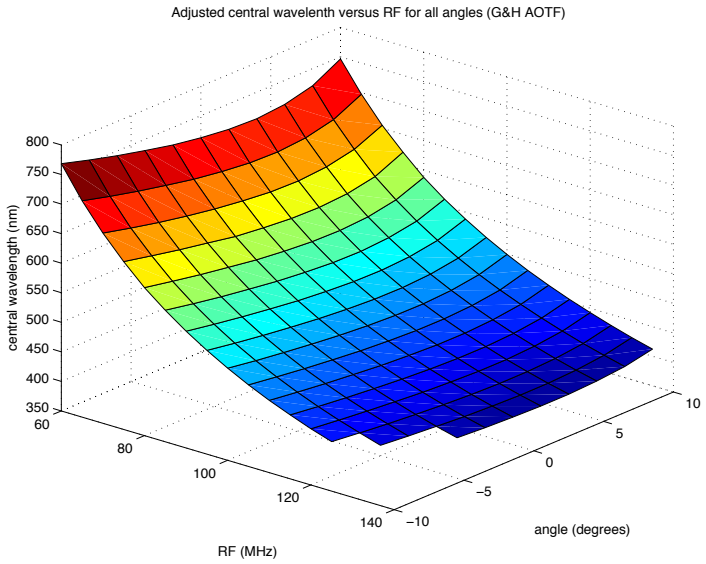

Figure 6.22. Central wavelength of the diffracted light (Gaussian adjustment) as a function of RF frequency and incident angle for the Gooch & Housego AOTF.

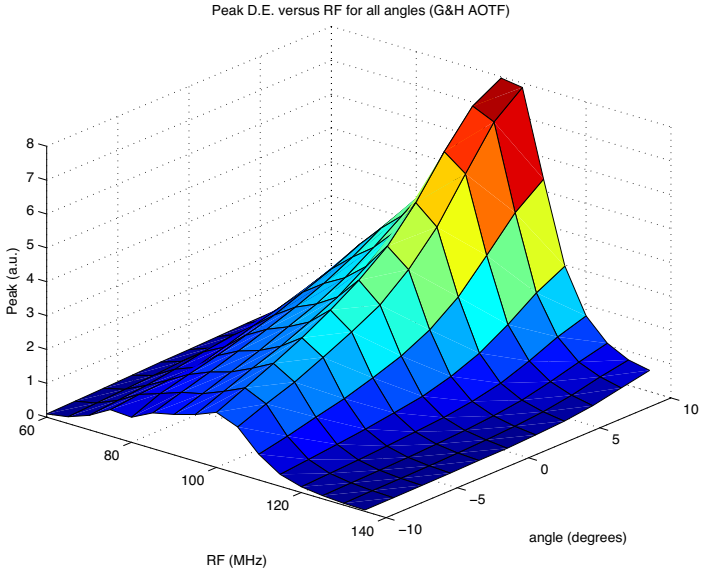

Figure 6.23. Peak of the diffraction efficiency of the Gooch & Housego AOTF as a function of RF frequency and incident angle.

The Gooch & Housego AOTF shows the worst performance of the three models. At low frequencies, the efficiency of the crystal is very low while the bandwidth is large due to the "two peak" shape of the bandpass. The peak DE and the bandwidth suggest a great deviation of the optimal angle of incidence from the preliminary one towards higher values, especially at high frequencies. However, the greater incident angles cause the double peak effect at low frequencies, making them useless. However, the position of the wavelength minimum suggests an optimal angle close to 4º from the preliminary position, and almost constant with frequency.

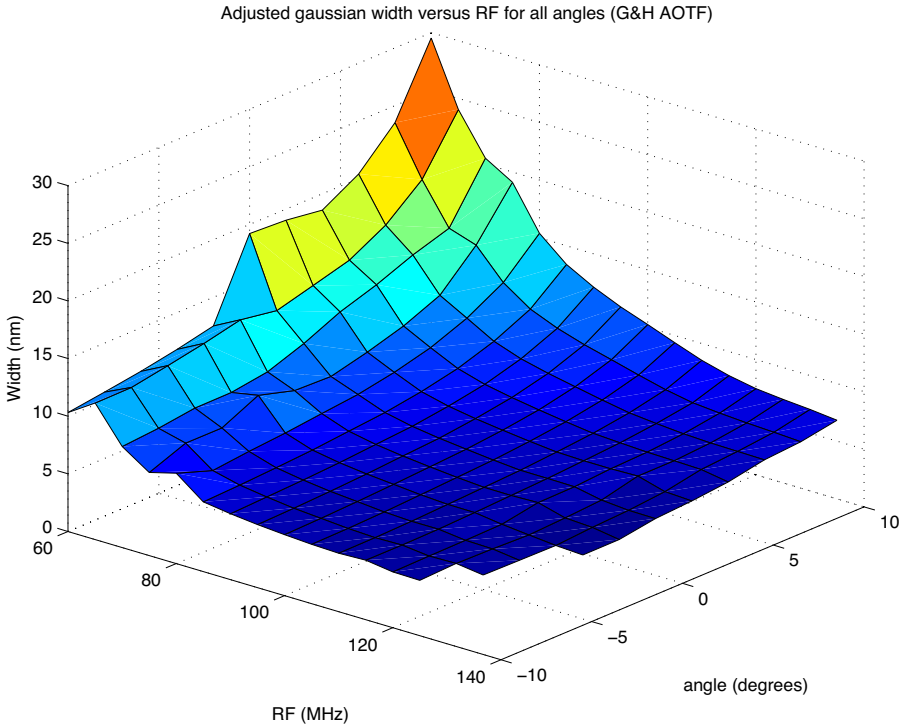

Figure 6.24. Bandwidth of the diffracted light (Gaussian adjustment) as a function of RF frequency and incident angle for the Gooch & Housego AOTF.

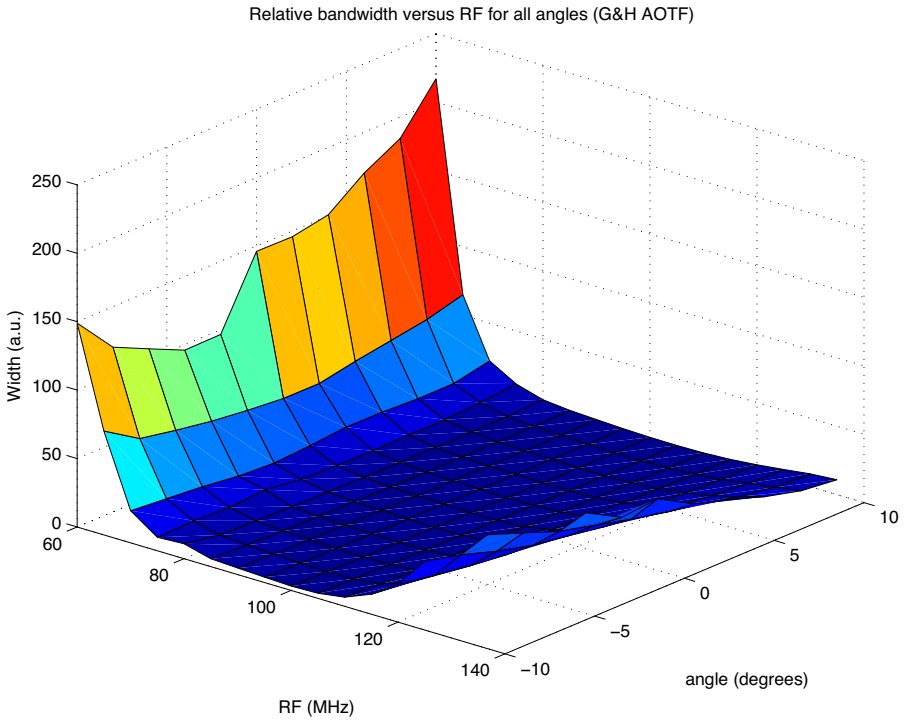

Figure 6.25. BW/DE index of the diffracted light as a function of RF frequency and incident angle for the Gooch & Housego AOTF.

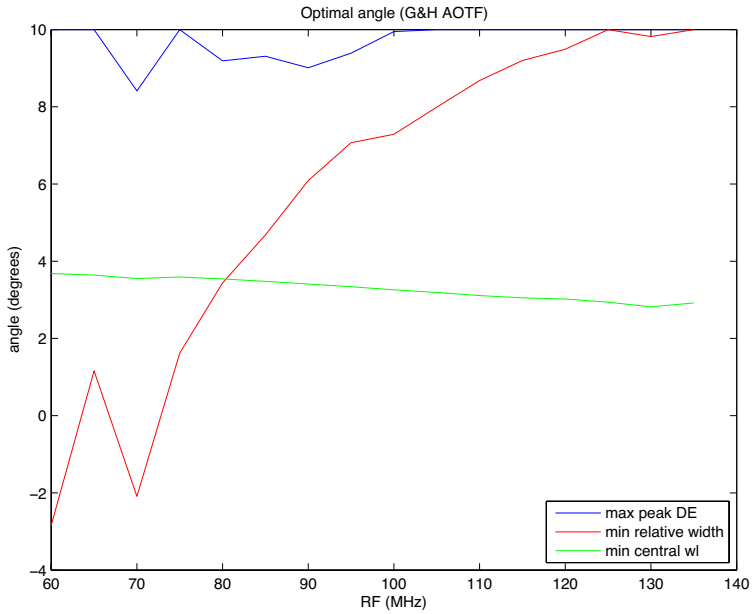

Figure 6.26. Optimal incident angle of the Gooch & Housego AOTF as a function of the RF frequency, according to the three different criteria.

6.2.2.4. Analysis of the results

All the crystals present a similar behaviour. As we move the incident angle from the optimum, we observe a shift on the central wavelength position of the passband, always towards longer wavelengths, for both directions of angular variation. However, the most evident effects of the incident angle variation are the increment of the bandwidth and decrement of the DE of the passband spectrum as the crystal is farther away from the optimal angle. The bandwidth increment is more noticeable with positive increments of the incident angle. This effect can be explained by the fact that the more positive the incident angle the more perpendicular is the crystal respect to the incident light, and therefore the matching condition for the first-order diffraction is fulfilled for a broader range of wavelengths.

6.2.3. Characterisation of diffraction behaviour

In the following experiments we try to find a relationship between the diffraction behaviour and the RF frequency and power. The diffraction behaviour is analysed in terms of central wavelength of the passband, bandwidth of the passband, and peak diffraction efficiency (DE). These features were analysed for all the crystals respect to RF frequency (for three different power values), and respect to RF power (for eight different RF frequencies).

6.2.3.1. Generation of results

We have analysed the acquired spectra with MATLAB. By taking into account the spectrum of the collimated light source, acquired before this experiment with the same spectroradiometer, we convert the diffracted output light radiance to relative transmittance with the Eq. 5.1.

On this equation, the diffracted spectrum $O(\lambda)$ has been calculated removing the residual order-zero light from the acquired spectrum. This residual light, $DC(\lambda)$, was measured before each set of measurements. Taking into account the differences on the integration time for each acquisition, and knowing that the spectroradiometer is linear respect to the integration time, the expression we used to calculate $O(\lambda)$ was:

$$O(\lambda) = (S(\lambda) / T_{int}) - (DC(\lambda) / 272ms) \qquad \textbf{(Eq. 5.5)}$$

where $S(\lambda)$ is the acquired diffracted spectrum, T_{int} the integration time for this particular acquisition, and $DC(\lambda)$ the residual order-zero spectrum, measured for a integration time of 272ms.

For each acquired spectrum, which corresponds to the diffracted output for a certain combination of RF frequency and applied power, we evaluate the central wavelength, bandwidth characteristics and maximum efficiency of the diffracted passband light. The central wavelength has been obtained from an adjusted Gaussian curve of the output spectra, calculated with the MATLAB "fit" function. This function approximates the diffracted spectra to the Gaussian expression of Eq. 5.2. We use from this function the output parameter "b1", which denotes the centre of the Gaussian curve, as the central wavelength of the diffracted passband.

The bandwidth of the diffracted passband was measured numerically from the spectrum. The bandwidth was calculated as the full width half maximum value (FWHM). The function used to calculate the bandwidth is listed on the attached CD.

In the following section we show the most relevant results of the analysis on the response of the three AOTF crystals for different RF frequencies and powers.

6.2.3.2. AA AOTF

Next figures show the performance of the AA AOTF respect to the RF frequencies. Figure 6.27, Figure 6.28, and Figure 6.29 show the diffracted spectra for some of the applied RF frequencies at maximum, medium, and minimum applied power, respectively. Figure 6.30, Figure 6.31, and Figure 6.32 show the central wavelength, bandwidth and peak diffraction efficiency of the diffracted spectra for all the measured frequencies and powers. The central wavelength was very close for all the applied powers, so that the represented curve corresponds to averaged values.

These figures show a similar response of the AA crystal with frequency for all the range of applied powers, except for the maximum power configuration. At maximum power, the output passband is severely distorted, especially on the frequency range between 100 and 120 MHz, producing an increase of the bandwidth and a reduction of the peak efficiency. Except for the maximum power, the DE can be considered quite constant in the range from 70 to 120 MHz.

This experiment shows that if we increase too much the RF power applied to the AA crystal, we degrade the output passband (broader bandwidth and lower DE) instead of increasing efficiency. Therefore, the optimal power is lower than the maximum power recommended by the manufacturer.

At 72MHz, we observe a punctual odd reduction of the DE and an increase on the bandwidth of the diffracted spectrum. This behaviour is also observed on the other crystals but at different frequencies. So that, we cannot consider this effect a malfunction of the RF driver, but a problem of the matching of the RF signal with the acoustic transducer of the crystal.

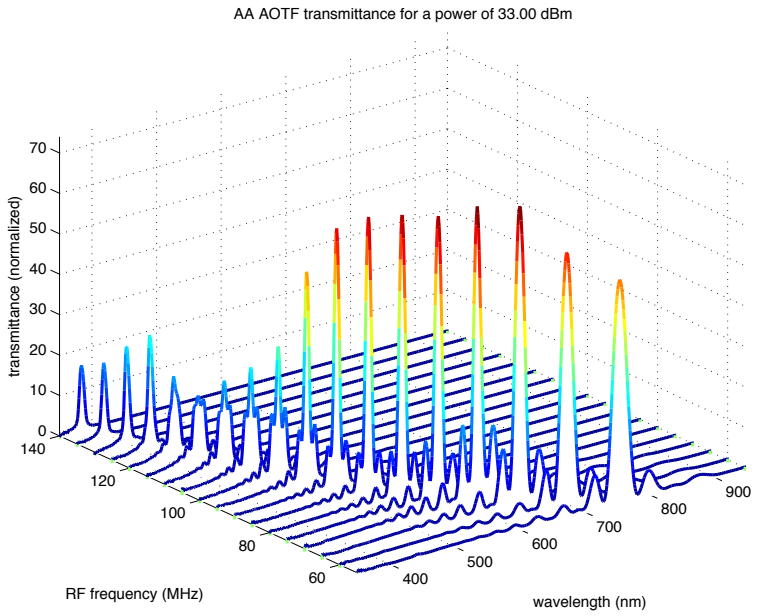

Figure 6.27. Diffraction efficiency of the AA AOTF at different RF frequencies at the maximum power (+33dBm).

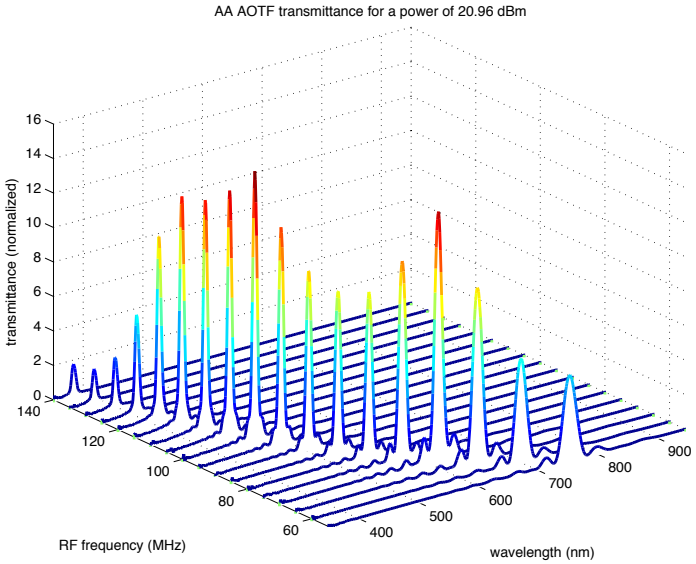

Figure 6.28. Diffraction efficiency of the AA AOTF at different RF frequencies at medium power (+21dBm).

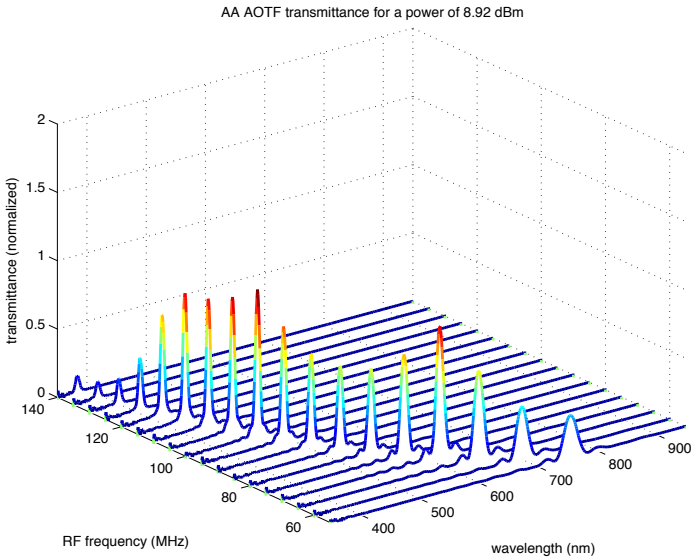

Figure 6.29. Diffraction efficiency of the AA AOTF at different RF frequencies at low power (+9dBm).

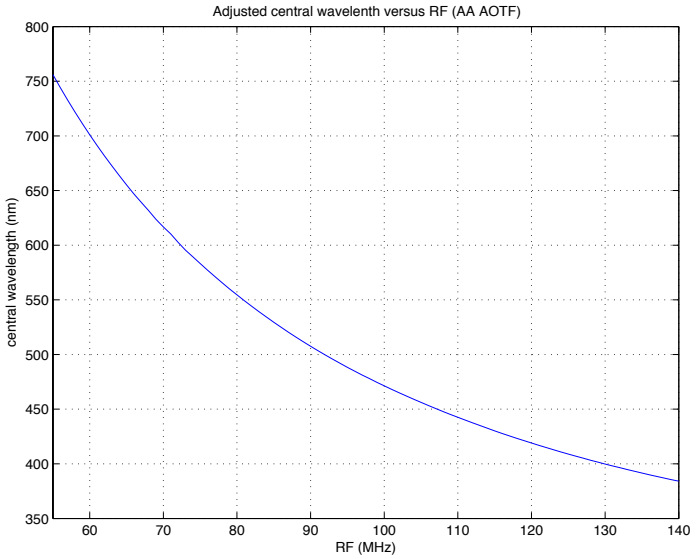

Figure 6.30. Central wavelength of the diffracted light (Gaussian adjustment) versus RF frequency for the AA AOTF (average of the values for the different powers).

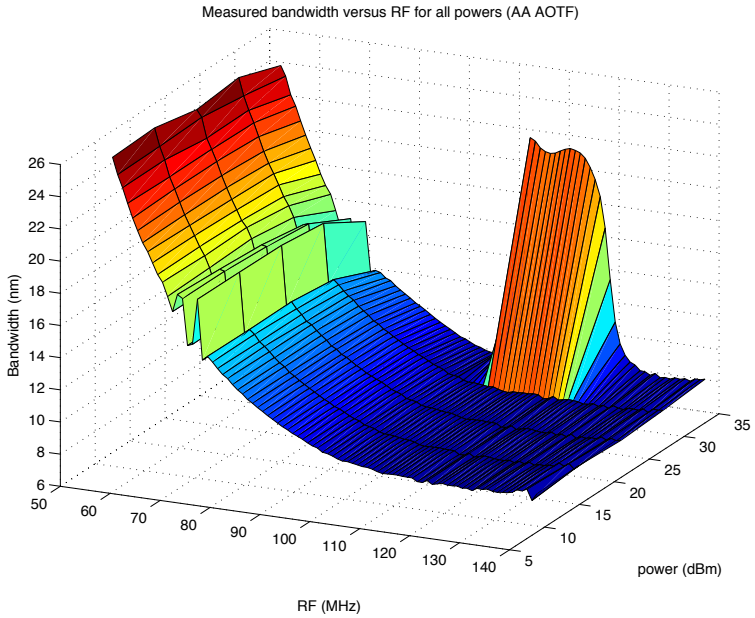

Figure 6.31. Bandwidth of the diffracted light passband in all the RF range for the different applied powers for the AA AOTF.

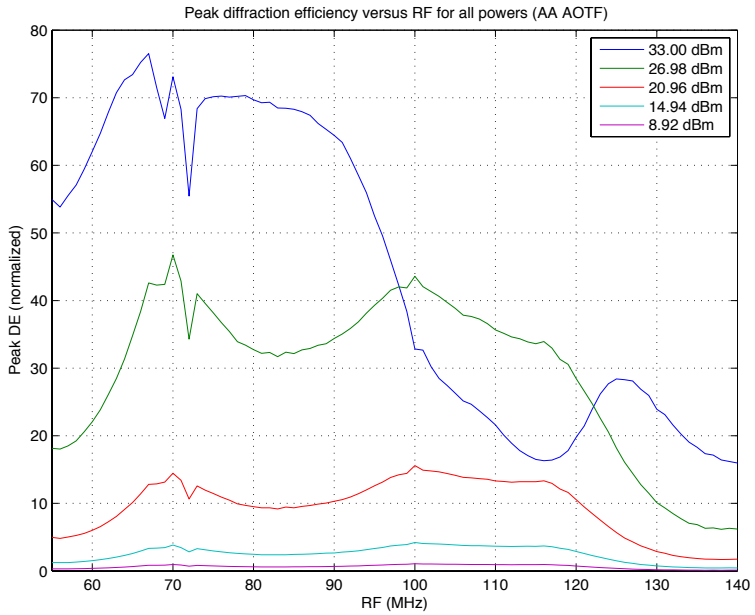

Figure 6.32. Peak diffraction efficiency of the AA AOTF in all the RF range for the analysed applied powers.

A deeper analysis of the AOTF behaviour with respect to power was performed on the third set of experiments. The results for the AA crystal are shown on the following figures.

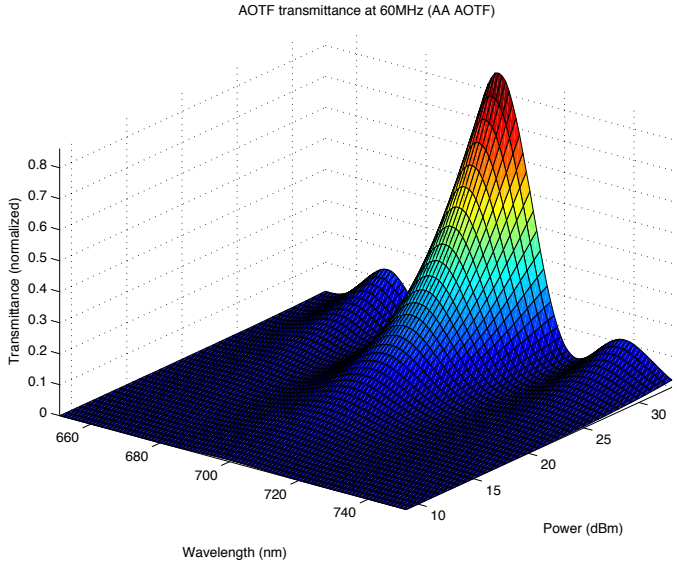

Figure 6.33. Diffraction efficiency of the AA AOTF when driven by an RF signal of 60MHz for different power values.

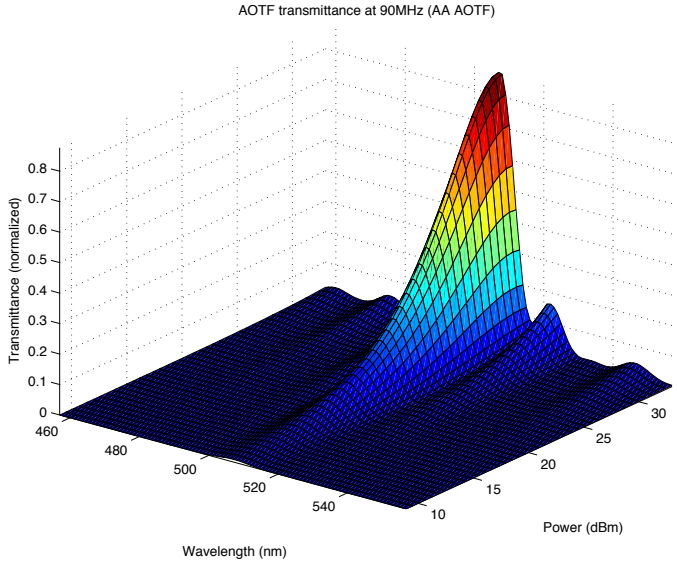

Figure 6.34. Diffraction efficiency of the AA AOTF when driven by an RF signal of 90MHz for different power values.

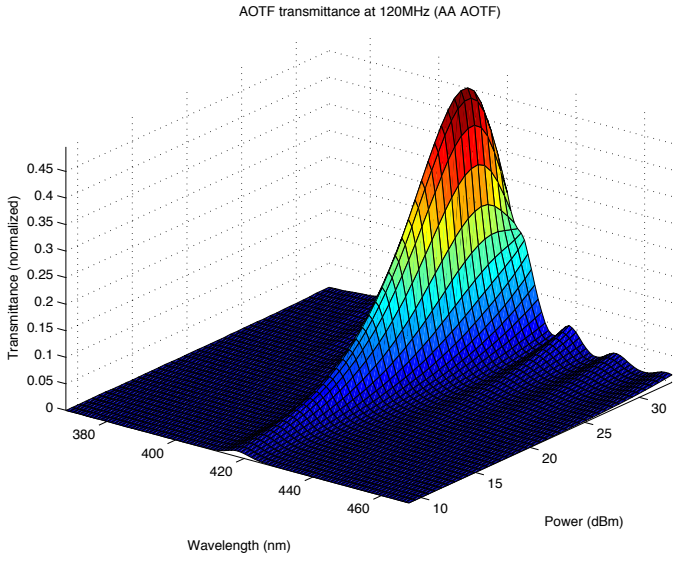

Figure 6.35. Diffraction efficiency of the AA AOTF when driven by an RF signal of 120MHz for different power values.

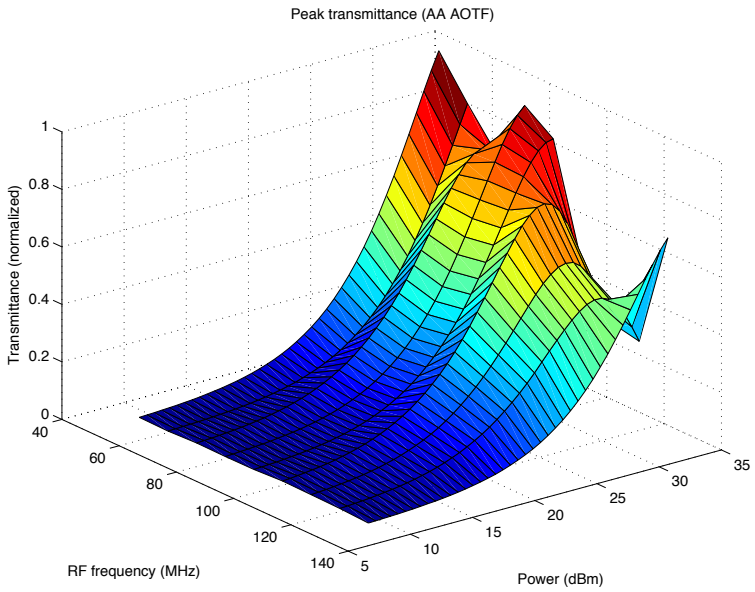

Figure 6.36. Peak transmittance of the AA AOTF as a function of applied power and RF frequency.

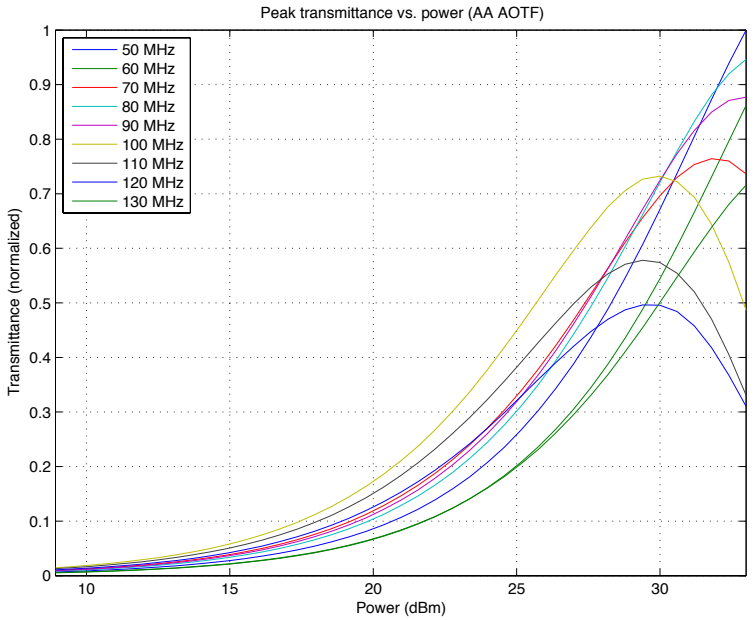

Figure 6.37. Peak transmittance of the AA AOTF versus applied power for the analysed RF frequencies.

These figures show a Gaussian behaviour of the peak DE respect to power. However, the peak DE position varies with frequency without following a deterministic behaviour. At the same time, it is noticeable that the amplitude of the Gaussian curve is modulated by the crystal response to frequency. That is, the amplitude of the Gaussian curves follows the shape of the AOTF peak DE response versus RF frequency.

6.2.3.3. MolTech AOTF

Next figures show the performance of the MolTech AOTF with respect to the RF frequencies. Figure 6.38, Figure 6.39, and Figure 6.40 show the diffracted spectra for some of the applied RF frequencies at maximum, medium, and minimum applied power, respectively. Figure 6.41, Figure 6.42, Figure 6.43 show the central wavelength, bandwidth and peak diffraction efficiency of the diffracted spectra for all the measured frequencies and powers.

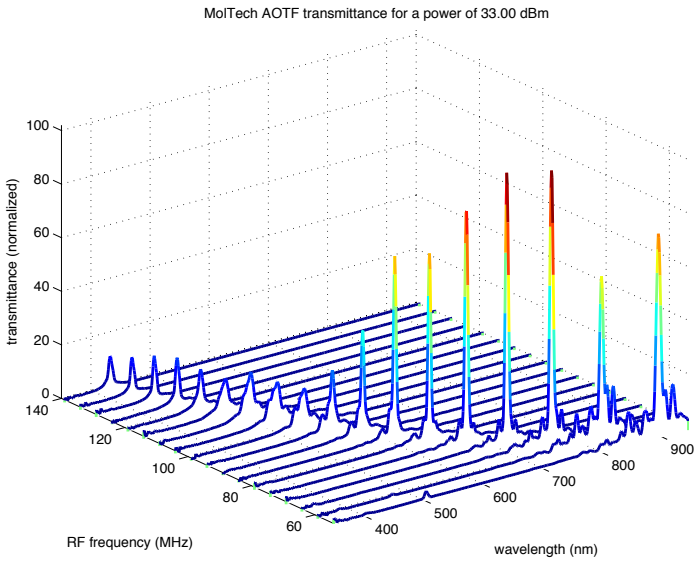

Figure 6.38. Diffraction efficiency of the MolTech AOTF at different RF frequencies at the maximum power (+33dBm).

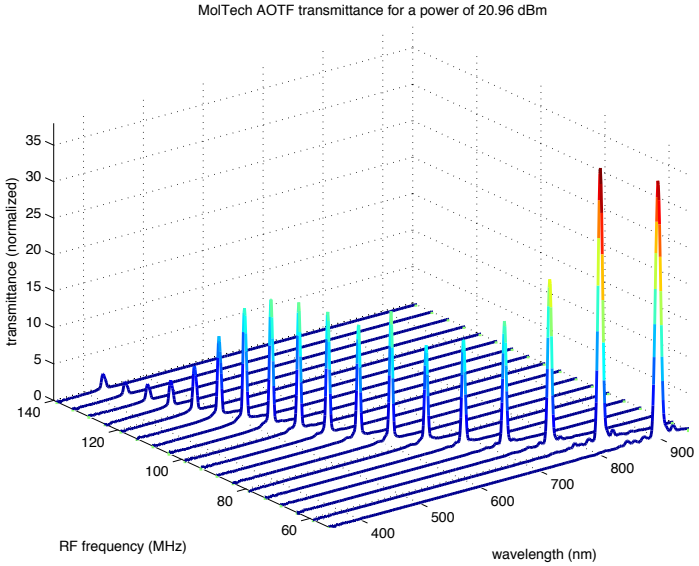

Figure 6.39. Diffraction efficiency of the MolTech AOTF at different RF frequencies at medium power (+21dBm).

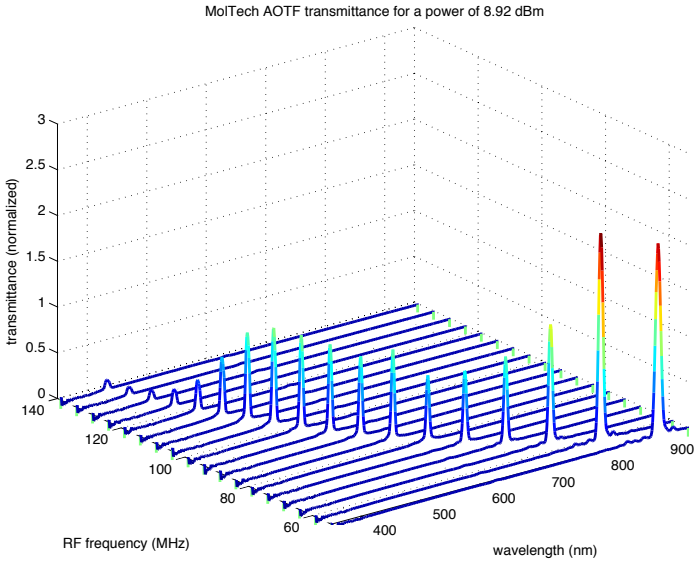

Figure 6.40. Diffraction efficiency of the MolTech AOTF at different RF frequencies at low power (+9dBm).

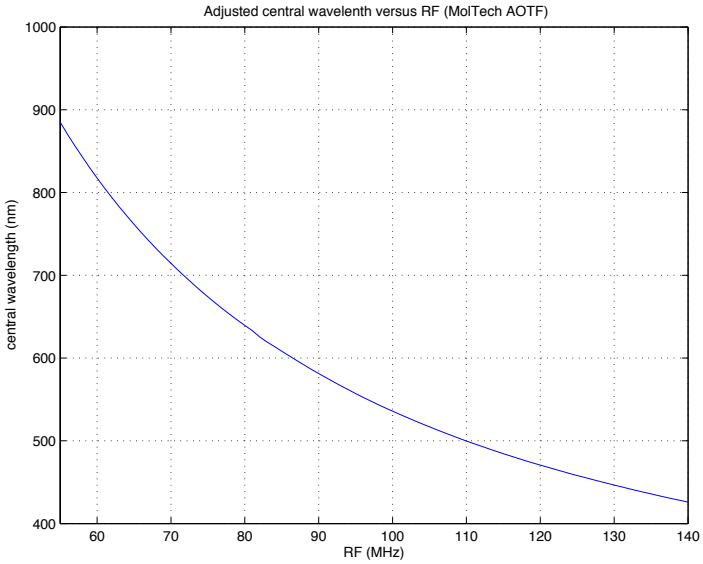

Figure 6.41. Central wavelength of the diffracted light (Gaussian adjustment) versus RF frequency for the MolTech AOTF.

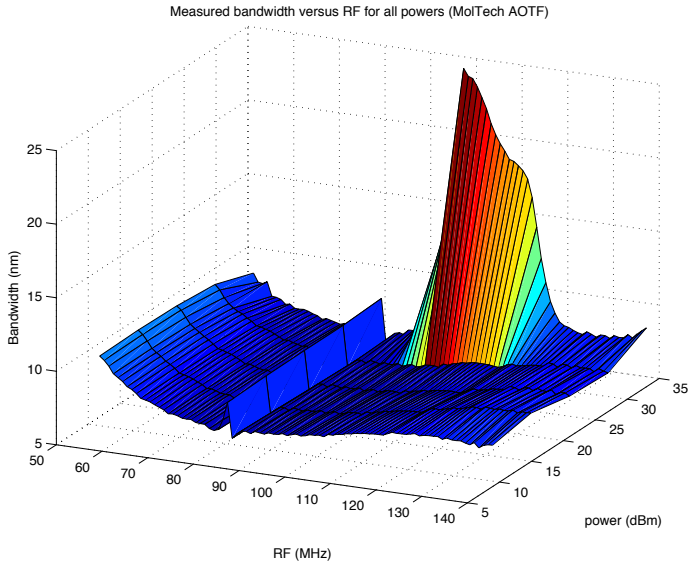

Figure 6.42. Bandwidth of the diffracted light passband in all the RF range for the different applied powers for the MolTech AOTF.

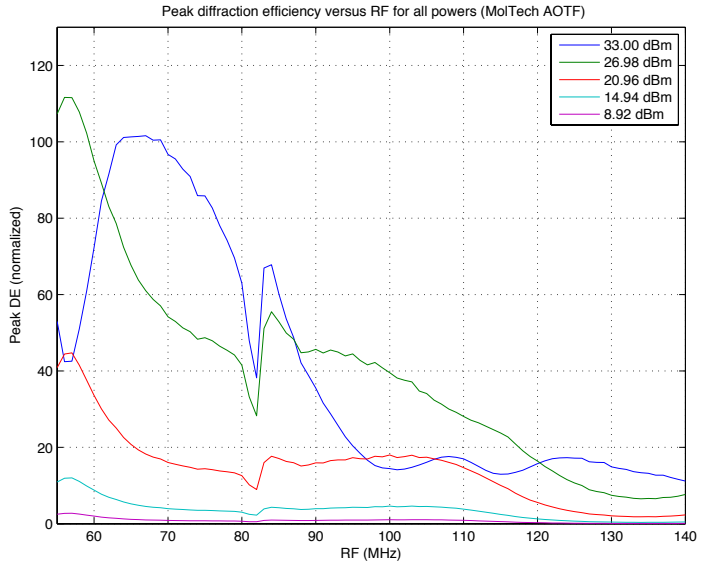

Figure 6.43. Peak diffraction efficiency of the MolTech AOTF in all the RF range for the analysed applied powers.

These figures show that, except for the maximum power configuration, the response of the MT crystal is better than that of the AA model, with a very narrow bandwidth and a quite constant DE for most of the RF range. In concrete, the DE for an applied power of 27dB is almost flat from 65 to 115MHz. However, the DE is increased considerably at low RF frequencies at expense of an increased bandwidth. Similarly, the output passband is severely distorted at the maximum RF power at a expense of an increased bandwidth and a lower DE (especially on the range between 85 and 125 MHz).

As mentioned for the AA crystal, we found a local degradation of the crystal efficiency for a frequency of 82MHz. The degradation is shown as a deep decrease of the DE, especially for high RF powers, and an increase on the output bandwidth.

A deeper analysis of the AOTF behaviour with respect to power was performed on the third set of experiments. The results for the MolTech crystal are shown on Figure 6.44, Figure 6.45, and Figure 6.46.

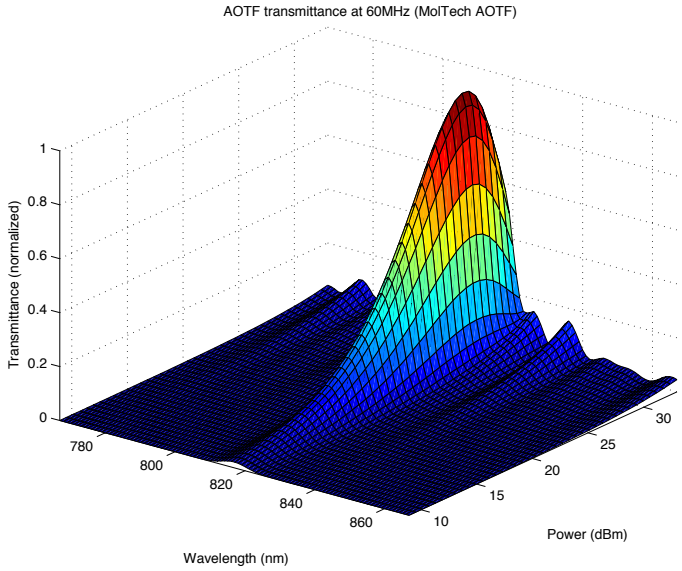

Figure 6.44. Diffraction efficiency of the MolTech AOTF when driven by an RF signal of 60MHz for different power values.

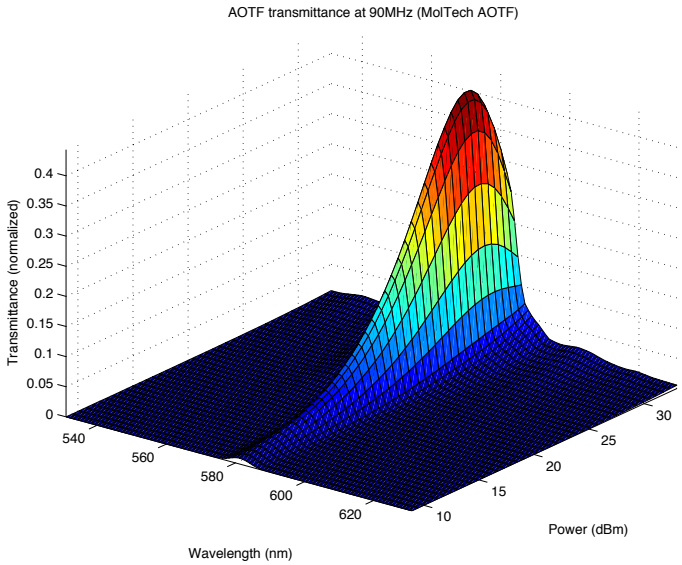

Figure 6.45. Diffraction efficiency of the MolTech AOTF when driven by an RF signal of 90MHz for different power values.

Again, these figures show a Gaussian behaviour of the peak transmittance with respect to power, modulated by the efficiency response to frequency. Also in this crystal the peak DE position is not related to the applied frequency.

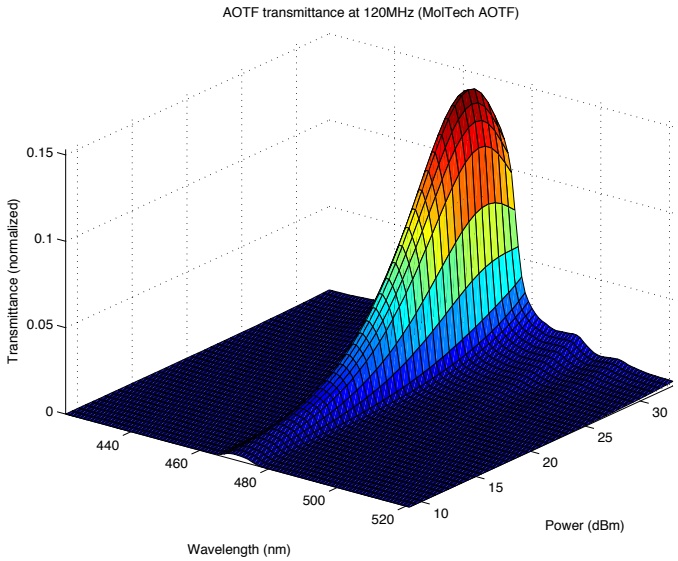

Figure 6.46. Diffraction efficiency of the MolTech AOTF when driven by a RF signal of 120MHz for different power values.

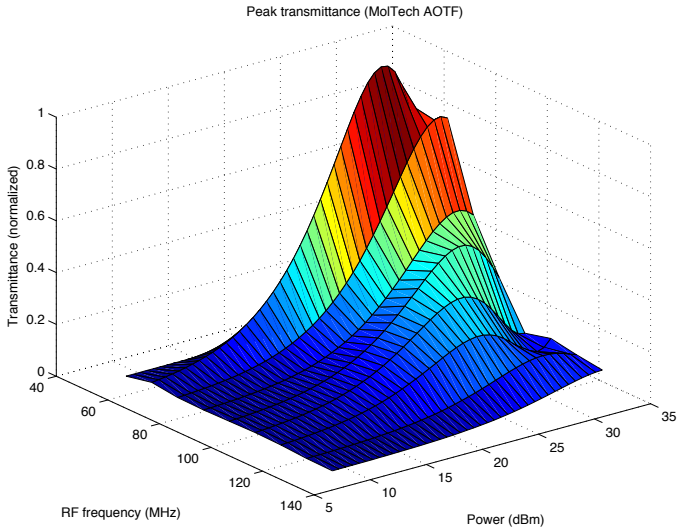

Figure 6.47. Peak transmittance of the MolTech AOTF as a function of applied power and RF frequency.

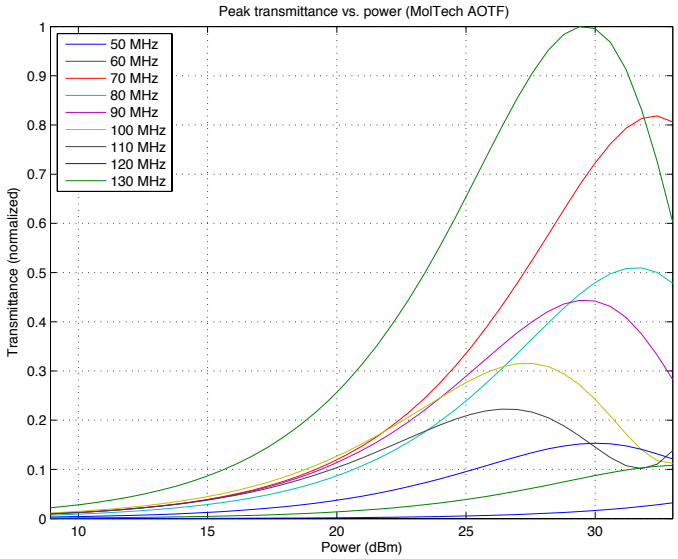

Figure 6.48. Peak transmittance of the MolTech AOTF versus applied power for the analysed RF frequencies.

6.2.3.4. Gooch & Housego AOTF

Next figures show the performance of the Gooch & Housego AOTF with respect to RF frequencies. Figure 6.49, Figure 6.50, and Figure 6.51 show the diffracted spectra for some of the applied RF frequencies at maximum, medium, and minimum applied power, respectively. On the other hand, Figure 6.52, Figure 6.53, and Figure 6.54 show the central wavelength, bandwidth, and peak diffraction efficiency of the diffracted spectra for all the measured frequencies and powers. Note that for this crystal, the maximum power applied was +21dBm (0.5W), which was the maximum recommended by the manufacturer.

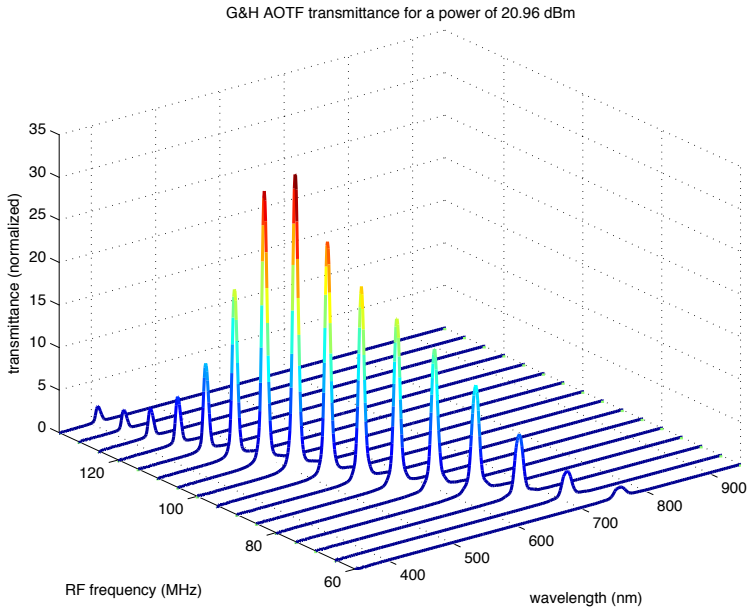

Figure 6.49. Diffraction efficiency of the Gooch & Housego AOTF at several RF frequencies at the maximum power (+21dBm).

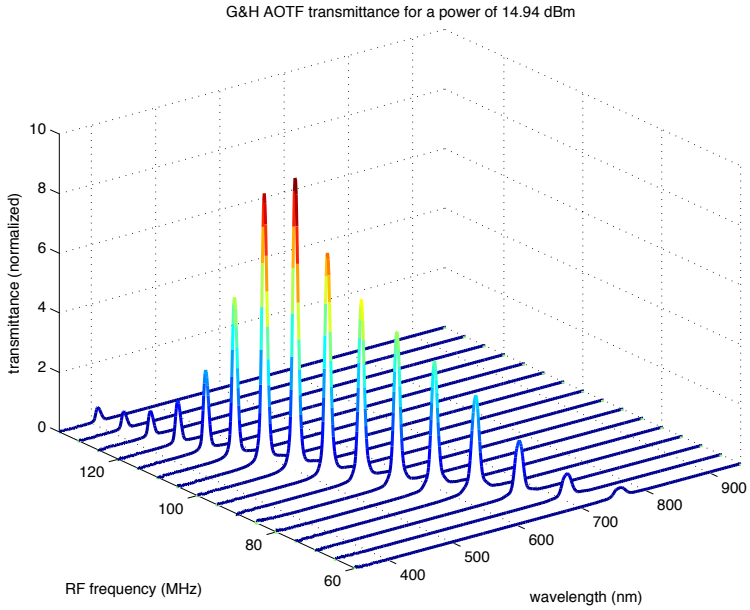

Figure 6.50. Diffraction efficiency of the Gooch & Housego AOTF at several RF frequencies at medium power (+15dBm).

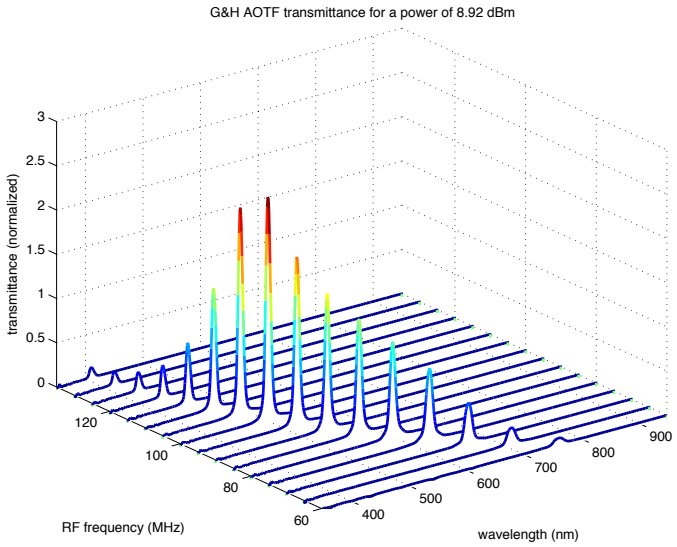

Figure 6.51. Diffraction efficiency of the Gooch & Housego AOTF at several RF frequencies at low power (+9dBm).

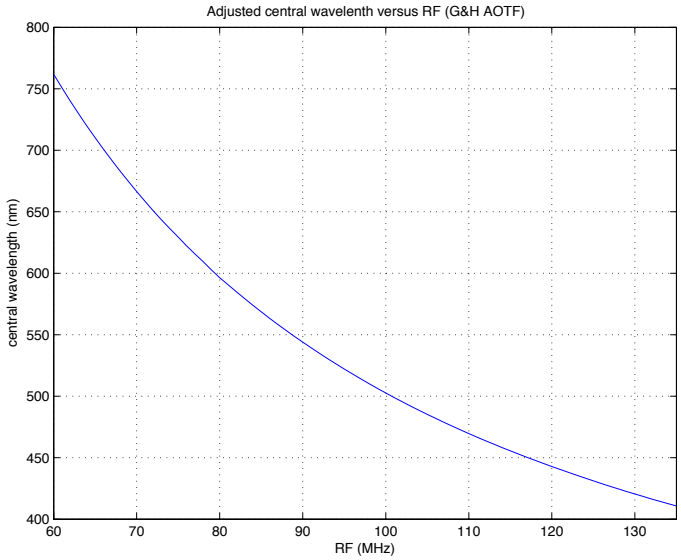

Figure 6.52. Central wavelength of the diffracted light (Gaussian adjustment) versus RF frequency for the Gooch & Housego AOTF.

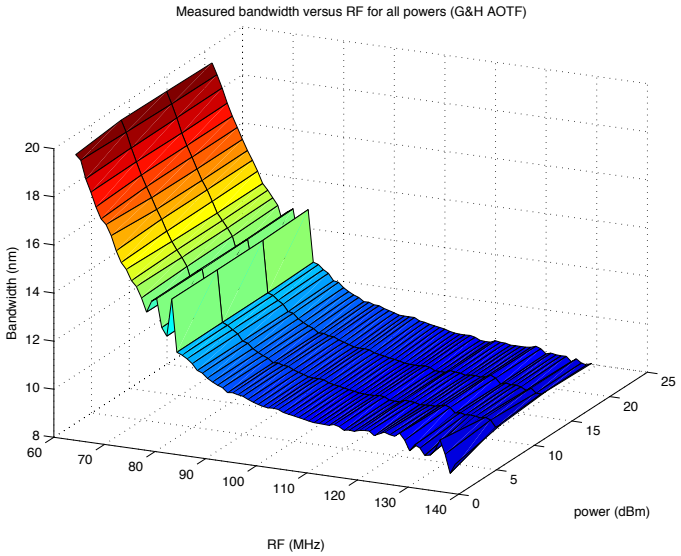

Figure 6.53. Bandwidth of the diffracted light passband in all the RF range for the different applied powers for the Gooch & Housego AOTF.

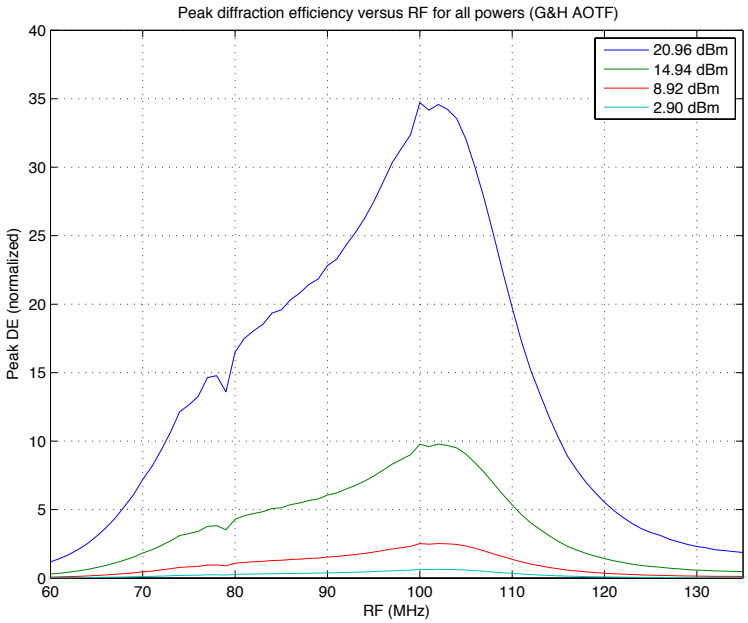

Figure 6.54. Peak diffraction efficiency of the Gooch & Housego AOTF in all the RF range for the analysed applied powers.

Due to the lower power applied to the Gooch & Housego crystal respect to the other models, the obtained passband spectra are much cleaner and present no sidelobes (which are typical of high values of RF power). However, the DE is consequently very low. On the other side, the bandwidth is higher than in the other models, especially at low frequencies. Taking into account the low DE of the crystal at those frequencies, the resulting balance of bandwidth versus DE is very poor. Additionally, we observe that the DE of this crystal is very dependent on the RF frequency, and follows a pronounced peak shape independently of the applied power.

An analysis of the AOTF behaviour respect to power was performed on the third set of experiments. The results are shown in the following figures.

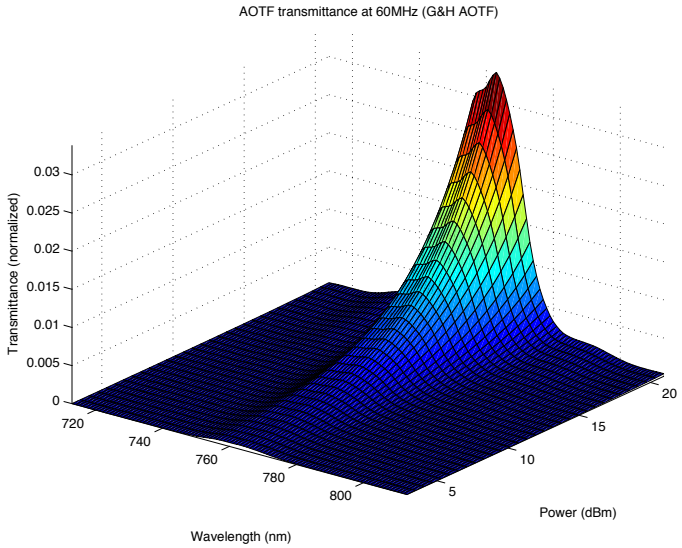

Figure 6.55. Diffraction efficiency of the Gooch & Housego AOTF when driven by an RF signal of 60MHz at different power values.

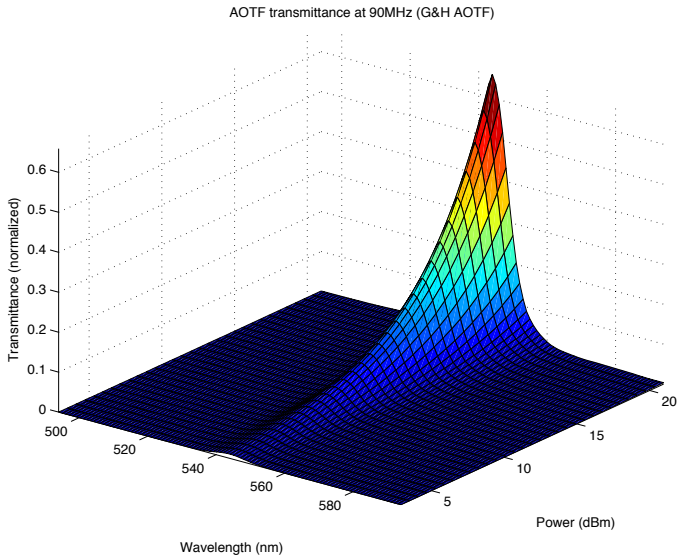

Figure 6.56. Diffraction efficiency of the Gooch & Housego AOTF when driven by an RF signal of 90MHz at different power values.

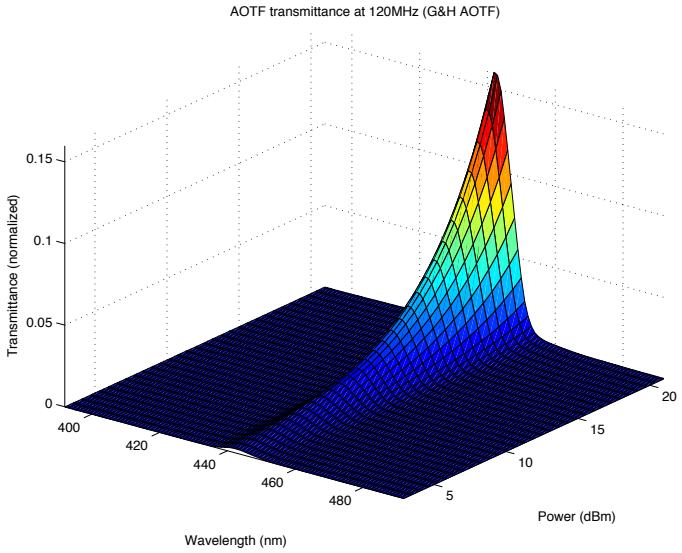

Figure 6.57. Diffraction efficiency of the Gooch & Housego AOTF when driven by a RF signal of 120MHz at different power values.

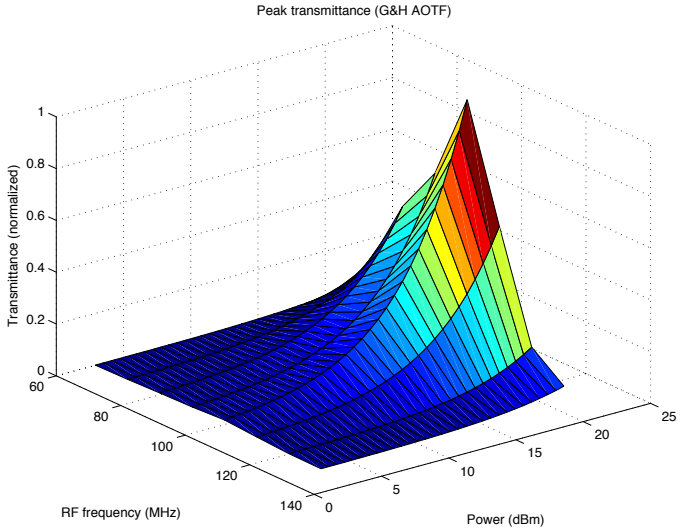

Figure 6.58. Peak transmittance of the Gooch & Housego AOTF versus applied power for the analysed RF frequencies.

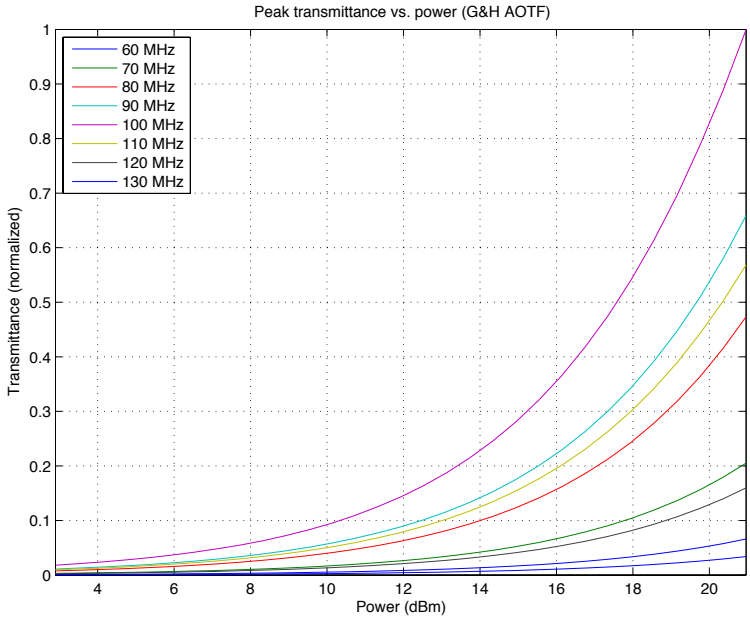

Figure 6.59. Peak transmittance of the Gooch & Housego AOTF versus applied power for the analysed RF frequencies.

Despite the fact that this crystal also follows a Gaussian curve, the applied power range falls on the tail of the Gaussian curve, which suggests that the maximum power that can be applied to the crystal is higher than the one indicated by the manufacturer. Again, these figures also show the modulation of the frequency response on the amplitude of the Gaussian responses.

6.2.3.5. Analysis of the results

The diffraction efficiency of the crystals depends on the applied RF frequency and power. Both peak efficiency and bandwidth greatly vary on all the working RF range, without following any evident analytical expression, and being quite different for each crystal. However, the relationship between RF frequency and central wavelength of the diffraction light closely follows a parabolic curve, with similar characteristics for all the crystals. Respect to power, the diffraction efficiency follows a Gaussian curve. On the Gooch & Housego model, the DE curves suggests than the power applied to the crystal can be higher than the one recommended by the manufacturer.

The Moltech model presents the best performance, with a quite constant behaviour in terms of bandwidth and DE for a wide range of RF frequencies. The cleanest output passband is the one produced by the Gooch & Housego model, but at the expense of a very low and variable DE.

6.3. AOTF impedance matching

As the above-mentioned analysis shows, the AOTF diffraction behaviour varies with the RF frequency. Further attention must be paid to the AOTF diffraction behaviour on a narrow range of frequencies around 70MHz. The cause of this uneven behaviour might be found on one or several stages of the energy transfer path between the RF generation and the light diffraction:

- The RF output amplitude of the Power Amplifier of the driver.
- The matching circuit between the PA and the AOTF transducer.
- The interface between the transducer and the crystal.

The first two stages can be monitored by a spectrum analysis and an oscilloscope. The last stage cannot be observed directly because it is internal to the AO filter.

Within this context, we performed an experiment to analyse the behaviour of both the power amplifier and matching circuits of a set of different AOTF models. Results are presented on next section.

6.3.1. Output power characterisation

On a previous analysis (section 5.2) we measured the output amplitude of the power amplifier on the DAC-based driver. This analysis was performed by driving a spectral analyser with a 50Ω-matched input, at the maximum DAC power value. We concluded that the output amplitude was linearly reduced over the RF range, and no special behaviour was shown on the region around 70MHz.

Now, we evaluate the matching between the RF power output and the 50Ω load of the crystal transducer. For this experiment, a 50Ω RF power resistor was driven from the driver output while we measured the signal amplitude with a scope. The experimental set-up, shown on Figure 6.60, allowed measuring the output signal amplitude by using an oscilloscope connected through a T-connector to the signal path. Due to the high impedance of the scope input, this element does not affect the signal matching between the observed elements.

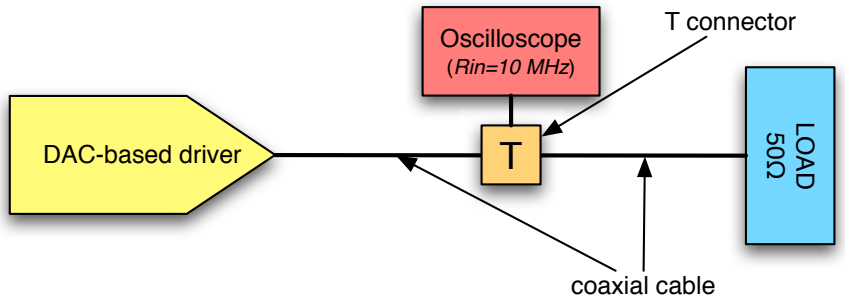

Figure 6.60. DAC-driver matching measurement set-up.

The used scope was an Agilent MSO6002 model, connected via GPIB to a PC running a MATLAB automated script. With this set-up we measured the output amplitude of the system from 50MHz to 100MHz (the upper frequency limit of the scope) with different power values. Figure 6.61 shows the measured amplitude respect to frequency at the maximum power of the driver. The figure shows an amplitude drop with frequency, due to the inherent sinc-shaped output of the DAC [Kester, 1996].

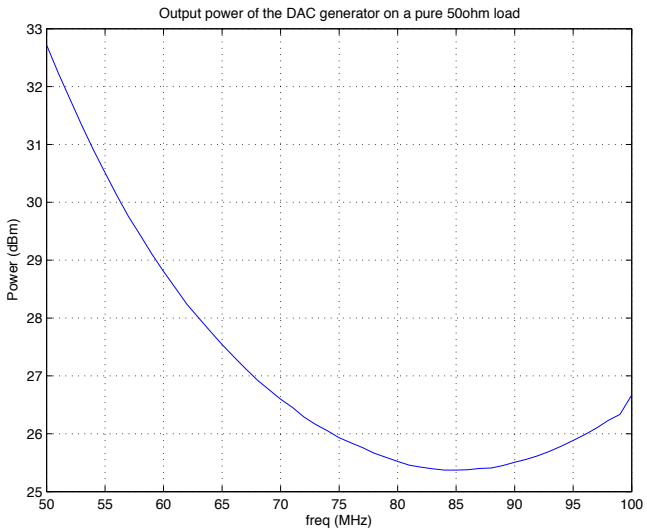

Figure 6.61. Measured signal amplitude of the DAC-based driver for a pure 50Ω load.

Afterwards, we repeated the measurements substituting the 50Ω load with the purchased AOTF models (see Table 2.3 and Table 2.4). We drove all the AOTF at their maximum power limits from 50MHz to 100MHz and measured the signal amplitudes.

Figure 6.62 shows the behaviour of the different AOTF models, using the measured behaviour of the 50Ω RF power resistor as a reference. Note that for the AOTF models that were driven with reduced power amplitudes, the signal has been normalised to the maximum power amplitude (+33dBm).

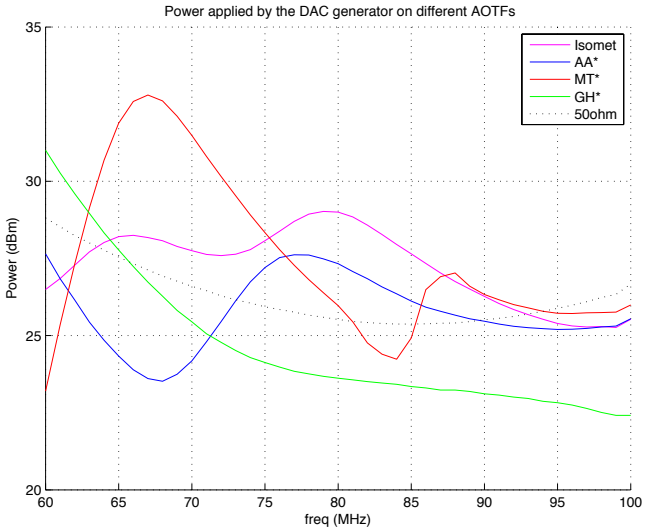

Figure 6.62. Measured signal amplitude of the DAC-based driver for a pure 50Ω load and for several AOTF models (**Note*: output power normalised).

This figure shows that the matching of the AOTF input transducers greatly differs from the ideal 50Ω behaviour. The Isomet, AA, and MT models present some resonances at several frequencies, while the GH model presents a closer behaviour to a pure resistive load. The differences are related to the internal design of the matching circuit, whose details are not provided by the manufacturers.

VII

ATFS characterisation

In this section we present the spectral characterisation of the ATFS instrument when driven by both signal generators. The ATFS instrument mounts an Isomet 614-08 AOTF on a custom optical layout, as described in Chapter 3. We have characterised the spectral performance of the system, the system repeatability on the diffraction efficiency and, at last, the thermal behaviour of the crystal.

7.1. ATFS spectral performance

We have characterised the spectral performance of the ATFS instrument by applying the same set of RF signals described in the previous chapter. However, as the AOTF is fixed on the instrument layout, the performance is measured taking into account the whole optical path of the instrument. On the other AOTF's, the spectral performance was measured over the bare crystal.

7.1.1. Experimental procedure

The experimental procedure was the following:

- We configure the system with the following experimental set-up: the ATFS was located on the optical path of the collimated light source ahead of the detector of the ASD FieldSpec FR spectroradiometer.
- The radiance of the light had been previously acquired by illuminating a Spectralon white panel with the collimated light beam. This radiance spectrum was stored as the white reference vector WR_λ.
- Then, we acquired the stray light (SL_λ) at the optical ATFS output while the RF generator was switched off.
- Finally, we applied sequentially the set of RF signals, acquiring the diffracted light (DL_λ), at the output of the ATFS for each RF signal.
- The diffraction efficiency was calculated for from the acquired spectra as follows:

$$DE_\lambda = \frac{DL_\lambda - SL_\lambda}{WR_\lambda} \qquad \textbf{(Eq. 7.1)}$$

where the operations were applied band by band on the spectra vectors. Note that the obtained DE_λ was relative, as the WR radiance values was not measured on the same optical path configuration used for the ATFS. Therefore, we have normalised the DE_λ for a better understanding and comparability of the figures.

All the measurement acquisition and analysis was automated with MATLAB scripts. The code of these scripts is listed on the attached CD.

7.1.2. Results

For the case of the DDS driver, we obtained the results shown on the following figures: Figure 7.1 for a 90MHz pure signal at several powers, and Figure 7.2 for a sweeping signal of 11 steps around 90MHz (from 87 to 93MHz). We repeated these measurements for the DAC driver, obtaining Figure 7.3 for a 90MHz pure signal and Figure 7.4 for a composite RF signal of 11 components around 90MHz (from 87 to 93MHz in 0.6MHz steps), corresponding to the same frequencies used on the DDS sweep of the Figure 7.2. Note that for the DAC driver the maximum output power was normalised to 0dB in all cases.

In both cases, the AOTF performance is severely degraded for high RF power values. However, the spectral purity is worse in the case of the DDS driver.

For a composite signal, the crystal behaves as expected in terms of DE, generating a broad passband on the spectral domain. As the power delivered by the driver is distributed among multiple frequencies, the spectral purity of the diffracted light, for the same applied power, is better than in the case of pure signal at high powers. This is clearly noticeable in the case of the DAC driver, which produces a passband with sharper characteristics. Note also the effect of the RF harmonics of the DDS driver on the DE, which causes a small

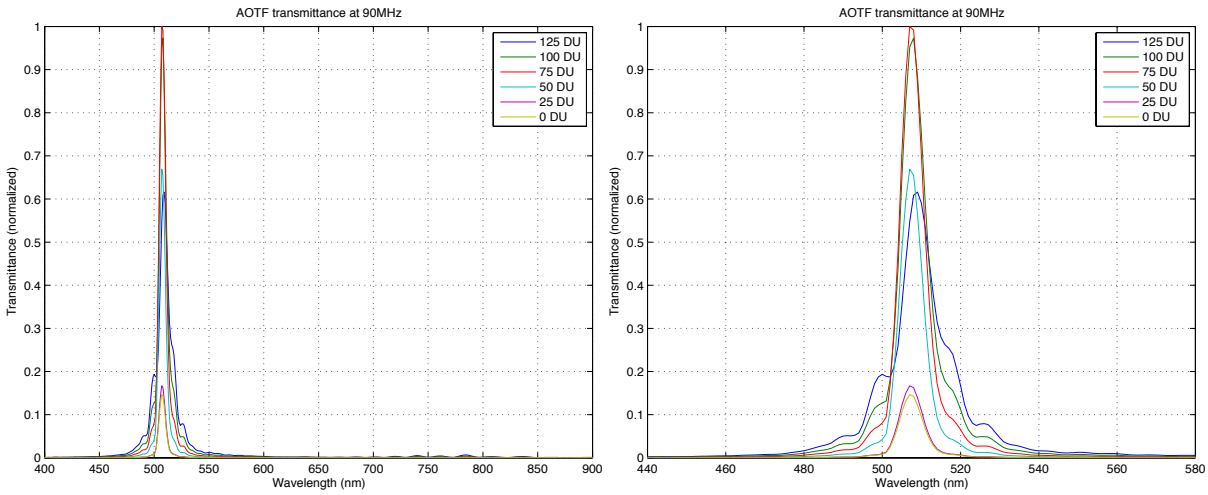

Figure 7.1. Diffraction efficiency for the DDS driver generating a 90MHz pure sine at different power values. *Left*: entire working range of the AOTF. *Right*: centred at the passband wavelength.

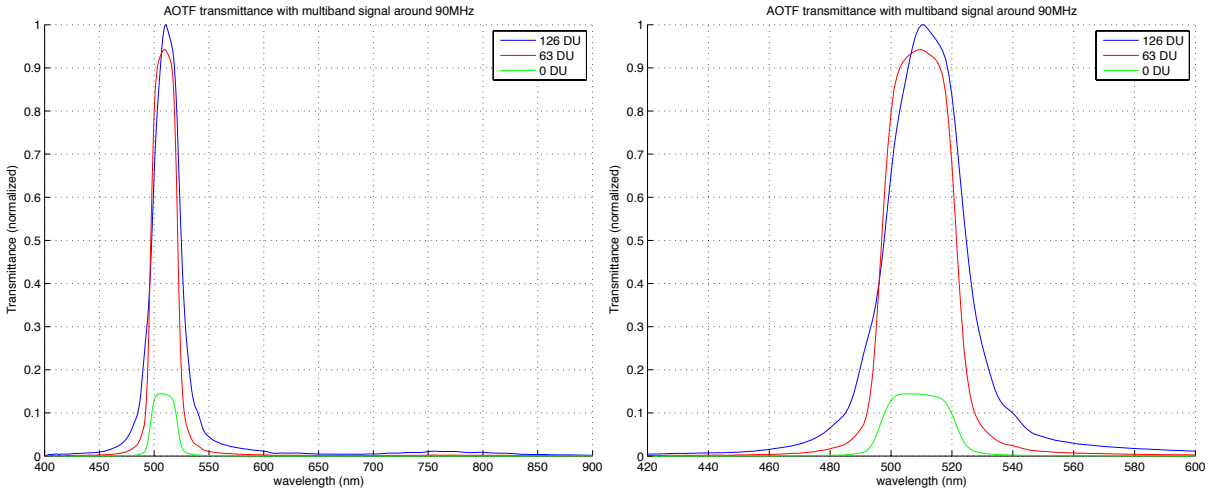

Figure 7.2. Diffraction efficiency for the DDS driver generating a sweeping signal of 11 steps around 90MHz at different power values. *Left*: entire working range of the AOTF.

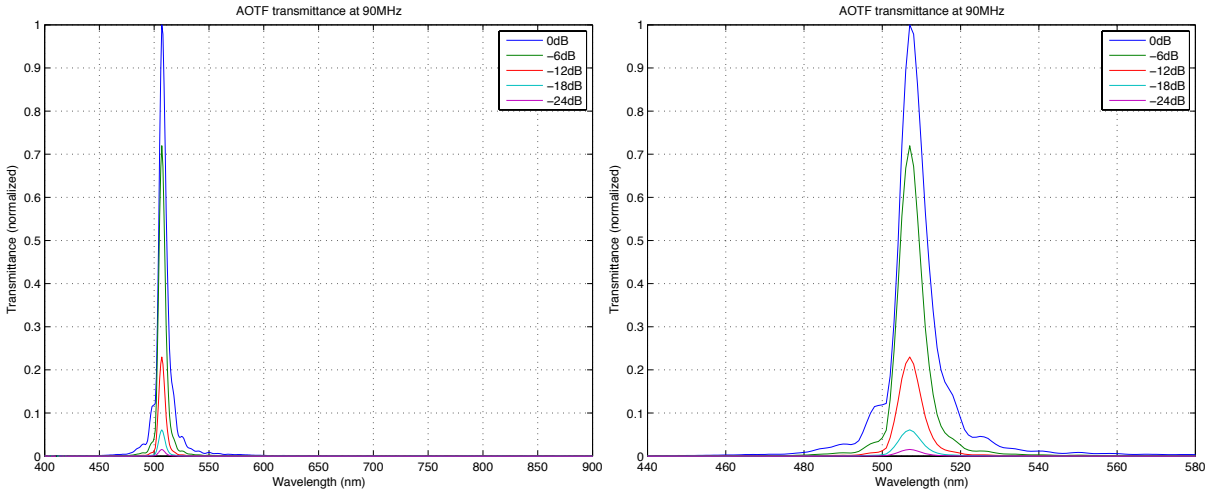

Figure 7.3. Diffraction efficiency for the DAC driver generating a 90MHz pure sine at different power values. *Left*: entire working range of the AOTF. *Right*: centred at the passband wavelength.

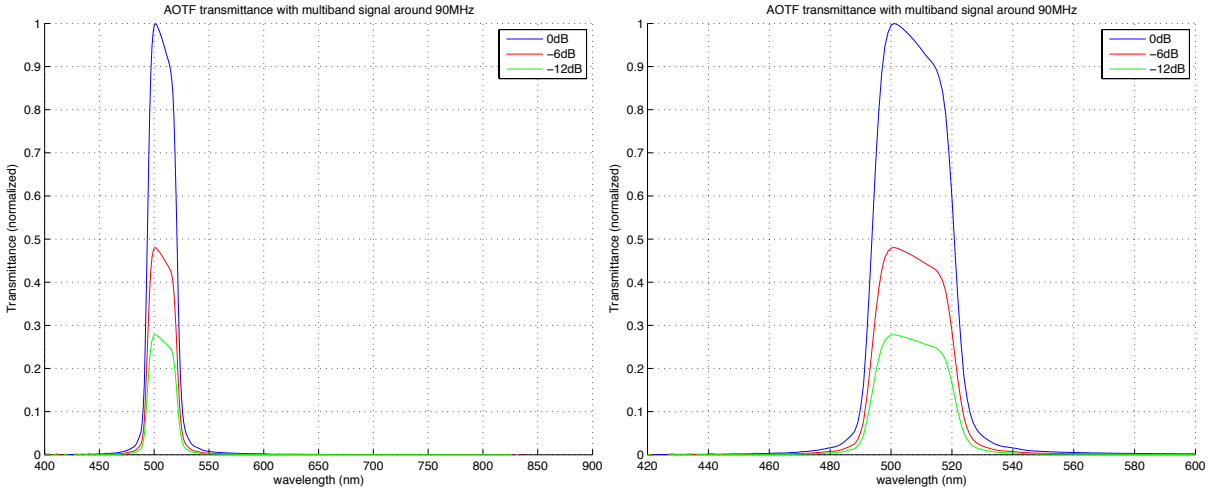

Figure 7.4. Diffraction efficiency for the DAC driver generating a sweeping signal of 11 steps around 90MHz at different power values. *Left*: entire working range of the AOTF.

amount of light to pass through the crystal on a passband around 775nm (corresponding to the diffracted wavelength by the first RF harmonic of the 90 MHz signal)

We also evaluated the diffraction efficiency as a function of the driving power. For this experiment, we measured a series of diffraction efficiencies for a pure driving signal of 90MHz with 100 different power values. The results are shown in Figure 7.5.

From Figure 7.5 we observe that the peak of the crystal DE is not linear with respect to the power, but follows a Gaussian behaviour. However, in the case of the DDS driver this behaviour is distorted at very high and very low power values due to the limitations of the electronics. This fact can be clearly noticed in Figure 7.7, which shows the peak DE as a function of the power for a set of driving frequencies for the DDS and the DAC driver, respectively.

Although the applied RF power of the driving signal is almost constant in frequency (see Figure 5.5 and Figure 5.6), this is not the case for the DE of the crystal. The DE does not follow any trend respect to frequency, and it is not either proportional to the applied power. Figure 7.7 shows the observed DE for the DDS driver as a function of frequency for a set of powers.

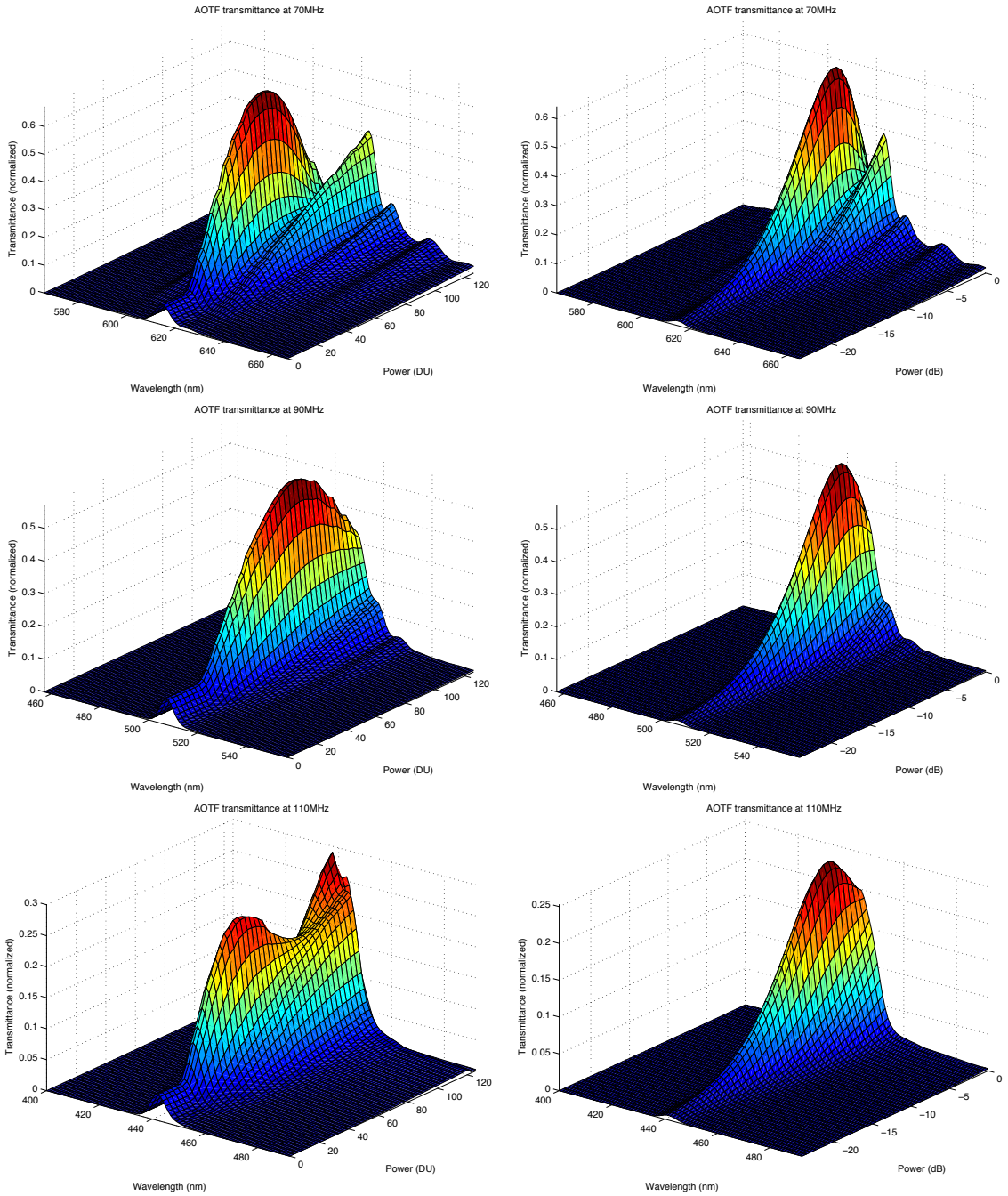

Figure 7.5. Diffraction efficiency for the AOTF as a function of the RF power, at three different RF frequencies. *Left*: DDS driver. *Right*: DAC driver. *From top to bottom*: central frequency of 70MHz, 90MHz, and 110MHz.

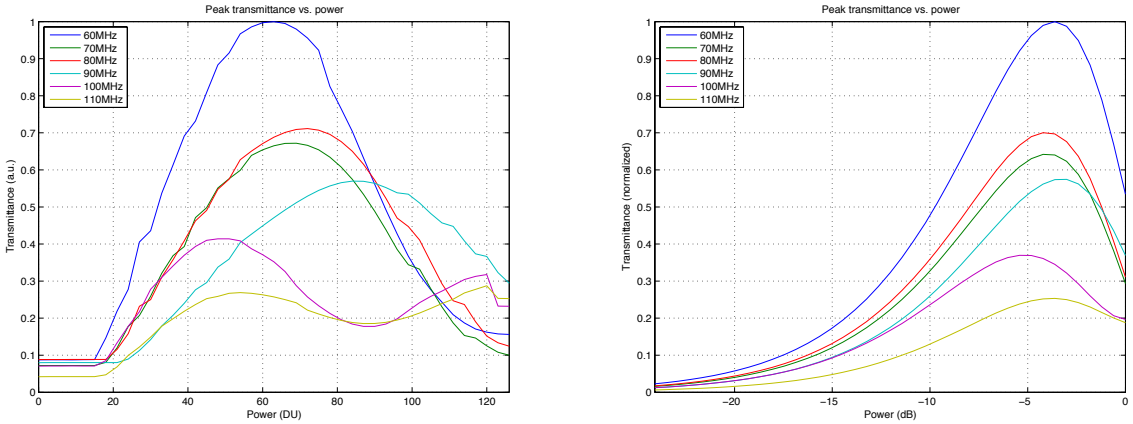

Figure 7.6. Peak DE of the AOTF driven by the DDS driver (*left*) and the DAC driver

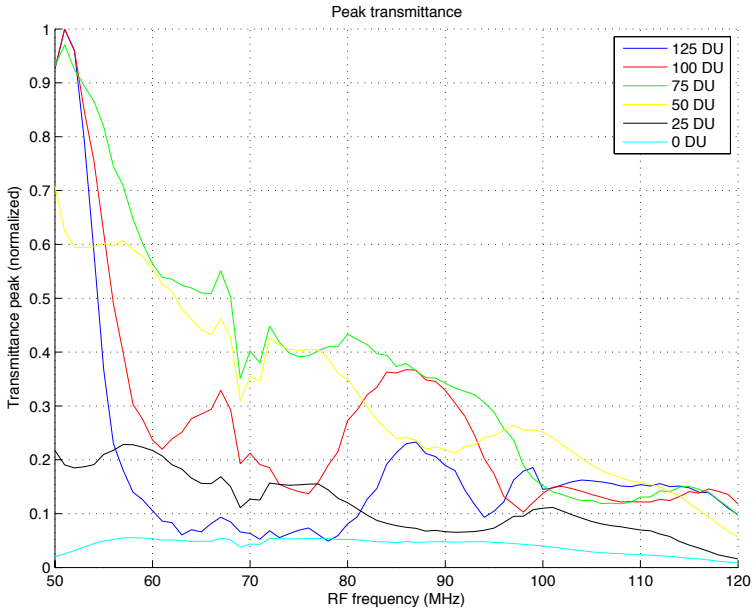

Figure 7.7. AOTF transmittance for the DDS driver as a function of the driving frequency at different powers, measured at the nominal central wavelength for each frequency.

It is worth noting that the DE is measured at the nominal central wavelength of the passband light. Note that this wavelength is shifted from the wavelength of the peak DE in the case of high powers at low frequencies (see Figure 7.5). If we represent the peak DE, we obtain a slightly different response for the highest power measurements –125 and 100 DU– (Figure 7.8).

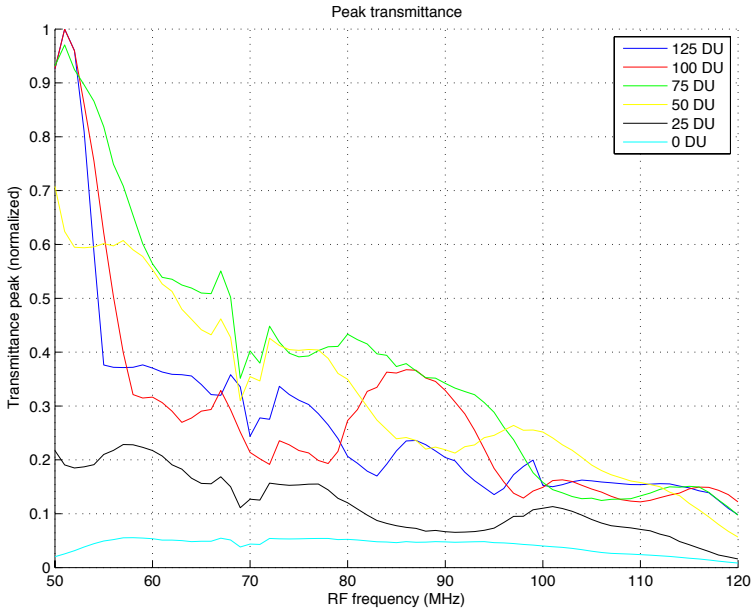

Figure 7.8. AOTF transmittance for the DDS driver as a function of the driving frequency at different powers, measured at the wavelength of maximum DE.

When we repeat the same measurements for the DAC driver we obtain quite similar results, as the RF behaviour of both drivers is very similar Figure 7.9 and Figure 7.10 show the results. In this case, as the RF performance of the driver is better at higher output powers than in the case of the DDS driver, there is no shift between the DE peak position and the central wavelength for the highest power values.

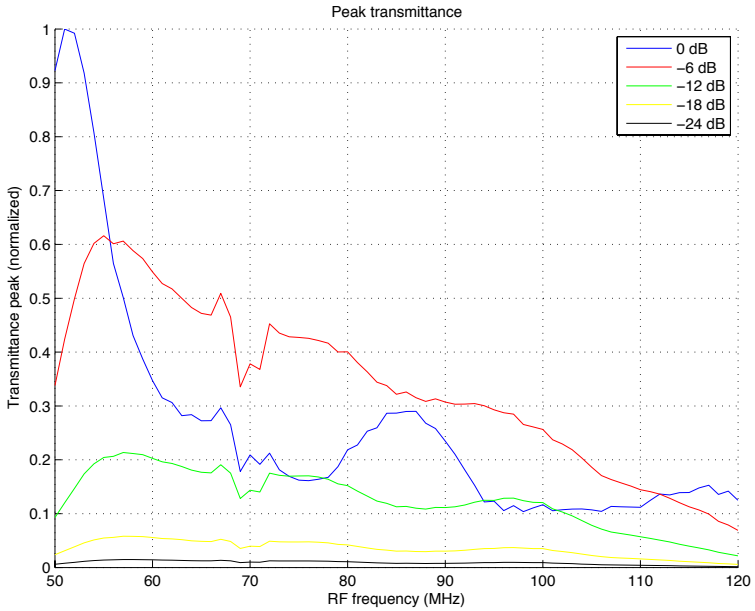

Figure 7.9. AOTF transmittance for the DAC driver as a function of the driving frequency at different powers, measured at the nominal central wavelength for each frequency.

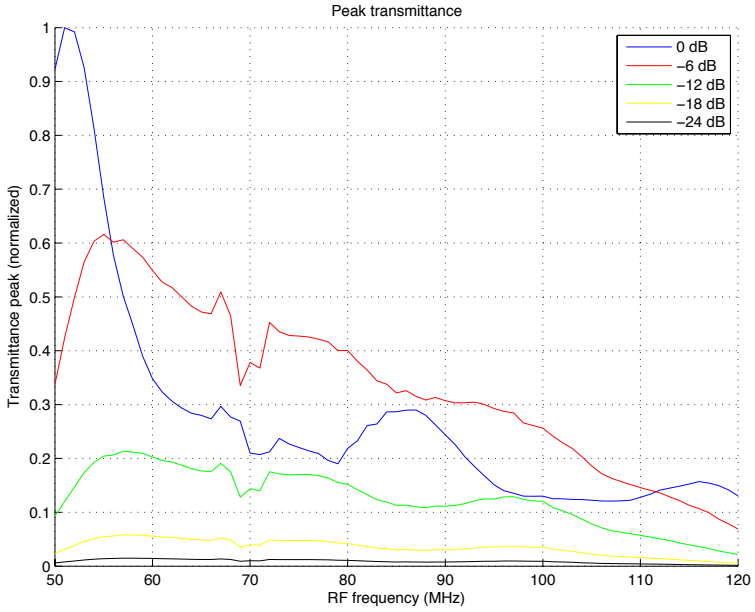

Figure 7.10. AOTF transmittance for the DAC driver as a function of the driving frequency at different powers, measured at the wavelength of maximum DE.

7.2. ATFS spectral performance in multiband configuration

The DAC driver makes use of the linearity of the AOTF crystals when driven by a composite RF signal to generate a broadband signal. This linearity means that the DE of the crystal, when driven by a composite signal, is equivalent to the sum of the DE achieved by each of the separate RF components. However, this linearity is only reached on DE wavelength but not on DE amplitude. This is due to the fact that AOTF crystals are not linear with respect to the applied RF power. Therefore, when applying two close enough RF frequencies, the effect on the crystal is equivalent to the application of a single RF frequency with increased power, but its DE is lower than the arithmetic sum of the DE of the pure signals.

We have verified empirically this behaviour with a set of measurements. Each set consisted on measuring the AOTF behaviour for three different RF pure signals, and comparing the generated DE with the result of applying a composite RF signal formed by the same three components simultaneously.

First we used the frequencies of 70, 80, and 90MHz. Figure 7.11 shows the results of this experiment. In this case, as the frequencies are far enough, the AOTF behaviour is linear respect to individual DE amplitudes.

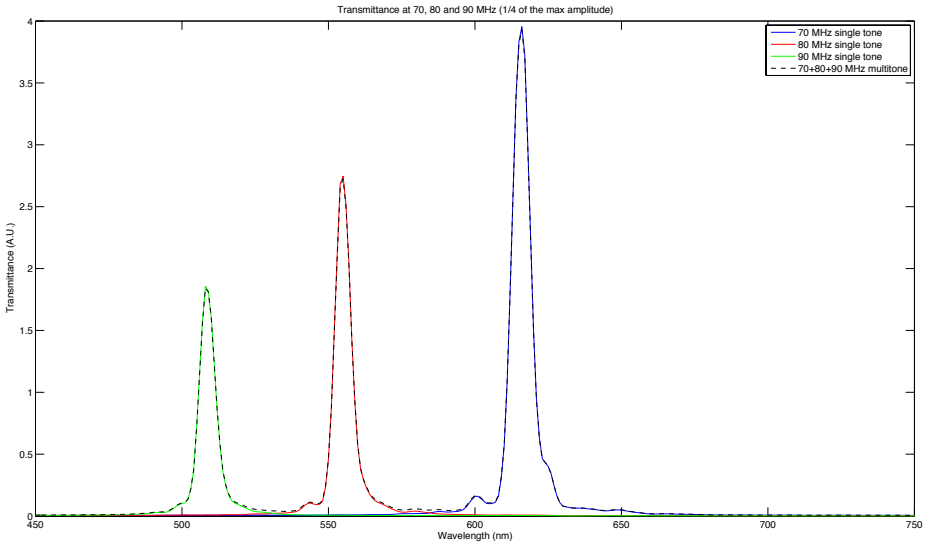

Figure 7.11. DE of the AOTF when driven by three RF pure sine signals with a frequency of 70, 80, and 90MHz, and DE of the AOTF when driven by a composite signal with the 3 frequencies applied simultaneously.

However, if we repeat the experiment for closer frequencies for the three components, we observe the effect of the non-linearity with the RF power. Figure 7.12 shows the case of a composite signal with frequencies of 88, 90, and 92MHz.

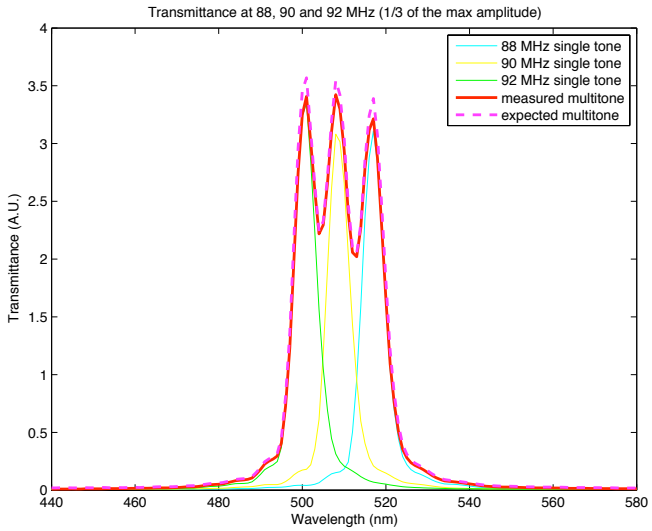

Figure 7.12. DE of the AOTF when driven by three RF pure sine signals of 1/3 of the maximum amplitude with frequencies of 88, 90, and 92MHz, and DE when driven by a composite signal with the 3 frequencies applied simultaneously. Shown is the expected efficiency considering linearity with the RF power, and the measured one.

In this figure, each RF component has an amplitude of 1/3 of the maximum amplitude of the DAC, in order not to saturate the digital output. If we further reduce the amplitude of each component, a behaviour closer to the expected one is observed (in Figure 7.13 we show the results for an amplitude of 1/4). This is due to the Gaussian behaviour of the DE with power, which is almost linear at a certain power range between very high and very low values (see Figure 7.6). Therefore, for multiband signals that keep the total applied power within this linear range, the DE is also linear respect to the individual bands DE.

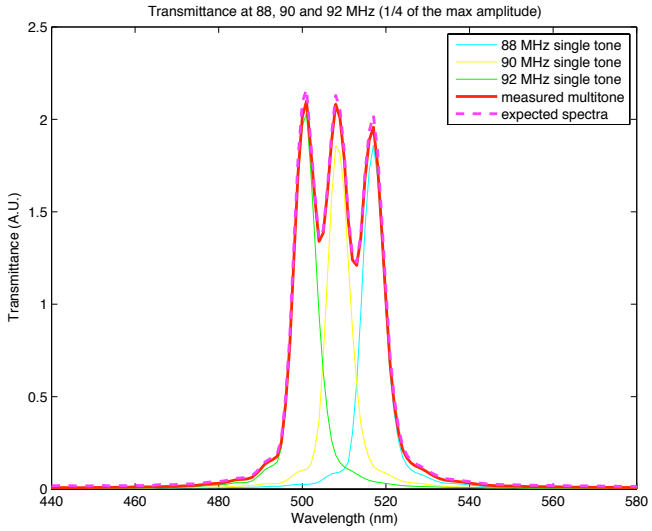

Figure 7.13. Diffraction efficiency of the AOTF when driven by three RF pure sine signals of 1/4 of the maximum amplitude with frequencies of 88, 90, and 92MHz, and DE when driven by a composite signal with the 3 frequencies applied simultaneously. Shown is the expected efficiency considering linearity with the RF power, and the measured one.

7.3. System repeatability

A relevant question regarding the performance of any system based on AOTF technologies is the repeatability of the measurements. In order to assess it, we took a series of repetitive measurements with exactly the same configuration and compared the results. The measurements were taken with the ATFS complete optical system mounted around the Isomet AOTF crystal and the DAC-based RF driver. We performed two different sets of measurements: one for measuring the long-term repeatability of the system, and another one measuring the short-term performance.

For the long-term performance, we repeated the same set of DE measures three times with an interval of one week between measurements. The set of DE measures was formed by the response of the crystal to two successive sequences of RF signals. Each RF sequence consisted on the generation of RF pure signals at different frequencies of the working frequency range of the system with five different power levels.

For the short-term performance, we repeated the same sequence of DE measures for four consecutive times, without powering off the system between measurements. The interval between measurements was approximately two hours (the time that took each sequence of RF to be measured).

7.4. Experimental set-up

As we have mentioned above, the repeatability measurements were performed over the Isomet 614-08 model on the ATFS instrument. The DE was measured by registering the response of this optical layout to a collimated light source using an ASD FieldSpec FR spectroradiometer. The collimated light source was the same one used in previous experiments (KI-120 Koehler Illuminator from LabSphere), whose spectral response is well known. The spectroradiometer sensor was fixed at the optical output of the ATFS system and finely adjusted for the maximum sensitivity. Once adjusted, the experimental set-up was fixed and was not moved at all during the complete extent of the measurements.

The RF driver used for the experiment was the DAC-based system. The sequence of RF signals was the following:

- We adjusted the output amplitude sequentially to 1, 1/2, 1/4, 1/8, and 1/16 (5 values). For each amplitude:
- We generated sequentially a RF signal from 50 to 120MHz in 1MHz steps (71 values).

In total, the sequence consisted on 5 x 71 different measurements. The acquisition of the sequence of spectra was automated with a MATLAB script for each repeatability experiment. Code of these scripts is listed on the attached CD.

Due to the great differences on the DE value depending on the applied power, we adjusted the integration time of the spectroradiometer for each power value. Afterwards, we normalised the DE values respect to the integration time (the normalisation is valid because the spectroradiometer measurements are linear with the integration time).

This set of measurements has been also used to characterise the response of the ATFS to the driving frequency and power. From this characterisation we have generated the wavelength to driving RF frequency calibration curve used by the DAC software driver.

7.4.1. Long-term repeatability performance

For the long-term performance of the system we adjusted an experimental set-up as described above, and we took the same sequence of measurements for three times with an interval of one week between measurements. For each acquisition set, two successive measurements were taken. The first set of measurements of each acquisition started after a 30min warming-up of all the instruments (spectroradiometer, lamp, and power amplifier), and the second was run immediately after the first one finished. The whole sequence of measurements (5 power values x 71 RF frequencies) took about 2 hours to finish. Therefore, the second set of measurements of each day started approximately 2 hours and a half after powering on the instruments.

We labelled the set of measurements sequentially from "a" to "f". As an example of the obtained results, Figure 7.14 and Figure 7.15 show the results for set "a", corresponding to the first set of measurements of the first day, and set "f", corresponding to the second set of measurements of the last day, respectively.

We have analysed the measurements in MATLAB. Each set of measurements is composed by 355 measurements (corresponding to the spectral response of the crystal at 71 frequencies with 5 different power amplitudes). For each measurement, we computed the ATFS instrument transmittance, dividing the acquired spectra by the WR radiance spectra.

From the calculated transmittance spectra we formed a matrix of the peak DE values of each measurement, organising the power amplitudes as rows and the RF frequencies as columns.

Figure 7.16 to Figure 7.20 show the plots of the DE of the ATFS instrument for the five power amplitude values used. Each figure shows the DE for the six sets of measurements corresponding to the indicated power amplitude.

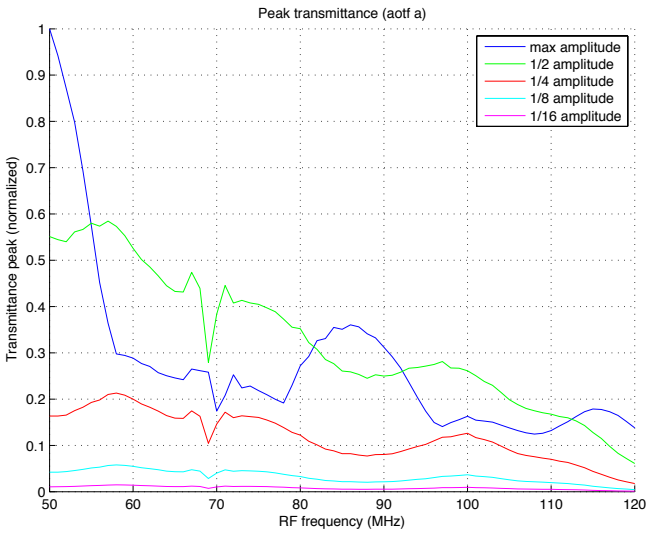

Figure 7.14. Peak transmittance of the ATFS instrument for the first set of measurements.

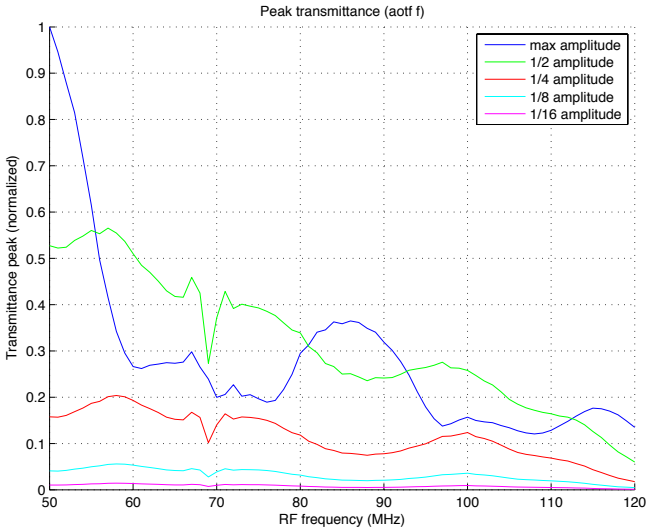

Figure 7.15. Peak transmittance of the ATFS instrument for the last set of measurements.

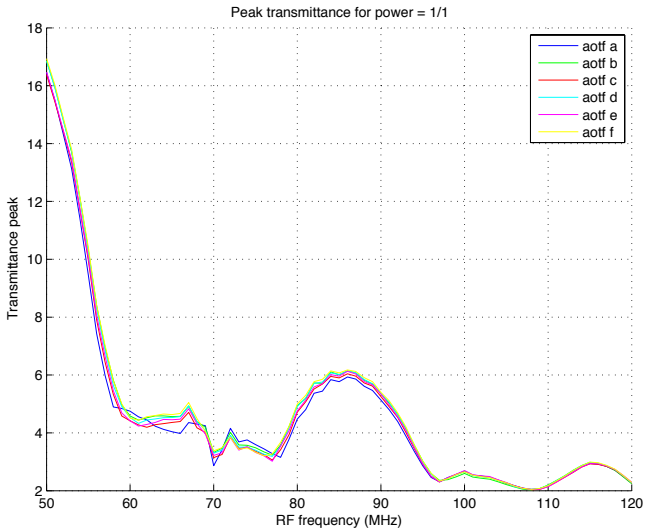

Figure 7.16. Peak transmittance of the ATFS instrument for a driving signal of the maximum amplitude for the six measurement sets.

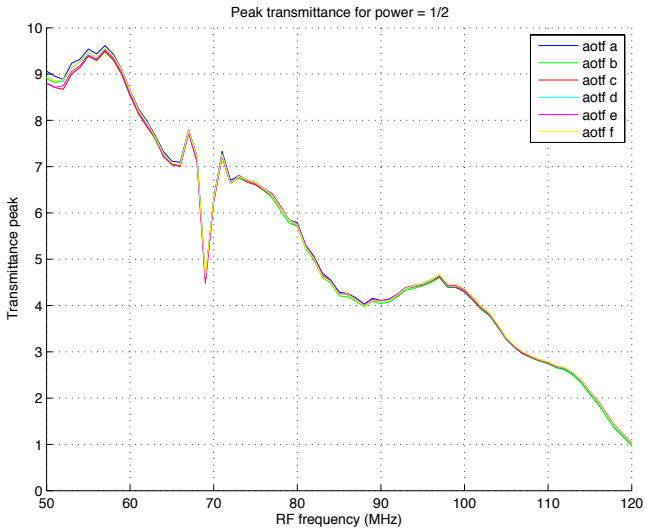

Figure 7.17. Peak transmittance of the system for a driving power of ½ of the maximum amplitude as a function of the driving RF frequency, for the six measurement sets.

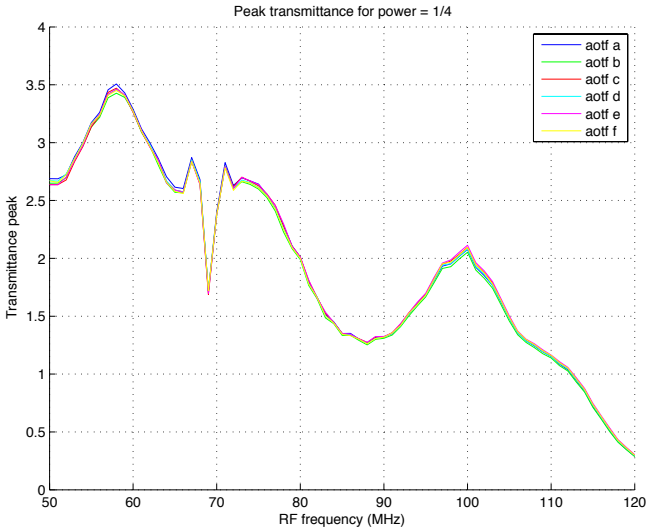

Figure 7.18. Peak transmittance of the system for a driving power of ¼ of the maximum amplitude as a function of the driving RF frequency, for the six measurement sets.

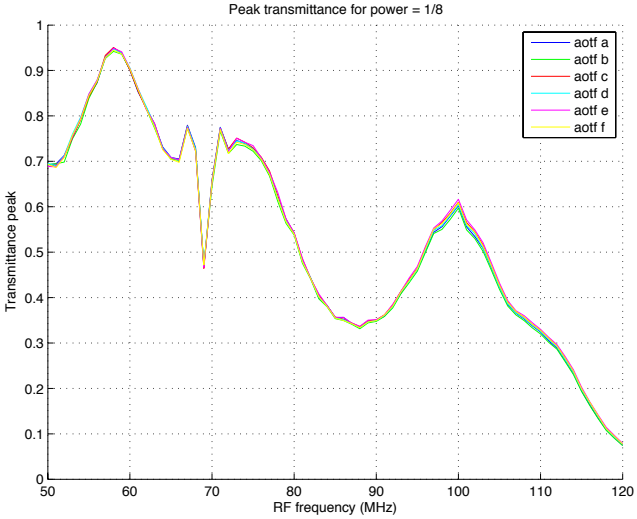

Figure 7.19. Peak transmittance of the system for a driving power of 1/8 of the maximum amplitude as a function of the driving RF frequency, for the six measurement sets.

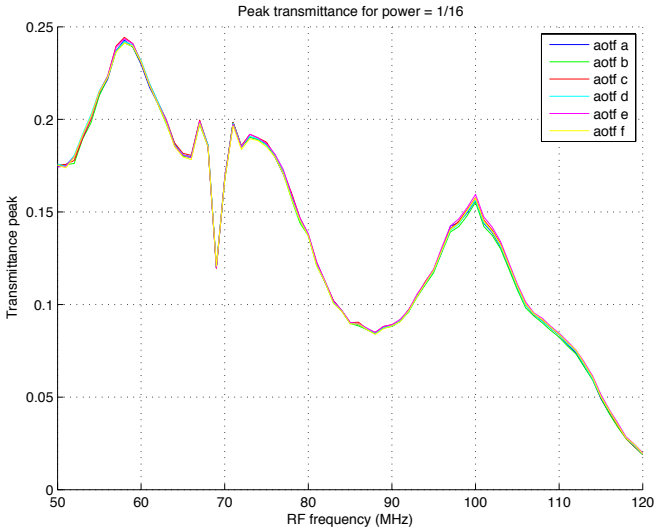

Figure 7.20. Peak transmittance of the system for a driving power of 1/16 of the maximum amplitude as a function of the driving RF frequency, for the six measurement sets.

These figures show that the repeatability of the system is very high, as it can be considered that the small variations between measurements sets to be produced by measurement uncertainness instead of the effect of a long-term drift of the DE performance. Analysing the trend of the maximum DE along the measurements corroborates this fact. This is reflected on Figure 7.21, which represents the evolution of the maximum DE of each set of measurements for the five power amplitudes.

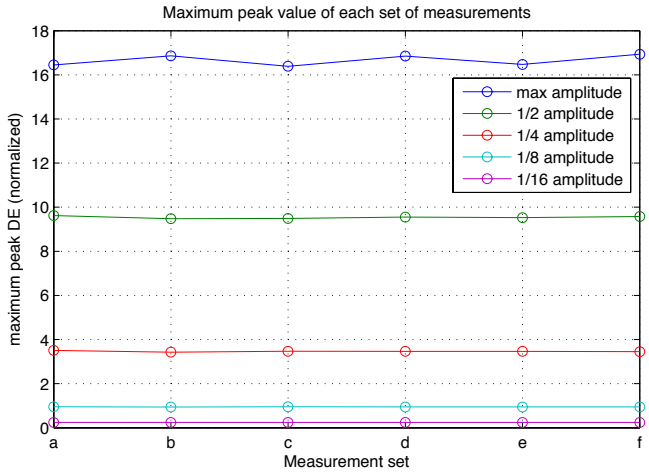

Figure 7.21. Evolution of the maximum DE of the ATFS instrument during the experiment.

As the DE is proportional to the power amplitude, this graph does not clearly show the evolution of the DE for the lowest power amplitude values. For the sake of clarity we have represented on Figure 7.22 the DE normalised to its maximum for each power amplitude value.

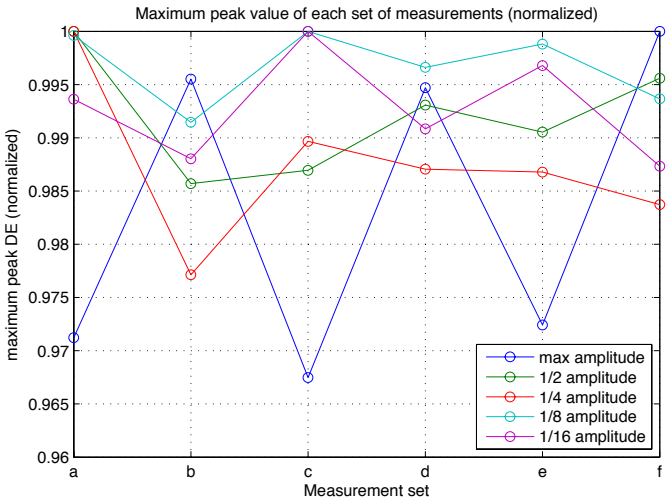

Figure 7.22. Evolution of the maximum DE of the ATFS instrument during the experiment, normalised to the maximum DE of each power amplitude value.

We can infer from the results of this experiment that, although we allowed a warming-up time for all the instruments, this warming time was not enough, as there is a noticeable increment of the DE between the first and the second set of measurements of each day, specially on the maximum amplitude measurements (which corresponds to the first measurements taken for each set). However, if we compare the DE maximum values between different days, we found an arbitrary variation due only to the measurement noise.

Finally, we have also estimated the characteristics of the filtered passband (bandwidth and central wavelength) from these sets of measurements, in order to analyse any temporal variation of these parameters. However, as Figure 7.23 and Figure 7.24 show, there is not any important variation of these values apart from the ones derived from the inherent noise on the measurements.

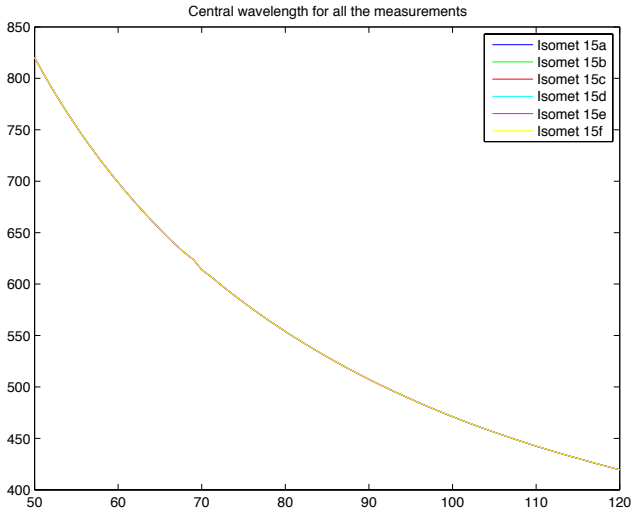

Figure 7.23. Central wavelength of the diffracted band as a function of the RF signal frequency, for the six measurement sets.

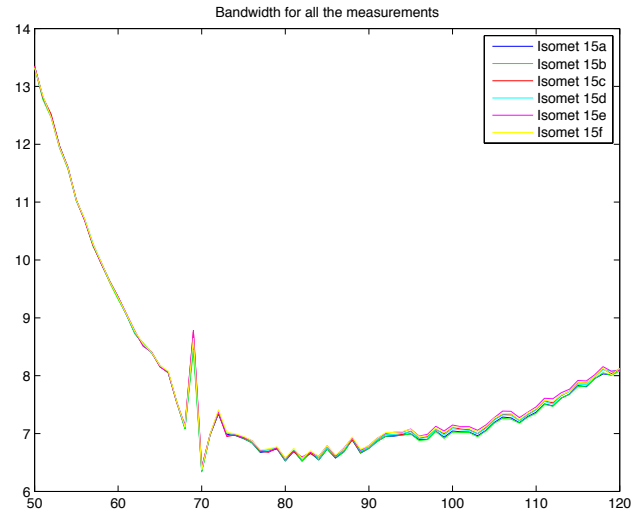

Figure 7.24. bandwidth of the diffracted band as a function of the RF signal frequency, for the six measurement sets.

Given the good long-term repeatability of these measurements, we have used the averaged values of the central wavelength and bandwidth as the calibration curve for the ATFS instrument performance. We have obtain the ATFS response as a polynomial adjustment of these curves. In the case of the RF to wavelength relationship, the response we have approximated is the inverse relationship (wavelength to RF frequency) as this is the curve that the DAC software driver uses to generate the required frequencies for the user wavelength requests.

7.4.2. Short-term repeatability performance

For characterising the short-term performance of the system, we performed four successive sets of measurements without powering off or moving any of the instruments between the measures. Each set of measurements consisted, as in the previous case, of a sequence of pure RF signals at five different power amplitudes (from maximum amplitude to 1/16 of the maximum amplitude), sweeping the frequency from 50 to 120MHz in 1MHz step for each power adjustment.

The first set of measurements started after a 45min warming-up of all the instruments (spectroradiometer, halogen lamp and power amplifier). The whole sequence of measurements (5 power values x 71 RF fre-

quencies) took about 2 hours to finish. Therefore, the complete experiment took about 9 hours to complete. During the whole duration of the experiment the experimental set-up was not moved and no instrument was adjusted or powered off.

We labelled the set of measurements sequentially from "a" to "d". As an example of the obtained results, Figure 7.25 and Figure 7.26 show the results for the first and the last set of measurements, respectively.

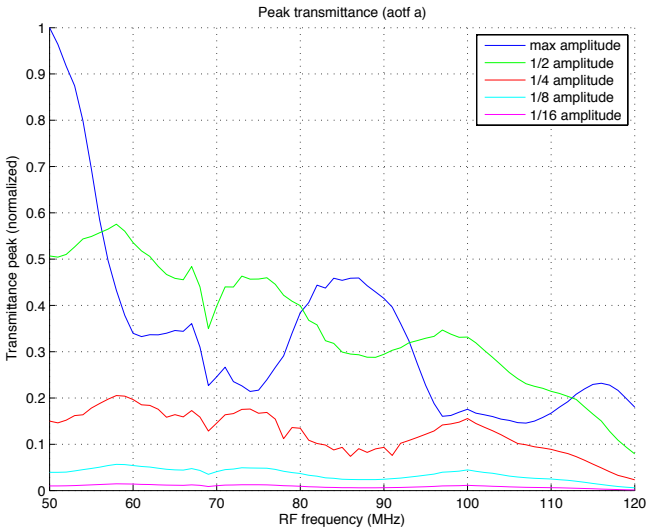

Figure 7.25. Peak transmittance of the system for the first set of measurements (set "a").

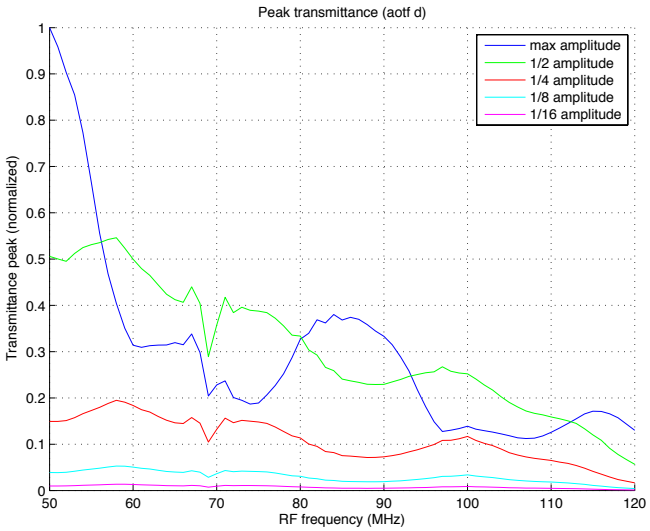

Figure 7.26. Peak transmittance of the system for the last set of measurements (set "d").

As in the case of the previous experiment, we analysed in MATLAB the evolution of the DE for each power amplitude value with the same analytical procedure. Figure 7.27 to Figure 7.31 show the calculated DE values for the four sets of measurements.

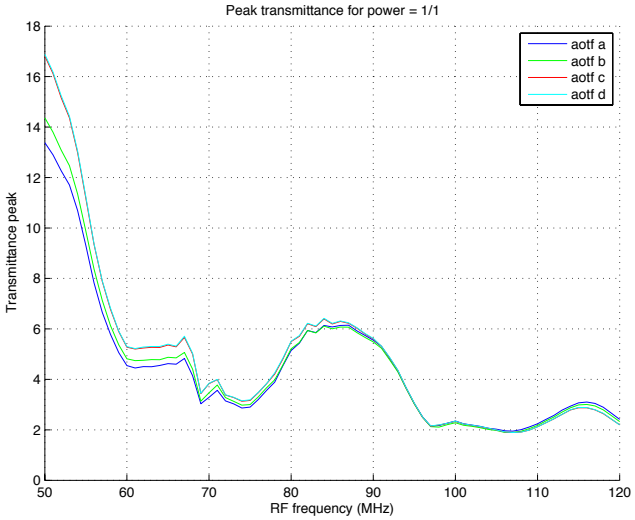

Figure 7.27. Peak transmittance of the ATFS instrument for a driving signal with maximum amplitude for the four measurement sets.

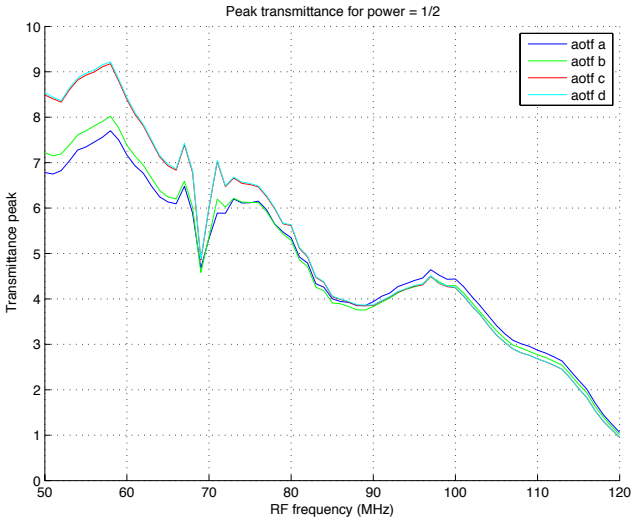

Figure 7.28. Peak transmittance of the ATFS instrument for a driving power of 1/2 of the maximum amplitude for the four measurement sets.

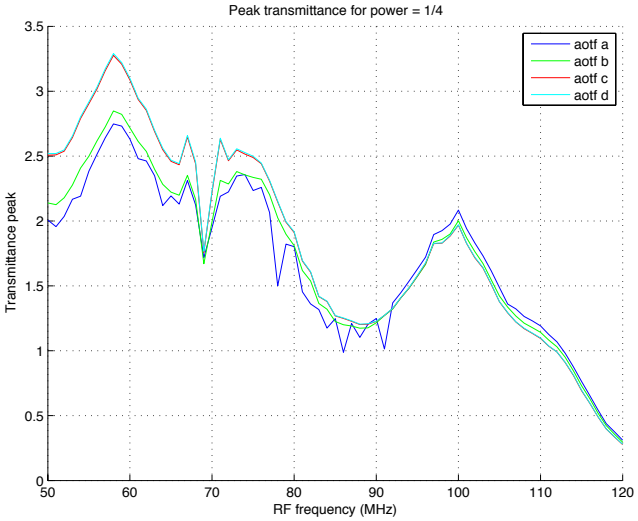

Figure 7.29. Peak transmittance of the ATFS instrument for a driving power of ¼ of the maximum amplitude for the four measurement sets.

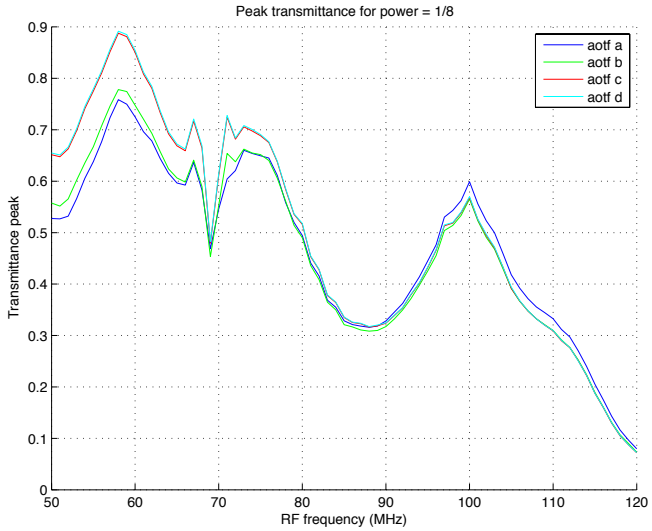

Figure 7.30. Peak transmittance of the ATFS instrument for a driving power of 1/8 of the maximum amplitude for the four measurement sets.

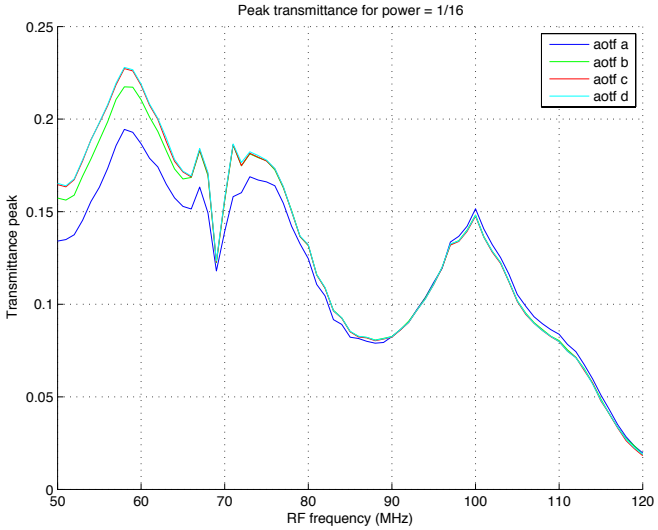

Figure 7.31. Peak transmittance of the ATFS instrument for a driving power of 1/16 of the maximum amplitude for the four measurement sets.

These figures show an apparent small shift in the efficiency of the system for the second and following sets of measurements. In order to better analyse this shift, we have plotted in Figure 7.32 and Figure 7.33 the evolution of the maximum DE during the experiment.

These figures confirm the shift on the maximum DE to greater values after the system has been powered on. However, the system stabilises its response after the third set of measurements (which corresponds to about 4 hours after powering on the system). As the spectroradiometer and the halogen lamp source are proven to be very constant with time [Hatchell, 1999], the cause of the shift is found on the RF power amplifier, which modifies its gain with self-heating, or on the AOTF crystal, which also suffers from a temperature drift [Korablev, 2006; Ohmachi, 1972].

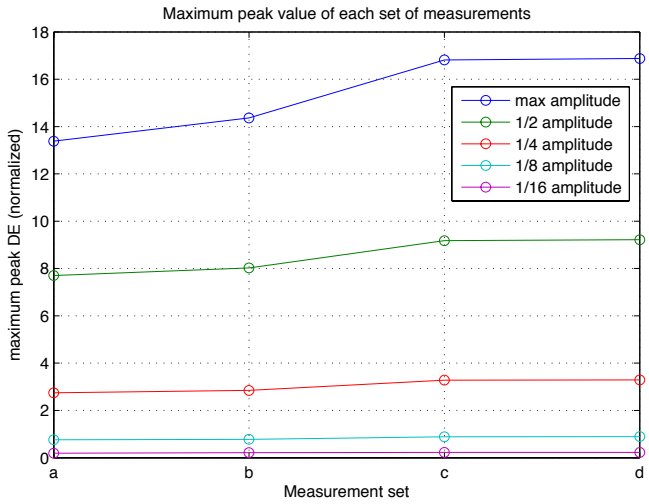

Figure 7.32. Evolution of the maximum DE of the ATFS instrument during the experiment.

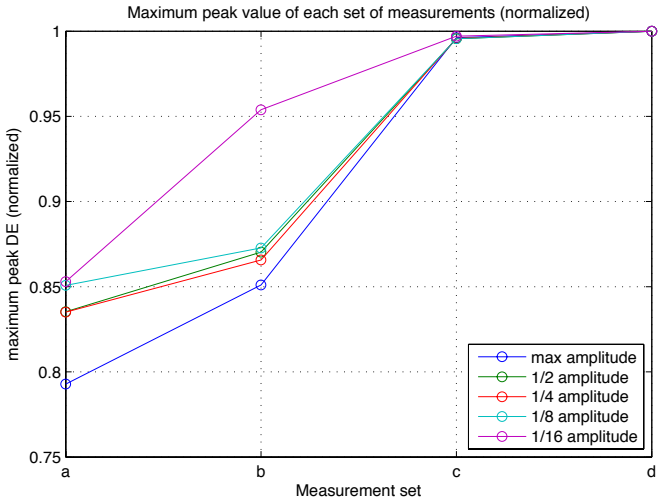

Figure 7.33. Evolution of the maximum DE of the ATFS instrument during the experiment, normalised to the maximum DE for each power amplitude value.

7.5. Thermal behaviour

One of the main reasons of AOTF break is thermal disruption due to an excess of applied power [Goutzoulis, 1994]. Therefore, we performed an experiment to observe the thermal behaviour of the used AOTF, in order to evaluate the power dissipation capabilities of the crystal and estimate the risk of crystal damage. This experiment consisted on applying several RF signals to the crystal at different powers and frequencies, and observing the surface temperature of the crystal with a thermal camera. For each applied signal, we observed the thermal behaviour of the crystal surface until the crystal reached a thermal equilibrium and the subsequent recovery when the signal was powered off.

7.5.1. Experimental set-up

In this experiment we have used the Isomet 614-08 AOTF and the DAC-based driver. The temperature of the crystal surface was registered with a NEC Thermo Tracer TH9100 Pro thermal camera. This camera works over a single band at 8–14 μm, with an IFOV of 22º x 16º and adjustable emissivity operation mode. It ranges from -40ºC up to 120ºC with a sensitivity of 0.1 K.

We applied four different RF signals at the maximum power, corresponding to three single bands at 60, 90 and 120 MHz, and a multiband RF signal composed by 11 components around 90 MHz. For each signal, we

applied the RF power continuously during 45 minutes and after that switched off the power for 15 minutes. During these 60 minutes, the camera automatically took thermal images of the AOTF crystal every minute.

7.5.2. Results

The acquired images of the thermal camera registered the temperature of the crystal surface and the surrounding elements during the experiment. Two control points were measured on each image, one on the crystal and other on the image background, to track the increase of temperature between the crystal and the surrounding ambient.

Figure 7.34 show the evolution of the surface temperature of the crystal for all the signals, after subtracting the background temperature; and Figure 7.35 show the thermal map of the crystal at four different instants of the experiment for the 60MHz signal at maximum power.

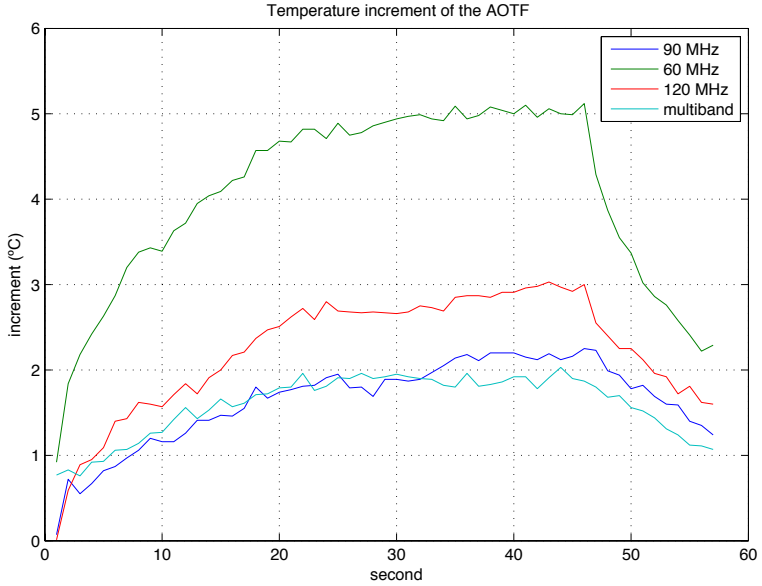

Figure 7.34. Evolution of the AOTF surface temperature when applying different RF signals, after subtracting the background temperature.

From Figure 7.34 we can observe that the frequency that corresponds to the highest DE (60MHz) generates the highest temperature increase (approximately 5ºC). As the power applied by the driver is the same for all the frequencies, we can assume that the power matching of the acoustic transducer is better at the frequencies with higher DE, delivering more acoustic energy to the crystal. Therefore the power dissipated into the crystal and its temperature increase accordingly.

However, none of the observed temperature increments on the crystal surface is high enough to produce any physical rupture effect, as the ambient temperature variation on a normal instrument use can easily exceed these values.

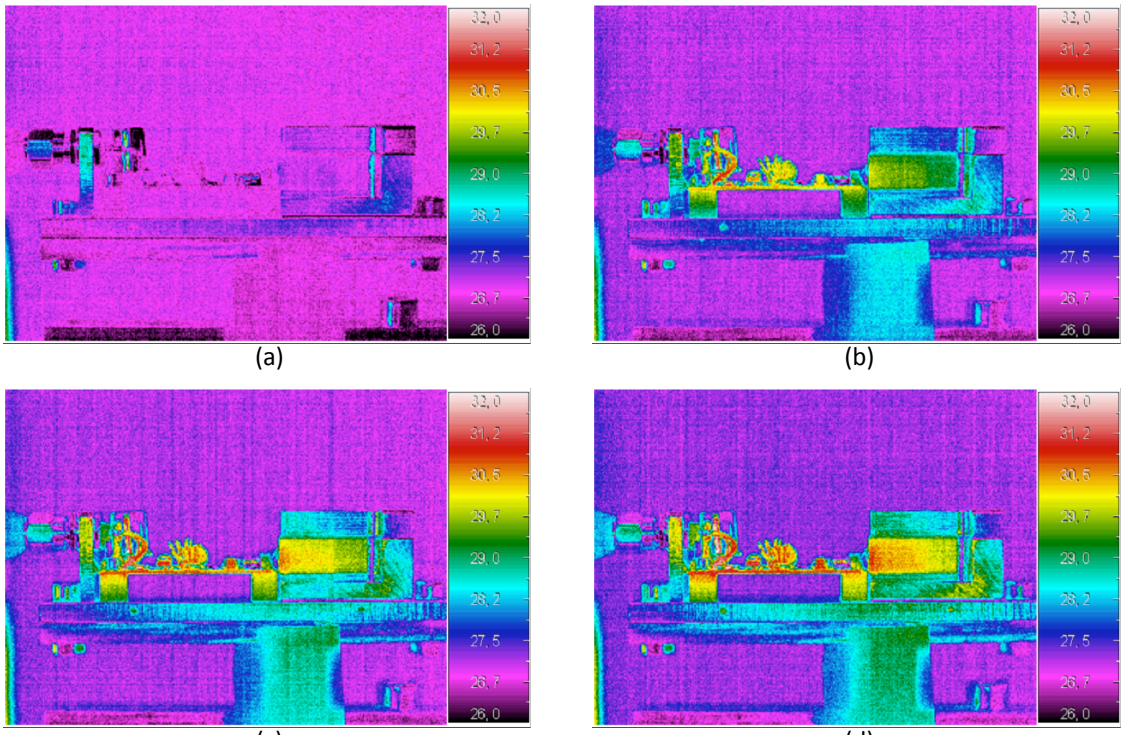

Figure 7.35. Thermal images of the AOTF crystal surface at different instants of the experiment (driven by a 60MHz signal at maximum power), (a): at t=0s; (b): at t=1000s; (c): at t=2000s; at t=3000s.

VIII

ATFS imaging performance

The main objective of this thesis is the implementation of a multispectral imaging system based on an AOTF. In this section, we expose the experimental results obtained with the implemented ATFS instrument on the acquisition of different spectral images.

In concrete, we have evaluated the imaging performance of the Isomet 614-08 AOTF mounted on the optical layout of the ATFS for both RF drivers. The first experiment used the DDS-based driver, and was performed in the context of an ESA Field Study campaign. This experiment consisted on mapping the hyperspectral reflectance and transmittance of a variety of plant leaves. From this hyperspectral data we also estimated the chlorophyll content of the leaves. On the second experiment, we used the DAC-based driver to map the hyperspectral reflectance of a colourful target, in order to evaluate the narrowband, broadband and multiband capabilities of the DAC-driver on imaging applications.

8.1. Imaging performance with the DDS-based driver

We evaluated the imaging performance of the ATFS system driven by the DDS RF generator on a experiment realised during the SEN2FLEX Campaign, held in July 2005 on the Barrax test site (Albacete, Spain) and organised by the Institute for Agronomical Technologies of the Albacete Province (ITAP). The SENtinel-2 and Fluorescence Experiment (SEN2FLEX) is an European Space Agency (ESA) Campaign that combines different activities in support of initiatives related both to fluorescence experiments (AIRFLEX) for observation of solar induced fluorescence signal over multiple vegetation targets and to GMES Sentinel-2 initiative for prototyping of spectral bands, spectral widths, and spatial/temporal resolutions to meet mission requirements[1]. On the context of this campaign, the ATFS was used to map the reflectance and transmittance of some sample leaves taken on the field from the SEN2FLEX studied crops.

The leaf reflectance and transmittance was studied for the minimum bandwidth resolution of the system[2] (10nm), in the bands ranging from 450nm to 800nm in 10nm steps. The images were processed to compensate for dark current and chromatic aberration, and saved as ENVI hyperspectral files. The results have been

[1] More information can be found on the website of the SEN2FLEX campaign, http://www.uv.es/leo/sen2flex

[2] The resolution of the ATFS instrument (given by the AOTF bandwidth) is not constant for all the working range. Therefore, in order to use a constant bandwidth for all the acquired bands, we fixed the bandwidth at the maximum bandwidth for a single band generation (10nm) and used the sweeping mode in order to get a constant bandwidth for all the acquired bands.

incorporated to the ESA Campaign DataBase (CDB)[3]. The measured leaves were collected from the same crop fields used for the other analysis of the SEN2FLEX. Table 8.1 summarises the measured samples and its correspondence code with the other SEN2FLEX studies.

Table 8.1. List of measured samples.

Crop	Site Code	Coordinates (UTM-E,UTM-N)	Images
Alfalfa	A-2	569230 4320809	4 [L1,L2,L3,L4]
garlic	G-1	568812 4320809	2 [L1,L2]
Sugar-beet	SB-1	570483 4321597	4 [L1,L2,L3,L4]
Corn	C-9	596144 4330287	2 [L1,L2]
Sunflower	SF-1	575242 4326009	2 [L1,L2]
Vineyard	V	577713 4323840	2 [L1,L2]
Potato	P1	579830 4323238	2 [L1,L2]
Onion	On-3	576002 4324786	2 [L1,L2]

8.1.1. Experimental set-up

The sample leaves were collected from the study fields and analysed on a dark room of the ITAP premises situated very close to the fields. On this room we mounted an experimental set-up consisting on a leaf holder illuminated by a metal halide lamp, the ATFS pointing to the centre of the leaf holder and a Coolview EM1000 camera attached to the ATFS output. Depending on the measured characteristic of the leaf (transmittance or reflectance), the light was positioned in different locations, while the other parts of the set-up were fixed for all the experiment. Figure 8.1 shows a diagram of the experimental set-up for the reflectance measurements where leaves were positioned on the holder over a completely black panel (with a measured reflectance lower than 2% on the working range of the system). For the transmittance measurements, the light was moved to the position shown on Figure 8.2, where illuminated a white Spectralon panel which provided a diffuse back lighting to the leaf holder. On these measurements, the leaves were standing between two transparent crystal layers. Figure 8.3 shows two pictures of the experimental set up for both measurements.

We marked the correct positions of the lamp on the table, in order to get repetitive measurements when moving back and forth the lamp between the reflectance and transmittance positions.

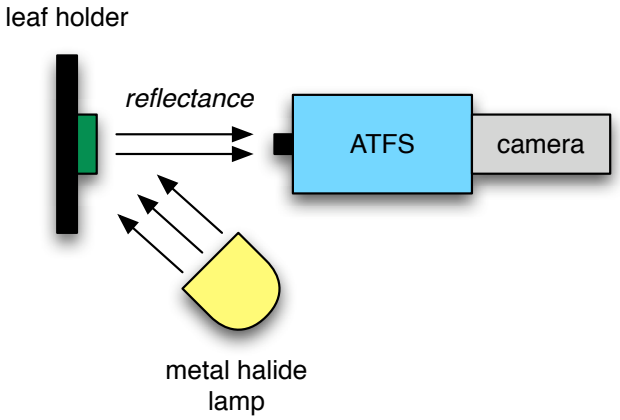

Figure 8.1. Scheme of the experimental set-up for the reflectance measurement.

[3] The CDB is a generic database for earth observation data generated by ESA Campaigns [Vik et al., 2005]. The CDB is available online at http://nadir.nilu.no/cdb/ for registered users.

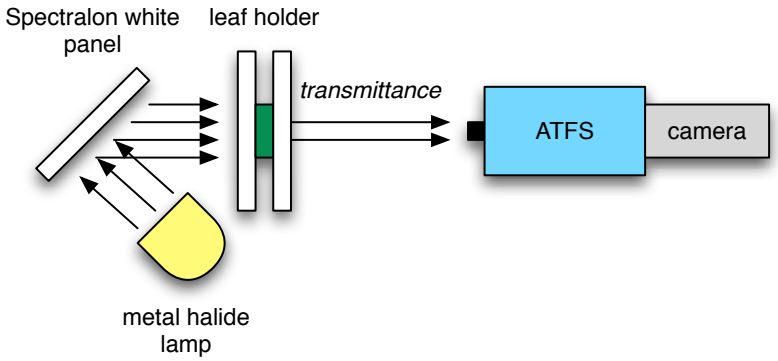

Figure 8.2. Scheme of the experimental set-up for the transmittance measurement.

Figure 8.3. Picture of the experimental set up for the measurements of the reflectance (*left*) and the transmittance (*right*).

8.1.2. Measurement procedure

We defined a procedure for optimising the measure of the reflectance and transmittance of the leaves. This procedure was designed to allow a measurement of all the required data in a fast, reliable, and repetitive way. The procedure comprises two separate steps: the experimental acquisition of the leaf data, and the subsequent data processing and hypercube image generation.

Reflectance and transmittance are estimated as a ratio between the leaf reflected / transmitted radiance and the radiance of the light source (white reference), respectively. The radiance of the light source is estimated as the reflected radiance of the light source on a spectrally flat surface with an estimated reflectance of 100%. In our case, we use a calibrated Spectralon panel. The light source radiance is measured in both reflectance and transmittance configuration once, and stored as the white reference hypercube.

8.1.2.1. Image acquisition

The image acquisition was carried out with the ATFS GUI application described on Section 4.5.3. We applied the same procedure to the sample leaves in a sequential way. That is, we took a leaf, measured all its parameters and then start again with the following leaf. The procedure for each leaf is the following:

1. Before starting the acquisition of each individual leaf, we register the stray light and dark current (SL + DC) and the white reference (WR) for the reflectance and transmittance datasets:
   1.1. Reflectance mode: we place the lamp pointing the leaf holder and we locate the Spectralon panel on the position of the holder. In this configuration, we measure:
      1.1.1. The WR dataset: the application takes an image of the WR at each band with short exposure time and calculates the optimal exposure times in order to maximise the dynamic range of the camera. Then, the application acquires the reflectance of the Spectralon panel for all the bands with the estimated optimal times. As a result, we obtain the WR raw data

hypercube and a vector with the optimal exposure times for the transmittance measurements.

1.1.2. The SL + DC dataset: the application estimates the contribution of the SL + DC on the image by switching off the RF generator and acquiring two images with different exposure times. The result of this step is a SL + DC dataset for the reflectance images.

1.2. Transmittance mode: the light is pointed to the Spectralon panel, which is located behind the leaf holder. The holder is fitted with the two crystal panels without any leaf. The panel reflects the light, which passes through the transparent crystals of the leaf holder and reaches the ATFS instrument. In this configuration, we measure:

1.2.1. The WR dataset: the application takes an image of the WR at each band with short exposure time and calculates the optimal exposure times in order to maximize the dynamic range of the camera. Then, the application acquires the reflectance of the Spectralon panel for all the bands with the estimated optimal times. As a result, we obtain the WR raw data hypercube and a vector with the optimal exposure times for the transmittance measurements.

1.2.2. The SL + DC dataset: the application estimates the contribution of the SL + DC on the image by switching off the RF generator and acquiring two images with different exposure times. The result of this step is a SL + DC dataset for the transmittance images.

2. For each sample leaf, we acquire its reflectance and transmittance for all the bands with the following procedure:

2.1. Optimisation of the dynamic range of the sensor: the expected reflectance and transmittance values of the leaves are know, because they follow a common pattern for all the vegetation tissues [Gates, 1965]. As these values are very low in some spectral regions, we optimise the dynamic range of the system by increasing the exposure time for those bands with the DRA feature of the ATFS application.

2.2. Reflectance measurement: we dispose the leaf on a dark panel and put both elements on the holder and we locate the light source at the reflectance mode position (pointing to the holder from one side). We acquire sequentially the reflected radiance of the leaf for all the bands using the optimal exposure times estimated in step 1.1.1, for both adaxial and abaxial sides of the leaf. As a result we get two raw data reflectance hypercubes.

2.3. Transmittance measurement: we remove the dark panel from the holder and we put back the leaf on the holder, fitted between the two transparent crystals. We locate the Spectralon panel at the back of the holder and move the light source to the transmittance mode location. In this position, we acquire sequentially the transmitted radiance of the leaf for all the bands using the optimal exposure times estimated in step 1.2.1, for both adaxial and abaxial sides of the leaf. As a result we get two raw data transmittance hypercubes.

8.1.2.2. Image processing

The images obtained following the above-mentioned procedure were processed in MATLAB in order to obtain the absolute reflectance and transmittance values of the analysed leaves.

All the raw images were first corrected in terms of SL+DC and then corrected in terms of chromatic aberration. The SL+DC is estimated from the corresponding reflectance / transmittance SL+DC datasets following the procedure described in Chapter 4. We compensated the CA by applying a horizontal shift to each band, whose value was obtained from a look-up table (LUT). The LUT was generated on a previous calibration experiment. The values of the LUT, as well as the MATLAB functions used for correcting the SL+DC and CA of the images are listed on the attached CD.

Finally, we calculated the reflectance and the transmittance of each leaf from the corrected images using Eq. 4.10. For each leaf we obtained four hypercube images: reflectance of the adaxial side, reflectance of the abaxial side, transmittance of the adaxial side, and transmittance of the abaxial side.

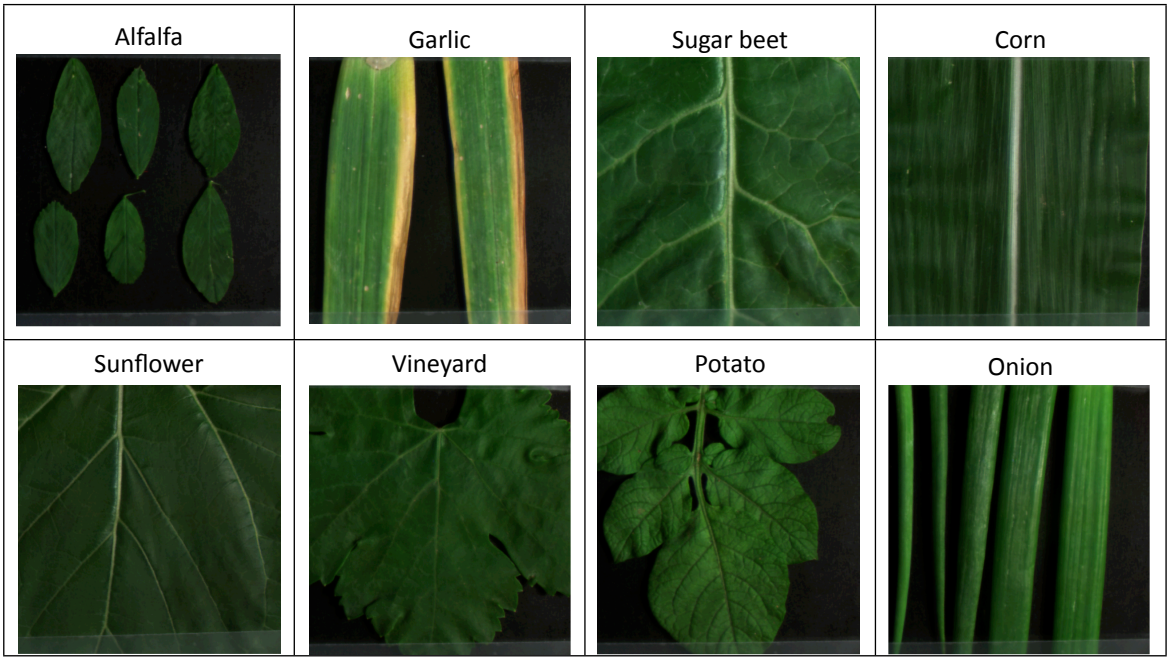

Figure 8.4. RGB Images of the acquired leaves (adaxial reflectance)

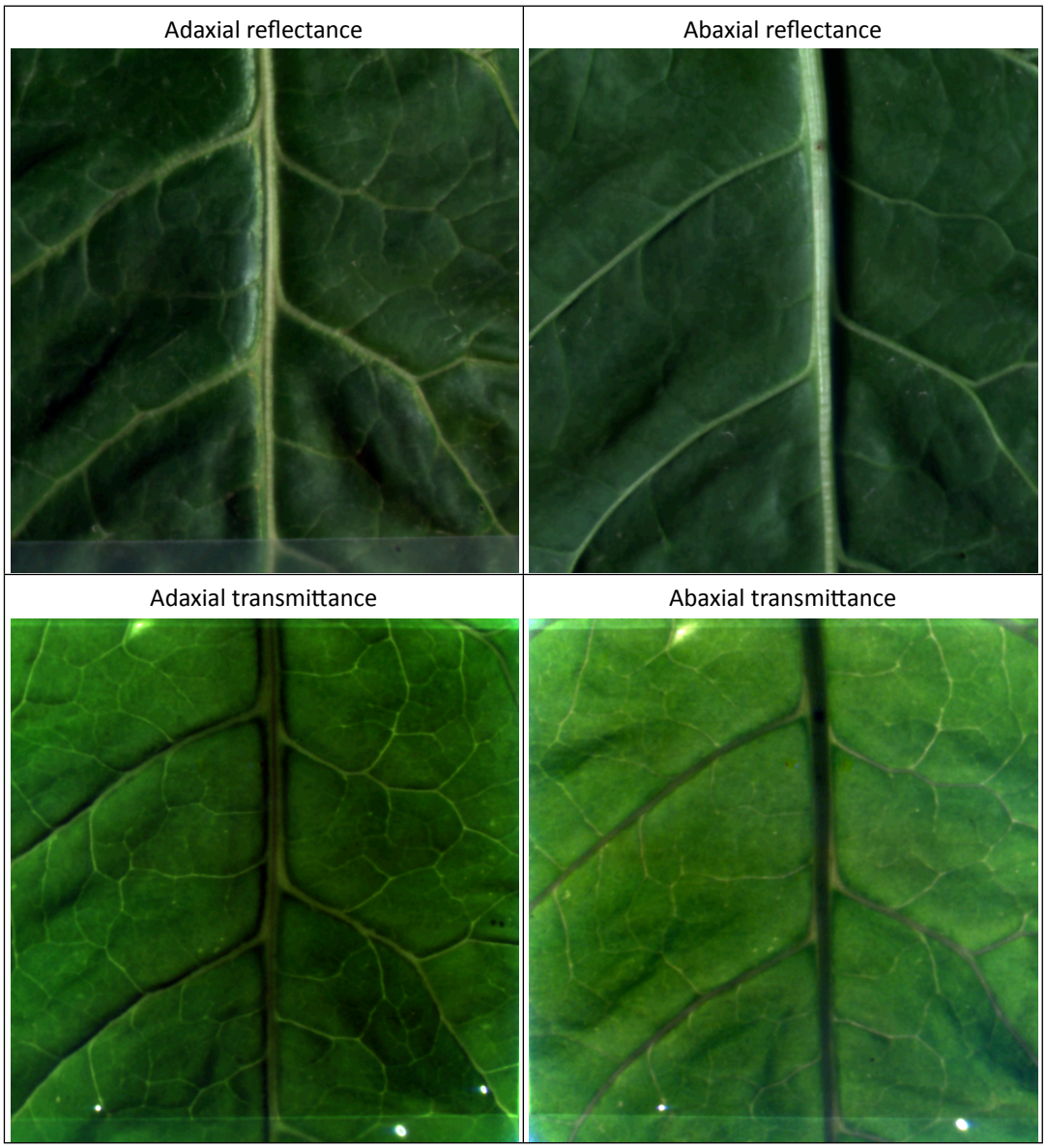

Figure 8.5. RGB images of the Sugar beet leaf L2 on the four measurement configurations.

8.1.3. Results

The resulting hyperspectral images (hypercubes) from each leaf were all submitted to the ESA CDB database, which can be consulted online by registered users. In total, 180 hypercubes were submitted, corresponding to the four measuring configurations –adaxial reflectance, abaxial reflectance, adaxial transmittance and abaxial transmittance– for each one of the 20 samples leaves listed on Table 8.1. The hypercubes are in ENVI format (header file '*.hdr' and a file data '*.bsq'). In the header file are included the exposure times of the acquired images in "Band names" metadata.

Figure 8.4 shows an example of each type of acquired leaves. These figures correspond to the reconstructed RGB images for the adaxial reflectance of the leaves. The RGB images were generated from the spectral bands 650nm (red), 550nm (green), and 470nm (blue).

Figure 8.5 shows the RGB reconstructed images corresponding to the four measurements of one of the Sugar beet leaves. Figure 8.6 details the images corresponding to the spectral bands used on the RGB composition of the reflectance adaxial image (650, 550 and 470nm).

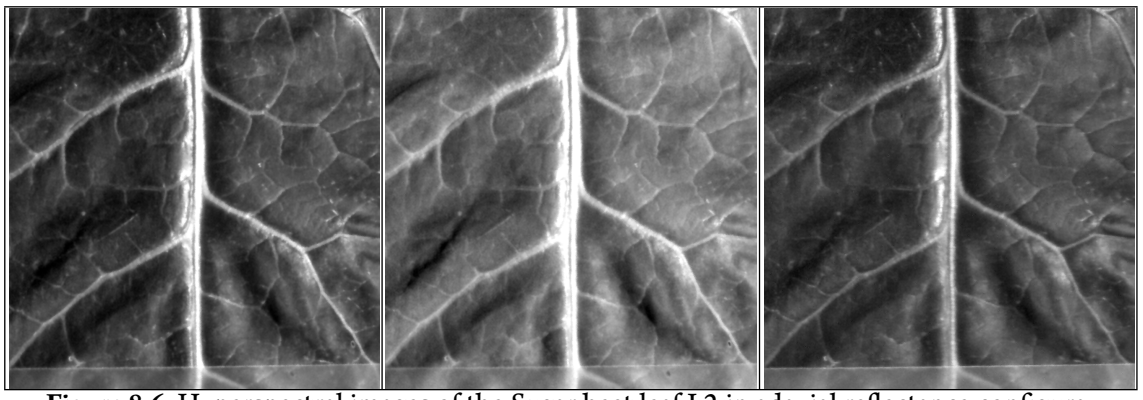

Figure 8.6. Hyperspectral images of the Sugar beet leaf L2 in adaxial reflectance configuration for the bands 650nm (*left*), 550nm (*centre*), and 470nm (*right*).

As the acquired images are hyperspectral, we can plot the spectral dimension of any pixel. For example, in Figure 8.7 we have represented the spectral reflectance of the Sugar beet leaf by integrating the central area of the image. We have compared this reflectance value with the reflectance measured with the ASD FieldSpec FR spectroradiometer over the same area (Figure 8.8 shows the area integrated by the ASD instrument). Both measurements are very similar, showing the good spectral performance of the ATFS instrument. However, if we observe the standard deviation of the reflectance measurement we can realise the variability of the reflectance inside the measure area, due to the inherent variation of the reflectance over the leaf surface. This variability can be appreciated by a spectral imaging system like the ATFS instrument but not by a point spectrometer like the ASD Fieldspec FR.

Another example of the spectral performance of the ATFS instrument is shown on Figure 8.9. In this figure we represent the reflectance, transmittance and estimated absorption of the Sugar beet leaf as a function of the wavelength. These values are calculated as the average of the central area of the image. The leaf absorption is estimated as the portion of the light in each spectral band which is not reflected neither transmitted by the leaf:

$$A(\lambda) = 1 - R(\lambda) - T(\lambda) \qquad \textbf{(Eq. 8.1)}$$

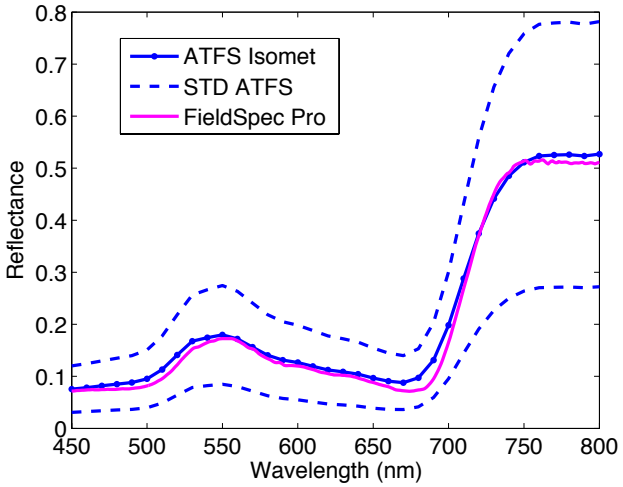

Figure 8.7. Spectral reflectance of the Sugar beet leaf (mean value and standard deviation), measured with the ATFS instrument and the ASD Fieldspec FR spectroradiometer.

Figure 8.8. Field of view of the ASD instrument on the spectral measurement of Figure 8-

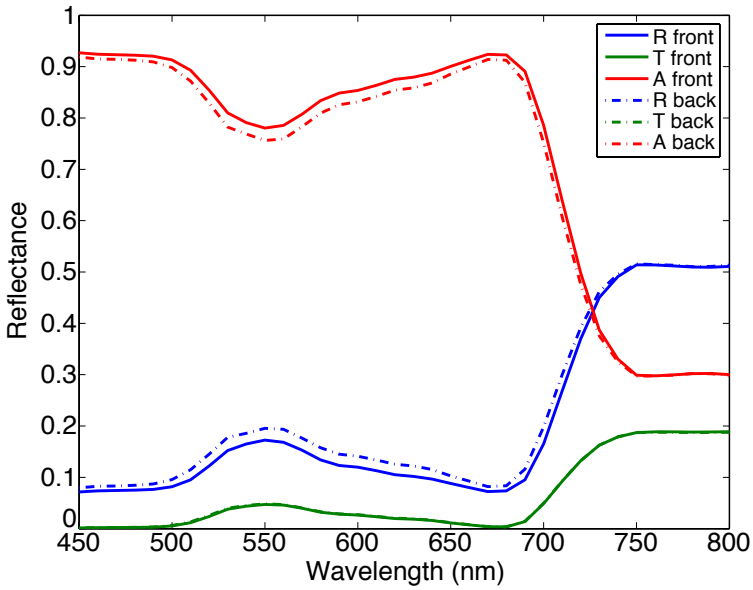

Figure 8.9. Spectral reflectance (R), transmittance (T) and estimated absorption (A), measured at both sides of the Sugar beet leaf.

From the reflectance hypercube we have estimated the chlorophyll content of the leaves. We use the normalised differences vegetation index (NDVI) proposed by [Blackburn, 1998]:

$$NDVI = \frac{R_{800} - R_{680}}{R_{800} + R_{680}} \qquad \textbf{(Eq. 8.2)}$$

where R_{800} and R_{680} are the reflectance images of the leaf at 800 nm and 680 nm, respectively. Figure 8.10 shows the chlorophyll map content of a sunflower (*Helianthus annuus*) leaf using this index (taken with an early prototype of the ATFS instrument [Vila, 2005]). The leaf was previously treated with herbicide so that it shows a large variation of the chlorophyll content distribution, due to the uneven distribution of the herbicide damage.

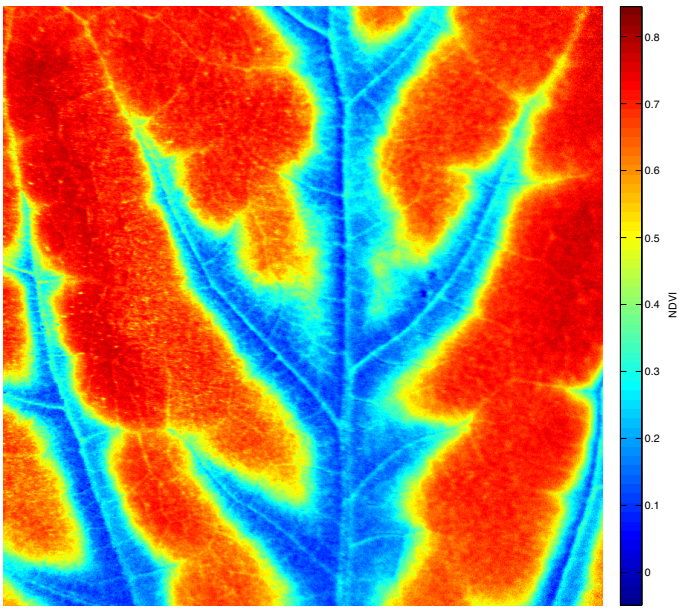

Figure 8.10. Chlorophyll content estimate for a sunflower (*Helianthus annuus*) leaf treated with herbicide, using the NDVI index.

8.2. Imaging performance with the DAC-based driver

We have done an experiment to evaluate the spectral and spatial performance of the ATFS system when using the DAC-based driver. The experiment consisted on imaging two colourful targets with different driving configurations (singleband, broadband, and multiband), and a black and white spatial resolution pattern.

8.2.1. Experimental setup

The system was configured for the experiment on the following way: the ATFS system was equipped with a Schneider Xenoplan 1.4/23 input optics and a scientific grade Retiga EX monochrome camera from QImaging. The AOTF was driven by the output signal of the DAC board amplified through a RFPA 2W power amplifier. A square 10" Spectralon panel was used as a spectrally flat (white) reference for the reflectance conversion of the acquired images. The targets were illuminated by a 50W halogen lamp powered by a 12V 20A stabilised DC power supply.

The targets used on this experiment are shown on Figure 8.11 (the 'calendar' target) and Figure 8.12 (the 'colour sheets' target). We chose these targets because of their broad range of colours and the presence of different spatial patterns. These targets allow us to evaluate on the same images the spectral and spatial performance of the system. Additionally, the 'colour sheets' target is made from plain colour sheets that can be analysed with a high performance point spectrometer. In our experiment, we have analysed the individual colour sheets with the ASD FieldSpec FR spectroradiometer, in order to compare with the spectral performance of the ATFS instrument.

Finally a resolution pattern was also imaged in order to evaluate the spatial resolution of the system. The pattern was focussed on different wavelengths and acquired in all the spectral range for each focussing adjustment. The resolution pattern used was a printed version of the image shown in Figure 8.13.

All the image acquisition was automated in MATLAB with an hyperspectral acquisition toolbox specifically developed for the control of the ATFS instrument. The processing was also performed on MATLAB with another toolbox developed for the hyperspectral image analysis. The content of these toolboxes is described on the Chapter 4.

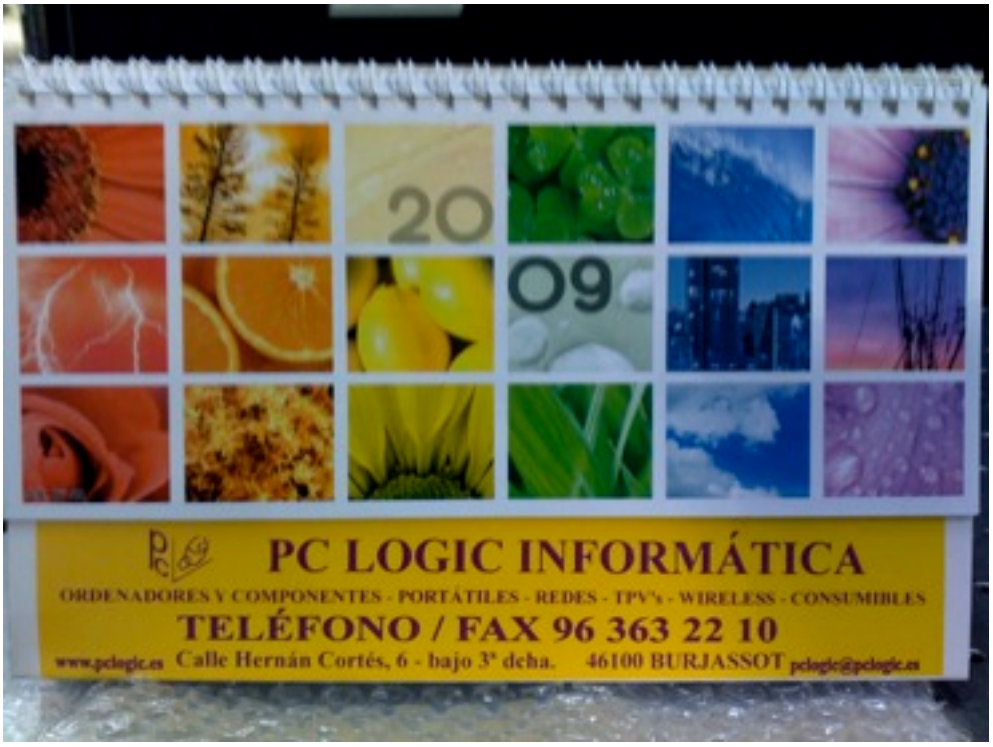

Figure 8.11. Image of the 'calendar' target used on the experimental setup.

Figure 8.12. Image of the 'colour sheets' target used on the experimental setup.

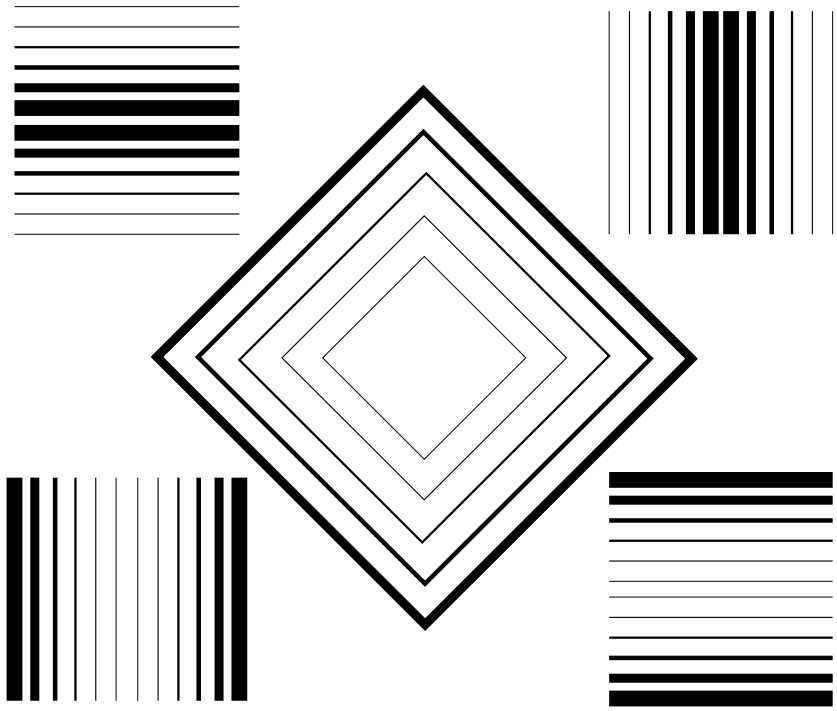

Figure 8.13. Resolution pattern used for evaluating the spatial resolution of the ATFS sys-

The hyperspectral acquisition toolbox configures and acquires images with the Retiga QImaging camera, making use of the low-level camera driver supplied by the Imaging Acquisition Toolbox. At the same time, the toolbox initialises the DAC board and sends the waveforms required to drive the AOTF as required by the experiment. Finally, the toolbox stores, retrieves and processes the hyperspectral images. The acquired images are converted into an ENVI format hypercube before being processed.

8.2.2. Measurement procedure

In this experiment we measure the reflectance of the targets for different driving configurations of the DAC-based generator. The reflectance is estimated as the ratio between the radiance reflected by the target and the one reflected by the white reference.

As stated on the previous experiment, the acquired images comprise not only the contribution of the target reflectance but also the contribution of the dark current of the sensor and the stray light that passes through the ATFS. We compensate this effect by estimating their values from the acquired images and subtracting them to the resulting hypercube.

8.2.2.1. Image acquisition

We took two sets of acquisitions, the first one using single band signals (for the calendar and the colour sheets targets) and the second one using multiband signals with different spectral steps (just for the colour sheets target). Each series of measurements consisted on acquiring the calendar target and the white reference with exactly the same geometry and using the same driving signals. The exposure time was optimised for each single acquisition. For each series, two additional images of each target were acquired in order to estimate the DC and SL contribution to the images (see section 4.2.1.2.). Those images were acquired with the DAC driver turned off for an exposure time of 1 and 10 seconds.

On the first set of measurements, we acquired two hyperspectral images of the target and the WR, composed by 31 bands from 450nm to 750nm in 10nm steps. The AOTF was drove by single RF bands, whose frequencies were calculated from a 6^{th} order polynomial approximation to the RF to wavelength relationship

of the ATFS. This polynomial was obtained from the ATFS calibration detailed on Chapter 7 (long-term repeatability measurements). The values of the polynomial can be found on the adjustment function listed on the attached CD.

On the second set of measurements, we drove the AOTF with different multiband signals, whose details are listed on Table 8.2. The same signals were used to drive the target and the WR.

Table 8.2. Multiband configurations used on the experiment.

Number of bands	Band separation	Initial wavelength	Final wavelength
3	10nm	590nm	610nm
	50nm	550nm	650nm
	100nm	500nm	700nm
5	10nm	580nm	620nm
	25nm	550nm	650nm
	50nm	500nm	700nm
7	10nm	570nm	630nm
	25nm	525nm	675nm
	50nm	450nm	750nm
9	10nm	560nm	640nm
	25nm	500nm	700nm

Finally, we took another set of acquisitions of the resolution pattern. We focused the ATFS system when imaging the pattern at the bands 450nm, 600nm, and 750nm, corresponding to the low end, middle, and high end of the working range. For each focusing adjustment, we acquired the image of the target at the bands from 450nm to 750nm in 50nm steps.

8.2.2.2. Image Processing

The images were processed in order to obtain the absolute reflectance of the target. The processing was done with the MATLAB hyperspectral acquisition toolbox described in Chapter 4.

For all the experiments, the images were corrected in terms of SL+DC. On the first and third experiment, the images were shifted to correct the chromatic aberration. However, this correction could not be applied to the experiment of the multiband imaging.

Finally, the hyperspectral reflectance images were obtained by dividing band by band the corrected target images by the corrected WR images.

8.2.3. Results

In this section we present the images acquired during the experiments carried out with the DAC-based generator, after being processed in MATLAB.

8.2.3.1. Single band performance

In the first experiment, we imaged with the ATFS instrument the 'calendar' and the 'colour sheets' targets in single band configuration, acquiring the reflectance images for the spectral bands from 450nm to 750nm in 10nm steps. The images were processed to remove the DC and SL of the images, correct the chromatic aberration and finally estimate the target reflectance by using a white reference image. Figure 8.14 shows the resulting image of the calendar as an RGB image. This image has been generated from the reflectance images at the bands 460nm (blue), 550nm (green), and 650nm (red), which are shown on Figure 8.15.

Figure 8.14. RGB image of the calendar target taken with the ATFS system. Circled areas show the areas used to plot the spectral reflectance.

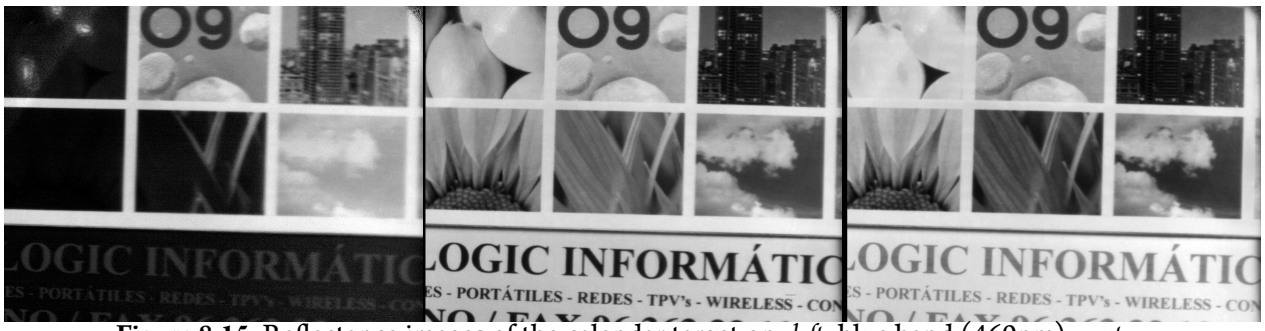

Figure 8.15. Reflectance images of the calendar target on: *left*: blue band (460nm), *centre*: green band (550nm), *right*: red band (650nm).

As we have acquired the complete hypercube of the calendar image, we can represent the spectral information for each spatial position of the image. Figure 8.14 shows five selected groups of pixels, corresponding to similar areas on the calendar, and Figure 8.16 shows the calculated reflectance for these selected pixels in all the spectral range.

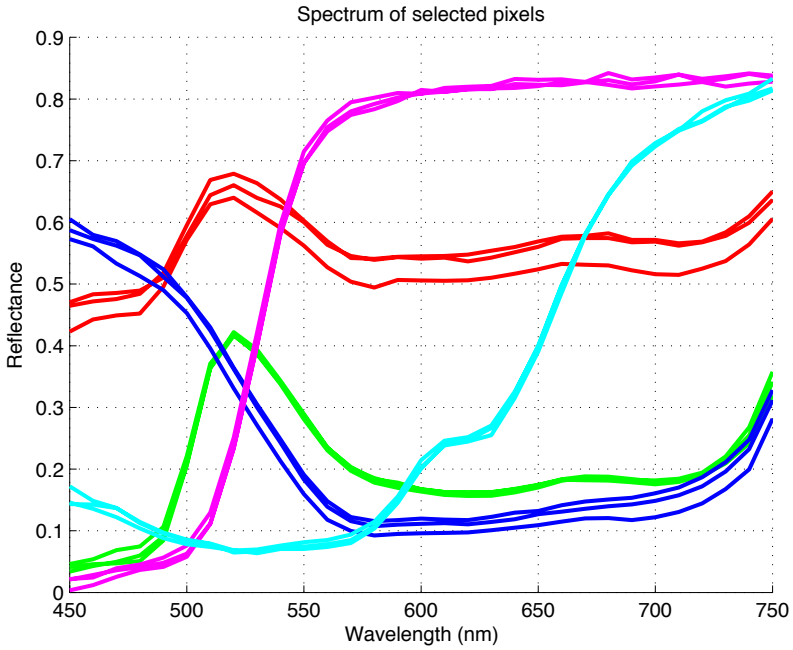

Figure 8.16. Reflectance spectra of the pixels marked on Figure 8.14.

We have performed the same processing to the images in the 'colour sheets' target. Figure 8.17 shows the RGB image of the target, generated from the reflectance bands 460nm (blue), 550nm (green), and 650nm (red). These bands are shown individually on Figure 8.18.

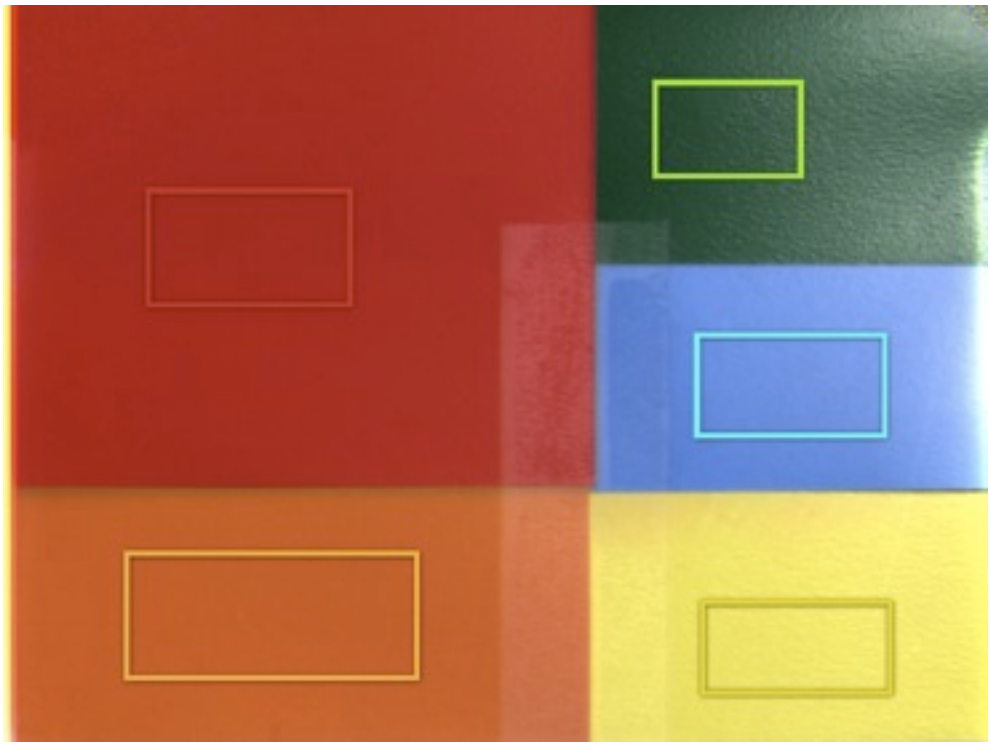

Figure 8.17. RGB image of the colour sheets target taken with the ATFS system. The overlapped rectangles mark the areas used to integrate the spectral reflectance of each colour.

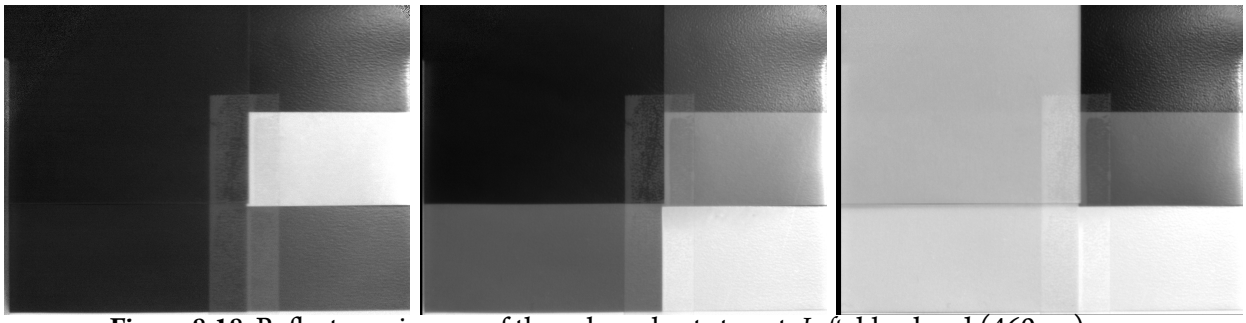

Figure 8.18. Reflectance images of the colour sheets target. *Left*: blue band (460nm), *centre*: green band (550nm), *right*: red band (650nm).

As the target is composed by areas of plain colours (plastic sheets), we have performed a spatial averaging for each area in order to obtain the reflectance spectra from each single sheet. We have compared these reflectance spectra with the one obtained by the ASD FieldSpec FR spectroradiometer. Figure 8.17 shows the areas taken into account in order to calculate the spectra for each colour. The reflectance has been calculated as the average value of the rectangle on each spectral band. Figure 8.19 shows the calculated reflectance spectra from the ATFS data. Also shown in this figure is the reflectance spectra of the same sheets acquired with the FieldSpec FR spectroradiometer. The spectra are very similar between both instruments for all the sheets.

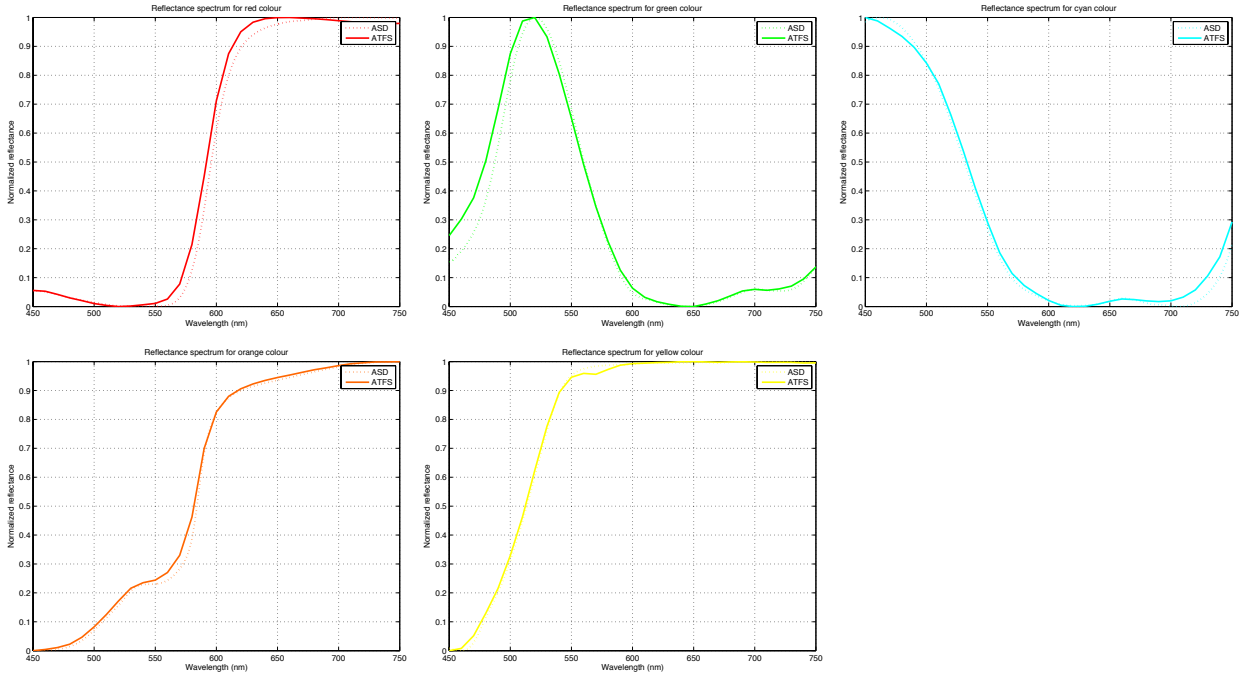

Figure 8.19. Reflectance spectra of the selected area for each colour, measured with the ATFS instrument (*continuous line*) and the ASD FieldSpec FR spectroradiometer (*dashed line*).

8.2.3.2. Multiband performance

For the colour sheets pattern we also evaluated the response of the system for multiband signals. We drove the DAC-based generator with the multiband signals detailed in Table 8.2, and we acquired the target for each signal. For each multiband configuration, we also acquired an image from the white reference, in order to calculate the target reflectance. However, the chromatic aberration cannot be corrected in these images because they are composed by the contribution of different diffracted wavelengths, having each wavelength component a different shift. The results are presented as follows.

3-bands signal

We drove the AOTF with 3 bands centred at 600nm with different wavelength separation (10nm, 50nm and 100nm). For a 10nm separation, the ATFS system acts as a broad passband filter with an approximate bandwidth of 30nm, due to the overlapping of the individual signal bandwidths. Figure 8.20 shows the reflectance of the colour sheets target acquired with this configuration. Figure 8.21 simulates the equivalent estimated reflectance obtained by adding the reflectance values of the same individual bands, taken with the single band configuration on the previous experiment. The estimated reflectance value is divided by 3 in order to keep the reflectance values within the range [0-1]. The integration time of the multiband image was very close to the sum of the integration times o the three individual band images.

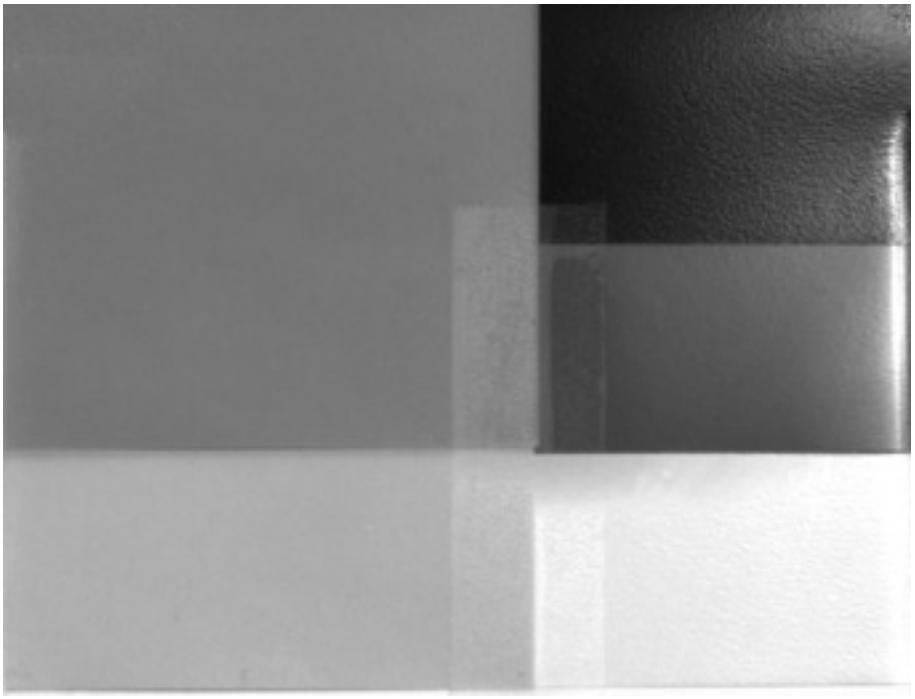

Figure 8.20. Reflectance of the colour sheets target for a multiband driving signal with 3 bands (590nm, 600nm, and 610nm).

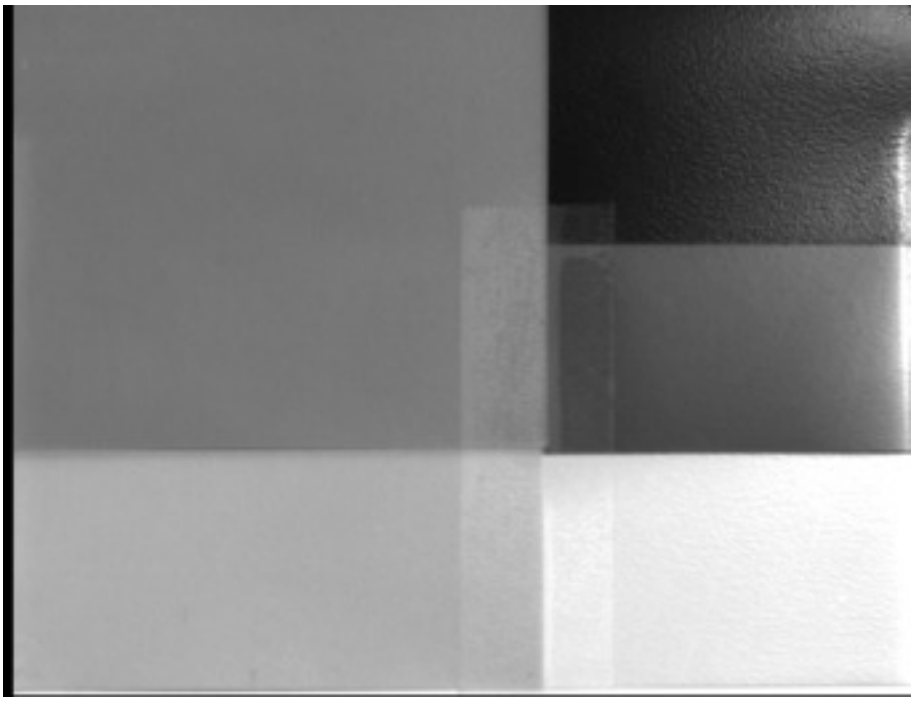

Figure 8.21. Estimated reflectance of the colour sheets target as the linear contribution of 3 bands (590nm, 600nm, and 610nm).

Because of the linearity of the AOTF diffraction, both images are very similar. In fact, the histograms of the images show a close correspondence (Figure 8.22). However, the image quality of the multiband image is slightly worse than the quality of the simulated image.

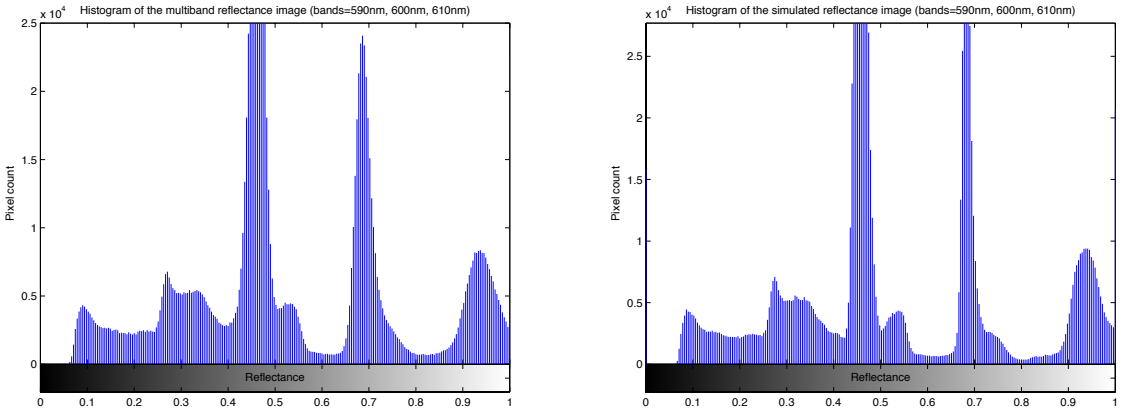

Figure 8.22. *Left*: histogram of the multiband reflectance image with the bands 590nm, 600nm, and 610nm. *Right*: histogram of its equivalent estimated reflectance image.

However, as we further separate the band wavelengths, the differences on the AOTF diffraction efficiency and light radiance intensity for each wavelength causes a divergence between the acquired reflectance and the simulated one. This fact can be seen on the Figure 8.23, corresponding to a multiband configuration with 3 bands centred at 600nm and separated 100nm, and its equivalent simulated reflectance. The histograms of these images, represented on Figure 8.24, show more clearly this divergence.

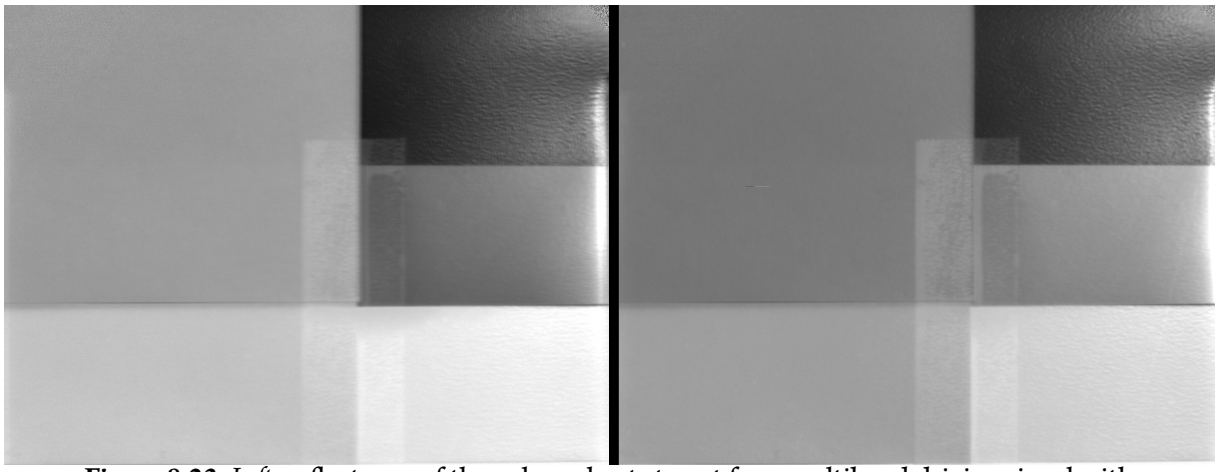

Figure 8.23. *Left*: reflectance of the colour sheets target for a multiband driving signal with 3 bands at 500nm, 600nm and 700nm. *Right*: estimated reflectance of the colour sheets target as the linear contribution of the same 3 bands.

5-bands signal

We excited the AOTF with 5 bands centred at 600nm with different wavelength separation (10nm, 25nm, and 50nm). For a 10nm separation, the ATFS system acts as a broad passband filter with an approximate bandwidth of 50nm, due to the overlapping of the individual signal bandwidths. In fact, both the multiband reflectance image and its histogram are very similar to the simulated reflectance ones (Figure 8.25 and Figure 8.26, respectively). As in the previous case, the quality of the multiband image is slightly degraded respect to the simulated image, but it is not worse than in the case of the 3-band image.

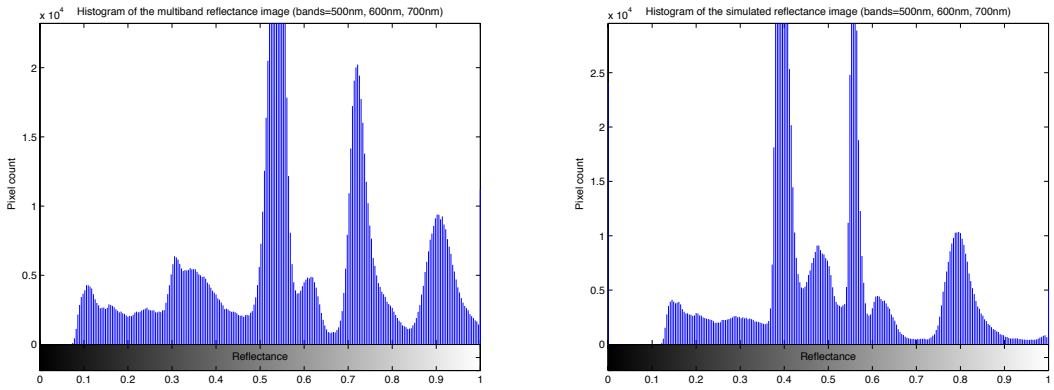

Figure 8.24. *Left*: histogram of the multiband reflectance image with the bands 500nm, 600nm, and 700nm. *Right*: histogram of its equivalent estimated reflectance image.

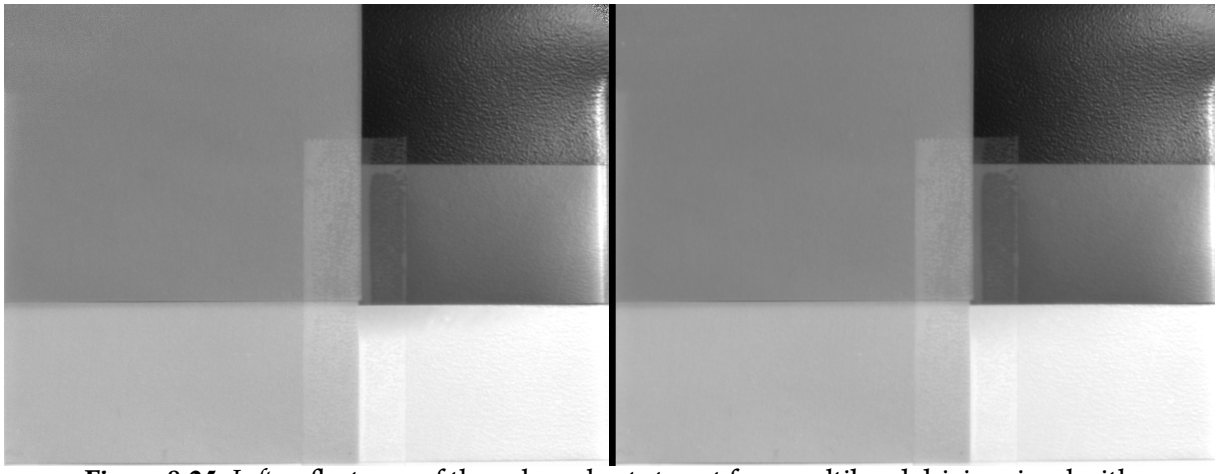

Figure 8.25. *Left*: reflectance of the colour sheets target for a multiband driving signal with 5 bands (from 580 to 620 in 10nm steps). *Right*: estimated reflectance of the colour sheets target as the linear contribution of the same 5 bands.

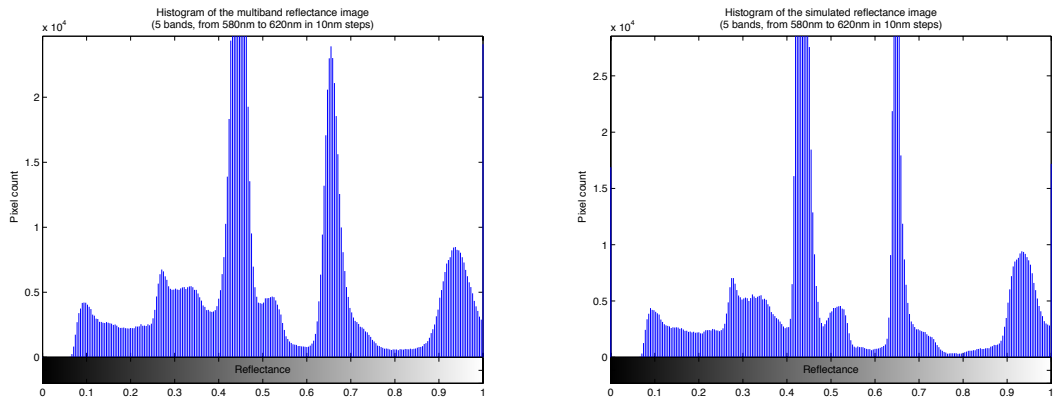

Figure 8.26. *Left*: histogram of the multiband reflectance image with 5 bands (from 580 to 620 in 10nm steps). *Right*: histogram of its equivalent estimated reflectance image.

However, when we increase the separation between bands to 50nm, the differences between the acquired and the simulated reflectance also increases (Figure 8.27). This fact is noticeable on the images and is more evident on the histogram plots (Figure 8.28).

7-bands signal

Finally, we also show the results of driving the AOTF with seven different bands at the same time. Figure 8.29 shows the images resulting of imaging the 'colour sheets' target with seven bands centred at 600nm

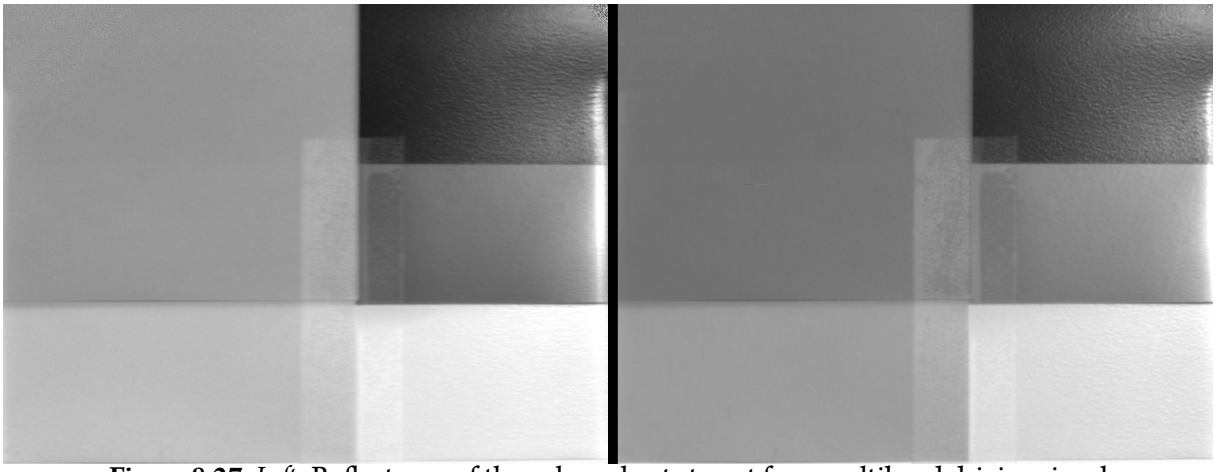

Figure 8.27. *Left*: Reflectance of the colour sheets target for a multiband driving signal with 5 bands (from 500 to 700 in 50nm steps). *Right*: estimated reflectance of the colour sheets target as the linear contribution of the same 5 bands.

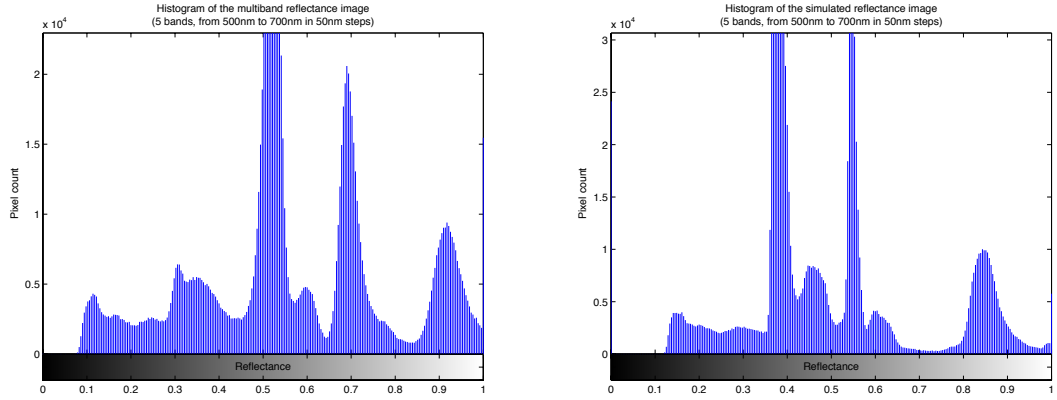

Figure 8.28. *Left*: histogram of the multiband reflectance image with 5 bands (from 500 to 700 in 50nm steps). *Right*: histogram of its equivalent estimated reflectance image.

with a separation of 10nm and 50nm, and also the simulated images from the individual band reflectance images. The histograms of these four images are shown on Figure 8.28. Again, the multiband images present a lower image resolution that degrades even further for the case of the 50nm separation between bands. The degradation produced by the multiband configuration is much more dependent on the separation between bands, due to the chromatic aberration, than to the number of bands.

8.2.3.3. Spatial Resolution

In order to evaluate the spatial performance of the system and the resolution dependency with the diffracted wavelength, we acquired a resolution pattern image (Figure 8.13). We took three sets of images of the pattern, focusing the system at different diffracted wavelengths.

For the first set of wavelengths, we focused the ATFS system when diffracting the band of 600nm (in the centre of the working range). When the system was focused, we acquired the resolution pattern for three bands (450nm, 600nm, and 750nm). The images on Figure 8.31 show the reflectance values after removing the SL+DC and correcting the CA, as in the previous experiments.

Next, we focused the ATFS system at the lower end (450nm) and acquired again the pattern at different bands. The results are shown on Figure 8.32 for 450nm, 600nm, and 750nm.

Finally, we focused the ATFS system at the higher end (750nm). The acquired images in this case are shown on Figure 8.33.

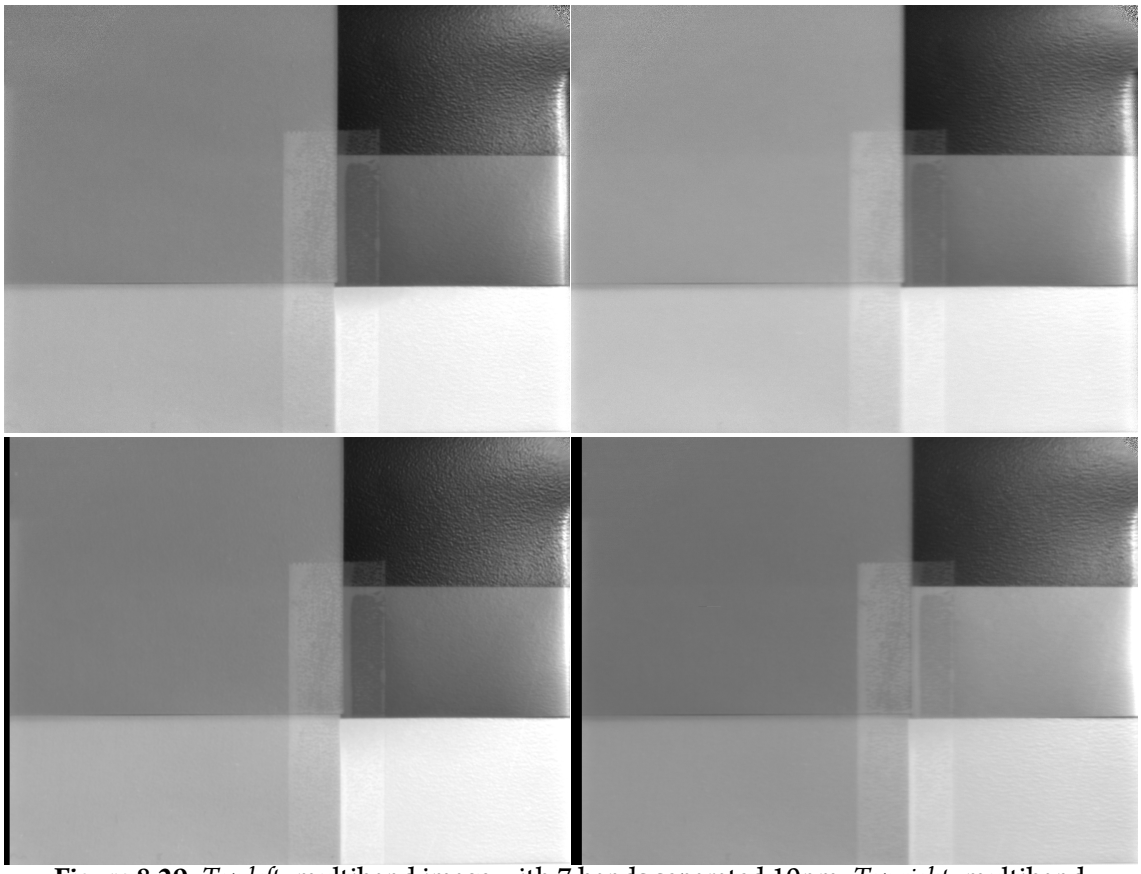

Figure 8.29. *Top left*: multiband image with 7 bands separated 10nm. *Top right*: multiband image with 7 bands separated 50nm. *Bottom left*: simulated image from 7 bands at 10nm separation. *Bottom right*: simulated image from 7 bands at 50nm separation.

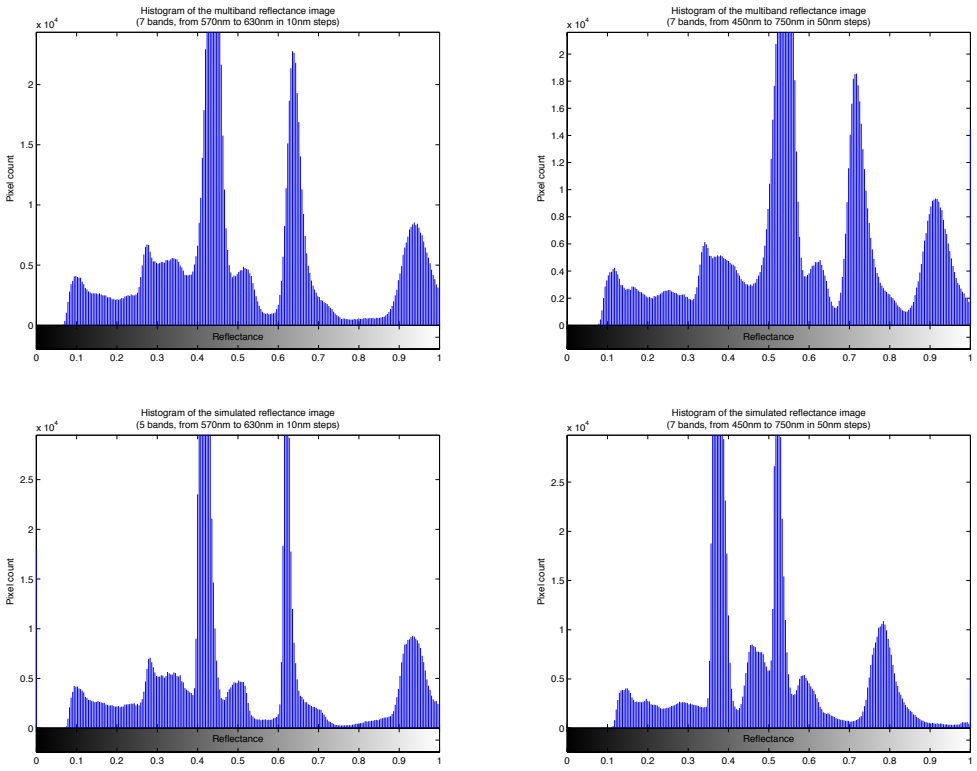

Figure 8.30. *Top left*: histogram of the multiband reflectance image with 7 bands separated 10nm. *Top right*: histogram of the multiband reflectance image with 7 bands separated 50nm. *Bottom left*: histogram of the equivalent estimated reflectance image for 7 bands separated 10nm. *Bottom right*: histogram of the equivalent estimated reflectance image for 7

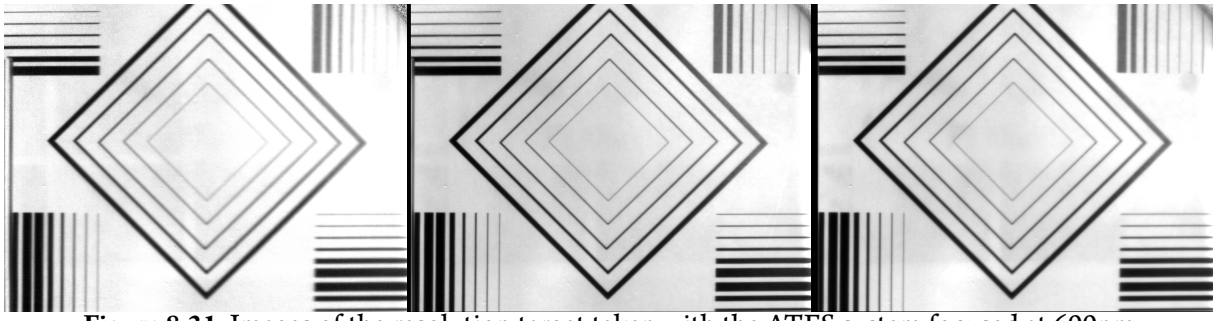

Figure 8.31. Images of the resolution target taken with the ATFS system focused at 600nm for the bands 450nm (*left*), 600nm (*centre*) and 750nm (*right*).

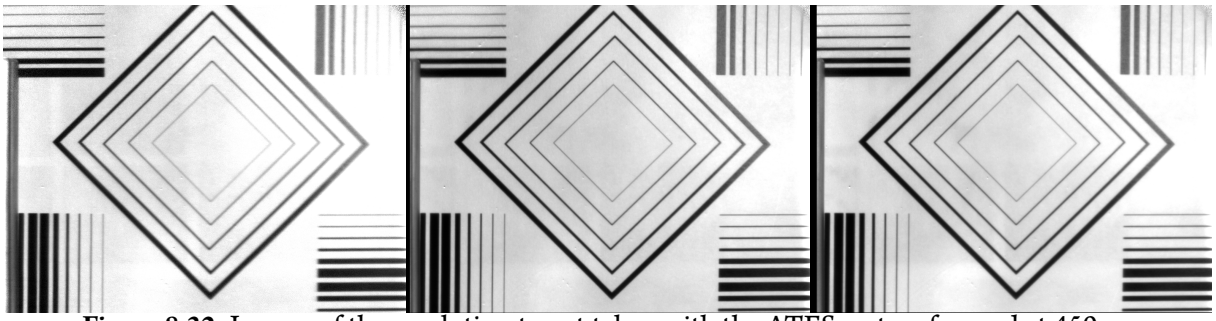

Figure 8.32. Images of the resolution target taken with the ATFS system focused at 450nm for the bands 450nm (*left*), 600nm (*centre*) and 750nm (*right*).

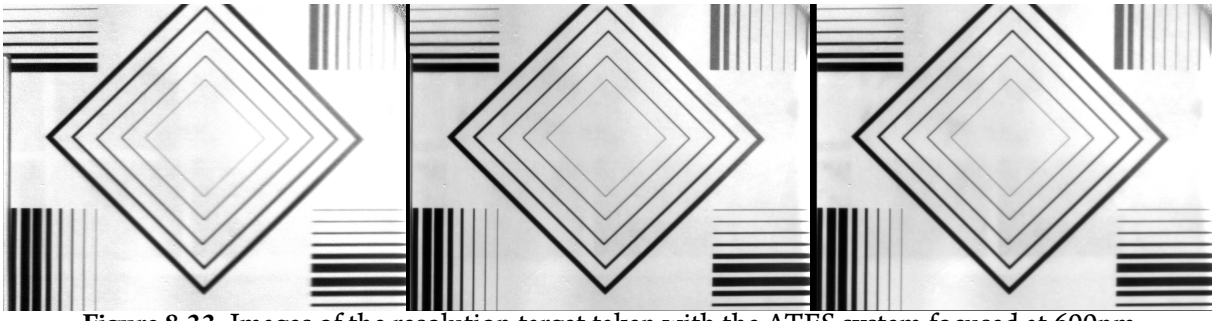

Figure 8.33. Images of the resolution target taken with the ATFS system focused at 600nm for the bands 450nm (*left*), 600nm (*centre*) and 750nm (*right*).

As these figures show, there is not a great difference on focusing the ATFS system at different wavelengths. This fact is corroborated with a plot of the horizontal intensity transect of the three images corresponding to the different focussing set-ups for the 600nm band (Figure 8.34). It is noticeable that the resolution is much lower on the lower end of the working wavelength range, and in a lesser degree on the higher end, than in the central wavelength, independently of the wavelength used for focusing. We can also observe that the image is slightly sharper at 600nm for the focusing done at 450nm than for the focusing done at 600nm. This fact points out that the imprecision on the manual focussing of the instrument is greater than the variation in focus due to the differences in the diffracted wavelength.

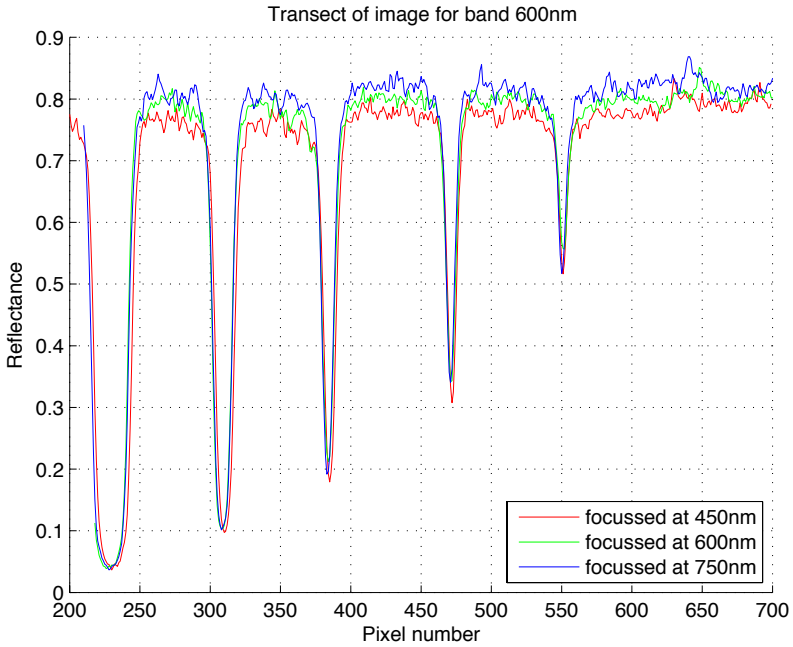

Figure 8.34. Horizontal transect of the images for the band 600nm when focussed at different wavelengths.

Part IV
Conclusions

IX

Conclusions

9.1. Summary and conclusions

This Thesis analyses the use of Acousto-Optic Tunable Filters for the realisation of a multispectral imaging system. For the pursuit of this objective, the author has designed, implemented and experimentally verified an AOTF-based spectral instrument called Autonomous Tunable Filtering System (ATFS). The implementation comprised three steps:

- Construction of a proper RF driver for the AOTF excitation. Two different approaches have been evaluated.
- Implementation of a robust optical housing for the AOTF.
- Developing of algorithms for capturing and processing multispectral images.

Then, and no less important, a complete methodology for AOTF characterisation has been developed. Finally, some images taken with the instrument are presented.

The following paragraphs details the remarks and conclusions of the different steps of the Thesis work.

Implementation of a multispectral imaging system

The author has developed an imaging system called Autonomous Tunable Filtering System (ATFS), which integrates an AOTF with a digital camera and a proper RF driver generator. The AOTF is inserted into the optical path of the camera, so that it filters a certain wavelength from the scene being viewed by the camera, generating a spectrally filtered image. By sequentially changing the wavelengths diffracted by the AOTF, the system generates a set of spectral images of the scene (multispectral image).

The finally implemented ATFS instrument uses a 614-08 AOTF from Isomet Co. that has a spectral working range of 450-800nm with a maximum spectral resolution of 7nm. The optical path has been designed to provide telecentricity to the AOTF, while maintaining an unconstrained incoming optics design. The non-diffracted light is cancelled through the combined use of two crossed polarisers and a mechanical beam stopper. The instrument can work with several Firewire camera models.

Two different RF generation approaches have been proposed, developed, and evaluated, one is based on a Direct Digital Synthesizer (DDS), and the other is based on a high-speed Digital-to-Analog Converter (DAC). Both approaches allow a very fast frequency adjustment and the possibility of using the AOTF as a broadband spectral filter, which represents a novelty with respect to the existing AOTF drivers.

The DDS approach has been evaluated using a complete RF generation circuit based on an AD9858 DDS chip. The developed board uses two cascaded RF power amplifier chips with closed loop output power con-

trol, with a maximum output power of +30dBm. This circuit generates a sweeping signal in order to implement broadband spectral imaging capabilities.

The DAC approach has been analysed using an evaluation board for the MB86064 DAC and a discrete RF power amplifier with an output power of +33dBm. This board can simultaneously generate multiple RF bands, allowing the AOTF to filter a broadband spectrum or multiple independent spectral bands at the same time.

Evaluation of the RF performance of driver

Both generation techniques have been evaluated on the RF domain by analyzing the output spectra. Both have demonstrated to work properly on the RF domain and when applied to AOTF driving. However, the DDS circuit presented a lower signal to noise ratio and higher harmonic distortion. The broadband and multiple band filtering works correctly with both generators.

Evaluation of the spectral performance of AOTFs

The author has used the developed DAC RF generator in order to characterise three different AOTF models that work on the visible and NIR range of the spectrum. These AOTF were manufactured by AA Opto Electronics, Gooch & Housego, and MolTech.

The characterised parameters were the optimal incident angle, the diffraction efficiency of the system respect to the frequency and the power of the acoustic signal, the output wavelength selection, and the output spectral bandwidth. Each one of the analysed models presented a different behaviour on these parameters, showing the great variability of these devices. None of the analysed parameters were analytically described, since such studies are out of the scope of this thesis

Definition of a calibration procedure for using AOTF multispectral systems in quantitative applications

Based on the characterisation of the different AOTF models, the author has implemented a calibration procedure that can be applied to fully characterise any AOTF in quantitative applications. This procedure is divided into three steps:

- Characterisation of the optimal incident angle of the AOTF.
- Characterisation of the diffraction response to RF frequency.
- Characterisation of the diffraction response to RF power.

From the two later steps, the procedure estimates a calibration curve for the central wavelength and bandwidth of the AOTF respect to the power and frequency of the driving signal. By using the proposed methodology with the ATFS instrument, reliable spectral indexes can be obtained such as the reflectance or the transmittance of the targets.

Results in imaging applications

The application of the AOTF as a spectroscopic imaging system is shown with several sets of images acquired with the ATFS instrument. For imaging applications, it is necessary to process the acquired images in order to remove the dark current and stray light and also to compensate for the chromatic aberration. A complete methodology has been developed and implemented in MATLAB to carry out both actions.

We have demonstrated the imaging capabilities of the ATFS for both RF generators in two different experiments. The first experiment shows the mapping of the hyperspectral reflectance and transmittance of several types of plant leaves on the range of 450nm to 800nm. This experiment was carried out using the DDS-based generator and its results were incorporated to the ESA CDB Campaign Database in the context of the SEN2FLEX campaign. Spectrally speaking, the performance of the instrument is comparable to the ASD Fieldspec FR spectroradiometer. The reflectance has been used to estimate the chlorophyll content of the leaves.

On another experiment, several targets were imaged with the ATFS instrument driven by the DAC-based generator on the range from 450nm to 750nm. This experiment demonstrated the spatial and spectral capabilities of the system, and also the multiband imaging performance. For the single band configuration, the spectral performance of the system is good, as shown in the comparison with the ASD FieldSpec RF spectroradiometer. In addition, spatial resolution is high in all the working range except for the lower end, where the efficiency of the system is also lower.

However, for the multiband configuration the system introduces a soft degradation on the imaging quality. The multiband configuration shows also two additional problems. The first drawback is that the chromatic aberration cannot be compensated for, as each single acquisition mixes image components with different spatial shifts. Additionally, as the efficiency of the system is not equal for all the range, the acquired images are formed by the contribution of the different components on a different proportion. These two problems become more evident as the number and separation of the driving bands increase. Therefore, the multiband configuration is only practically useful to generate a broadband spectral filter with a small number of closely spaced bands. This configuration can be use to increase the light throughput of the instrument when a high spectral resolution is not required.

9.2. Contributions to the science

This Thesis adds new knowledge to the subject of multispectral imaging in the following ways:

Development of new AOTF driving techniques. Both AOTF drivers described use standard electronic equipment to implement novel driving modes for AOTF's. With the DDS-bases driver, we can achieve a configurable broadband filtering using a sweeping RF signal. The DAC-based driver adds more versatility to the instrument allowing also the imaging of different bands in a single snapshot with a simultaneous multiple band generation.

Imaging of broadbands with an AOTF. In all previous works the use of AOTFs in imaging applications has been focussed to the reduction of the bandwidth of the instrument. However, we propose in this thesis to increase the bandwidth of the passband so that in certain applications we can increase the light throughput of the system without reducing the spectral capabilities.

Definition of a characterisation procedure for the calibration of AOTF based systems. AOTF's have shown very different behaviours between different models or even in the same device for different driving signals. Therefore, it is very important to define a characterisation procedure in order to allow using the AOTF in quantitative measurements requiring a repetitive and well-known behaviour.

Automation of the acquisition and processing of multispectral images. The MATLAB toolbox we have developed for the control of the ATFS instrument is an open framework that can be easily adapted to different models of AOTF's or cameras. Any imaging system based on an AOTF can be automated with this toolbox in terms of image acquisition (band definition, estimation of optimal exposure times, and sequential acquisition of stray light, white reference, and target) and image processing (automatic chromatic aberration and stray light corrections, and reflectance and transmittance calculations).

Demonstration of the performance of an AOTF imaging system for spectroscopic application. We illustrate the quantitative spectroscopic performance of an AOTF imaging system with the estimation of biophysical indices on leaves. Spectroscopic performance compares successfully with a high resolution point spectroradiometer.

9.3. Future work

The developed ATFS opens the possibility for multiple imaging spectroscopy applications. It is especially relevant the new use of the AOTF as a configurable broadband filter. Several research areas can benefit from the application of this configurability in order to improve the results of the multispectral analysis. For example, this work can be focussed to the field of biophysical parameters estimation, in which the author has been involved through several research works [Camps-Valls et al., 2005, 2006, 2009].

The AOTF models characterised in this Thesis have shown a good spectral performance. Therefore, all of them are valid to be integrated on an imaging spectrometer like the developed ATFS instrument. Last of all, the imaging quality of the implemented ATFS can be improved by reducing the image blur with a deconvolution technique, as the one used on [Wachman et al., 1996].

9.4. Achievements and relevance

The conclusions of this work has been presented on several conferences and published as research papers on different international journals. Following is a list of the published papers and proceedings related to this work:

- Calpe-Maravilla, J., Vila-Francés, J., Ribes-Gómez, E., Duran-Bosch, V., Muñoz-Marí, J., Amorós-López, J, Gómez-Chova, L., Tajahuerce-Romera, E., 400-1000nm imaging spectrometer based on acousto-optic tunable filters. *11th SPIE International Symposium on Remote Sensing Europe 2004. Proceedings of SPIE*, 5570: 460-471, 2004.
- Calpe-Maravilla, J., Vila-Francés, J., Gómez-Chova, L., Ribes-Gómez, E., Muñoz-Marí J., Amorós-López, J., and Navarro, M. 2-D hyperspectral imaging systems for the retrieval of biophysical parameters. *Proceedings of the SPARC Final Workshop*, ESRIN, Frascati, Italy. ESA-WPP-250, ESA Publications Division, 2005.
- Vila-Frances, J., Ribes-Gómez, E., Ibáñez-López, C., Gomez-Chova, L., Muñoz-Marí, J., Amorós-López, J., Calpe-Maravilla, J., Configurable-bandwidth imaging spectrometer based on an acousto-optic tunable filter. *Proceedings of SPIE*, 5953:216-227, 2005.
- Vila, J., Calpe, J., Pla, F., Gómez, L., Connell, J., Marchant, J., Calleja, J., Mulqueen, M., Muñoz, J., Klaren, A., SmartSpectra: Applying multispectral imaging to industrial environments. *Real-Time Imaging*, 11:85-89, 2005.
- Calpe, J., Vila, J., Ribes, E., Muñoz, J., Gómez, L., Amorós, J., Navarro, M., Hyperspectral images acquired in the SEN2FLEX Campaign for vegetation characterization. *Final SEN2FLEX 2005 Campaign presentation*, 2006.
- Vila-Francés, J., Calpe-Maravilla, J., Muñoz-Marí, J., Gómez-Chova, L., Amorós-López, J., Ribes-Gómez, E., Durán-Bosch, V., Configurable-bandwidth imaging spectrometer based on an acousto-optic tunable filter. *Review of Scientific Instruments*, 77, 2006.
- Calpe-Maravilla, J., Vila-Francés, J., Ribes-Gómez, E., Duran-Bosch, V., Muñoz-Marí, J., Amorós-López, J, Gómez-Chova, L., Tajahuerce-Romera, E., 400-1000nm imaging spectrometer based on acousto-optic tunable filters. *Journal of Electronic Imaging*, 15(2):1-8, 2006.
- Vila-Francés, J., Gómez-Chova, L., Amorós-López, J., Calpe-Maravilla, J. Configurable Passband Imaging Spectrometer Based on Acousto-optic Tunable Filter. *Proceedings of the 10th International Conference on Advanced Concepts for Intelligent Vision Systems. Lecture Notes In Computer Science*, 5259:206-127, 2008.

Additionally, the outcomes of this work are relevant to the research carried out by the author and his colleagues at the University of Valencia in the context of different research projects in which they are involved. Following is a list of the projects in which the author has participated in the field of spectral imaging:

- "Smart Multispectral System for Commercial Applications (SMARTSPECTRA)", European Commission IST 5th Framework [2002-2005], code: IST-2001-37306.
- "Contribución al diseño de futuras misiones ESA de observación de la tierra mediante el uso optimizado de nuevos sensores hiperespectrales (HYPERTEL)", Ministerio de Educación y Ciencia (Spain) [2004–2005], code ESP2004-06255-C05-02.
- "SPECTRA Barrax Campaign (SPARC)", European Space Agency (ESA) [2004].

- "SENtinel-2 and FLuorescence EXperiment (SEN2FLEX)", European Space Agency (ESA) [2005].
- "Desarrollo de un sistema integrado de procesamiento de datos hiperespectrales de observación de la Tierra aplicado al diseño de futuras misiones de la ESA (DATASAT)", Ministerio de Educación y Ciencia (Spain) [2005–2008], code: ESP2005-07724-C05-03.
- "CarboEurope, FLEx and Sentinel-2 Campaign (CEFLES2)", European Space Agency (ESA) [2007].
- "Metodologías avanzadas en observación de la Tierra: Calibración de datos ópticos y extracción de la información (EODIX)", Ministerio de Educación y Ciencia (Spain) [2009 – 2011], code: AYA2008-05965-C04-04/ESP.

9.5. Acknowledgements

This research work has been possible thanks to the support of the following projects:

- "Beca de Formación del Profesorado Universitario (FPU)", Ministerio de Educación, Cultura y Deporte, [2002-2005].
- "Smart Multispectral System for Commercial Applications (SMARTSPECTRA)", European Commission IST 5th Framework [2002-2005], code: IST-2001-37306.
- "Contribución al diseño de futuras misiones ESA de observación de la tierra mediante el uso optimizado de nuevos sensores hiperespectrales (HYPERTEL)", Ministerio de Educación y Ciencia (Spain) [2004–2005], code ESP2004-06255-C05-02.
- "Metodologías avanzadas en observación de la Tierra: Calibración de datos ópticos y extracción de la información (EODIX)", Ministerio de Educación y Ciencia (Spain) [2009 – 2011], code: AYA2008-05965-C04-04/ESP.

Part V
Appendixes

A

DDS-based RF generator design

The DDS-based RF generator is an electronic circuit that generates a RF power signal from a AD9858 DDS chip. The circuit has been implemented as a single Printed Circuit Board (PCB). This Appendix describes the design of the PCB, which block diagram is depicted in Figure A.1.

The schematics of the board and the PCB lay-out are represented at the end of this Appendix.

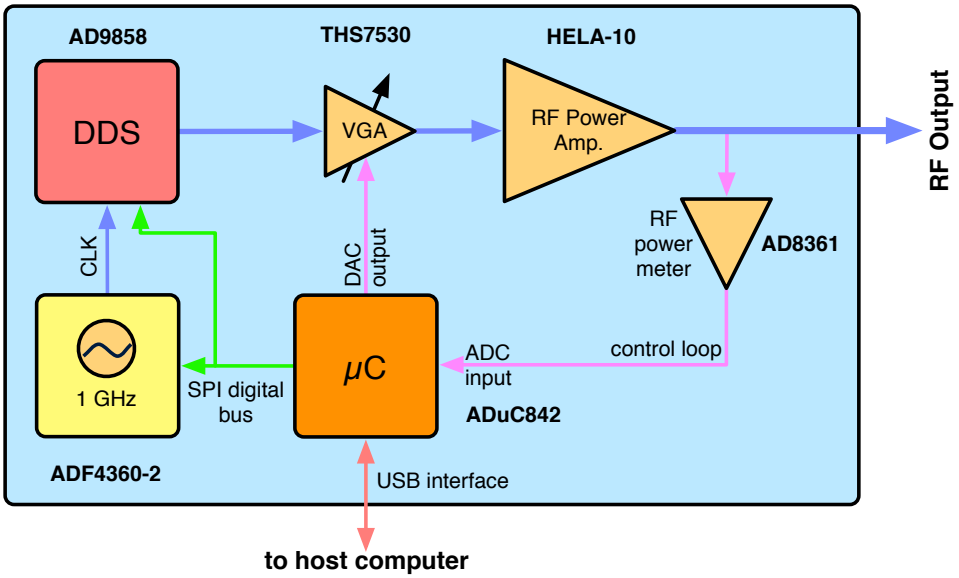

Figure A.1. Block diagram of the DDS-based RF generator.

A.1. 1GHz clock

The RF board uses the ADF4360-2 chip as a 1GHz clock. The ADF4360-2 is an integrated synthesiser and Voltage Controlled Oscillator (VCO), designed for a central frequency of 2GHz. In addition, a divide-by-2 option is available, whereby the user gets an RF output of between 925 and 1075 MHz. In the RF generation board, the ADF4360-2 chip generates an output signal of exactly 1GHz. The chip is controlled by the value of three internal registers, which are programmed through a 3-wire interface.

The ADF4360-2 works as a Phase-Lock Loop (PLL) circuit. The output of the VCO is compared with a reference clock and the phase difference is used as a control feedback to stabilise the VCO frequency. The ADF4360 uses an integer-N prescaler that allows generating output frequencies that are scaled only by the reference frequency divided by the content of the R divider. The VCO frequency equation is:

$$f_{VCO} = N \times f_{RFIN}/R \qquad \textbf{(Eq. A.1)}$$

Where f_{RFIN} is the external reference frequency oscillator. The division ratio N is fixed by the values of the dual-modulus prescaler (P/P+1) along with the A and B counters, according to the expression N = BP + A.

The RF generator uses an external reference frequency of 10 MHz. Therefore, the chosen values to obtain a 2GHz output frequency are:

- B = 312 (0x138)
- A = 16 (0x10)
- P = 32 (32/33 prescaler value)
- R = 50 (0x32)

These values have been calculated by the ADISimPLL software (provided by the manufacturer of the chip). These values and other control parameters are programmed into three internal registers of the chip. The R counter register contains the R value, while the control register defines the control parameters of the chip, and finally the N counter register contains the A and B values. The registers are written through the 3-wire interface after power-up in a defined order.

Schematic design

The 1GHz clock has been designed following the manufacturer's reference circuit diagram for the ADF4360-2 [EVAL-ADF4360-2EB1]. The 1GHz signal is obtained from a PLL circuit formed by the ADF4360-2 and a passive loop filter.

The reference clock for the ADF4360-2 is obtained from an integrated 10MHz oscillator (model SPXO018036 from C-MAC Frequency Products Ltd.). The loop filter is a third order passive low pass filter. The values have been chosen for a centre frequency of 2GHz, a channel spacing of 200kHz and a bandwidth of 10kHz. The values of the filter components have been also calculated by the ADIsimPLL software.

The ADF4360-2 is programmed through a 3-wire interface connected to the board microcontroller. The CLK and DATA input lines of the ADF4360-2 are connected to the SPI CLOCK and SPI DATA lines of the SPI port on the microcontroller, respectively. The Latch Enable (LE) input pin is connected to a general port pin of the microcontroller, configured as an output. Additionally, the MUXOUT output of the ADF4360-2 is connected to a general port pin of the microcontroller, configured as an input. The MUXOUT is configured to show the "Lock Detect" signal, and therefore is monitored by the microcontroller in order to check the PLL status.

The ADF4360-2 implements a differential output, which has been matched to a 50Ω load with a broadband matching circuit. The outputs are tied to Vdd through a 51Ω resistor and connected in series to a dc bypass capacitor of 100pF. The differential output of the clock feeds directly the differential reference clock of the DDS, which presents an input impedance of 50Ω.

A.2. Direct Digital Synthesiser

The RF board uses the AD9858 as an RF signal generator. The AD9858 chip integrates, apart from the DDS core, an analogue mixer, a charge pump and a phase frequency detector for PLL functionality. However, in this design only the DDS core is used, maintaining the other parts of the chip powered down.

The DDS is programmed in frequency-sweeping mode. In this mode, the DDS generates a sine signal whose frequency is increasing (or decreasing) in fixed steps from an initial frequency at fixed time steps. The initial frequency, the frequency step and the time step are defined by the value of three internal registers, called Frequency Tuning Word (FTW), Delta Frequency Tuning Word (DFTW) and Delta Frequency Ramp Rate Word (DFRRW), respectively. These registers are programmed by the board microcontroller through a

serial port. The DDS cannot stop the frequency sweep automatically, so that the microcontroller has to update the "autoclear frequency accumulator" periodically in order to restart the sweep.

The microcontroller is programmed to restart the sweep every 5ms. The rest of the sweep parameters (initial frequency and frequency and time steps) are calculated by the ATFS application on the host computer and sent to the microcontroller though the control bus.

Schematic design

The DDS incorporates an integrated 10-bit DAC with complementary current outputs. The output current is converted to a differential voltage signal through two precision resistors. All the signal path of the board is kept in differential mode in order to reduce the amount of common-mode noise and increase the signal-to-noise ratio.

The full-scale current is controlled by means of an external resistor. This resistor has been fixed to 1.96kΩ, which gives a full-scale current of 20mA. According to the manufacturer, this current provides the best spurious-free dynamic range performance.

The output current goes through two 20Ω resistors, generating a differential voltage signal of $1V_{peak}$ over the Vdd voltage. This signal needs to be attenuated 20dB before being coupled to the VGA. The VGA amplifies the signal with a variable gain between 11.6 dB and 46.5 dB, and therefore higher signal amplitude will lead to a saturated output. The attenuation is implemented with a resistor network.

As some integration functionalities on the DDS chip are not used in the design, some pins are not connected. The communication with the board microcontroller uses the serial port. Therefore, the pins of the parallel port are tied to ground to avoid noise interferences. The serial port uses independent input and output pins (SDIO, SDO), and a clock input pin (SCLK). In addition, the chip uses an input-output reset (IOReset) and a Chip Select (CS/) pins. The three serial pins are connected to the SPI bus on the microcontroller, while the other two pins are connected to two general port pins on the microcontroller, configured as output pins.

A.3. Variable Gain Amplifier

The DDS output signal is fed to a differential VGA that adjusts the signal amplitude in order to control the power applied to the crystal. Neither the DDS, which has a fixed output amplitude, nor the RFPA, which has a fixed gain, can adjust the power of the RF signal. The board uses a THS7530 that has a signal bandwidth of 300MHz, and a linear in dB gain control that gives a gain from 11.6 dB to 46.5 dB.

Schematic design

The THS7530 is configured with an AC-coupled differential input and an AC-coupled differential output. The amplifier presents high impedance differential inputs, and low impedance differential outputs. Both input and output require a 50Ω impedance matching circuit. The matching is achieved with two 24.9Ω resistors from the differential inputs to ground, on the amplifier input, and two 24.9Ω resistors on the output signal path. The AC-coupling is achieved with 100nF capacitors on the differential line.

The amplifier gain is controlled by the voltage applied to the Vg+ pin. This pin is connected to one of the µC internal DAC. The voltage range will be between 0V and 0.9V. Since the DAC output can vary in the range 0 to the internal Vref (2.5V), the voltage must be limited by software.

The THS7530 requires a supply voltage of 5V, while the rest of the circuit, except for the power amplifier, works at 3.3V. Therefore, the board incorporates a small DC-DC up-converter to generate 5V from the 3.3V main supply. The converter uses a Maxim MAX682 charge-pump regulator. This chip delivers up to 250mA, requiring only one resistor and three capacitors.

A.4. Power amplifier

The power amplification of the RF signal is implemented with an integrated RF power chip, in order to reduce circuit size and cost. The most suitable chip in the market is the HELA-10D amplifier from MiniCircuits (www.minicircuits.com). HELA-10D is a balanced power amplifier with a 11dB gain, and a nominal output power of 30dBm (1W). HELA-10D presents a 50Ω differential input impedance, and can work from 8MHz to 300MHz.

In order to get the maximum power from the amplifier, the input of the HELA-10D must be +19dBm. However, the VGA chip has a maximum output swing of 2Vpp over 50Ω (10dBm). Therefore, the RF board needs an additional stage driver between the VGA and the power amplifier, with a minimum gain of 9dB and a maximum output of +19dBm. The HELA-10D chip accomplishes both conditions, and it is cascadable. Therefore, for the sake of simplicity, we use two cascaded HELA-10D in our design.

Schematic design

The RF board implements the first HELA-10D chip with both differential AC-coupled input and output. The second HELA-10D amplifier presents also a differential AC-coupled input, while the output is converted to single-mode with a balun.

Both chips use the same schematic design, except for the shunt resistance. The shunt resistance is used to control the supply current of the chip. The first HELA-10D is used as a driver, requiring low power consumption. On the other hand, the second HELA-10D must drive the highest achievable power to the load. Consequently, the first HELA-10D uses a 100Ω shunt resistance to ground, which reduces the power consumption on the chip, while the second chip uses a voltage divider that increases the supply current of the chip but providing increased output power. The value of the shunt resistance of the first HELA-10D and the resistances that form the voltage divider of the second chip are given by the manufacturer on the datasheet.

The chip uses a +12V supply, which is obtained from a power connector on the board. Large transients of the supply voltage can damage the HELA-10D chip. Therefore, the board incorporates a transient voltage suppressor. The chosen part is a SMBJ13 fast diode from Microsemi, which has a breakdown voltage of 14.4V and a transient dissipation capacity of 600W.

A.5. RF power meter

The purpose of the RF power meter is to measure the RF power applied to the load (an AOTF with 50Ω input impedance in this case). Therefore, the RF power meter must perform a non-intrusive measuring. In our design, we have chosen the AD8361 chip from Analog Devices to perform the measure. The AD8361 is a mean-responding power detector with analogue output.

The AD8361 senses the power output of the board though a voltage divider. The impedance of the divider seen by the power amplifier is very high, assuring that the measure circuitry only takes a tiny fraction of the output power.

The RF measure circuitry design is explained in [SmartSpectra, 2006b].

A.6. Microcontroller

All the elements of the RF board are controlled by an ADuC842 MicroConverter. The ADuC842 is a microcontroller that integrates a single-cycle 8052 core with 12-bit multichannel ADC, a dual DAC, and an embedded flash. The chip runs on an external 32kHz crystal.

The microcontroller executes a program that generates a frequency-sweeping signal. The sweep period is fixed to 5ms and the rest of the signal parameters are configured by the host computer. These parameters are: initial frequency, frequency step, time step, and output power. The final frequency is not specified because it is fixed by the frequency and time steps, as the sweep period is 5ms.

The microcontroller communicates with the host computer through a standard serial bus, which is connected to the UART port. The communication with the 1GHz clock and the DDS chip is implemented though an Serial Port Interface (SPI) bus connected to the SPI port. The VGA gain is controlled with the analogue output form one of the internal DAC. The measurement of the RF power is connected to an ADC input.

Schematic design

The ADuC842 is a complete microcontroller solution that requires only an external crystal and a few decoupling capacitors to work. The chip maintains two separate power domains, one for the digital and another for the analogue part, with separate supply and ground nets for each part. Moreover, the analogue inputs and outputs are buffered with rail-to-rail single supply op amps, connected also to the analogue power domain.

The chip requires two push buttons. One button is used to enter the debugger mode, which is used to program to chip, while the other is used to reset the part. The circuit presents a LED connected to one general purpose I/O pin (P1.7), which is used by the program to signal different working states. The serial transmit (TXD) and receive (RXD) pins are conducted to an on-board connector, which contains also a +VCC and GND pins. The power supply is required by the host computer cable, which contains a level-conversion logic that converts the logic signal of the microcontroller in RS-232 compatible signals.

The ADuC842 contains an SPI port, which is configured to act as a SPI master in the RF board. The SPI clock signal (SCLOCK) and SPI output (MOSI, Master Output Slave Input) are used as outputs and therefore can be connected in parallel to the two SPI slaves on the board, the 1 GHz clock and the DDS chip. The slaves use a selection line to discriminate which serial words are addressed to each particular device. The 1 GHz clock uses the Latch Enable (LE) signal, whereas the DDS uses the Chip Select (DDS_CS) signal. Moreover, the DDS can send serial data as an SPI slave, using the SPI input of the microcontroller (MISO, Master Input Slave Output).

A.7. PCB layout

The RF board has been implemented on a two layer PCB. The PCB has been traced using the Protel software package. The lay-out has been done in a semi-automatic way, taking into account several considerations about the high-frequency and thermal aspects of the design.

The PCB layout is shown at the end of this Appendix.

A.7.1. High frequency considerations

We have carefully traced the lines that drive very high frequency signals. Most of these lines are part of a differential pair, so symmetrical tracing was used. The most important lines are:

- The connection between the clock and the DDS. It is a differential line driving a 1GHz signal. A symmetrical routing with a very short length has been used.
- The connection between the DDS and the VGA. It is a differential line driving a weak RF signal. Symmetrical routing and short leads have been used. The lines have been kept away from noise sources.
- The connection between the VGA and the first power amplifier, and between the first and the second amplifiers. Again, the connections are formed by differential lines, but in this case the driving signals have a higher amplitudes. Caution has been taken with the symmetrical routing of these lines.

A.7.2. Thermal considerations

Some integrated circuits on the board dissipate a high amount of power. Therefore, some mechanisms are needed in order to keep the board at an admissible temperature. All the affected integrated circuits are provided with a thermal pad on the bottom of the package, connected thermally to the die. These thermal pads

are connected through a group of vias to a copper ground plane on the solder layer of the PCB. Each ground plane acts as a heat sink for the upper IC. In order to further improve the thermal dissipation, the ground planes are connected to the metallic chassis of the system through a thermally conductive elastometer. Additionally, these circuits have been provided with a heat sink on the upper side.

A.7.3. Mechanical implementation

The RF generator PCB has been integrated into a metallic chassis. This chassis is made from extruded aluminium, which, closed with two aluminium covers, forms a closed box. Each side of the box has a low profile fan attached, which produces an air flow inside the box for cooling the electronics. Figure A.2 shows a picture of the box.

Figure A.2. Box of the DDS-based RF generator.

A.8. Power supply

The RF board uses three different voltage supplies: +12V@900mA, +3.3V @700mA, and +5V@100mA. The +12V supply is required to be very stable and noise-free, as it supplies power to the RF amplification stage. The +3.3V supplies mainly the digital part of the board, and therefore can admit more relaxed specifications. The +5V supply is used to power the VGA and the RS-232 transceiver for the serial port. The +12V and the +3.3V supplies are generated by an external power supply unit (PSU) that runs from a mains AC input (220V@50Hz), while the +5V supply is generated on board from the +3.3V voltage by a charge pump circuit. As no off-the-shelf adapter has been found that accomplishes the required specifications, a custom PSU has been developed.

The PSU consists on three cascaded commercial grade power supplies. The first power supply is a switched regulator that gives +13.5V (1.1A maximum) from the mains input, the model SB-131B1F-11 from Sinpro. At the output of this power supply, a linear Low Drop-Out (LDO) regulator provides a stable +12V (model LT1086CT from Linear Technology, www.linear.com) from which a small DC-DC switched regulator (model Tel 5-1210 from Traco Power, www.tracopower.com) supplies +3.3V to the digital circuitry. The LDO and the DC-DC regulator are integrated into the RF generator box, to avoid noise coupling with the +12V line. The +3.3V to +5V charge pump is implemented with a MAX682 chip, from Maxim.

Figure A.3 shows a diagram of the power supply scheme.

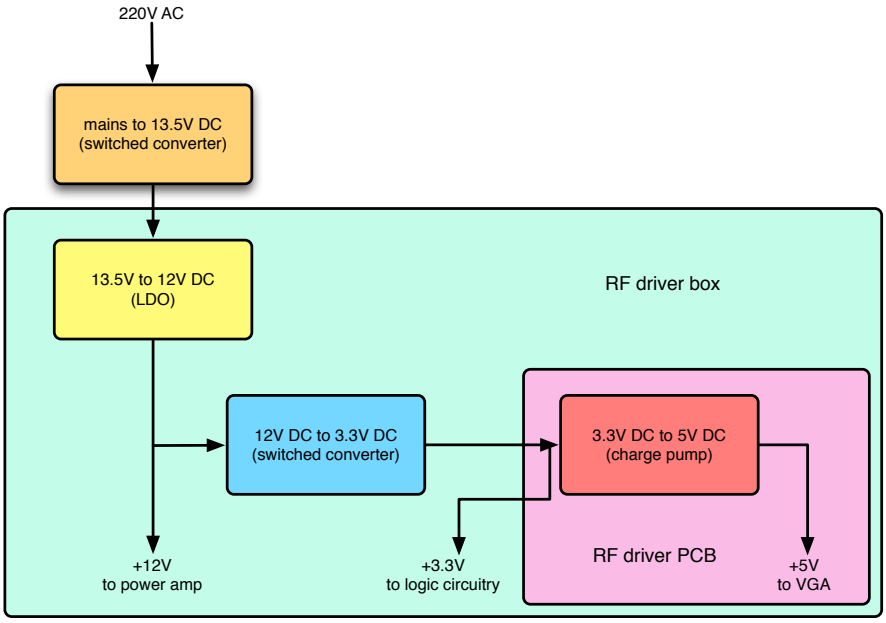

Figure A.3. Power supply scheme.

A.9. Schematics

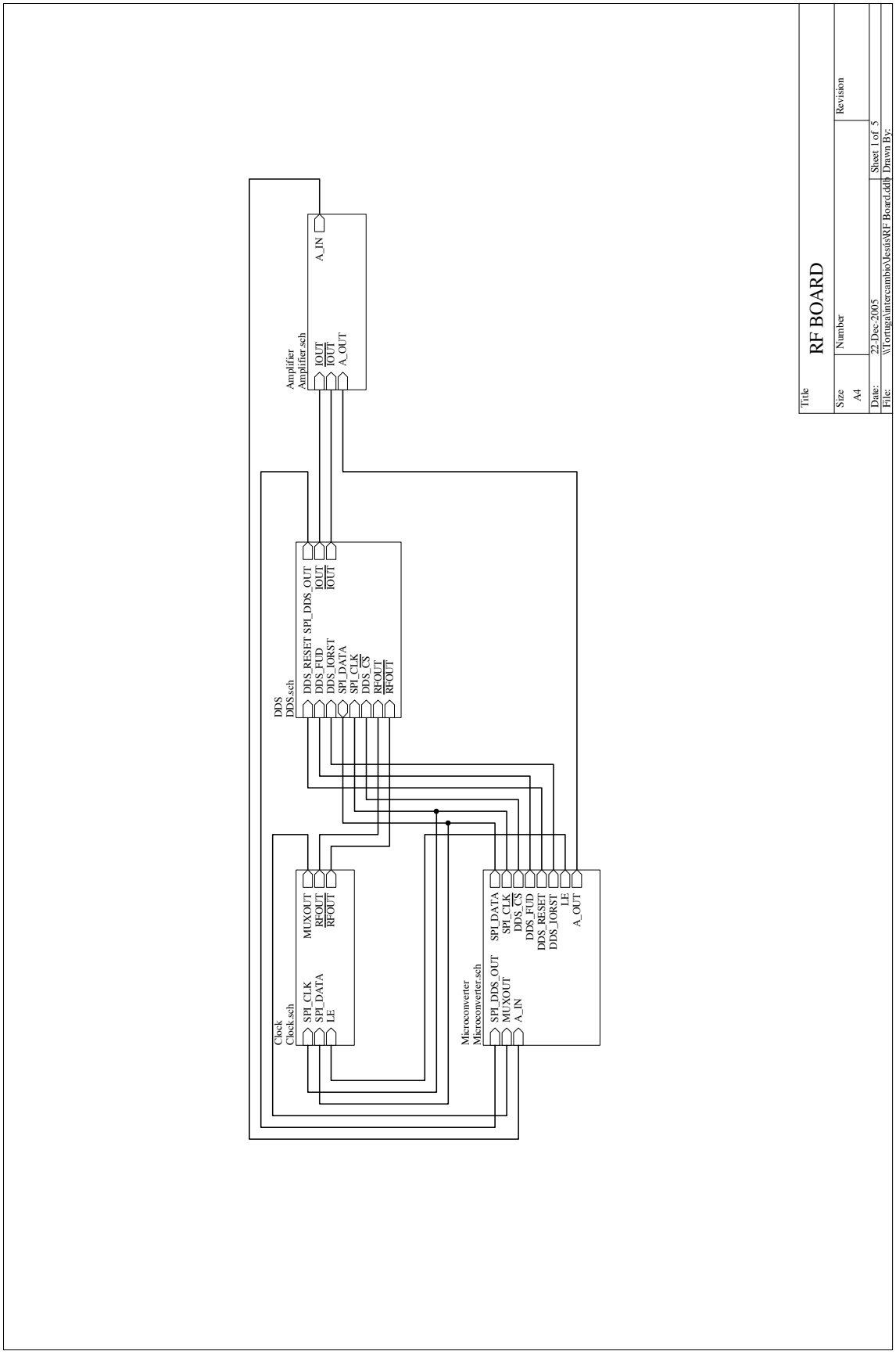

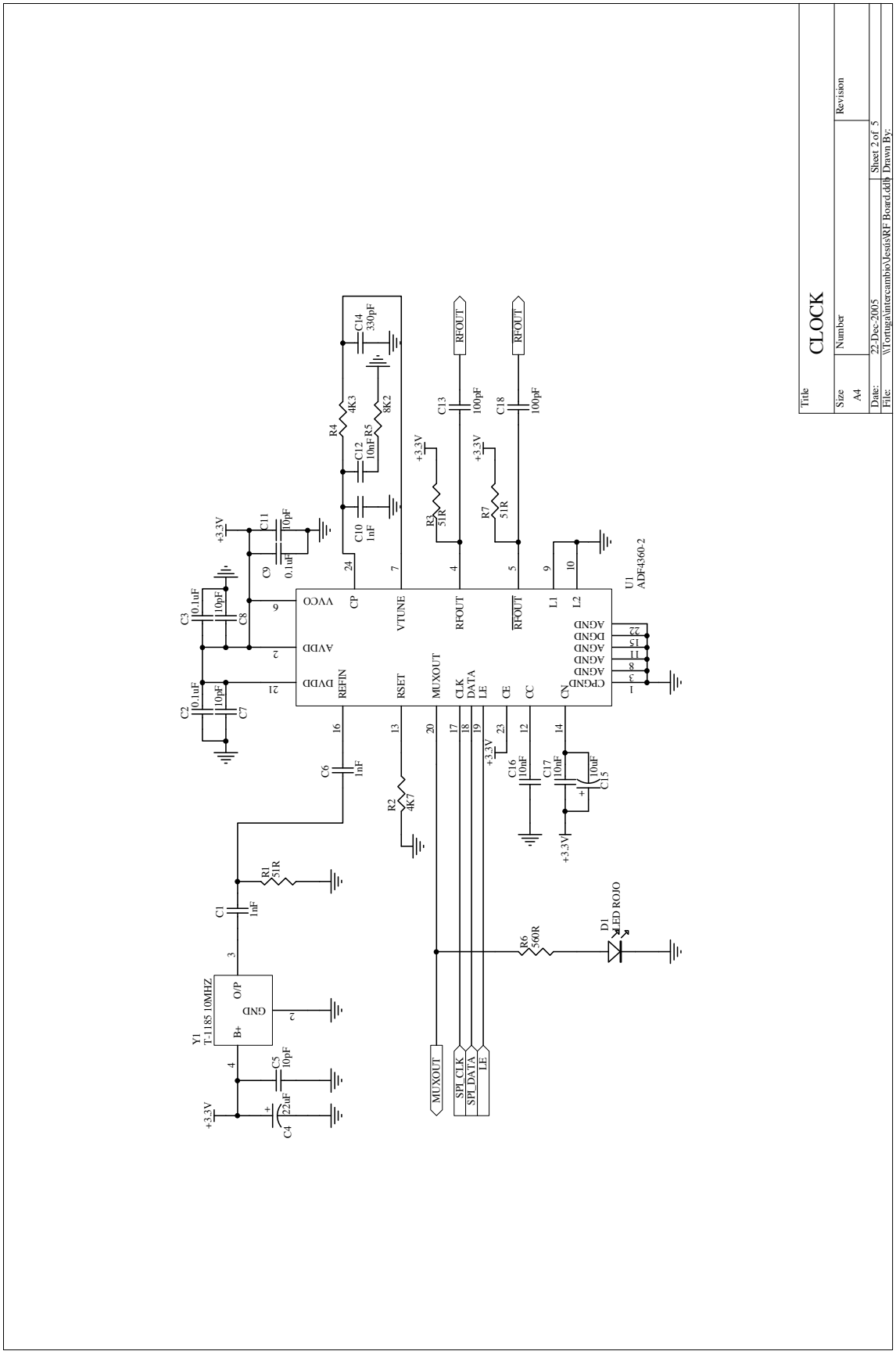
Title
CLOCK
Size
A4
Number
Revision
Date:
22-Dec-2005
Sheet 2 of 5
File:
\\Fortuga\intercambio\Jesus\RF Board.ddb
Drawn By:
U1
ADF4360-2
VVCO
AVDD
DVDD
REFIN
CP
VTUNE
RSET
RFOUT
RFOUT
MUXOUT
CLK
DATA
LE
CE
CC
CPGND
AGND
DGND
L1
L2
Y1
T-1185 10MHZ
O/P
GND
B+
R1 51R
R2 4K7
R3 51R
R4 4K3
R5 8K2
R6 560R
R7 51R
C1 1nF
C2 0.1uF
C3 0.1uF
C4 2.2uF
C5 10pF
C6 1nF
C7 10pF
C8 10pF
C9 0.1uF
C10 1nF
C11 10pF
C12 10nF
C13 100pF
C14 330pF
C15 10uF
C16 10nF
C17 10nF
C18 100pF
D1 LED ROJO
+3.3V
MUXOUT
SPI_CLK
SPI_DATA
LE

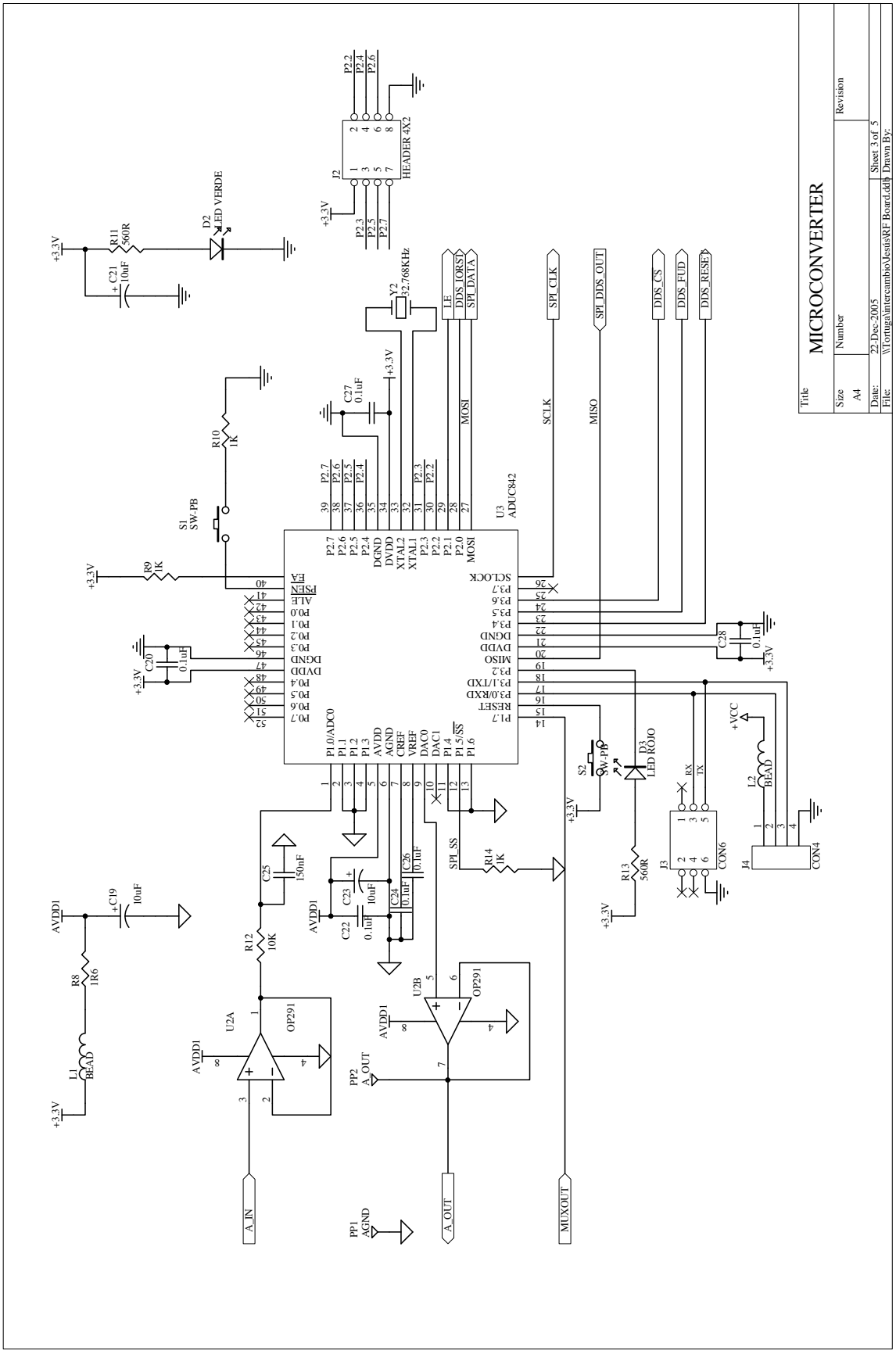
MICROCONVERTER
Title
Size
A4
Number
Revision
Date: 22-Dec-2005
Sheet 3 of 5
File: \\Fortuga\intercambio\Vesids\RF Board.ddb
Drawn By:
U3
ADUC842
SCLOCK
MISO
MOSI
SCLK
P2.7
P2.6
P2.5
P2.4
P2.3
P2.2
P2.1
P2.0
DGND
DVDD
XTAL2
XTAL1
P1.0/ADC0
P1.1
P1.2
P1.3
AVDD
AGND
CREF
VREF
DAC0
DAC1
P1.4
P1.5/SS
P1.6
P1.7
RESET
P3.0/RXD
P3.1/TXD
P3.2
P3.3
P3.4
P3.5
P3.6
P3.7
PSEN
ALE
P0.0
P0.1
P0.2
P0.3
P0.4
P0.5
P0.6
P0.7
FA
SPI_CLK
SPI_DDS_OUT
DDS_CS
DDS_FUD
DDS_RESET
LE
DDS_IORST
SPI_DATA
Y2
32.768KHz
C27
0.1uF
R10
1K
S1
SW-PB
R9
1K
C20
0.1uF
C28
0.1uF
J2
HEADER 4X2
D2
LED VERDE
R11
560R
C21
10uF
S2
SW-PB
D3
LED ROJO
R13
560R
J3
CON6
RX
TX
L2
BEAD
J4
CON4
+VCC
R14
1K
SPI_SS
C25
150nF
C23
10uF
C22
0.1uF
C24
0.1uF
C26
0.1uF
R12
10K
C19
10uF
R8
1R6
L1
BEAD
U2A
U2B
OP291
AVDD1
PP2
A_OUT
A_IN
PP1
AGND
MUXOUT
+3.3V

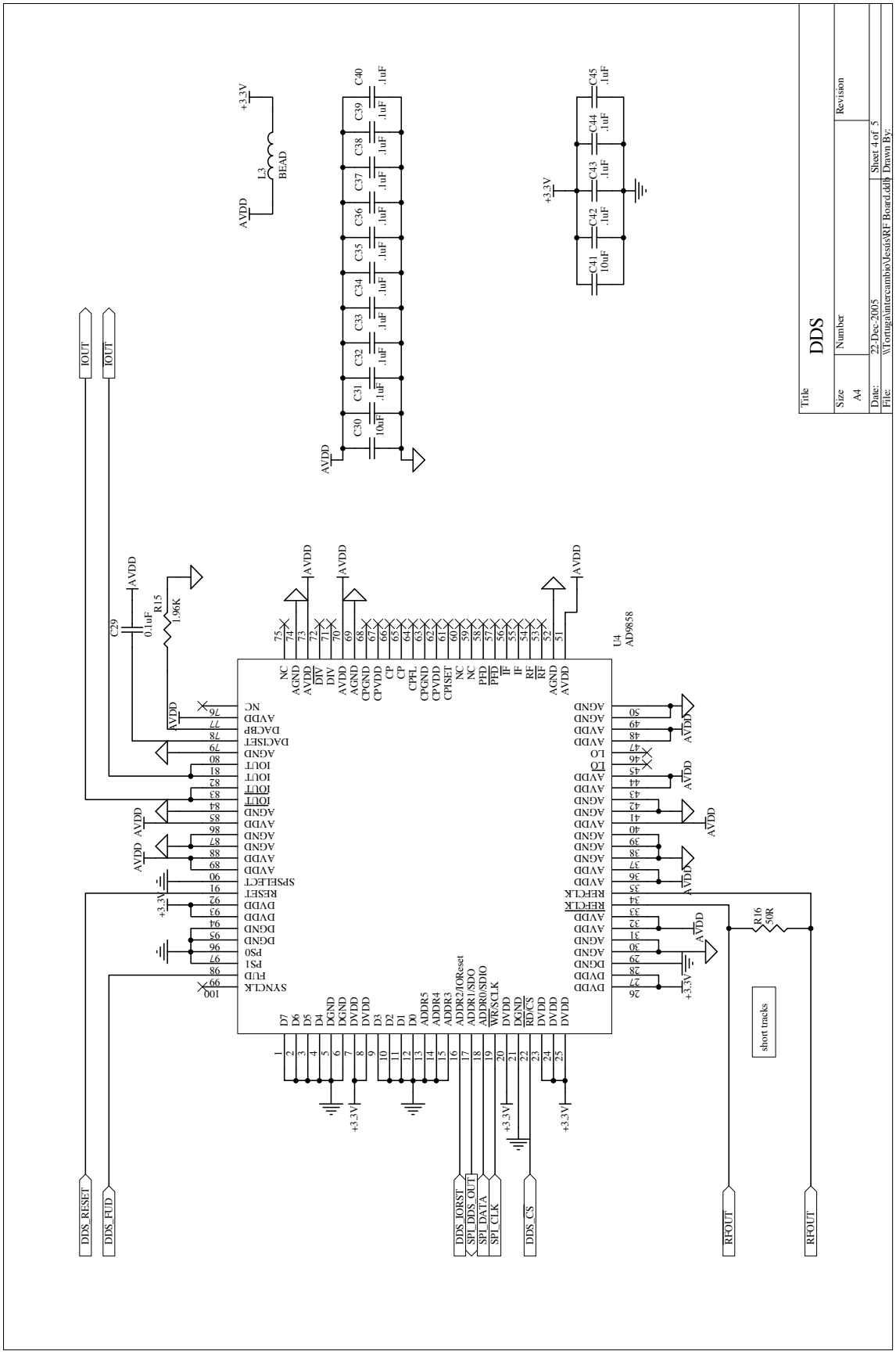
Title
DDS
Size
A4
Number
Revision
Date:
22-Dec-2005
Sheet 4 of 5
File:
\\Fortuga\intercambio\Jesus\RF Board.ddb
Drawn By:
U4
AD9858
+3.3V
AVDD
L3
BEAD
C30
10uF
C31
.1uF
C32
.1uF
C33
.1uF
C34
.1uF
C35
.1uF
C36
.1uF
C37
.1uF
C38
.1uF
C39
.1uF
C40
.1uF
C41
10uF
C42
.1uF
C43
.1uF
C44
.1uF
C45
.1uF
C29
0.1uF
R15
1.96K
IOUT
IOUT
R16
50R
short tracks
DDS_RESET
DDS_FUD
DDS_IORST
SPI_DDS_OUT
SPI_DATA
SPI_CLK
DDS_CS
RFOUT
RFOUT

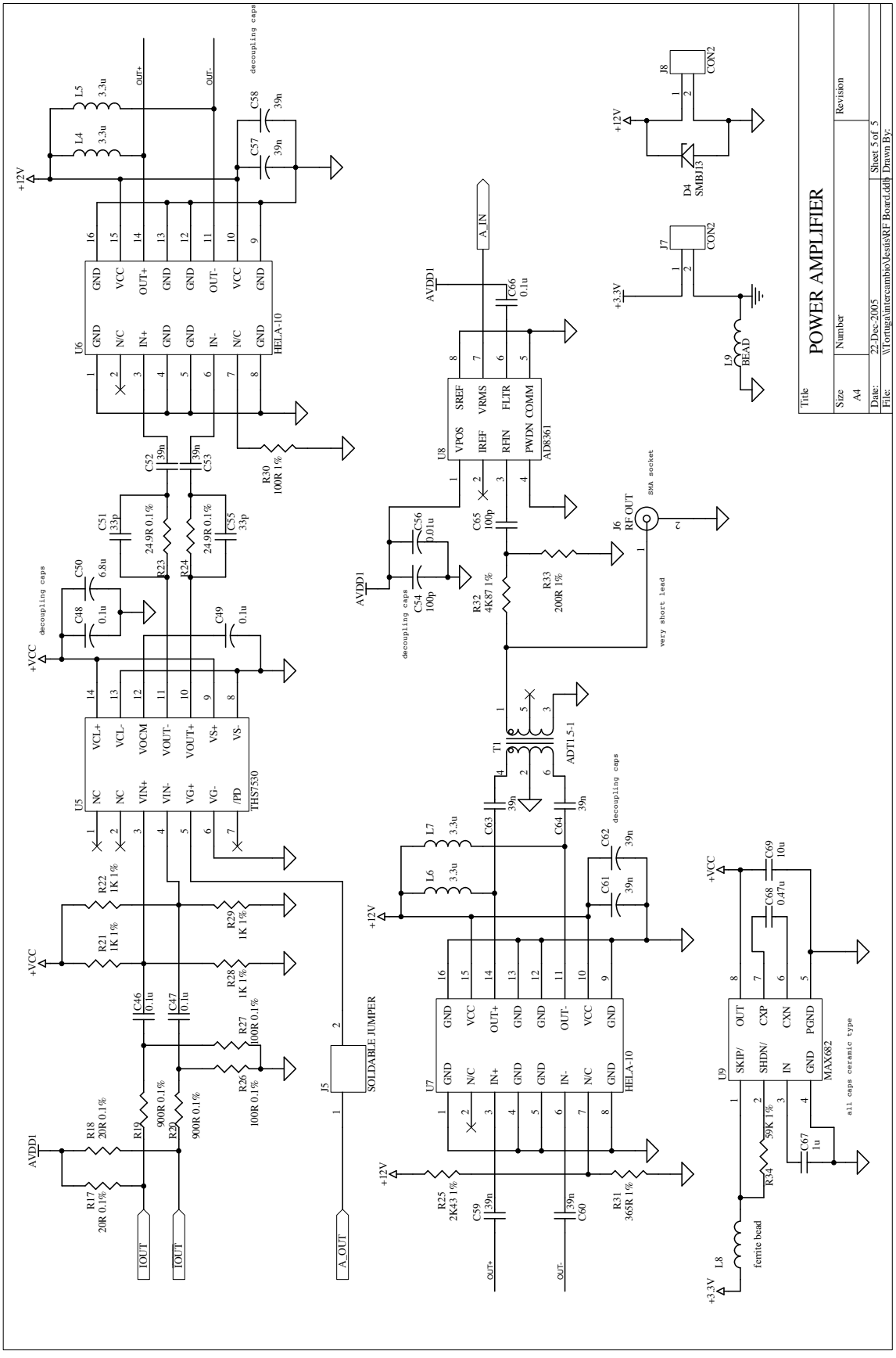
POWER AMPLIFIER
Size: A4
Number
Revision
Date: 22-Dec-2005
Sheet 5 of 5
File: \\Fortuga\intercambio\Vesdis\RF Board.ddb
Drawn By:
THS7530
HELA-10
ADL8361
MAX682
ADT1.5-1
SOLDABLE JUMPER
SMA socket
very short lead
ferrite bead
all caps ceramic type
decoupling caps
+12V
+VCC
+3.3V
AVDD1
IOUT
A_OUT
A_IN

B

DDS generator firmware

The DDS-based RF generator board contains a microcontroller (μC) that manages the RF generation as asked by the host computer. In order to do that, the μC is programmed with a custom firmware written in ASM language. The firmware controls the signal generation and also implements the transmission protocol between the host computer and the board. The protocol defines the format and contents of the communication between the host computer and the μC.

The firmware program follows the flow diagram shown in Figure B.1.

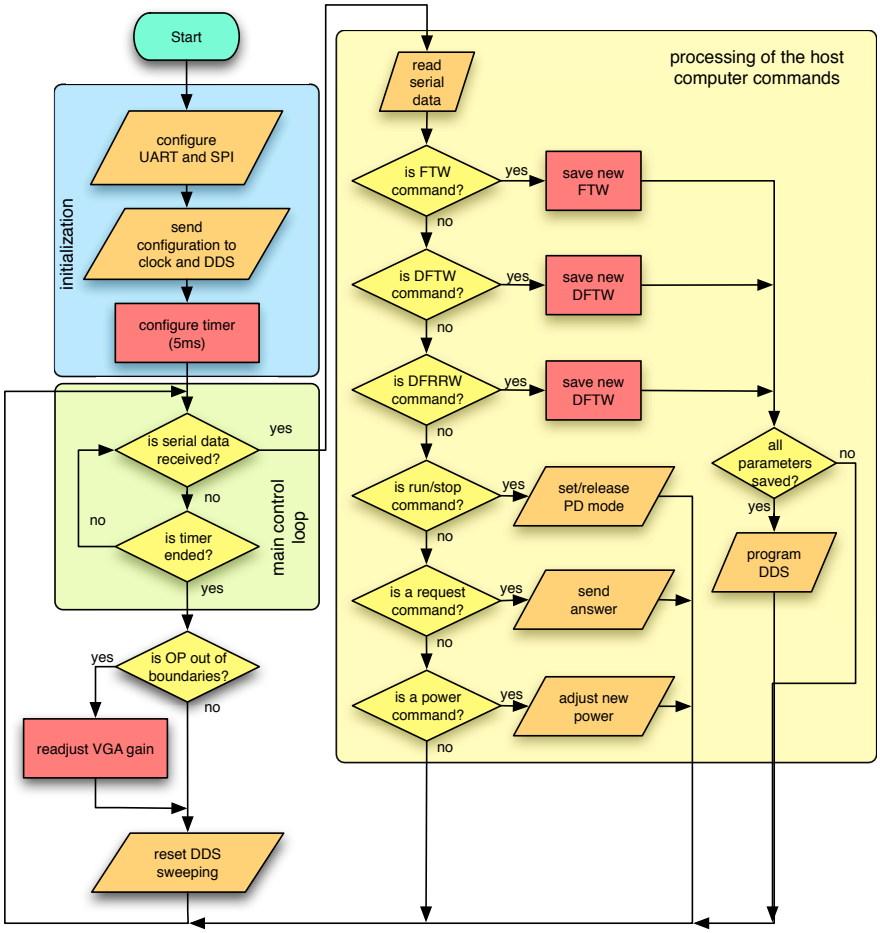

Figure B.1. Flow diagram of the microcontroller firmware.

The program has three main blocks:

- Initialisation
- Main Loop
- Processing of the serial commands

In the Initialisation block, the program configures the μC, and then the rest of the elements on the board: the clock, the DDS and the VGA. The clock is configured to output a clock signal of 1GHz. The DDS is configured to work in sweep mode and it is put into sleep mode, until any serial command is received. Finally, the VGA is configured to its minimum gain.

After that, the program enters the main loop, which is a wait loop that resets the phase register of the DDS to the initial frequency every 5ms.

The power control is implemented with a proportional control scheme. The VGA gain is modified proportionally to the discrepancy between actual and desired output power. At the end of each 5ms loop, the output power is acquired and compensated for possible deviations.

When any serial command is detected, the program enters the processing routine. In this routine, the serial command is read and executed. The DDS needs three parameters to configure completely any swept: the FTW, the DFTW, and the DFRRW. Only when the three parameters have been updated, the DDS is programmed with the new configuration. Additionally, the host computer can program the RF power output with another command.

The complete code of the firmware program is listed on the attached CD.

B.1. Communication protocol

The implemented communication protocol defines the format and contents of the communication between the host computer and the microcontroller. Every communication is started by the host computer, and normally followed by an answer from the μC. However, the answer is not required in some circumstances.

The PC can send the following commands to the ATFS:

<table>
<tr><th>COMMAND</th><th>CODE</th><th>BYTES*</th><th colspan="5">DATA FORMAT</th></tr>
<tr><td rowspan="2">Initial RF frequency</td><td rowspan="2">07h</td><td rowspan="2">5</td><td>Band</td><td>F(7:0)</td><td>F(15:8)</td><td>F(23:16)</td><td>F(31:24)</td></tr>
<tr><td colspan="5">FTW = F(31:0) [32-bit unsigned int]</td></tr>
<tr><td rowspan="2">Δt</td><td rowspan="2">08h</td><td rowspan="2">3</td><td>Band</td><td>T(7:0)</td><td>T(15:8)</td><td></td><td></td></tr>
<tr><td colspan="5">DFRRW = T(15:0) [16-bit unsigned int)</td></tr>
<tr><td rowspan="2">Δf</td><td rowspan="2">09h</td><td rowspan="2">5</td><td>Band</td><td>F(7:0)</td><td>F(15:8)</td><td>F(23:16)</td><td>F(31:24)</td></tr>
<tr><td colspan="5">DFTW = F(31:0) [32-bit signed int]</td></tr>
<tr><td rowspan="2">RF Power</td><td rowspan="2">1Ah</td><td rowspan="2">1</td><td colspan="3">AV</td><td colspan="2">RFP(6:0)</td></tr>
<tr><td colspan="5">AV = ATFS version, can be:
'0' old board, without RF power control
'1' new board, with RF power control
RFP = RF Power (in Digital Units), [7-bit unsigned int]</td></tr>
<tr><td>Performance functions</td><td>0Bh</td><td>1</td><td colspan="5">Control Byte (CB)
Where CB(3:0) can be:
0x0F RUN command
0x00 STOP command
0x05 ask firmware version
0x07 ask information about current band
0x09 ask current state</td></tr>
</table>

**the number of bytes does not include the COMMAND byte*

The ATFS replies only to some Performance functions, with the following commands:

COMMAND	CODE	BYTES*	DATA FORMAT
FW version	10h	1	Firmware version (FV[7:0]) FV[7:4] = major version number FV[3:0] = minor version number (sub-version)
Band	11h	11	Band | FTW(31:0) | DFTW(31:0) | DFRRW(15:0) Where: FTW = (32-bit unsigned int) DFTW = (32-bit signed int) DFRRW = (16-bit unsigned int)
ATFS Ready	13h	1	Band Band = number of the band that is configured and ready
State	12h	1	ATFS status (AS) Where AS can be: 0x00 the output is OFF 0x01 the output is ON

B.2. Adjustment of the output power

The RF board has a control loop that adjusts and maintains the output power in a desired value. In order to understand the power adjustment algorithm, we must look at the RF signal path, which is detailed in Figure B.2. This figure shows the expected RF amplitude and signal gains. However, the noted RF amplitude does not take into account the "sinc" response of the DDS neither the power mismatching between elements.

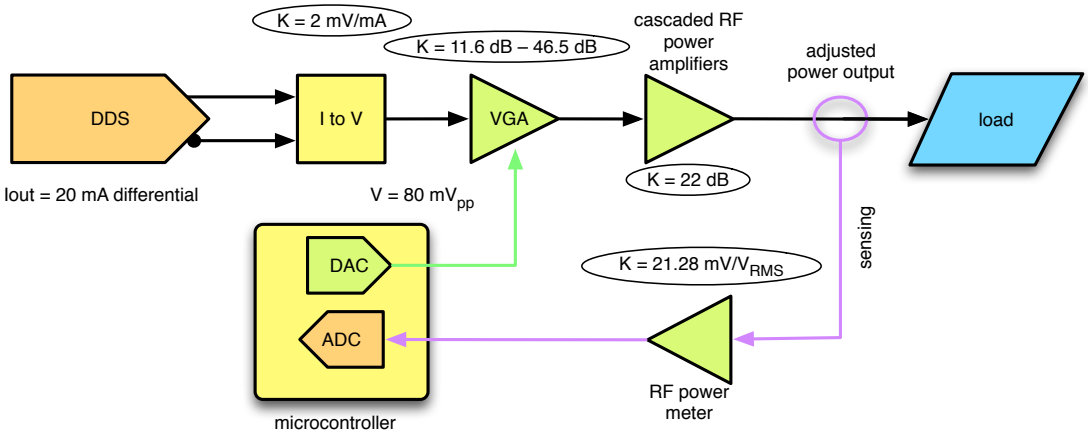

Figure B.2. Detailed signal chain.

We assume a very simple first-order model of the signal chain, where the only pole is the one formed by the RC filter at the DAC input (f_c=53Hz). There are more poles on the system, but their cut-off frequencies are much higher than the former one, and therefore can be neglected.

The 20mA differential output of the DDS is converted to voltage through two 20Ω resistors, giving a differential voltage of 800mVpp. This voltage is divided by 10 with a resistor network (the values of the resistors have been chosen in such a way that they do not load the DDS output). Therefore, the VGA sees a low impedance 80mVpp (-18dBm) differential input.

The VGA has a variable gain between 11.6dB and 46.5dB (3.802V/V to 211.35V/V), with a gain slope of 38.8dB/V. The lowest gain adjustment gives an output of 302mVpp (-6.4dBm), while the highest gain gives a value over the output range of the chip (16,9Vpp, 28.5dBm). The 1dB compression point of the chip is 13dBm –2.82Vpp– at 50MHz (10dBm –2Vpp– at a 50Ω load).

Each HELA-10 amplifier has a gain of 11dB. Assuming the signal path is perfectly matched, the overall gain of the cascaded power amplifiers is +22dB (12.59V/V). The minimum output power is +15.6dBm (36.31mW).

A resistor network precedes the AD8361 RF meter, which combined with the input impedance of the chip has a gain of 21.28mV/V. The internal gain of the chip is 7.5V/V_{RMS}, and it is programmed to provide an offset of 350mV at the output when the input is 0V_{RMS}, in order to avoid missing codes due to the single-supply buffer stage.

Adjustment algorithm

The system does not act as a complete close-control loop, due to the μC computational power limitations. We assume that, once the gain is adjusted on the VGA, the output power does not change, or changes very slowly. Studying the response to a step impulse on the gain, the system has demonstrated to be a first order system with a very slow time constant (t_{rise} is about 3.5ms). Therefore, we assume that once the power gain has been adjusted, the power can be monitored and readjusted each 5ms (the period that the μC takes to update the DDS sweeping), without loosing the output reference value.

The adjustment uses a proportional control scheme. That is, the modification on the gain value is proportional to the difference between desired and current RF power values. Despite the proportional-only control is not very robust, the lack of precision on the gain values produces an error on the RF value greater than the error that the control might introduce. In fact, it has been observed that a unity change on the gain value causes a change of three units on the ADC input. Therefore, it is impossible to adjust the power with a precision better than 3 D.U. The flow chart of the power adjustment is shown in Figure B.3.

Note that the power adjustment takes two phases, first a rough approximation and then a fine-tuning of the gain. The fine-tuning is repeated every 5ms interrupt, but without the feedback loop when modifying the gain. Therefore, every 5ms the system can correct a power deviation of ± 2 D.U. respect to the reference value.

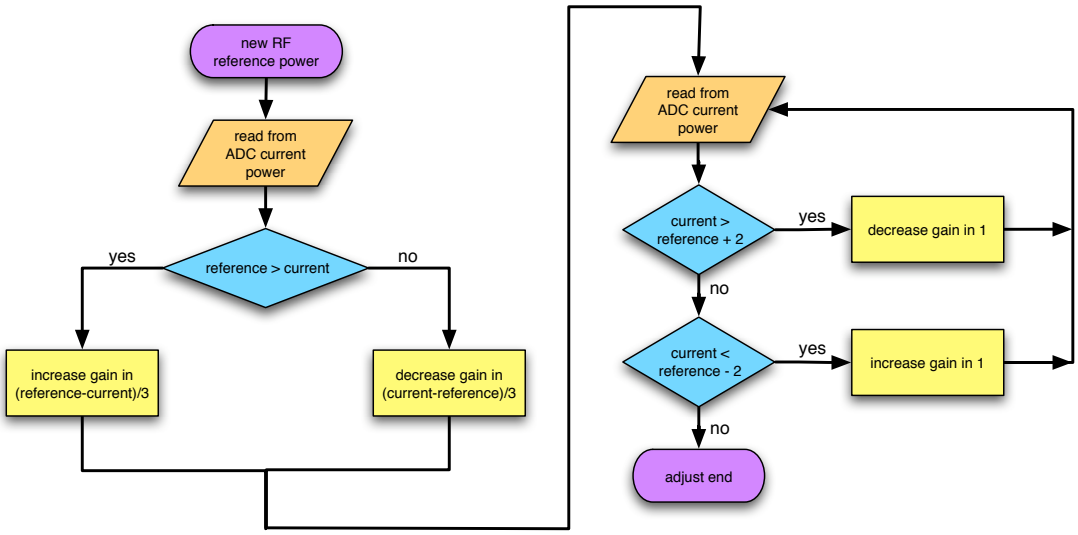

Figure B.3. Flow chart of the output power adjustment algorithm.

Part VI
Summary in Spanish

Resumen

Esta Tesis analiza el uso de los filtros ajustables acusto-ópticos (*Acousto-Optic Tunable Filter*, AOTF) en la implementación de sistemas de visión espectral. Un AOTF es un filtro espectral pasabanda ajustable electrónicamente. Está formado por un cristal que, al ser excitado con una onda acústica, difracta una determinada longitud de onda y por tanto la separa del resto del espectro lumínico. La longitud de onda de la luz separada es función de la frecuencia de la señal acústica aplicada al cristal.

Para la realización de esta Tesis Doctoral hemos diseñado un instrumento de visión industrial denominado Sistema de Filtrado Ajustable Autónomo (*Autonomous Tunable Filtering System, ATFS*), el cual incluye un AOTF para la adquisición de imágenes multiespectrales a través de una cámara de video monocroma. El sistema ha sido diseñado y calibrado específicamente para permitir su uso en aplicaciones de espectroscopía. El uso de una fuente adecuada de señales de radio frecuencia (RF) para excitar el AOTF permite configurar dinámicamente el funcionamiento del filtrado espectral. En esta Tesis presentamos dos nuevas técnicas de excitación por RF: una basada en un Sintetizador Digital Directo (*Direct Digital Synthesiser, DDS*) y otra basada en un Conversor Digital-Analógico (*Digital-to-Analog Converter, DAC*) de alta velocidad. Ambas técnicas presentan la novedosa característica de que se pueden utilizar para ajustar dinámicamente el ancho de banda de filtrado del AOTF.

El instrumento diseñado se ha utilizado en la presente Tesis para evaluar el uso de los AOTF en aplicaciones de visión espectral. Para ello, presentamos una metodología de caracterización del comportamiento espectral del AOTF respecto a su señal de excitación. Hemos aplicado esta metodología para la caracterización de tres modelos distintos de AOTF suministrados por diferentes fabricantes. El comportamiento en imagen de los AOTF presenta ciertos problemas, debido a su baja eficiencia espectral y a la existencia de aberraciones cromáticas. Sin embargo, proponemos una metodología de procesado que soluciona estos inconvenientes.

Por último, esta Tesis demuestra el uso de esta tecnología de imagen espectral en varias aplicaciones. Entre otras, mostramos el mapa de reflectancia y transmitancia espectral de las hojas de diversas especies vegetales, y la adquisición de imágenes multiespectrales de diversos objetos.

Visión general

La visión multiespectral es una técnica de imagen con la que se analiza el espectro electromagnético de los objetos. Los sistemas de visión multiespectral adquieren una serie de imágenes del objeto, cada una de las cuales contiene la información de un determinado rango del espectro radiomagnético. El rango del espectro adquirido en cada imagen se conoce como "banda espectral". El conjunto de todas las imágenes del objeto adquiridas se combinan formando una matriz tridimensional de datos denominada cubo hiperespectral o "hipercubo", en el cual las dos primeras dimensiones corresponden al dominio espacial del objeto y la tercera dimensión corresponde al dominio espectral.

Existen tres tipos distintos de sistemas de visión multiespectral atendiendo al modo de adquisición de la información: *whiskbroom, pushbroom* o *staring*. En los sistema de tipo *staring*, la información espectral se adquiere secuencialmente mientras que las dos dimensiones espaciales se adquieren simultáneamente. Para ello, utilizan un filtro espectral ajustable colocado delante de un sensor de imagen bidimensional. Los filtros ajustables pueden ser de tipo electrónico o mecánico (rueda de filtros). Los filtros ajustables electrónicamente ofrecen varias ventajas sobre los mecánicos: mayor velocidad y más flexibilidad para la selección de bandas.

Existen dos tipos de filtros electrónicos ajustables: los filtros ajustables de cristal líquido (*Liquid Crystal Tunable Filter, LCTF*) y los filtros ajustables acusto-ópticos (*Acousto-Optic Tunable Filter, AOTF*). Un AOTF consiste en un cristal birrefringente en el cual la aplicación de una señal acústica produce la difracción y por tanto separación de una longitud de onda lumínica determinada de la luz incidente. La onda acústica es generada por un transductor Piezoeléctrico unido al cristal, a partir de una señal eléctrica de la misma frecuencia. La frecuencia de la señal eléctrica determina la longitud de onda difractada. Los AOTF se excitan en el rango de las radio-frecuencias (RF). Además, cambiando las características de la señal de RF se puede modificar el comportamiento de filtrado, permitiendo la configuración del ancho de banda de filtrado.

Recientemente se ha establecido una iniciativa para tratar de extender las técnicas de visión multiespectral en los campos científico e industrial. Esta iniciativa se ha concretado en un proyecto de I+D financiado con fondos europeos denominado SmartSpectra (*Smart Multispectral System for Commercial Applications*), cuyo objetivo es la creación de un nuevo paradigma de espectrómetro de imagen. Esta Tesis se enmarca dentro de esta iniciativa.

Objetivos de la tesis

En el contexto del proyecto SmartSpectra, esta Tesis persigue la implementación de un sistema de imagen multiespectral basado en un AOTF, haciendo un especial énfasis en el diseño del generador de señales de RF. El generador debe permitir una gran flexibilidad en la generación de señales, para lo cual debe de poder funcionar en un amplio rango de potencias y frecuencias, con un tiempo de establecimiento muy corto y una configuración fácil y rápida. A continuación listamos los objetivos de esta Tesis:

- Estudio del principio de funcionamiento de los AOTF. Análisis de cómo realizan la separación espectral de la luz incidente, y los requerimientos de excitación necesarios.
- Análisis del mercado actual de AOTF y selección de un dispositivo adecuado comercialmente.
- Análisis del funcionamiento de diversos AOTF. Para ello diseñaremos una metodología de caracterización del cristal en cuanto a eficiencia espectral, resolución espectral y comportamiento en imagen.
- Diseño de un generador de señales de RF para excitar un AOTF. El generador presentará varias novedades sobre los sistemas actuales:
    - Ancho de banda de filtrado configurable.
    - Filtrado simultáneo de múltiples bandas.
- Implementación de un instrumento de visión multiespectral.
- Análisis del funcionamiento del instrumento diseñado. Caracterización del comportamiento espectral y espacial del mismo.
- Evaluación del instrumento en una aplicación práctica.

Organización de la tesis

Esta Tesis ha sido dividida en 4 partes: (1), una introducción al trabajo; (2), implementación del sistema de visión multiespectral; (3), evaluación del funcionamiento del sistema; (4), resumen y conclusiones del trabajo realizado.

En la primera parte revisamos el concepto de visión multiespectral y el funcionamiento de los AOTF.

En la segunda parte detallamos la implementación de un sistema de visión multiespectral basado en AOTF denominado ATFS. Este apartado describe en primer lugar la construcción del sensor multiespectral, haciendo un especial hincapié en los dos métodos utilizados de generación de señales de RF, y a continuación detalla el diseño del software de control del instrumento desde un ordenador personal.

La tercera parte se centra en la evaluación de los AOTF y del sistema implementado. Para ello se presenta la metodología desarrollada para la caracterización espectral de los AOTF y los resultados obtenidos sobre tres AOTF de distintos fabricantes. Se evalúa asimismo el funcionamiento de los dos generadores de RF diseña-

dos y su funcionamiento aplicados al ATFS, y se caracteriza espectral y espacialmente este instrumento. Por último, se presentan los resultados obtenidos en varias aplicaciones del sistema.

La última parte es un resumen de los objetivos y conclusiones del trabajo de Tesis realizado. Esta parte también analiza la relevancia del trabajo realizado y muestra las líneas de trabajo futuras.

Sistemas multiespectrales

Los sistemas de visión multiespectral están adquiriendo un creciente interés por su capacidad de análisis no destructivo de los objetos. Mediante esta técnica, se puede conocer el espectro electromagnético de un objeto en cada una de sus coordenadas espaciales, creando lo que se conoce como "hipercubo": una matriz de datos tridimensional que representa las dos dimensiones espaciales del objeto más una tercera dimensión con las bandas espectrales. Esta tercera dimensión espectral proporciona la información necesaria para realizar una clasificación sobre la escena, identificar elementos o estimar índices biofísicos [Treitz, 1999; Casa, 2004; Chang, 2007].

Las imágenes multiespectrales no se restringen al rango visible del espectro, sino que se pueden extender a las regiones del infrarrojo cercano o medio (NIR y SWIR). Su versatilidad y su posibilidad de medida a distancia hacen del análisis espectral una técnica adecuada para una gran cantidad de aplicaciones, entre las que cabe destacar:

- Observación remota de la tierra.
- Clasificación por visión industrial.
- Control de calidad en las industrias farmacéutica y alimentaria.
- Diagnóstico médico.
- Investigación en pinturas y antigüedades.
- Análisis químico.

Sistemas de visión multiespectrales

Los sistemas de visión multiespectrales están formados por un sensor de imagen bidimensional delante del cual se coloca un dispositivo de filtrado espectral que permite seleccionar secuencialmente las bandas espectrales a adquirir.

Existen dos tipos principales de dispositivo de filtrado; los filtros ajustables electrónicamente y los mecánicos. Entre los ajustables electrónicamente cabe destacar los filtros de cristal líquido (*Liquid Crystal Tunable Filter*, LCTF) y los acusto-ópticos (*Acousto-Optic Tunable Filter*, AOTF). Los filtros mecánicos suelen estar basados en una rueda de filtros.

Un LCTF está formado por una pila de discos de cristal líquido de retardo ajustable [Chrien, 1993; Gat, 2000]. Mediante el principio de diseño del filtro de Lyot, estos discos presentan una característica de transmisión determinada al ser polarizados. La combinación de las transmisiones de todos los discos generan una función de transferencia global ajustable.

En cambio, el AOTF es un cristal en el cual la banda espectral a filtrar es separada del resto por difracción, gracias a la aplicación de una señal acústica en el rango de las radio-frecuencias [Chang, 1976]. La frecuencia de la señal de RF determina la longitud de onda difractada.

La tabla 1.1 muestra las diferencias entre ambos tipos de filtro. Para la realización de esta tesis se ha optado por utilizar un filtro del tipo AOTF debido a sus mejores prestaciones en cuanto a resolución, eficiencia y tiempo de cambio, y al hecho de que seleccionando adecuadamente la técnica de generación de señales podemos modificar el ancho de banda de filtrado.

Filtros Ajustables Acusto-Ópticos

Historia y principio de funcionamiento

El fenómeno de la difracción de la luz por ondas acústicas fue predicho por L. Brillouin en 1922 [Brillouin, 1922] y corroborado experimentalmente en 1932 [Debye and Sears, 1932; Lucas and Biquard, 1932]. Posteriormente, se describió matemáticamente su funcionamiento, anunciándose el primer AOTF en 1969 [Harris and Wallace, 1969]. En 1975 se desarrolló la configuración no colineal de los AOTF [Chang, 1975, 1976]. Los AOTF actuales están construidos en su mayoría de TeO_2, material descubierto en 1976 [Yano and Watanabe, 1976].

En un cristal acusto-óptico, la propagación de ondas acústicas a su través produce una compresión y relajación alternas de su estructura reticular. Este fenómeno, conocido como efecto elasto-óptico, se manifiesta como una fluctuación del índice de refracción que puede producir la difracción de la luz incidente. El cristal difracta solamente el rango de la luz incidente que satisface la condición adecuada de correspondencia de fases (*phase-matching*). Para una frecuencia acústica determinada, sólo una banda espectral limitada cumple la condición de correspondencia de fases. Por tanto, la variación de la frecuencia acústica que atraviesa el cristal cambia el centro de la banda espectral pasante para mantener la condición de correspondencia de fases. Además de producir la difracción, las ondas acústicas también cambian la polarización de la luz difractada.

El efecto elasto-óptico se puede utilizar de diversas maneras. En un filtro acusto-óptico, se aprovecha la difracción de una determinada longitud de onda para separar esta banda del resto de la luz incidente en el cristal.

Hay dos configuraciones de AOTF, la colineal y la no-colineal. Se diferencian en el ángulo que forman las ondas acústicas respecto a la dirección del rayo óptico dentro del cristal.

En el diseño inicial de AOTF, la luz incidente y la propagación de las ondas acústicas son coincidentes –colineales– (Figura 2.2). En esta configuración, la luz difractada y la no difractada salen del cristal con el mismo ángulo, pero la luz difractada sufre un cambio ortogonal de polarización. Por tanto, mediante un polarizador se puede separar la luz difractada de la no difractada.

En 1975 se introdujo el diseño no-colineal [Chang, 1975]. En esta configuración (figura 2.3), la luz difractada y el resto de la luz incidente salen del cristal con ángulos diferentes, lo que permite separar ambos rayos con un simple bloqueador del haz de luz (*beam-stopper*).

Características de los AOTF

El funcionamiento de un AOTF viene determinado por una serie de características del cristal. Las más importantes son:

Ángulo de aceptación y apertura

En general, cuanto mayor es el ángulo de aceptación, mayor es la apertura óptica del filtro y por tanto más cantidad de luz se podrá capturar. Sin embargo, el aumento de este ángulo produce un aumento del ancho de banda pasante y una degradación de la resolución en frecuencia, lo que se traduce en aberraciones cromáticas en aplicaciones de captura de imagen.

Ancha de banda de la luz difractada

Por construcción, el ancho de banda de la luz difractada es proporcional a λ^2, siendo λ la longitud de onda difractada. Por tanto, en un mismo dispositivo siempre tendrán menor ancho de banda las longitudes de onda más cortas.

Material del AOTF

Los AOTF se pueden construir en diferentes materiales. Para medir la bondad de un determinado material, se utiliza un índice denominado figura de mérito (*Figure of Merit, FOM*) Acusto-Óptica. La tabla 2.1 resume los principales materiales utilizados para la construcción de AOTF con sus valores característicos.

Excitación del AOTF

Los dispositivos acusto-ópticos se excitan mediante una señal acústica en el rango de las RF (20-200 MHz aproximadamente). Esta señal se genera eléctricamente y es convertida en onda acústica de la misma frecuencia mediante un transductor Piezoeléctrico. La frecuencia de la señal determina la longitud de onda difractada, y su potencia determina la amplitud de las ondas acústicas que a su vez fija la eficiencia de la difracción. Por otro lado, la pureza espectral de la señal eléctrica influirá en el ancho de banda de la señal difractada.

Por tanto, un generador de señales de RF para excitar AOTF debe cumplir ciertas propiedades:

- Una gran pureza espectral.
- Una alta velocidad de cambio de la frecuencia de salida.
- Un rango dinámico de salida amplio que permita modular la potencia entregada.
- Un rango de funcionamiento que cubra todo el espectro de las RF, para permitir su uso en cualquier modelo de AOTF.

Debido al principio de funcionamiento del AOTF, éstos presentan un comportamiento lineal respecto a la señal de RF aplicada. Por tanto, los AOTF se pueden excitar con varias señales de RF simultáneamente. En este caso, la luz difractada está compuesta por la combinación de las bandas espectrales difractadas individualmente por cada señal de RF. Sin embargo, la eficiencia de la difracción no se combina linealmente, produciéndose una disminución de la eficiencia de cada banda.

Listado de fabricantes de AOTF

La tabla 2.2 lista los distintos fabricantes de AOTF contactados por el consorcio SmartSpectra, detallando sus modelos más adecuados para la construcción del sistema SmartSpectra.

Atendiendo a los requerimientos del instrumento SmartSpectra y a la vista de las características expuestas por los fabricantes, se decidió la compra de cuatro modelos distintos de AOTF:

- Isomet 614-08 (ver tabla 2.3)
- Gooch and Housego TF15-230-4-5-VU1 (ver tabla 2.4)
- AA Opto Electronics AA.AOTF-3/LR (ver tabla 2.4)
- MolTech AOTF-MT VIS (ver tabla 2.4)

El primero de estos modelos, que fue el primero adquirido por el consorcio SmartSpectra, se integró en el sistema de visión multiespectral desarrollado (ATFS), y los tres restantes fueron caracterizados espectralmente.

Implementación de un sistema de visión multiespectral

Esta Tesis presenta un nuevo sistema de visión multiespectral llamado Sistema de Filtrado Ajustable Autónomo (*Autonomous Tunable Filtering System, ATFS*).

Descripción del instrumento ATFS

El ATFS está dividido en dos bloques (figura 1.5): el sensor multiespectral, y el software de control.

El sensor multiespectral realiza la selección de bandas mediante un AOTF y la adquisición de imágenes mediante una cámara monocroma y un conjunto óptico. El software de control está formado por un controlador del sistema (*driver*) y una aplicación de usuario.

Sensor multiespectral

El sensor multiespectral del instrumento ATFS utiliza un AOTF modelo 614-08 de Isomet sobre un sistema óptico que por un lado enfoca adecuadamente las imágenes a adquirir en el cristal; y por otro separa y enfoca las imágenes ya filtradas en el plano focal de la cámara de video.

Sub-sistema óptico

El sistema óptico está optimizado para el comportamiento particular de los AOTF. Debido al reducido ángulo de aceptación de estos filtros, se utiliza una óptica telecéntrica formada por un diafragma y un objetivo óptico convencional (Schneider Xenoplan 1.9/35mm) delante del cristal. Detrás del mismo se ha colocado otro objetivo idéntico que enfoca la imagen sobre el plano óptico de la cámara, a la vez que un segundo diafragma hace la función de bloquear la luz no difractada. Un par de polarizadores cruzados aumentan la eficiencia del bloqueo de la luz no difractada, aumentando la eficiencia de filtrado del sistema. La figura 3.2 muestra el diagrama del montaje óptico, y la figura 3.3 muestra una foto del sistema final construido.

Cámara

El sensor del ATFS puede funcionar con distintas cámaras monocromas de alta sensibilidad. En concreto, se ha implementado el control para los tres modelos de cámara listados en la tabla 3.1.

Sub-sistema de excitación

Hemos desarrollado dos sistemas de excitación de AOTF diferentes para generar una señal de RF con la potencia y frecuencia requeridas para excitar un cristal AO. Ambos sistemas son capaces de generar tanto una señal espectralmente pura como una señal de banda ancha, con el fin de obtener una función de filtrado espectral de banda ancha.

Generación de una señal de barrido en frecuencia

Una técnica propuesta para conseguir un espectro de filtrado de banda ancha es la generación de una señal de RF en barrido de frecuencia. Se utiliza un generador de señales capaz de generar una señal de RF cuya frecuencia varía muy rápidamente creando un barrido cíclico. El cristal es capaz de adaptarse a este cambio y generar una señal difractada cuya longitud de onda varía respondiendo a la frecuencia de excitación instantánea. Sin embargo, el tiempo de exposición de la cámara es mucho mayor que el tiempo de barrido y por tanto el sensor integra las distintas longitudes de onda difractadas en una misma adquisición, generando una imagen equivalente a un filtrado de banda ancha.

Este tipo de generador se ha puede implementar con un sintetizador digital directo o *Direct Digital Synthesiser* (DDS). Un DDS es un circuito digital capaz de generar múltiples frecuencias a partir de una referencia de frecuencia.

El diseño propuesto en la presente tesis utiliza un AD9858 de Analog Devices Inc. El AD9858 es un DDS que funciona a 1 Giga-muestra por segundo (1GSPS) con una resolución de salida de 10-bits. Se programa con una palabra de ajuste en frecuencia de 32 bits, lo que permite una resolución en frecuencia de 232,83 mHz a 1GSPS). El AD9858 puede cambiar su frecuencia de salida con un intervalo de 1/125MHz.

El generador de RF diseñado se completa con los elementos descritos en la figura 3.8. La señal se sintetiza con el AD9858, cuya señal de reloj es generada por un AD4360-2 (chip que integra un sintetizador y oscilador controlado en frecuencia o VCO). La salida de RF del DDS pasa por un amplificador de ganancia variable o VGA (*Variable Gain Amplifier*) antes de atacar un amplificador de potencia de RF compuesto por dos integrados HELA10 en cascada. La combinación de estos elementos genera una señal de salida en el rango de 20 a 200 MHz con una potencia máxima de +30dBm. Un medidor de potencia de RF AD8361 realiza un control en bucle cerrado de la potencia de salida instantánea.

El sistema está controlado por un microcontrolador ADuC842, que además se encarga de la comunicación con el software de control en el PC a través de un puente serie-USB. El diseño de la placa de excitación se detalla en el apéndice A, y la programación del microcontrolador (*firmware*) en el apéndice B.

Generación de una señal multibanda

La otra técnica de excitación que proponemos consiste en la generación digital de una señal multibanda. Al excitar el AOTF con varias frecuencias a la vez se produce un filtrado equivalente a la combinación de la difracción producida por cada frecuencia individual. Si las frecuencias están muy separadas, se consigue el filtrado simultáneo de varias bandas diferenciadas, mientras que si las frecuencias están lo suficientemente próximas se consigue el filtrado de una banda pasante ancha, debido al solape de los anchos de banda de cada banda pasante en particular.

La generación de una señal compuesta de RF se realiza en el dominio digital y es posteriormente convertida a señal eléctrica mediante un conversor digital a analógico (*Digital-to-Analog Converter*, DAC) de alta velocidad. Normalmente este proceso requiere de una interconexión de muy alta velocidad entre el generador digital de ondas y el DAC, con los problemas de diseño que eso conlleva.

Sin embargo, nuestro generador se ha implementado con un DAC MB86064 que contiene una memoria interna de alta velocidad en la que se almacena la forma de onda a generar. Este DAC tiene una resolución de 14-bit, una memoria interna de 16000 muestras, y funciona a 1GSPS a partir de un reloj externo de 500MHz. De esta manera, generamos la forma de onda a convertir a priori para ser posteriormente descargada al DAC, sin que la generación y la descarga se tengan que realizar en tiempo real.

El generador diseñado utiliza una placa de evaluación del MB86064, a la que se une un generador de reloj PROMAX GR-104 y un amplificador de RF modelo AP5300-2 de 2W de potencia del fabricante RFPA. El control y descarga de formas de onda del DAC se realiza mediante un interfaz USB que se maneja directamente desde un programa escrito en MATLAB. La figura 3.4 muestra el diagrama de bloques del generador.

Software de control

El instrumento ATFS se controla desde un PC. Se ha creado un software de control que realiza tres tareas: control del sensor multiespectral, captura de imágenes y procesado. El resultado final del software es una imagen hiperespectral (hipercubo) del objeto capturado. El software se divide en dos capas (figura 4.1): una capa de controladores (*drivers*) para la cámara y el generador de RF, y una capa de aplicación con una interfaz de usuario para gestionar la captura, procesado y almacenamiento de los datos.

Capa de controladores

Controlador de la cámara

El control de la cámara se realiza mediante el driver proporcionado por cada fabricante. Desde la aplicación de usuario se llama a las funciones del driver para configurar y capturar imágenes.

Controlador del generador basado en DDS

El controlador del generador basado en DDS se encarga de configurar los registros internos del DDS para que implemente el barrido en frecuencia adecuado a los requerimientos del usuario.

Para ello, el controlador realiza unos cálculos a partir de las especificaciones del usuario respecto a la frecuencia central y ancho de banda deseados. Como resultado, el controlador obtiene los valores de los tres registros que controlan el DDS: FTW, DFTW y DFRRW, los cuales fijan la frecuencia inicial, salto de frecuencia e intervalo de tiempo, respectivamente. Para realizar estos cálculos el controlador utiliza los datos de calibración del AOTF obtenidos en el proceso de caracterización.

El controlador realiza la programación del DDS a través de un puerto serie virtual implementado sobre una interfaz USB. El controlador también se encarga de sincronizar la cámara con el generador, de manera que cada captura se realiza cuando la salida del generador se ha estabilizado con el barrido programado.

Controlador del generador basado en DAC

El controlador del generador basado en DAC se encarga de generar la forma de onda que se usará para excitar el AOTF según los requerimientos del usuario. También se encarga de la transferencia de la forma de onda a la memoria interna del DAC y del control de su funcionamiento.

Se ha fijado la longitud de las formas de onda a 10000 puntos formando períodos completos, con lo que la resolución en frecuencia del sistema es de 100kHz. El controlador puede generar cualquier forma de onda con un número arbitrario de componentes, definiendo para cada uno su frecuencia y amplitud.

Posteriormente, la forma de onda generada se transfiere al DAC mediante un puerto serie virtual implementado sobre una interfaz USB. Una serie de comandos permite iniciar y parar la generación de la señal de RF almacenada.

Capa de usuario

El usuario del instrumento ATFS controla la captura de imágenes desde una aplicación que automatiza la adquisición a partir de los requerimientos de banda y su posterior procesado. Esta aplicación de usuario genera como resultado una imagen hiperespectral de la reflectancia o transmitancia del objeto.

Se han implementado dos aplicaciones de usuario distintas según el generador de RF utilizado.

Características de la imagen del ATFS

Las imágenes capturadas por el ATFS presenta una serie de problemas inherentes al funcionamiento de los AOTF. Los principales son: no-homogeneidad espacial, luz parásita y corriente de oscuridad (*stray light + dark current, SL + DC*), y aberración cromática (AC).

No homogeneidad espacial

La eficiencia de difracción de los AOTF no es constante en toda su superficie, por lo que las imágenes filtradas presentan una falta de homogeneidad. La no-homogeneidad es constante cuando se aplica una misma señal de RF. Por tanto, esta no-homogeneidad se puede compensar al normalizar las imágenes capturadas por otra imagen capturada en las mismas condiciones.

Esta compensación ocurre automáticamente al calcular la reflectancia o la transmitancia de un objeto mediante su normalización respecto a la imagen de la referencia blanca.

Luz parásita y corriente de oscuridad

La luz parásita es la luz que atraviesa el camino óptico del ATFS sin ser difractada por el AOTF y alcanza el sensor, debido al funcionamiento no perfecto del bloqueo del orden cero de la luz. Al mismo tiempo, en el sensor se genera una señal de ruido debido a la energía térmica, proporcional al tiempo de integración.

Conjuntamente, la luz parásita y corriente de oscuridad generan una señal en la imagen que es proporcional al tiempo de integración del sensor, y que se suma a la imagen capturada por el sensor de la luz difractada por el filtro. Esta señal se puede modelizar y por tanto quitar de las imágenes adquiridas. El modelo de esta señal parásita está expresado en la ec. 4.8. Los valores de DC_{offset} y DC_{slope} se pueden estimar a partir de dos imágenes capturadas con el AOTF apagado para dos tiempos de exposición diferentes (1 y 10 s) según la ec. 4.9.

Aberración cromática

El ángulo de salida del AOTF varía ligeramente con la frecuencia de la señal aplicada. Esto se traduce en un desplazamiento de la imagen sobre el sensor según la longitud de onda capturada (aberración cromática).

Se puede medir el desplazamiento causado por el sistema en función de la longitud de onda y compensarlo aplicando el desplazamiento inverso a cada banda adquirida.

Se ha desarrollado una serie de rutinas en MATLAB para calibrar el desplazamiento del sistema a partir de una secuencia de imágenes del mismo objeto en todo el rango de bandas, y para compensar posteriormente este desplazamiento en las imágenes adquiridas.

La calibración demuestra que el desplazamiento es lineal respecto a la longitud de onda (figuras 4.7 y 4.8). Por tanto, los desplazamientos vertical y horizontal de la imagen se definen con un polinomio de primer orden. La posterior corrección de las imágenes se realiza aplicando una transformación afín con una matriz definida por el desplazamiento horizontal y vertical correspondiente a la longitud de onda adquirida.

Adquisición de imágenes

El software de usuario automatiza la secuencia de adquisición de imágenes con el instrumento ATFS. Normalmente el usuario quiere obtener la reflectancia o transmitancia de una muestra, para lo cual hay que adquirir a parte de la muestra una referencia blanca de reflectividad conocida que sirva para normalizar los valores obtenidos.

El proceso seguido es el siguiente:

1. El usuario define las bandas a adquirir.
2. El software calcula los tiempos de exposición adecuados para cada banda. Para ello, se adquiere cada banda sobre la referencia blanca con un tiempo de exposición muy corto, y de ahí se analiza la intensidad de la imagen para obtener el tiempo de exposición que maximice el rango dinámico del sensor sin llegar a saturar.
3. Se adquieren dos imágenes de la luz parásita sobre la referencia blanca con el AOTF apagado y distintos tiempos de exposición.
4. Se adquiere la referencia blanca en todas las bandas definidas por el usuario.
5. Se adquieren dos imágenes de la luz parásita sobre la muestra con el AOTF apagado y distintos tiempos de exposición.
6. Se adquiere la muestra en todas las bandas definidas por el usuario.

El diagrama de la secuencia de adquisición se muestra en la figura 4.9.

Procesado de imágenes

El software procesa las imágenes obtenidas en la secuencia de adquisición descrita en la sección anterior, y a partir de ellas obtiene el hipercubo de reflectancia o transmitancia de la muestra. El flujo de procesado se resume en la figura 4.10. Los pasos seguidos son los siguientes:

1. Se estiman los valores del modelo de luz parásita de las imágenes a partir de las medidas de los puntos 3 y 5.
2. Se compensa la aberración cromática y la luz parásita de las secuencias de imágenes adquiridas en los puntos 4 y 6.
3. Se calcula el valor de reflectancia o transmitancia para cada banda, usando las imágenes ya corregidas, según la ec. 4.10.

Aplicación de control del ATFS

Se ha desarrollado una aplicación en la capa de usuario para controlar el instrumento ATFS a través de una interfaz de usuario gráfica. Esta aplicación realiza tanto la adquisición de los datos como el posterior procesado de los mismos. Esta aplicación funciona sobre el generador de RF basado en DDS.

Adquisición de imágenes

La figura 4.11 muestra la ventana de adquisición en la aplicación de control del ATFS. Mediante esta ventana el usuario especifica las bandas a adquirir y sus respectivos anchos de banda. A partir de estas bandas el software estima los tiempos de exposición adecuados mediante el algoritmo de auto-exposición. Este algoritmo optimiza el tiempo de exposición para cada banda de manera que el máximo nivel de gris de la imagen esté en el 90% del rango dinámico del sensor.

Estos tiempos se aplican a la adquisición secuencial de las bandas sobre la referencia blanca. Sin embargo, a la hora de adquirir la muestra se puede optimizar el rango dinámico del sistema aún más si el usuario conoce la máxima reflectividad estimada (RE) de la muestra. En este caso, se aplica un proceso de ajuste dinámico

de rango (*dynamic range adjustment, DRA*) que aumenta el tiempo de exposición de manera inversamente proporcional a la RE según la ec. 4.11.

Procesado de imágenes

La figura 4.12 muestra la ventana de procesado de la aplicación. Para cada secuencia de imágenes adquiridas, el software corrige automáticamente la aberración cromática y la luz parásita. Adicionalmente, el software puede estimar la reflectividad o la transmisividad de las muestras cuando se dispone de la información de la referencia blanca.

Librería de adquisición hiperespectral en MATLAB

Para utilizar el instrumento ATFS con el generador de RF basado en DAC hemos creado una librería de funciones en MATLAB. Esta librería contiene una serie de funciones que automatiza la adquisición, procesado y almacenamiento de las imágenes hiperespectrales. La tabla 4.1 lista las funciones implementadas en esta librería junto a su descripción.

Funcionamiento del sistema

Funcionamiento en RF

En esta sección analizamos y comparamos el funcionamiento en RF de ambos generadores de señal. Se analiza tanto el funcionamiento para la generación de señales de banda única como en el modo de generación de banda ancha.

Procedimiento experimental

Ambos generadores han sido evaluados con el mismo analizador de espectros (SA) de Anritsu (MS2661C). El SA está conectado con una interfaz GPIB a un ordenador. Este mismo ordenador se conecta al generador correspondiente por USB. Las medidas se ha automatizado con varios scripts de MATLAB que a la vez controlaban el funcionamiento del generador y adquirían los datos del SA. Las figuras 5.1 y 5.2 muestran el montaje experimental seguido.

Resultados del funcionamiento en RF

Las medidas realizadas muestran el espectro de salida del sistema para las frecuencias entre 50 y 120 MHz en pasos de 10 MHz, así como la máxima amplitud alcanzada en cada una de estas frecuencias. Las figuras 5.3 y 5.4 muestran el espectro del generador a 90MHz para ambos generadores, y las figuras 5.5 y 5.6 la amplitud máxima.

También se ha medido el funcionamiento en banda ancha, para lo cual se ha generado una señal centrada en 90MHz y un ancho de banda de 6MHz, compuesto por 11 pasos en el sistema basado en DDS y 11 bandas en el sistema basado en DAC. Los resultados se muestran en las figuras 5.7 y 5.8, respectivamente.

De estas figuras se observa que el generador basado en DAC tiene un mejor comportamiento espectral que el basado en DDS, debido principalmente a la mayor calidad del amplificador de potencia del primer sistema.

Caracterización de los AOTF

En el contexto del proyecto SmartSpectra, se han comprado tres AOTF de distintos fabricantes (ver tabla 6.1).

Hemos desarrollado una metodología de caracterización de AOTF que hemos aplicado a los tres modelos comprados. Esta metodología comprende la determinación del ángulo óptimo de incidencia del AOTF y posteriormente la evaluación de la eficiencia de difracción del cristal para una matriz de combinaciones de frecuencia y potencia de excitación. Esta caracterización se ha realizado con el generador de RF basado en DAC.

Metodología de caracterización

Colocamos el AOTF a caracterizar sobre un soporte óptico rotativo, en el camino óptico entre una lámpara colimada KI-120 de LabSphere y un espectroradiómetro FieldSpec FR de ASD. Usamos un diafragma óptico como bloqueador del haz de luz para permitir que al espectroradiómetro sólo le llegue la luz difractada.

La caracterización se realiza en tres pasos diferenciados. El primer paso consiste en la caracterización del ángulo óptimo entre el cristal y la luz incidente. Una vez determinado este ángulo, se deja fijo y se caracteriza el comportamiento espectral respecto a la variación de frecuencia y de potencia, en el segundo y tercer paso respectivamente.

La caracterización respecto al ángulo mide la respuesta del cristal para los ángulos desde -10º hasta +10º en pasos de 2º, considerando como ángulo 0º aquel que a priori era óptimo para una frecuencia de 90MHz. Para cada ángulo analizado, se ha realizado un barrido en frecuencia para todo el rango de funcionamiento de cada AOTF, con intervalos de 10MHz.

Para la caracterización del comportamiento espectral, primero se ha realizado un barrido en frecuencia, utilizando el rango de valores mostrado en la tabla 6.3. Por último, hemos caracterizado el comportamiento espectral respecto a la potencia realizando un barrido con los valores mostrados en la tabla 6.4.

Toda la caracterización se ha automatizado con una serie de scripts en MATLAB. Estos scripts sincronizaban el generador de RF con la adquisición del espectro por parte del ASD. El posterior procesado y análisis de los datos también se ha realizado sobre MATLAB.

Resultados: determinación del ángulo óptimo

A partir de los espectros adquiridos se obtiene la eficiencia de difracción relativa del AOTF dividiendo cada espectro por el espectro de la referencia blanca (ec. 5.1). Este espectro se ha obtenido midiendo la radiancia reflejada por una referencia blanca de Spectralon iluminada con la luz colimada KI-120. Cada uno de los espectros obtenidos corresponden a un filtro pasabanda, cuyas características de longitud de onda central y ancho de banda se obtienen ajustando la forma del espectro a una gaussiana (ec. 5.2). En algunos casos, la luz parásita es tan intensa como la propia luz dentro de la banda pasante, por lo que se ajusta el espectro a dos gaussianas (ec. 5.3), la primera de las cuales se ajusta a la luz parásita y la segunda corresponde a la banda pasante.

El procedimiento de análisis determina tres parámetros para cada uno de los ángulos de incidencia medidos:

- Longitud de onda central de la banda pasante.
- Eficiencia de difracción.
- Ancho de banda pasante.

A partir de estos tres parámetros obtenemos el ángulo de incidencia óptimo según cada uno, para todos los espectros adquiridos:

- menor longitud de onda.
- máxima eficiencia de difracción.
- menor ancho de banda. Como el ancho de banda depende del pico de difracción, normalizamos cada ancho de banda por su pico de difracción.

Obtenemos así tres curvas de optimización distintas que indican el mejor ángulo en función de la frecuencia de excitación.

En las figuras 6.3 a 6.10 mostramos los resultados obtenidos en el modelo AA.AOTF-3/LR de AA Opto Electronics. En este modelo de AOTF, el ángulo óptimo es cercano a los 3º. Para el modelo AOTF-MT-VIS de MolTech los resultados se muestran en las figuras 6.11 a 6.18. En este modelo el ángulo óptimo es muy cercano al considerado inicialmente (0º). Por último, los resultados del modelo TF515-230-4-5-VU1 de

Gooch & Housego se muestran en las figuras 6.19 a 6.26. En este modelo, el ángulo óptimo atendiendo al mínimo de la longitud de onda es de 4º, aunque las curvas respecto a la eficiencia de difracción y ancho de banda indican un ángulo cercano a 10º.

En general, los tres modelos tienen un comportamiento similar respecto al ángulo de incidencia. La longitud de onda central alcanza un valor mínimo para el ángulo óptimo y se incrementa cuando se desplaza el ángulo hacia los dos extremos. Por otro lado, el ancho de banda también aumenta y la eficiencia de difracción disminuye al movernos respecto al ángulo óptimo, siendo más marcado el aumento del ancho de banda para incrementos positivos del ángulo. En los modelos de AA y de Moltech hay una concordancia entre los tres parámetros analizados, mientras que en el modelo de Gooch & Housego hay una discrepancia entre el mínimo de la longitud de onda y el resto de parámetros.

Resultados: eficiencia de difracción

Se ha estudiado la variación de la eficiencia de difracción respecto a la frecuencia y a la potencia de la señal de RF de excitación del cristal. Para ello, se ha adquirido el espectro de transmisión del cristal para una serie de valores de RF con 5 potencias diferencias y otra serie de valores de potencia con 8 frecuencias distintas.

Para analizar los datos, se ha obtenido la eficiencia de difracción de cada caso restando al espectro la luz parásita y dividiendo por la radiancia de la referencia blanca (ec. 5.5). Cada espectro se modeliza como una curva gaussiana, cuyos parámetros determinan la longitud de onda central y ancho de banda del filtrado pasabanda realizado por el cristal.

En las figuras 6.27 a 6.32 vemos el funcionamiento del modelo de AA Opto Electronics respecto a la frecuencia. Observamos que la eficiencia de difracción es muy variable respecto a la frecuencia, y que para determinadas frecuencias (rango de 100MHz a 125MHz) la máxima potencia produce una eficiencia de difracción peor que para potencia menores. Al mismo tiempo, el ancho de banda sufre un incremento considerable para este rango de frecuencias a máxima potencia. Por otro lado, en las figuras 6.33 a 6.37 vemos el comportamiento de este mismo modelo respecto a variaciones de potencia. El pico de la eficiencia de difracción tiene un comportamiento gaussiano respecto a la potencia, con un valor máximo que depende de manera no lineal de la frecuencia de la señal de excitación. En casi todo el rango de excitación, el máximo de eficiencia de excitación se produce para valores de potencia por debajo del máximo recomendado por el fabricante (+33dBm).

En las figuras 6.38 a 6.43 vemos la respuesta frente a la frecuencia del modelo de Moltech. El comportamiento es muy similar al caso anterior: el valor máximo de potencia genera una eficiencia de difracción menor y un ancho de banda considerablemente mayor para un amplio rango de frecuencias. Además, la eficiencia de difracción no se ajusta a ninguna curva modelizable respecto a la frecuencia. La respuesta frente a las variaciones en la potencia de excitación se muestra en las figuras 6.44 a 6.48. El comportamiento del pico de difracción es gaussiano respecto a la potencia con un máximo en todos los casos por debajo de la potencia máxima, excepto para la frecuencia de 50MHz para la cual, en cualquier caso, la eficiencia es muy baja.

Por último, las figuras 6.49 a 6.54 muestras la respuesta del modelo de Gooch & Housego respecto a la frecuencia. El comportamiento en este caso difiere bastante de los dos modelos anteriores. La eficiencia de difracción es mayor para las frecuencias centrales y disminuye en los dos extremos del rango de funcionamiento. Por otro lado, la máxima potencia de excitación se traduce en una mayor eficiencia en todo el rango de frecuencias, mientras que el ancho de banda permanece prácticamente constante respecto a la potencia. Por último, el análisis respecto a la potencia mostrado en las figuras 6.55 a 6.59 muestra que la eficiencia parece aumentar exponencialmente respecto a la potencia y alcanza un máximo para la máxima potencia aplicada. En este modelo, el fabricante especifica una potencia máxima de excitación de 0.5W, pero si el comportamiento es gaussiano como en el resto de modelos, las curvas sugieren que se puede aplicar una potencia de excitación mayor de la especificada.

Adaptación de impedancias del AOTF

Se ha realizado un análisis de la adaptación de impedancias entre el amplificador de RF y el transductor Piezoeléctrico del AOTF. Según los fabricantes, todos los modelos utilizados tienen una impedancia de entrada al transductor de 50Ω, la cual se adapta en teoría perfectamente con la impedancia de salida del amplificador, también de 50Ω.

Para realizar este análisis, observamos con un osciloscopio la amplitud de la señal de RF de salida del amplificador aplicada al transductor. Para ello acoplamos un osciloscopio al camino de la señal mediante un conector en T (figura 6.60). La alta impedancia de entrada del osciloscopio (10MHz) permite realizar la medida sin afectar a la señal.

La figura 6.62 muestra el comportamiento de los distintos modelos de AOTF en función de la frecuencia, así como el comportamiento de una carga resistiva de 50Ω utilizada como referencia. Como muestra la figura, el comportamiento de todos los modelos excepto el de Gooch & Housego dista bastante del comportamiento ideal.

Caracterización del instrumento ATFS

En la presente Tesis hemos realizado una caracterización completa del instrumento ATFS implementado. Esta caracterización contempla el comportamiento espectral del sistema, su repetitividad a corto y largo plazo y el comportamiento térmico del AOTF que monta el sistema.

Comportamiento espectral del ATFS

Procedimiento experimental

Hemos caracterizado el comportamiento espectral del instrumento ATFS para los dos generadores de RF implementados. Para ello utilizamos la misma serie de señales de excitación empleados en la caracterización de los distintos modelos de AOTF. Sin embargo, en este caso el cristal que monta el ATFS no se coloca sobre un banco óptico experimental sino que está colocado en el montaje óptico desarrollado para el instrumento.

Antes de medir la respuesta del instrumento para cada señal de excitación, tomamos un espectro de la referencia blanca y otro de la luz parásita, para poder calcular el espectro de difracción de cada medida según la ecuación 7.1. La adquisición y el análisis se han automatizado en MATLAB.

Resultados

Las figuras 7.1 y 7.2 muestran el comportamiento del instrumento con el generador basado en el DDS para una señal de banda única y una señal multibanda, respectivamente. Las figuras 7.3 y 7.4 muestran el comportamiento equivalente para el caso del generador basado en el DAC.

Las figuras 7.5 y 7.6 muestran la eficiencia de difracción del sistema en función de la potencia aplicada, para diversas frecuencias de excitación, usando ambos generadores. Estas figuras muestran una clara mejoría del comportamiento espectral del sistema con el generador basado en el DAC, especialmente para las mayores potencias de funcionamiento. Este comportamiento concuerda con un mejor funcionamiento en RF del generador basado en el DAC.

Si observamos el comportamiento del instrumento respecto a la frecuencia de excitación para distintas potencias (figuras 7.7 a 7.10) observamos que, al igual que en los AOTF de AA Opto Electronics y MolTech, la máxima potencia de excitación produce una eficiencia de difracción menor que la producida por potencias ligeramente inferiores. Por otra lado, las curvas del pico de eficiencia respecto a la frecuencia no siguen un modelo analítico y son diferentes para cada potencia aplicada.

Repetitividad del sistema

Procedimiento experimental

Se ha comprobado el funcionamiento repetitivo del instrumento ATFS para una misma señal a corto y largo plazo. Para ello, analizamos la respuesta espectral del instrumento al aplicar repetidamente una misma serie de señales de excitación, formadas por una matriz de valores con 71 frecuencias y 5 potencias distintas. Para este análisis usamos el generador basado en el DAC.

Para la medida de la repetitividad a largo plazo, medimos la respuesta del sistema ante la matriz de señales de RF una vez por semana durante tres semanas. Cada día de medida realizamos dos series de medidas consecutivas.

Para la medida de repetitividad a corto plazo medimos la respuesta a la serie de señales de la matriz de RF por cuatro veces seguidas, sin apagar el sistema entre medias. El promedio de las medidas obtenidas se ha utilizado como calibración del controlador software del generador basado en DAC.

Resultados a largo plazo

Para este experimento se realizaron un total de 6 series de medidas, correspondientes a dos medidas por día durante tres días de medida separados una semana. Etiquetamos cada serie de medidas con una letra desde "a" hasta "f". Las figuras 7.14 a 7.15 muestran los resultados de las series de medidas "a" y "f", respectivamente. Las figuras 7.16 a 7.20 muestran el pico de la eficiencia de difracción (DE) del sistema en función de la frecuencia en todas las series de medida, para las distintas potencias aplicadas.

Del análisis de los resultados se han obtenido las figuras 7.21 y 7.22, las cuales muestran la evolución del máximo de DE a lo largo del tiempo. En ellas observamos que para cada día se produce un aumento de la DE entre la primera y la segunda serie de medidas, debido al calentamiento del sistema, pero que la medida a lo largo de los diferentes días no sufre variaciones mayores que la propia incertidumbre en la medición. De hecho, la longitud de onda central y el ancho de banda de cada serie de medidas se mantienen constantes para las seis series de medidas (figuras 7.23 y 7.24).

Resultados a corto plazo

Para este experimento realizamos cuatro series de medidas consecutivas en el mismo día. Antes de realizar la primera serie, dejamos un tiempo de calentamiento de 45min. Etiquetamos cada serie de medidas con una letra de la "a" a la "d". Como ejemplo, las figuras 7.25 y 7.26 muestran la DE del instrumento en función de la frecuencia para las series "a" y "d" de medidas, respectivamente. Las figuras 7.27 a 7.31 muestran estas mismas curvas para todas las series de medidas, separadas por potencia de excitación.

Si observamos la evolución de la DE en función del tiempo (figuras 7.32 y 7.33) vemos que el pico de DE sufre un aumento desde la primera hasta la tercera medidas y se estabiliza entre la tercera y la cuarta. Esto parece indicar que el tiempo de estabilización del sistema es mucho mayor que los 45min que hemos dado para el calentamiento de los instrumentos.

Comportamiento térmico

Hemos analizado el comportamiento térmico del AOTF 614-08 de Isomet montado en el instrumento ATFS. Para ello, hemos capturado la temperatura superficial del cristal con una cámara térmica a intervalos constantes mientras se le aplicaban una serie de señales de RF al cristal.

Hemos aplicado cada señal de RF durante 45min y hemos seguido adquiriendo la temperatura durante los 15min siguientes. Las imágenes se han capturado a intervalos de 1min. Las señales aplicadas han sido: tres señales de banda única de 60, 90 y 120 MHz, y una señal multibanda formada por 11 componentes.

Para analizar los resultados, hemos medido en cada imagen la temperatura del entorno y la de la superficie del cristal y hemos calculado su diferencia. La figura 7.34 muestra la evolución del incremento de temperatura para las cuatro señales aplicadas. En la gráfica se observa que el incremento no es significativo (unos 5ºC en el peor de los casos). El mayor incremento de temperatura corresponde a la señal de 60MHz, que coincide con la frecuencia que produce una peor eficiencia de difracción.

Funcionamiento en imagen del ATFS

Esta sección analiza el comportamiento del instrumento ATFS en la adquisición de imágenes hiperespectrales. Hemos dividido el análisis en dos partes, según el modelo del generador de RF utilizado.

Funcionamiento en imagen utilizando el generador basado en el DDS

Se ha evaluado el funcionamiento del instrumento ATFS mediante un experimento realizado durante la campaña de medidas SEN2FLEX, que tuvo lugar en Barrax (Albacete, España) durante el mes de julio de 2005. El experimento consistió en la adquisición de imágenes hiperespectrales de la reflectancia y transmitancia de las hojas de una serie de cultivos analizados en el contexto de la campaña de medidas SEN2FLEX.

En concreto, se analizaron un total de 20 hojas correspondientes a 8 tipos de cultivo distintos (tabla 8.1). En cada hoja se adquirió la reflectancia y la transmitancia de ambas caras para las bandas de 450nm a 800nm en intervalos de 10nm.

Adquisición y procesado

Se implementó un protocolo de medida que fue seguido para cada una de las muestras. El protocolo consiste en una secuencia de adquisiciones de cada hoja:

Primero se mide la reflectividad por ambas caras de la hoja, midiendo previamente la referencia blanca y la luz parásita para esa configuración.

Posteriormente, se mide la transmisividad cambiando la posición del iluminante. Previo a la adquisición de ambas caras de la hoja se mide de nuevo la referencia blanca y la luz parásita en esta configuración.

La adquisición y posterior procesado se realizó con el software de usuario implementado para el ATFS. El procesado consistió en corregir la aberración cromática y la luz parásita de cada imagen y por último dividir cada banda por su referencia blanca para obtener los hipercubos de reflectancia y transmitancia.

Resultados

Las imágenes obtenidas se han incorporado a la base de datos CDB de la Agencia Espacial Europea. En total, se generaron 180 hipercubos en formato ENVI.

Como ejemplo, mostramos en la figura 8.3 una imagen RGB reconstruida de cada tipo de hoja estudiada. La figura 8.4 muestra la imagen RGB reconstruida para las cuatro configuraciones medidas en una hoja de remolacha. Las 3 bandas utilizadas para generar cada imagen RGB se muestran en la figura 8.5.

Para comprobar el comportamiento espectral del instrumento se ha comparado el espectro obtenido sobre una hoja de remolacha con el espectro obtenido sobre la misma hoja con un espectroradiómetro puntual FieldSpec FR (figura 8.6). En la figura se muestra el espectro promedio de la zona central de la imagen y la desviación estándar. Como se puede observar, el promedio obtenido por el instrumento ATFS es muy cercano al valor del espectroradiómetro puntual, pero a la vez la gran desviación estándar muestra una variabilidad en la reflectividad de la hoja que el espectrómetro puntual no puede medir. También se ha analizado la absorción de esta hoja, medida a partir de la reflectividad y la transmisividad según la ec. 8.1 (figura 8.9).

Por último, se ha utilizado la información de la reflectividad para crear un mapa de la estimación del contenido en clorofila de la hoja, usando el índice NDVI propuesto por [Blackburn, 1998] (figura 8.10).

Funcionamiento en imagen utilizando el generador basado en el DAC

Hemos evaluado el comportamiento espacial y espectral del instrumento ATFS excitado por el generador de RF basado en el DAC. Para ello, hemos adquirido una serie de imágenes hiperespectrales de reflectividad de diversos objetos en la configuración de banda única y multibanda.

Procedimiento experimental

Los objetos analizados han sido: un calendario de colores (figura 8.11), un patrón de hojas de colores (figura 8.12) y una plantilla de resolución espacial en blanco y negro (figura 8.13). Los objetos se han iluminado

con una lámpara halógena alimentada por una fuente estabilizada. Las imágenes han sido capturadas y procesadas con la librería de adquisición hiperespectral implementada en MATLAB.

Resultados

Sobre la imagen del calendario se ha adquirido un hipercubo de imágenes de reflectancia, en el rango de 450nm a 750 nm con intervalos de 10nm. Sobre cada imagen del hipercubo se ha aplicado una corrección de la aberración cromática, una compensación de la luz parásita y por último una normalización respecto a la referencia blanca para obtener el valor de reflectancia.

La figura 8.14 muestra la imagen RGB del calendario reconstruida a partir de las imágenes obtenidas por el instrumento. La figura 8.15 muestra las tres bandas individuales de reflectancia utilizadas para formar la imagen RGB. Para comprobar el funcionamiento espectral del sistema, se ha analizado la reflectancia respecto a la longitud de onda de una serie de puntos de la imagen. Los puntos elegidos se muestran en la misma figura 8.14, y los espectros de reflectancia correspondientes en la figura 8.16.

Se ha adquirido un hipercubo de imágenes con las mismas bandas de las hojas de colores. Después de procesar las imágenes obtenidas, se ha generado la imagen RGB mostrada en la figura 8.17 (la figura 8.18 muestra las bandas individuales de esta imagen). Se ha calculado el espectro de reflectividad de cada color de la imagen, y se ha comparado con el espectro obtenido por el espectroradiómetro FieldSpec FR para cada color. La figura 8.17 muestra también el área utilizada para el cálculo, y la figura 8.19 muestra los espectros de cada color medidos con ambos instrumentos.

Sobre este objeto también se ha realizado un análisis del comportamiento del sistema utilizando señales de excitación multibanda. Para ello, hemos excitado el ATFS con un número de bandas variable y distinta separación entre ellas, y hemos comparado las imágenes obtenidas y sus histogramas con imágenes simuladas a partir de las imágenes de banda única adquiridas previamente.

En las figuras 8.20 a 8.24 mostramos los resultados obtenidos al usar una señal de excitación de 3 bandas centrada en 600nm y con una separación de 10nm y de 100nm. En las figuras 8.25 a 8.28 mostramos los resultados de utilizar 5 bandas con separaciones de 10nm y 50nm. Por último, en las figuras 8.29 y 8.30 se han empleado señales de 7 bandas separadas por 10nm y 50nm. De estas imágenes se puede concluir que la calidad de imagen empeora al emplearse señales multibanda. Además, la aberración cromática no se puede corregir en estas imágenes, y la diferencia en las eficiencias de difracción de cada banda hace que el peso de cada banda sea diferente dentro de la imagen obtenida.

Por último, se ha comprobado la resolución espacial del sistema adquiriendo diversas imágenes del patrón espacial. De las imágenes obtenidas en los experimentos anteriores se observa que la nitidez del sistema depende de la banda seleccionada. En este experimento, se evalúa si la nitidez del instrumento varía al enfocar en distintas longitudes de onda.

Para ello, se ha enfocado el instrumento mientras éste filtraba la banda de 450nm, 600nm ó 750nm, y para cada una de estos ajustes de enfoque se han adquirido tres imágenes a 450nm, 600nm y 750nm. Las 9 imágenes obtenidas se muestran en las figuras 8.31 a 8.33. En las imágenes se observa que la banda seleccionada durante el enfoque no influye en la nitidez del sistema, que en todos los casos es peor en las bandas de 450nm y 750nm que en la banda de 600nm.

Conclusiones

Esta Tesis analiza el uso de filtros ajustables acusto-ópticos (AOTF) para la realización de un sistema de visión multiespectral. En esta Tesis presentamos el diseño, implementación, verificación experimental y uso de un sistema de visión multiespectral basado en AOTF llamado *Autonomous Tunable Filtering System* (ATFS).

A continuación comentamos las actividades realizadas en esta Tesis y una propuesta de línea de trabajo futura.

Implementación de un sistema de visión multiespectral

Hemos desarrollado un instrumento denominado ATFS, que integra un AOTF con una cámara digital y un generador de señales de RF. El AOTF actúa como filtro sintonizable delante de la cámara, de manera que ésta adquiere imágenes filtradas espectralmente. La configuración del generador de RF permite seleccionar la longitud de onda filtrada en cada instante. Cambiando secuencialmente la configuración del filtro, en sincronía con la cámara, podemos obtener un conjunto de imágenes en distintas bandas espectrales de la imagen observada.

El instrumento ATFS implementado funciona en el rango espectral de 450nm a 800nm con una resolución espectral máxima de 7nm.

Hemos desarrollado dos técnicas de generación de señales de RF para excitar el AOTF. Una se basa en el uso de un sintetizador digital directo (DDS)(y la otra en el uso de un conversor digital a analógico de alta velocidad (DAC). Ambas técnicas permiten el cambio de frecuencia a gran velocidad, y por tanto la posibilidad de usar el AOTF como un filtro espectral de ancho de banda configurable, lo que supone una novedad sobre el resto de circuitos de excitación de AOTF existentes.

La técnica basada en el DDS se ha implementado como una placa de circuito impreso que integra un DDS modelo AD9858 con una etapa de amplificación de potencia formada por dos circuitos en cascada. Esta placa genera una señal de barrido en frecuencia con la que se puede implementar un filtro de banda ancha.

La técnica basada en el DAC se ha implementado con una placa de evaluación del DAC modelo MB86064 conectada a un amplificador de RF de altas prestaciones. Con esta placa podemos generar simultáneamente varias bandas de RF, lo que permite que el AOTF filtre a su vez un una banda de paso ancha o varias bandas espectrales independientes. Además, la amplitud de cada una de estas bandas se puede variar de manera independiente.

Hemos desarrollado un software de control que automatiza la captura de las imágenes, gestionando y sincronizando la cámara y el generador de RF; y que realiza el procesado de las imágenes corrigiendo los efectos de la aberración cromática y luz parásita introducidos por el instrumento.

Evaluación del funcionamiento en frecuencia del generador

Con la ayuda de un analizador de espectro, hemos evaluado el funcionamiento en frecuencia de ambos generador. Ambos circuitos generan correctamente las señales de RF, si bien el generador basado en DDS presenta una menor relación señal-ruido y más distorsión armónica. El funcionamiento en barrido del generador basado en DDS y en multibanda del generador basado en DAC funcionan también de manera correcta.

Evaluación del funcionamiento espectral de los AOTF

Usando el generador basado en DAC, hemos definido un procedimiento de caracterización que hemos usado para caracterizar espectralmente tres modelos distintos de AOTF. Estos modelos han sido fabricados por AA Opto Electronics, Gooch & Housego y MolTech.

La caracterización de estos modelos nos muestra la variación de su eficiencia de difracción respecto a los valores de frecuencia y potencia aplicadas por el generador. Cada modelo sigue unos patrones de comportamiento diferentes, lo que muestra la gran variabilidad de estos dispositivos.

Calibración del instrumento ATFS

El procedimiento de caracterización también se ha aplicado al instrumento ATFS. Con ello, hemos calibrado el sistema para realizar con él medidas cuantitativas y poder procesar las imágenes para obtener índices espectrales confiables como las medidas de reflectancia o transmitancia.

Resultados en aplicaciones de visión

La finalidad del instrumento ATFS es la adquisición de imágenes multiespectrales. Hemos demostrado el buen funcionamiento del sistema en una serie de aplicaciones de visión.

La primera aplicación ha consistido en la adquisición hiperespectral de la reflectancia y transmitancia de diversas hojas por ambas caras. Este experimento se realizó en el marco de la campaña SEN2FLEX, y sus resultados fueron incorporados a la base de datos CDB de la Agencia Espacial Europea. Las imágenes obtenidas han sido comparadas espectralmente con un espectroradiómetro de alta resolución Fieldspec FR, mostrando una alta correlación.

Una segunda aplicación demuestra el buen funcionamiento del instrumento ATFS usando el generador basado en DAC. En esta aplicación, se ha obtenido una imagen hiperespectral de la reflectancia de una serie de objetos. El comportamiento espectral del sistema es adecuado y muestra una buena correlación con los espectros obtenidos por el espectroradiómetro FieldSpec FR. La resolución espacial del instrumento es también alta excepto en el extremo más bajo del rango de funcionamiento en longitud de onda, coincidiendo con la zona de menor eficiencia espectral del AOTF.

La generación de señales de RF multibanda sin embargo ha mostrado una pequeña degradación en la calidad de las imágenes y puede acarrear dos problemas adicionales. El primero es que la aberración cromática no se puede corregir en las imágenes obtenidas. Además, como la eficiencia de difracción del instrumento no es constante respecto a la longitud de onda, las imágenes obtenidas están formadas por la contribución de cada banda en distinta proporción. Por tanto, la configuración en multibanda del generador de RF sólo se puede utilizar de manera práctica para incrementar el ancho de banda de paso del filtro mediante la aplicación de un pequeño número de bandas cercanas entre sí. Esto permite aumentar la cantidad de luz filtrada en las aplicaciones que no requieran una resolución espectral máxima.

Contribuciones a la ciencia

Esta Tesis aporta el siguiente conocimiento al campo de la visión multiespectral:

Desarrollo de nuevas técnicas de excitación de AOTF. Los dos generadores de RF descritos implementan mediante equipamiento electrónico estándar dos métodos nuevos de excitación del AOTF. Con el generador basado en DDS, se puede obtener un ancho de banda de filtrado configurable mediante un rápido barrido en RF. Por otro lado, el generador basado en DAC aporta una gran versatilidad al instrumento permitiendo adquirir varias bandas espectrales en una única captura de imagen, gracias a su capacidad de generar simultáneamente varias bandas.

Filtrado de banda ancha basado en AOTF. En los trabajos previos el uso de AOTF en aplicaciones de visión se ha centrado en la reducción del ancho de banda del instrumento. Sin embargo, el método que proponemos para aumentar el ancho de la banda pasante puede beneficiar a ciertas aplicaciones que buscan una mayor eficiencia lumínica del instrumento a cambio de una resolución espectral reducida.

Definición de un procedimiento de caracterización para el calibrado de sistemas basados en AOTF. Los AOTF exhiben un comportamiento muy diferente en función del modelo o de las características de la señal de excitación empleada. Por tanto, es importante definir un procedimiento que permita el uso de AOTF en medidas cuantitativas de manera precisa y reproducible.

Automatización de la captura y procesado de imágenes multiespectrales. La librería desarrollada en MATLAB para el control del instrumento ATFS utiliza una estructura abierta lo que permite su adaptación a diferentes modelos de AOTF o cámaras. Cualquier sistema de visión basado en AOTF se puede automatizar con esta librería en cuanto a captura de imágenes y su posterior procesado.

Demostración del funcionamiento de un sistema de visión basado en AOTF en aplicaciones espectroscópicas. Hemos ilustrado el funcionamiento del sistema en una aplicación de medida cuantitativa con la estimación de índices biofísicos en hojas. El funcionamiento espectral del sistema es comparable al obtenido con un espectrómetro puntual de alta resolución.

Trabajo futuro

El instrumento ATFS que hemos desarrollado se puede utilizar en múltiples aplicaciones de visión multiespectral. Especialmente interesante es el hecho de poder configurar el ancho de banda de filtrado, ya que esto

permite reducir la dimensionalidad del conjunto de datos hiperespectrales sin disminuir la capacidad de discriminación del mismo. Un campo en la que se puede enfocar el uso del sistema es el de la estimación de parámetros biofísicos, campo en el que hemos colaborado en diversas investigaciones [Camps-Valls et al., 2005, 2006].

Los tres modelos de AOTF caracterizados en la Tesis presenta una buena resolución espectral, por lo que son buenos candidatos para ser integrados en futuras versiones del instrumento ATFS. Por último, la calidad de imagen del instrumento se puede mejorar reduciendo el desenfoque de la imagen mediante una técnica de deconvolución, como la sugerida en [Wachman et al., 1996].

Part VII
References

References

Analog Devices Inc. (2003). EVAL-ADF4360-2EB1. *User Manual*, rev. PrC 08/03.

Bei, L., Dennis, G.I., Miller, H.M., Spaine, T.W., and Carnahann, J.W. (2004). Acousto-optic tunable filters: fundamentals and applications as applied to chemical analysis techniques (review). *Progress in Quantum Electronics*, 28:67-87.

Bowker, D. E., Davis, R. E., Myrick, D. L., Stacy, K., and Jones, W. T. (1985). Spectral reflectances of natural targets for use in remote sensing studies. *NASA Reference Publication*, 1139.

Brando, V.E., and Dekker, A.G. (2003). Satellite hyperspectral remote sensing for estimating estuarine and coastal water quality. IEEE Transactions on Geoscience and Remote Sensing, 41(6):1378-1387.

Brillouin, L. (1922). Diffusion de la lumière et des rayons X par un corps transparent homogéne - Influence de l'agitation thermique. *Annales de Physique, Series IX*, 17:88-122.

Calpe-Maravilla, J., Vila-Francés, J., Gómez-Chova, L., Ribes-Gómez, E., Muñoz-Marí J., Amorós-López, J., and Navarro, M. (2005). 2-D hyperspectral imaging systems for the retrieval of biophysical parameters. *Proceedings of the SPARC Final Workshop*, ESRIN, Frascati, Italy. ESA-WPP-250, ESA Publications Division.

Camps-Valls, G., Gómez-Chova, L., Vila-Francés, J., Amorós-López, J., Muñoz-Marí, J., and Calpe-Maravilla, J. (2005). Relevance vector machines for sparse learning of biophysical parameters. *Bruzzone, L., editor, Proceedings of SPIE International Remote Sensing Symposium 2005*, 5982.

Camps-Valls, G., Gómez-Chova, L., Muñoz-Marí, J., Vila-Francés, J., Amorós-López, J., and Calpe-Maravilla, J. (2006). Retrieval of oceanic chlorophyll concentration with relevance vector machines. *Remote Sensing of Environment*, 105(1): 23-33.

Camps-Valls, G., Gómez-Chova, L., Muñoz-Marí, J., Vila-Francés, J., Amorós, J., del Valle-Tascón, S., and Calpe-Maravilla, J.(2009). Biophysical parameter stimation with adaptive gaussian processes. *Proceedings of IEEE International Geoscience and Remote Sensing Symposium, IGARSS09*.

Carlsohn, M.F. (2006). Spectral image processing in real-time. *Journal of Real-Time Image Processing*, 1(1).

Carrasco, O., Gomez, R., Chainani, A., and Roper, W. (2003). Hyperspectral Imaging Applied to Medical Diagnoses and Food Safety. *Proc. SPIE (Hyperspectral Systems and Applications)*, 5097:215.

Casa, R., and Jones, H.G. (2004). Retrieval of crop canopy properties: a comparison between model inversion from hyperspectral data and image classification. *International Journal of Remote Sensing*, 25(6):1119-1130.

Chang, C.I. (ed.) (2007). Hyperspectral data exploitation: theory and applications. Wiley-Interscience.

Chang, I.C. (1975). Analysis of the noncollinear acousto-optic filter. *Electronic Letters*, 11:617-618.

Chang, I.C. (1976). Acoustooptic Devices and Applications. *IEEE Transactions on Sonics and Ultrasonics*, 23(1):2-22.

Chen, Y.R., Chao, K., and Kim, M.S. (2002). Machine vision technology for agricultural applications. *Computers and Electronics in Agriculture*, 36(2-3):173-191.

Chrien, T.G., Chovit, C., and Miller, P.J. (1993). Imaging Spectrometer Using a Liquid Crystal Tunable Filter. *Proceedings of SPIE (Imaging Spectrometry of the Terrestrial Environment)*, 1937:256-261.

Clark, R.N. (1999). Spectroscopy of Rocks and Minerals, and Principles of Spectroscopy. *Remote Sensing for the Earth Sciences: Manual of Remote Sensing (3rd ed.)* [chapter], 3:3-58. John Wiley & Sons.

Cogdill, R. P., and Drenne, J.K. (2005). Near infrared spectroscopy in the pharmaceutical industry. *NIR news*, 16(7):23.

Creaser, C. S., and Davies, A. M. C. (1988). *Analytical Applications of Spectroscopy*. Royal Society of Chemistry, Cambridge.

Debye, P., and Sears, F.W. (1932). On the Scattering of Light by Supersonic Waves. *Proceeding of the National Academy of Science*, 18:409-414.

Denes, L.J., Gottlieb, M.S., and Kaminsky, B. (1998). Spectro-Polarimetric Imaging for Object Recognition. *Proc. SPIE (Imaging Sensors)*, 3240(8).

Denvir, D. J., and Conroy, E. (2003). Electron-multiplying CCD: The new ICCD. *Proceedings SPIE*, 4796:164-174.

Dixon, R. (1967). Acoustic diffraction of light in anisotropic media. *IEEE Journal of Quantum Electronics*, 3(2):85-93.

Farkas, D.L., and Becker, D. (2001). Applications of Spectral Imaging: Detection and Analysis of Human Melanoma and Its Precursors. *Pigment Cell Research*, 14:2-8.

Fellers, T.J., and Davidson, M.W. (2004). Acousto-Optic Tunable Filters (AOTFs). *Olympus FluoView Resource Center webpage*, available online at http://www.olympusconfocal.com/theory/aotfintro.html

Ferwerda, J.G. (2006). Charting the quality of forage: measuring and mapping the variation of chemical components in foliage with hyperspectral remote sensing. *ITC Dissertation*, Wageningen University.

Fischer, C., and Kakoulli, I. (2006). Multispectral and hyperspectral imaging technologies in conservation: current research and potential applications. *Reviews in conservation*, 7:3-16.

Fujitsu Microelectronics (2005). MB86064 Dual 14-bit 1GSa/s DAC. *Datasheet*.

Gat, N. (2000). Imaging Spectroscopy Using Tunable Filters: A Review. *Proceedings of SPIE (Wavelet Applications VII)*, 4056:50-64.

Gates, D.M., Keegan, H.J., Schleter, J.C., and Weidner, V.R. (1965). Spectral Properties of Plants. *Applied Optics*, 4(1):11-20.

Goetz, A., Vane, G., Solomon, J., and Rock, B. (1985). Imaging spectrometry for Earth remote sensing. *Science*, 228:1147–1153.

Gómez-Chova, L. (2002). *Pattern Recognition Methods for Crop Classification from Hyperspectral Remote Sensing Images*. Dissertation Com, Boca Raton, Florida, USA.

Gómez-Chova, L., Fernández-Prieto, D., Calpe, J., E. Soria, J. V., and Camps-Valls, G. (2004). Multi-spectral and multitemporal SAR data characterization for urban monitoring. *3rd International Workshop on Pattern Recognition in Remote Sensing*.

Goutzoulis, A.P., and Pape, D.R. (Eds.). (1994). *Design and Fabrication of Acousto-Optic Devices*. Marcel Dekker.

Gowen, A.A., O'Donnell, C.P., Cullen, P.J., Downey, G., and Frias, J.M. (2007). Hyperspectral imaging - an emerging process analytical tool for food quality and safety control. *Trends in Food Science & Technology*, 18(12):590-598.

Grahn, H., and Geladi, P. (2007). *Techniques and Applications of Hyperspectral Image Analysis*. John Wiley and Sons.

Gupta, N., Dahmani, R., Gottlieb, M.S., Denes, L.J., Kaminsky, B., and Metes, M. (1999). Hyperspectral imaging using acousto-optic tunable filters, *Proceedings of SPIE (Automatic Target Recognition IX)*, 3718: 512-521.

Hamilton, S.J., and Lodder, R.A. (2002). Hyperspectral Imaging Technology for Pharmaceutical Analysis. *Proceedings of SPIE (BiOS 2002)*.

Harris, S.E., and Wallace, R.W. (1969). Acousto-Optic Tunable Filter. *Journal of the Optical Society of America*, 59:744-747.

Hatchell, D.C. (ed.) (1999). ASD Technical Guide, 3rd ed. Analytical Spectral Devices, Inc.

Hecht, D.L. (1977). Multifrequency Acoustooptic Diffraction. *IEEE Transactions on Sonics and Ultrasonics*, 24(1):7-18.

Hillman, J.J., Glenar, D.A., Kuehn, D.M., Chanover, N.J., and Blass, W.E. (2000). Compact Imaging Spectrometers using Acousto-Optic Tunable Filters. *Proceedings of the Space Astrophysics Detectors and Detector Technologies meeting 2000.*

Hynecek, J. (2001). Impactron – A New Solid State Image Intensifier. *IEEE Transactions on Electron Devices*, 48(10):2238-2241.

Kester, W. (1996). High Speed DACs and DDS System [Chapter]. *High Speed Design Techniques*. Analog Devices Technical Reference Books.

Korablev, O. et al. (2006). SPICAM IR acousto-optic spectrometer experiment on Mars Express. *Journal of Geophysical Research*, 111.

Korpel, A. (1988). *Acousto-Optics*. Marcel Dekker.

Korpel, A., and Poon, T.C. (1980). Explicit formalism for acousto-optic multiple plane-wave scattering. *Journal of the Optical Society of America*, 70(7):817-820.

Lacar, F.M., et al. (2001). Use of hyperspectral imagery for mapping grape varieties in the Barossa Valley, South Australia. *IEEE International Geoscience and Remote Sensing Symposium, IGARSS'01*, 6:2875-2877.

Lucas, R., and Biquard, P. (1932). Propriétés optiques des milieux solides et liquides soumis aux vibrations élastiques ultra sonores. *Le Journal de Physique et le Radium*, 3:464-477.

Manyak, M.J., Javitt, M., Kang, P.S., Kreuger, W.R., and Storm, E.S. (2006). The Evolution of Imaging in Advanced Prostate Cancer. *Urologic Clinics of North America*, 33(2):133-146.

Martin, M.E., Wabuyele, M., Panjehpour, M., Overholt, B., DeNovo, R., Kennel, S., Cunningham, G., and Vo-Dinh, T. (2006). An AOTF-based dual-modality hyperspectral imaging system (DMHSI) capable of simultaneous fluorescence and reflectance imaging. *Medical Engineering & Physics*, 28(2):149-155.

Molchanov, V.Y., Lyuty, V.M., Esipov, V.F., Anikin, S.P., Makarov, O.Y., and Solodovnikov, N.P. (2002). An acousto-optical imaging spectro–photometer for astrophysical observations. *Astronomy Letters*, 28(10):713–20.

Ohmachi, Y., Uchida, N., and Niizeki, N. (1972), Acoustic wave propagation in TeO_2 single crystal. *Journal of Acoustical Society of America*, 51:164–168.

Papadakis, A., Stathopoulos, E., Delides, G., Berberides, K., Nikiforidis, G., and Balas, C. (2003). A novel spectral microscope system: application in quantitative pathology. *IEEE Transactions on Biomedical Engineering*, 50(2):207-217.

Park, B., Lawrence, K.C., Windham, W.R., and Buhr, R.J. (2001). Hyperspectral Imaging for Detecting Fecal and Ingesta Contamination on Poultry Carcasses. *2001 ASAE Annual Meeting*, Paper number 013130.

Pelagotti, A., Del Mastio, A., De Rosa, A., and Piva, A. (2008). Multispectral Imaging of Paintings. *IEEE Signal Processing Magazine*, 27.

Poger, S. and Angelopoulou, E. (2001). Multispectral sensors in Computer Vision. CS Report 2001-3. *Stevens Institute of Technology*.

Romier, J., Selves, J., and Gastellu-Etchegorry, J. (1998). Imaging spectrometer based on an acousto-optic tunable filter. *Review of Scientific Instruments*, 69(8):2859-2867.

SmartSpectra team (2005a). Final State of System Prototype. *SmartSpectra project Deliverable D11.2*. Available online at http://www.smartspectra.com

SmartSpectra team (2005b). ATFS calibration. *Internal SmartSpectra Document*. Available online at http://www.smartspectra.com

SmartSpectra team (2006a). ATFS calibration procedure. *Internal SmartSpectra Document*. Available online at http://www.smartspectra.com

SmartSpectra team (2006b). ATFS RF power control. *Internal SmartSpectra Document*. Available online at http://www.smartspectra.com

SmartSpectra team (2006c). ATFS Optimal power estimation. *Internal SmartSpectra Document*. Available online at http://www.smartspectra.com

Surhe, D. R., Theodore, J. G. (1996). White-light imaging by use of a multiple passband acousto-optic tunable filter. *Applied Optics*, 35: 4494-4501.

Swatland, H. J. (1989). A review of meat spectrophotometry (300 to 800 nm). *Canadian Institute of Food Science and Technology Journal*, 22:390-402.

Tilling, A.K., O'Leary, G.J., Ferwerda, J.G., Jones S.D., Fitzgerald, G.J., Rodriguez, D., and Belford, R. (2007). Remote sensing to detect nitrogen and water stress in wheat. *Field Crops Research*, 104(1-3):77-85.

Tran, C.D. (1992). Acousto-optic tunable filter as a polychromator and its application in multidimensional fluorescence spectrometry. *Analytical Chemistry*, 64(22): 2775–2782.

Tran, C.D. (2000). Acousto-Optic Tunable Filter: A New Generation Monochromator and more. *Analytical Letters*, 33(9):1711-1732.

Treitz, P.M., and Howarth, P.J. (1999). Hyperspectral remote sensing for estimating biophysical parameters of forest ecosystems. *Progress in Physical Geography*, 23(3):359-390.

Truchetet, F., and Laligant, O. (2008). Review of industrial applications of wavelet and multiresolution–based signal and image processing. *Journal of Electronic Imaging*, 17:031102.

Vik, A. F., Krognes, T., Bjørndalsæter, S., Stoll, C., Walker, S.E., Gloslie, B., Paltiel, R., Bårde, T., and Våler, R.L. (2005). A generic database for earth observation data, ESA Campaign Data Service. *Proceedings of the 31st International Symposium on Remote Sensing of Environment*.

Vila-Francés, J. (2003). Design of the Filtering and Sensing Part of the SmartSpectra Camera. *MSc Project Dissertation*, Dept. of Electronic Engineering, University of Valencia.

Vila-Francés, J., Calpe-Maravilla, J., Muñoz-Marí, J., Gómez-Chova, L., Amorós-López, J., Ribes-Gómez, E., and Durán-Bosch, V. (2006). Configurable-bandwidth imaging spectrometer based on an acousto-optic tunable filter. *Review of Scientific Instruments*, 77.

Vila-Francés, J., Ribes-Gómez, E., Ibáñez-López, C., Gomez-Chova, L., Muñoz-Marí, J., Amorós-López, J., and Calpe-Maravilla, J. (2005). Configurable-bandwidth imaging spectrometer based on an acousto-optic tunable filter. *Proceedings of SPIE*, 5953:216-227.

Wachman, E.S, Niu, W., and Farkas, D.L. (1996). Imaging acousto-optic tunable filter with 0.35-micrometer spatial resolution. Applied Optics, 35(25):5220-5226.

Ward, J., Pannell, C.N., Wachman, E.S., and Seale, W. (2006). Applications of acousto-optic devices for spectral imaging systems. *NEOS Technologies Inc. communication*.

Xu, J., and Stroud, R. (1992). *Acousto-optic Devices: Principles, Design and Applications*. Wiley-Interscience, New york.

Yano, T., and Watanabe, A. (1976). Acoustooptic TeO_2 tunable filter using far-off-axis anisotropic Bragg diffraction. *Applied Optics*, 15(9):2250–2258.